JPL PUBLICATION 78-40

Interplanetary Approach Optical Navigation With Applications

National Aeronautics and
Space Administration

Jet Propulsion Laboratory
California Institute of Technology,
Pasadena, California

1. Report No. JPL Pub. 78-40	2. Government Accession No.	3. Recipient's Catalog No.

4. Title and Subtitle	5. Report Date
Interplanetary Approach Optical Navigation With Applications	June 1, 1978
	6. Performing Organization Code

7. Author(s)	8. Performing Organization Report No.
Navin Jerath	

9. Performing Organization Name and Address	10. Work Unit No.
JET PROPULSION LABORATORY California Institute of Technology 4800 Oak Grove Drive Pasadena, California 91103.	
	11. Contract or Grant No. NAS 7-100
	13. Type of Report and Period Covered

12. Sponsoring Agency Name and Address	JPL Publication
NATIONAL AERONAUTICS AND SPACE ADMINISTRATION Washington, D.C. 20546	14. Sponsoring Agency Code

15. Supplementary Notes

16. Abstract

An investiagtion is conducted into the use of optical data from onboard television cameras for the navigation of interplanetary spacecraft during the planet approach phase. Three optical data types are investigated – the planet limb with auxiliary celestial references, the satellite-star and the planet-star two-camera methods. Analysis and modelling issues related to the nature and information content of the optical methods are examined. Dynamic and measurement system modelling, data sequence design, measurement extraction, model estimation and orbit determination, as relating optical navigation, are discussed, and the various error sources are analysed. The methodology developed has been applied to the Mariner 9 and the Viking Mars Missions. Navigation accuracies are evaluated at the control and knowledge points, with particular emphasis devoted to the combined use of radio and optical data. A parametric probability analysis techniques is developed to evaluate navigation performance as a function of system reliabilities.

17. Key Words (Selected by Author(s))	18. Distribution Statement
Astrodynamics Systems Analysis Space Sciences (General) Lunar and Planetary Exploration (Advanced)	Unclassified – Unlimited

19. Security Classif. (of this report)	20. Security Classif. (of this page)	21. No. of Pages	22. Price
Unclassified	Unclassified	274	

HOW TO FILL OUT THE TECHNICAL REPORT STANDARD TITLE PAGE

Make items 1, 4, 5, 9, 12, and 13 agree with the corresponding information on the report cover. Use all capital letters for title (item 4). Leave items 2, 6, and 14 blank. Complete the remaining items as follows:

3. Recipient's Catalog No. Reserved for use by report recipients.

7. Author(s). Include corresponding information from the report cover. In addition, list the affiliation of an author if it differs from that of the performing organization.

8. Performing Organization Report No. Insert if performing organization wishes to assign this number.

10. Work Unit No. Use the agency-wide code (for example, 923-50-10-06-72), which uniquely identifies the work unit under which the work was authorized. Non-NASA performing organizations will leave this blank.

11. Insert the number of the contract or grant under which the report was prepared.

15. Supplementary Notes. Enter information not included elsewhere but useful, such as: Prepared in cooperation with... Translation of (or by)... Presented at conference of... To be published in...

16. Abstract. Include a brief (not to exceed 200 words) factual summary of the most significant information contained in the report. If possible, the abstract of a classified report should be unclassified. If the report contains a significant bibliography or literature survey, mention it here.

17. Key Words. Insert terms or short phrases selected by the author that identify the principal subjects covered in the report, and that are sufficiently specific and precise to be used for cataloging.

18. Distribution Statement. Enter one of the authorized statements used to denote releasability to the public or a limitation on dissemination for reasons other than security of defense information. Authorized statements are "Unclassified—Unlimited, " "U. S. Government and Contractors only, " "U. S. Government Agencies only, " and "NASA and NASA Contractors only. "

19. Security Classification (of report). NOTE: Reports carrying a security classification will require additional markings giving security and down-grading information as specified by the Security Requirements Checklist and the DoD Industrial Security Manual (DoD 5220. 22-M).

20. Security Classification (of this page). NOTE: Because this page may be used in preparing announcements, bibliographies, and data banks, it should be unclassified if possible. If a classification is required, indicate separately the classification of the title and the abstract by following these items, with either "(U)" for unclassified, or "(C)" or "(S)" as applicable for classified items.

21. No. of Pages. Insert the number of pages.

22. Price. Insert the price set by the Clearinghouse for Federal Scientific and Technical Information or the Government Printing Office, if known.

Interplanetary Approach Optical Navigation With Applications

Navin Jerath

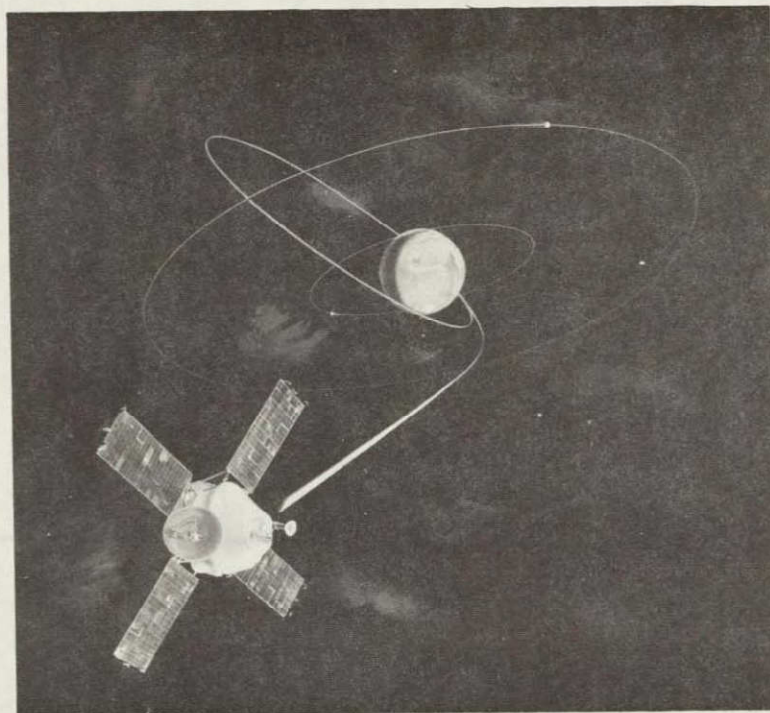June 1, 1978

O, Thomas, will a Race one day stand really tall
Across the Void, across the Universe and all?. . .
                                    —RAY BRADBURY

Ray Bradbury, When Elephants Last in the Dooryard Bloomed

PREFACE

The work described in this report was performed by the Systems Division of the Jet Propulsion Laboratory.

TABLE OF CONTENTS

LIST OF FIGURES

LIST OF FIGURES (Continued)

LIST OF FIGURES (Continued)

LIST OF FIGURES (Continued)

ACKNOWLEDGEMENT

ABSTRACT

An investigation is conducted into the use of optical data from
onboard television cameras for the navigation of interplanetary space-
craft during the planet approach phase. Three optical data types are
investigated — the planet limb with auxiliary celestial references, the
satellite-star and the planet-star two-camera methods. Analysis and
modelling issues related to the nature and information content of the
optical methods are examined. Dynamic and measurement system modelling,
data sequence design, measurement extraction, model estimation and orbit
determination, as relating to optical navigation, have been discussed.
The various error sources are analysed. The methodology developed has
been applied to the Mariner 9 and the Viking Mars Missions. Navigation
accuracies are evaluated at the control and knowledge points, with parti-
cular emphasis devoted to the combined use of radio and optical data.
A parametric probability analysis technique is developed to evaluate
navigation performance as a function of system reliabilities.

It has been determined that Optical Navigation can be a very
effective means of navigating an interplanetary spacecraft during its
approach phase to the planet, particularly with the combined use of radio
and optical data. Of the three observation methods examined the
satellite-star method is found most suited for the knowledge point and
the planet-star two-camera method for the control point. It has been
shown that optical and radio data provide complementary navigation
information and their major error sources are different; their combina-
tion yields the best results. However, delaying the maneuver timing as

much as feasible maximizes the benefit from the strength of optical data. A method developed to evaluate consistency between the optical and radio solutions is shown to be very effective in the detection of data anomalies.

CHAPTER 1

INTRODUCTION

It is in the nature of Man to explore his universe, to venture into outer space because, like the mountain, "it is there."

Functionally any exploration system must include the following three components:

i) the vehicle or means of transportation along with the associated equipment and the investigative instrumentation required for the exploration.

ii) the navigation system -- methods for directing the course of the vehicle to the desired destination and for pointing the instruments towards the desired sources of information.

iii) communication -- method of transmission of commands and retrieval of information gathered by the instruments on the craft, particularly during the navigation of largely non-autonomous vehicles.

Each of these three components is indispensable for the success of any exploratory project. However, after the vehicle has been built and the communication system and hardware set up, the principal job remaining is to navigate the craft effectively. At this point, assuming that all the hardware performs according to specifications, the navigation accuracy constitutes the chief source of uncertainty regarding the success of the mission.

1.1 Navigation for Space Exploration

Any navigation system in essence involves the relationship of two frames of reference, where one of these must be tied to the vehicle being navigated and the other to the destination. Navigation systems differ in the method employed to establish this relationship. The errors associated with the navigation system are therefore different not merely owing to the different characteristic instrumentation errors but also through the accuracy of establishing the relationship between the two frames of reference.

The earliest sophistication in the art of navigating a vehicle came about on the high seas in the use of the sextant (an optical device!) where the measurements essentially determined the orientation of the ship relative to the fixed stars in inertial space. This information was combined with a knowledge of the earth's orientation relative to the stars to determine the location of the ship on the earth, i.e., relative to an earth fixed coordinate frame of reference. This was possible since marine navigation is a two-dimensional problem, with the vehicle always (hopefully!) on the surface of the sea, and therefore orientation information is equivalent to location information.

Navigation methods developed along with the vehicles being navigated, through gyroscopic devices and acceleration sensors to radio navigation systems for aircraft. For space exploration the sole mode of navigation has historically been radio navigation wherein electromagnetic waves with stable frequency are transmitted to the spacecraft from an earth-based tracking station. The

spacecraft retransmits the signal back to the tracking station where
it is received with a change from the original frequency. This
doppler shift, Δf, in the frequency of transmitted electromagnetic
waves is used to infer $\dot{\rho}$ the instantaneous range-rate of the spacecraft
relative to the earth-based transmitting station, through the
relationship

$$\Delta f = - \frac{2\dot{\rho}}{c} f_t \quad ,$$

where,

   c = velocity of light

   f_t = transmitted frequency.

In addition the tracking station can measure the time the signal
takes to travel to the spacecraft and back again, which can be used
as a range measurement from the station to the spacecraft.

   If now the station is related to a geocentric frame of reference
and this in turn to the target, the relationship between the spacecraft
frame of reference and the target frame of reference is available. The
accuracy of this depends upon the cumulative effect of the error
sources from each of the steps in the process.

   Figure 1-1 illustrates the geometry involved in the acquisition
of radio data. The various coordinate frames of reference involved
in the process of obtaining target relative spacecraft trajectory are
indicated. The directions of the axes and the origins of the coordinate
systems are both relevant; for this simplified interpretation, the
spacecraft state vector would be referenced to each of these coordinate
frames successively:

3
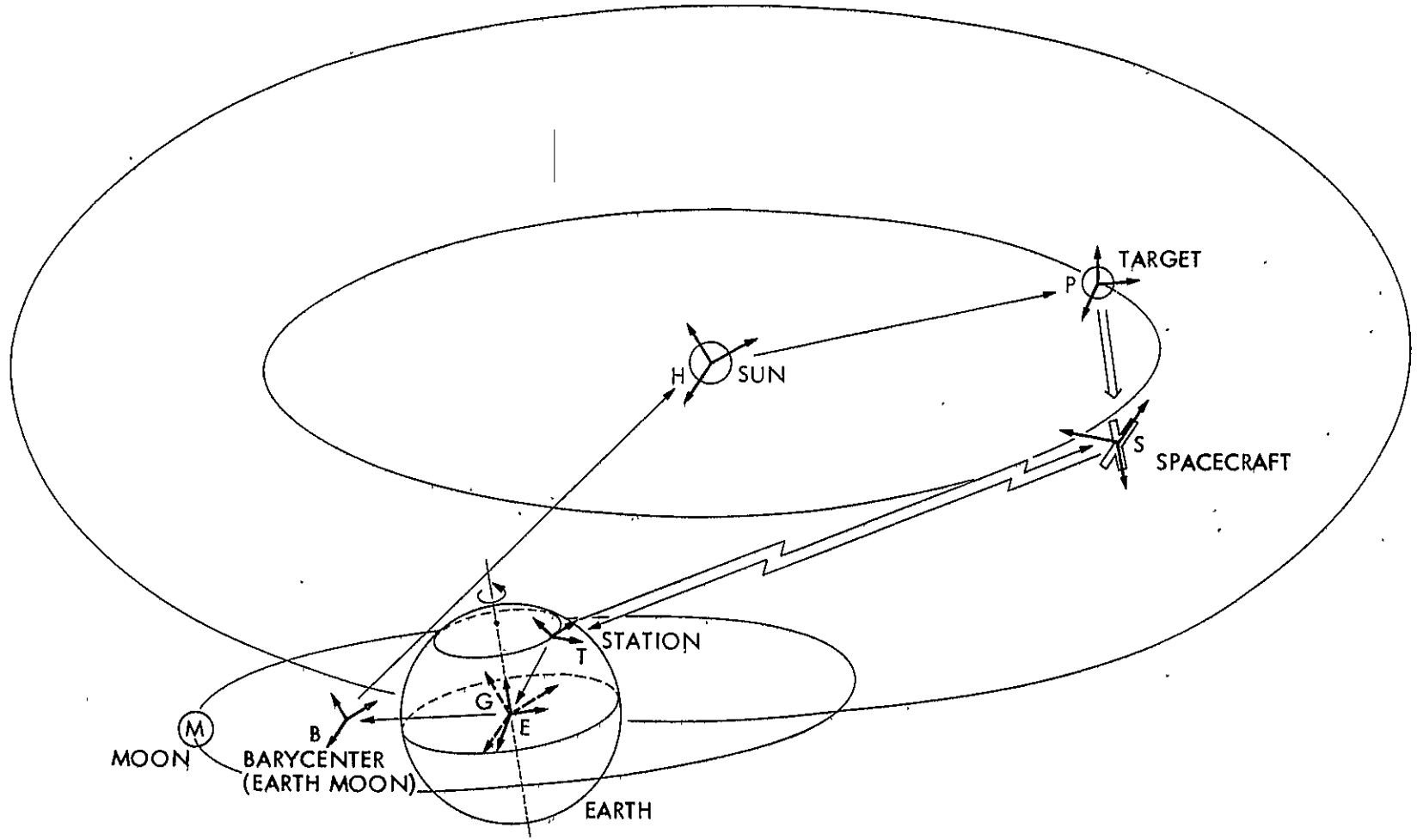
Figure 1-1. Coordinate Frames of Reference for Radio Navigation

S: The spacecraft and its coordinate system

T: Topocentric (station-centered) earth-fixed frame of reference

E: Geocentric (earth-centered) earth-fixed frame of reference

G: Geocentric space-fixed frame of reference

B: Barycentric (Earth-Moon) space-fixed frame of reference

H: Heliocentric (sun-centered) space-fixed frame of reference

P: Target centered frame of reference.

The purpose of navigation as outlined above is to (i) determine the course of the spacecraft with respect to the target along with its precision, and (ii) guide it to the desired configuration at the desired time within the desired accuracy. We restrict ourselves here largely to the former task. The problem can be regarded as the determination of the location and velocity of the spacecraft at an epoch along with a description of the accuracy of this determination. Given a model to propagate these through the use of Newton's second law and the frames-of reference involved, we can determine the target relative spacecraft state at any time.

1.2 Nature and Information Content of Radio Data

Space exploration requires very accurate determination and control of the location and destination of the spacecraft. Radio data has proved to be a powerful method for navigation particularly for near-earth spacecraft such as earth-orbiting satellites and lunar missions. The problems for interplanetary exploration, however, become much more demanding; this is particularly so for those space missions where the intent is to place the spacecraft into orbit around the target planet. To examine the reasons for the additional problems introduced in these situations we first discuss a simple model for the information content and strengths of radio navigation in this section (originally from References 1, 2, and 3). The error sources associated with it are discussed in Section 1.3.

Figure 1-2 illustrates the geometry for doppler tracking of a spacecraft from a station on the surface of the earth. The x y z frame of reference is a geocentric space fixed coordinate system with the z axis aligned with the spin axis; we disregard any errors for the discussion in this section.

The topocentric position and velocity vectors to the spacecraft, $\underline{\rho}$ and $\underline{\dot{\rho}}$, are given by

$$\underline{\rho} = \underline{r} - \underline{r}_{st} \qquad\qquad (1\text{-}2\text{-}1)$$

and

$$\underline{\dot{\rho}} = \underline{\dot{r}} - \underline{\dot{r}}_{st} \; , \qquad\qquad (1\text{-}2\text{-}2)$$
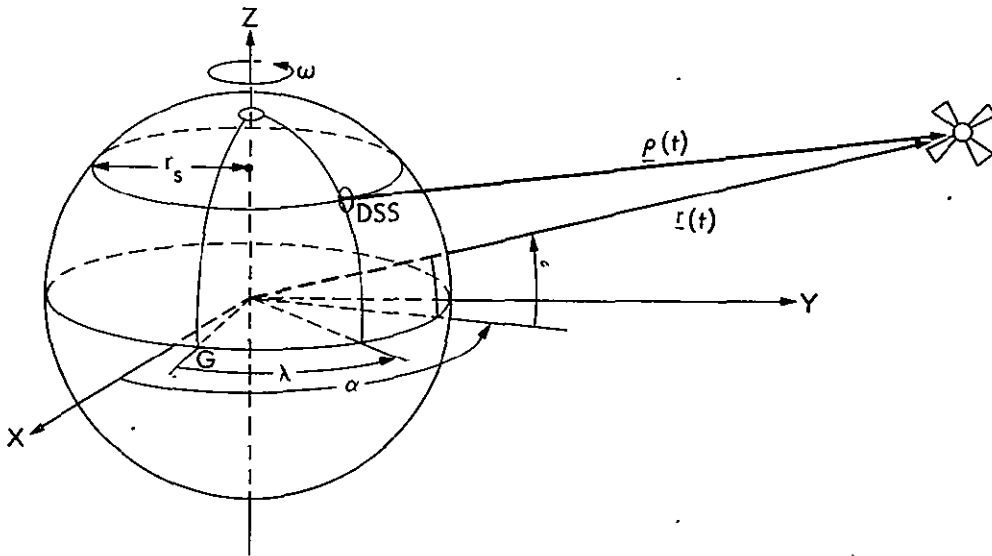
Figure 1-2. Geometry of Earth-Based Doppler Tracking
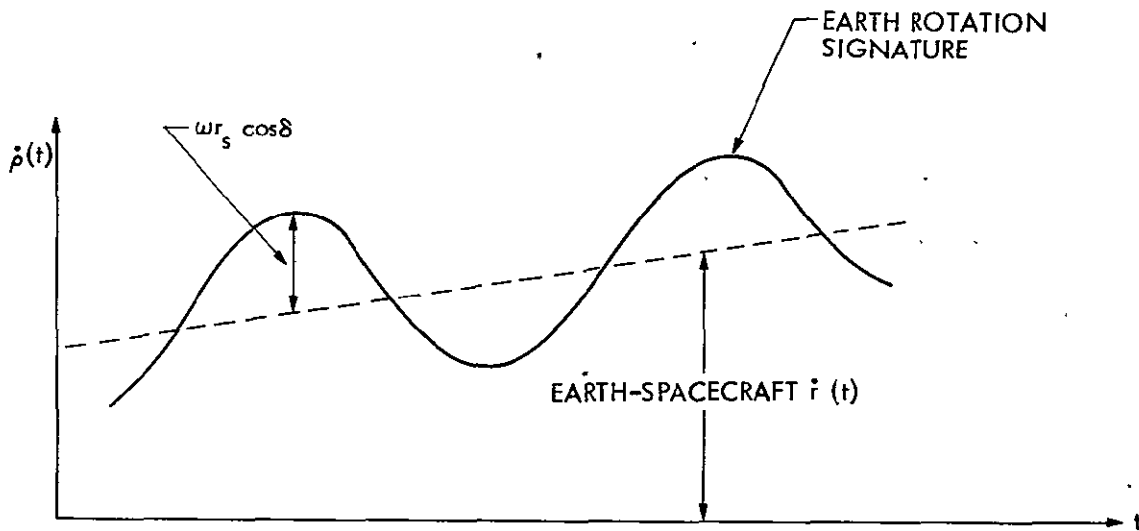
Figure 1-3. Information from Short-Arc of Doppler Data

where

$\underline{r}$ = geocentric position vector to spacecraft

$\underline{\dot{r}}$ = geocentric velocity vector to spacecraft

$\underline{r}_{st}$ = geocentric position vector to tracking station

$\underline{\dot{r}}_{st}$ = geocentric velocity vector to tracking station

From the doppler measurement $\dot{\rho}$ is therefore given by

$$\dot{\rho} = \underline{\dot{\rho}} \cdot \underline{\hat{\rho}} \, , \tag{1-2-3}$$

where

$$\underline{\hat{\rho}} = \frac{\underline{\rho}}{|\underline{\rho}|} = \frac{\underline{r} - \underline{r}_{st}}{|\underline{r} - \underline{r}_{st}|} \, . \tag{1-2-4}$$

Now, since $|\underline{r}_{st}| \ll |\underline{r}|$, we can write

$$\underline{\hat{\rho}} \approx \underline{\hat{r}} = \frac{\underline{r}}{|\underline{r}|} \, . \tag{1-2-5}$$

Equation (1-2-3) then becomes,

$$\dot{\rho} \approx \underline{\dot{\rho}} \cdot \underline{\hat{r}}$$

$$= \underline{\dot{r}} \cdot \underline{\hat{r}} - \underline{\dot{r}}_{st} \cdot \underline{\hat{r}} \, . \tag{1-2-6}$$

Letting

$\dot{r} = \underline{\dot{r}}$ = geocentric range-rate of the S/C,

ω = Earth's rotation rate,

λ = longitude of tracking station from prime meridian G,

r_s = distance of tracking station from the Earth's spin axis,

$\underline{\hat{r}}_\lambda$ = unit vector in the direction of increasing λ,

α = geocentric right ascension of the S/C,

δ = geocentric declination of the S/C,

and   t = time elapsed since coincidence of prime meridian with x axis.

8

we may write

$$\dot{r} = \underline{\dot{r}} \cdot \hat{\underline{r}} \qquad\qquad (1\text{-}2\text{-}7)$$

and

$$\underline{\dot{r}}_{st} \cdot \hat{\underline{r}} = \omega r_s \, \hat{\underline{r}}_\lambda \cdot \hat{\underline{r}} \qquad\qquad (1\text{-}2\text{-}8)$$

$$= -\omega r_s \cos\delta \, \sin(\omega t + \lambda - \alpha) \, . \qquad (1\text{-}2\text{-}9)$$

Substituting into equation (1-2-6), we obtain

$$\dot{\rho} = \dot{r} + \omega r_s \cos\delta \, \sin(\omega t + \lambda - \alpha) \, , \qquad (1\text{-}2\text{-}10)$$

which is the same result as originally derived by Hamilton and.
Melbourne in Reference 1. This indicates that the signature of one
pass of Doppler tracking data (see Figure 1-3) yields the geocentric
range rate, right-ascension and declination of the spacecraft which
are implicitly assumed to be constant over the pass. This is due to
the so-called "velocity parallax" induced by the motion of the
rotating tracking station; attention to this was originally called
in Reference 2.

From several days of tracking data it is then reasonable that
we should be able to determine the time rate of change of these
quantities -- viz the geocentric acceleration and the right ascension
and declination rates. Reference 3 showed this and pointed out that
the first of these quantities has information in it to determine
the geocentric range of the spacecraft. This was done by extending
the model to a six parameter model (References 3, 4).

$$\dot{\rho} = a + b \, \sin\omega t + c \, \cos\omega t$$
$$+ \, dt + et \, \sin\omega t + ft \, \cos\omega t \, , \qquad (1\text{-}2\text{-}11)$$

where

$$a = \dot{r}$$

$$b = \omega r_s \cos\delta$$

$$c = \omega r_s \cos\delta(\Delta\lambda - \Delta\alpha)$$

$$d = a_g + r(\dot{\alpha}^2\cos^2\delta + \dot{\delta}^2) \qquad\qquad (1\text{-}2\text{-}12)$$

$$e = -\omega r_s \sin\delta\dot{\delta}$$

$$f = -\omega r_s\{(\Delta\lambda - \Delta\alpha) \sin\delta\dot{\delta} + \dot{\alpha} \cos\delta\} \ .$$

In the expression for "d", the second term is the familiar V^2/r centripetal acceleration and a_g is the remaining geocentric acceleration due to gravitation, solar pressure etc., the centripetal acceleration term depends on the range, r. This can be supplemented by direct measurement of the range ρ as discussed in Section 1.1.

Thus all six components of a spacecraft's geocentric trajectory can be determined from a few days of Doppler tracking data. The precision, or lack thereof, with which these quantities are determined is of course the critical question, and that forms the subject of the next section.

10

1.3 Radio Navigation Error Sources and Limitations

In this section we list the major error sources for radio navigation, followed by a simple analysis of the effects of these on navigation accuracy. An excellent exposition on this topic is given in Reference 5. A slightly different viewpoint is taken here in presenting the error sources. We categorize the errors into three types:

    (i)   Measurement imprecision errors

    (ii)   Spacecraft acceleration model errors

    (iii)   Errors in relating frames of reference.

The first type of error stems from spacecraft and tracking station equipment hardware limitations. The most significant contributor of error in this category is the instability of the reference frequency in the station master oscillator. Other components include cycle slipping, ranging system biases and drifts and clock synchronization errors. In practice all these errors combined turn out to be much less significant than the other categories of errors, for the state of the art as it exists at present.

Spacecraft Acceleration Model Errors

This type of error includes any unmodeled or mismodeled forces that affect the motion of the spacecraft on its trajectory. Some of these forces are non-gravitational, resulting from un-certainties in spacecraft associated effects, e.g., solar pressure and gas leakage forces. Others are gravitational and arise from attractions by massive bodies; if the masses are not known accurately,

the computed trajectory will be in error.

1) Nongravitational: There are two principal nongravitational acceleration error sources. The first of these is caused by spacecraft generated effects such as gas leaks from the attitude control system and spacecraft propulsion system. These leaks arise from imperfections in the valve seats for these systems.

The second kind of nongravitational force is caused by the environment such as the radiation pressure due to the solar energy falling upon the spacecraft (S/C) structure.

Solar radiation pressure in the sun-S/C direction is modelled by

$$\Delta \ddot{R} = \frac{KA}{MR^2} G_R \; , \tag{1-3-1}$$

where

R is the probe-Sun distance

K is a solar radiation constant (= 1.031×10^8)

A is the spacecraft effective area normal to the sun-spacecraft direction

M is the spacecraft mass

G_R is the reflectivity coefficient

Acceleration errors from these sources are very small ($\sim 10^{-12}$ km/s^2), and are significant not for the amount by which they perturb the actual motion of the spacecraft, but rather for the way they affect the tracking data -- i.e., it is the uncertainty in the solar pressure accelerations (not the accelerations themselves) that impacts navigation accuracy.

2) Gravitational: In addition to the two types of non-

gravitational forces, a third spacecraft acceleration error source
is gravitational forces stemming from mismodelling (i) the masses
(as represented through the gravitational constants) and (ii) the
harmonic fields of the perturbing bodies. For the latter, only
the second harmonic, J_2 (of the Legendre harmonic expansion — see
Reference 6) is considered to be of any significance for the near-
planet phases of interplanetary orbit determination.

Errors in Relating Frames of Reference

We adopt the same viewpoint here as in Section 1.1, where the
frames of reference listed were, in order (see Figure 1-1),

$$S - T - E - G - B - H - P$$

$$\underbrace{\qquad}_{(1)} \quad \underbrace{\qquad}_{(2)} \quad \underbrace{\qquad}_{(3)}$$
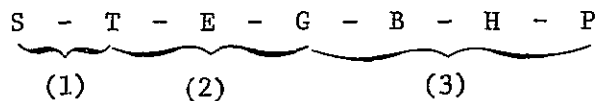
to establish the relative vector between the target P and the
spacecraft S. Errors in this category fall into three subdivisions
in accordance with the grouping of transformations indicated above.

1) Locating the spaceraft in topocentric coordinates: Errors
in this involve the effects of the intervening medium. The radio
signal in its path from the station to the spacecraft and back
again is distorted by the intervening medium through which it
travels. This occurs due to

(a) refraction effects in the earth's troposphere which cause re-
tardation and bending of the electromagnetic beam (Ref. 7); the
observation appears to have travelled through a longer distance.

(b) effects due to the radio signal interaction with charged par-
ticles in the earth's ionosphere and the plasma in interplanetary
space. The variation in particle density causes a time rate of

13

change in the ray path length (Ref. 8) and thereby introduces errors in the radio doppler measurements.

Representing the modelled spacecraft in topocentric coordinates -- i.e., relating frames of reference S and T -- therefore requires calibrating the effects in the transmission media. Residual errors after calibration corrupt the information content of the radio observations.

2) Locating the tracking station in geocentric space-fixed coordinates: This involves (a) the transformation from a topocentric frame of reference T to a geocentric earth-fixed frame of reference E and (b) the rotation from earth-fixed coordinates to the space-fixed geocentric frame G. The first consists of establishing the actual location of the tracking-station relative to the "earth-crust" by means of latitude, longitude, and radius vector, or equivalently in cylindrical coordinates -- i.e., distance from spin axis r_s, longitude λ relative to the prime meridian and height above the equator Z_s.

Errors in the rotation from E to G consist of three effects as follows:

(i) Polar motion -- the motion of the earth's crust relative to the spin axis which causes a change of position of the point on the earth's crust through which the spin axis passes (Ref. 9).

(ii) Timing irregularities caused by non-uniformities in the rotation speed of the earth. These errors can cause a degradation in the tracking data quality (Ref. 10).

(iii)   Precession and nutation models relating the instantaneous

spin axis direction to a space-fixed frame of reference.

Errors in these, however, are small (Ref. 11).

All of the effects discussed above in 1) and 2) have diurnal

signatures. At any instant their combined effects can be represented

by an equivalent set of station locations which would produce the

same effect. They are therefore referred to as equivalent

station location errors (ESLE).

3) Locating the earth in a target frame of reference: Errors

in this for an interplanetary target arise from transformations

between frames of reference (a) G and B (b) B and H and (c) H and P

(Figure 1-1).

(a) The error in the earth ephemeris relative to the earth-

moon barycenter stems primarily from uncertainties in the

precise masses of the earth and the moon; the lunar ephemeris

relative to earth is very accurately known. If $\underline{r}_B$, $\underline{r}_E$ are the

position vectors to the barycenter and the earth respectively,

in some inertial frame of reference, then by definition of

the barycenter,

$$\underline{r}_B = \underline{r}_E + \frac{\mu_M}{\mu_M + \mu_E} \ \underline{r}_{EM} , \qquad\qquad (1\text{-}3\text{-}2)$$

where

$\underline{r}_{EM}$ = earth centered lunar position vector

μ_M = gravitational constant of the moon

μ_E = gravitational constant of the earth .

Letting

$$\eta \triangleq \frac{\mu_M}{\mu_M + \mu_E} \tag{1-3-3}$$

$$\underline{r}_E = \underline{r}_B - \frac{1}{\eta} \underline{r}_{EM} \tag{1-3-4}$$

Taking variations on this equation, we obtain

$$\underline{\dot{r}}_E = \underline{\dot{r}}_B - \frac{\delta \eta}{\eta^2} \underline{r}_{EM} \tag{1-3-5}$$

where $\underline{r}_{EM}$ has been held fixed since it is very accurately determined. Ignoring $\delta\underline{r}_B$ for the present, since the effect of that is dealt with in effects (b) and (c), this yields

$$\delta\underline{r}_E = - \frac{\underline{r}_{EM}}{\eta^2} \, \delta\eta \quad . \tag{1-3-6}$$

Since $\underline{r}_{EM}(t)$ has a 28 day period, the error, $\delta\underline{\dot{r}}_E(t)$, in $\underline{r}_E(t)$ will vary in a sinusoidal fashion.

Using values

$$\eta \approx 80 \ ,$$
$$\sigma_\eta \approx 4 \times 10^{-6}$$

and
$$|\underline{r}_{EM}| \approx 4 \times 10^5 \ \text{km}$$

we obtain,

$$\sigma_{\underline{r}_E} \approx .02 \ \text{km} \ .$$

This is so small it would appear this error source is insignificant. However, differentiating Equation (1-3-6) we obtain

$$\delta\underline{\ddot{r}}_E = - \frac{\delta\eta}{\eta^2} \underline{\ddot{r}}_{EM} \quad .$$

Using an $r\omega^2$ centripetal acceleration, with

$$\omega \approx \frac{2\pi}{28} \ \text{radians/day}$$

16

this yields

$$\sigma \ddot{r}_E = \omega^2 \sigma_{\dot{r}_E}$$

$$\approx .15 \times 10^{-12} \text{ km/sec}^2 \ .$$

This is not insignificant relative to uncertainties in the unmodelled accelerations acting directly on the spacecraft, e.g., solar pressure.

(b) and (c): The second and the third of the sources of error arise from uncertainty in the Heliocentric ephemeris of the Earth-Moon barycenter and that of the target planet respectively. In our discussion later these are referred to as errors in the planetary ephemeris.

Classification of Error Sources; Effect on Navigation

It should be emphasized that the discussion above is a simplified picture of the errors. In practice correlations exist between various error sources. For instance errors in the heliocentric ephemeris of the target planet would be correlated with errors in that of the earth-moon barycenter. This is because the source of the ephemeris information is largely, if not entirely, observations taken from the earth. However, for ease in analyzing their effects, we group all the errors other than data measurement noise and random components of error, into the following classes according to their effect on navigation accuracy.

1) Equivalent station location errors (ESLEs)

2) Ephemeris errors

3) Unmodelled spacecraft accelerations.

These constitute the major error sources for space navigation based on earth-based radio data. We now discuss the effects of each class of errors keeping the discussion as simple as possible. The analysis, though greatly simplified shows some of the salient features of radio navigation limitations.

1) Effect of ESLEs

The effect of equivalent station location errors can be well represented through the Hamilton-Melbourne model. Following the terminology of Section 1.2, let Δr_s, $\Delta\lambda$ and ΔZ_s be the errors in the equivalent station location coordinates. The variation of equation (1-2-10) is given by

$$\Delta\dot\rho = \Delta\dot{r} + \omega\sin(\omega t + \lambda - \alpha)\{\Delta r_s \cos\delta - \Delta\delta\cdot r_s \sin\delta\}$$

$$+ \omega r_s \cos\delta \cos(\omega t + \lambda - \alpha)\{\Delta\lambda - \Delta\alpha\} . \quad (1\text{-}3\text{-}7)$$

The last term in Equation (1-3-7) indicates that an error in longitude will map directly into an error in spacecraft right-ascension,

$$\Delta\alpha = \Delta\lambda , \qquad\qquad\qquad (1\text{-}3\text{-}8)$$

yielding a position error in this direction given by

$$\sigma_{\ell_\alpha} = r \cos\delta \; \sigma_\lambda . \qquad\qquad\qquad (1\text{-}3\text{-}9)$$

Similarly, the second term of Equation (1-3-7) indicates that an error in station-radius produces an error in the declination of the probe

$$\Delta\delta = \frac{1}{\tan\delta} \frac{\Delta r_s}{r_s} , \qquad\qquad\qquad (1\text{-}3\text{-}10)$$

which yields a position error in this direction given by

$$\sigma_{\ell_\delta} = \frac{1}{\tan} \frac{\sigma r_s}{r_s} . \qquad\qquad\qquad (1\text{-}3\text{-}11)$$

Equations (1-3-9) and (1-3-11), show the linear dependence of the navigation accuracy for these components on the distance of the spacecraft from the earth. The latter equation also shows that the position uncertainty in this direction becomes very large when the geocentric declination approaches zero.

2) Effect of Ephemeris Errors

These are perhaps the most directly understood error sources, since the target relative spacecraft vector is the difference between the vectors to the target and to the spacecraft respectively. We note that (i) when the target is the Moon, these errors essentially vanish since the geocentric lunar ephemeris is known very accurately and (ii) the target ephemeris error increases with distance of the target from Earth since the ephemeris is established basically through observations from Earth.

3) Effect of Unmodelled Accelerations

The basic reason for these effects is the nature of the radio data. The "d" term of the six parameter model mentioned in Section 1.2 is useful in explaining the effects of the spacecraft acceleration errors. Since

$$d = a_g + r(\dot{\alpha}^2 \cos^2\delta + \dot{\delta}^2) \qquad (1-3-12)$$

and it is the only term containing r, any unmodelled acceleration will cause an error in the determination of the range from doppler tracking data. Errors in acceleration of the order of 10^{-12} km/sec^2 can cause a range error of hundreds of kilometers.

When the range data type, ρ, is included in the processing, range errors are essentially eliminated. In this case any errors in

acceleration are thrown into $\dot{\alpha}$ and $\dot{\delta}$, i.e., the velocities perpendicular to the line of sight. This does not cause errors in position at the time of the range measurement but the trajectory does not propagate well. More details on this can be found in Reference 3.

Summary

In summary then

 (i) errors in radio navigation increase as the spacecraft distance from earth increases, owing to ESLE effects and target ephemeris effects.

 (ii) particularly large errors can be induced for low geocentric declination geometries

 (iii) lunar ephemerides are much better known than the planetary ephemerides

 (iv) the unmodelled acceleration errors are peculiar to the nature of the radio data.

1.4 Optical Navigation

Optical Navigation, as used in this dissertation, is the use
of observations of celestial bodies viewed by the television
camera on-board the spacecraft to supplement the earth-based
radio data, in order to determine the orbit of the spacecraft.
In the previous sections we have seen that there are certain
limitations in the use of radio data for space navigation. As
pointed out, these limitations can become significant for trans-
lunar space exploration. The use of optical data from the TV
cameras can alleviate some of the difficulties, giving improved
navigation accuracies. As we shall see in the next chapter optical
data and radio data tend to complement each other for interplanetary
navigation; we therefore stress that the term "optical navigation"
is used in the context of the combination of radio and optical data
and not merely optical data by itself.

In our discussion we will restrict ourselves to only the
interplanetary portion of the mission where the spacecraft is
essentially in an elliptical path around the sun on a hyperbolic
trajectory relative to the target planet. As we shall see the
primary benefit in the use of optical data is gained when the
spacecraft reaches reasonably close to the planet -- how close
depends on the characteristics of the instrumentation available and
on the particular planet in question. Thus the utility of optical
navigation is primarily during the phase of the spacecraft's
"approach" towards the planet; navigation accuracies in this phase

are very important and can be quite critical. Since the laws of kinematics do not generally distinguish between the direction of motion and since the hyperbolic trajectory of one body relative to another is symmetric between the approach and departure legs, the method is equally applicable for the departure leg if there is any for the mission under consideration.

The idea of using imaging data from the television cameras turns out to be quite effective as we shall see in the following chapters, and yet is simple to execute. The simplicity arises from the fact that no additional instrumentation is required other than that which normally exists on most interplanetary spacecraft.

Instrumentation

The instrumentation that is normally aboard interplanetary spacecraft and relevant to optical navigation consists of (i) the television cameras, (ii) a platform, moveable relative to the spacecraft, upon which the television cameras are mounted along with other science instruments and (iii) an attitude control system to orient the spacecraft relative to inertial space.

The four photovoltaic solar panels in Fig. 1-4 (Ref. 12) which provide the energy for spacecraft functions, need to be oriented facing the sun. This is accomplished through the use of the sun sensor, the line of sight of which is perpendicular to the solar panels and establishes one basic orientation axis -- the spacecraft-fixed roll axis. This sensor, nominally pointed towards the sun, provides pitch and yaw axis control signals. The second reference direction required for the attitude of the spacecraft to be fixed is provided
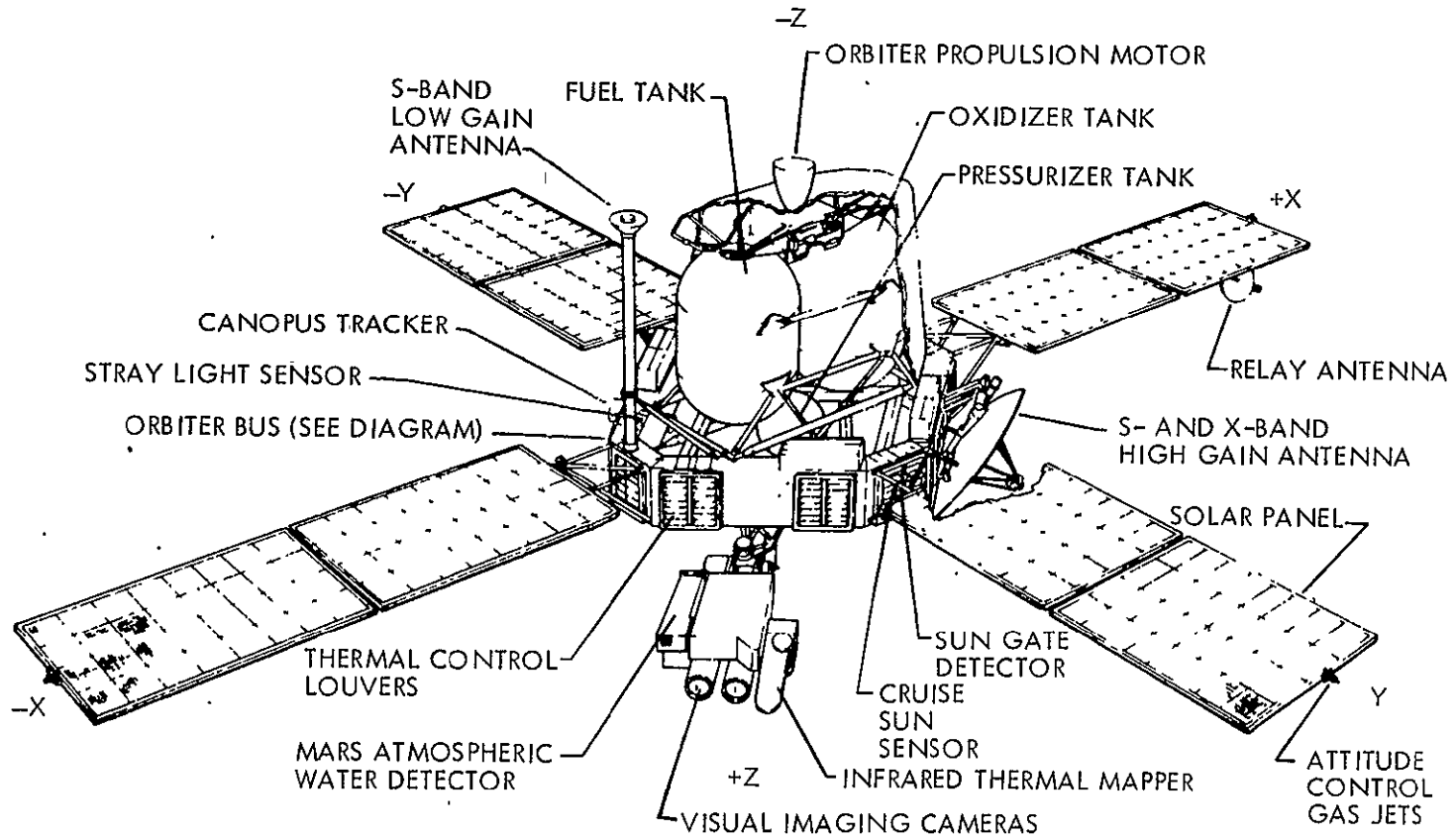
Figure 1-4. Spacecraft Schematic

by a roll axis control signal from the star tracker. The star used is normally Canopus; any bright star would do in general for this purpose so long as its direction is sufficiently non-parallel to the sun direction reference axis. The spacecraft orientation is maintained by using the pitch, yaw and roll control signals to actuate the attitude control reaction gas jets.

The television cameras along with other science instruments are mounted upon the scan platform. This is a support structure moveable relative to the spacecraft with two degrees of freedom by drive signals to the scan actuators. Platform position is detected by potentiometers mounted on the actuator shaft, yielding measurements of the two axes gimbal angles.

Observation Methods

The celestial bodies that the television cameras can view include stars, planets and satellites of planets. Figure 1-5 shows the three observation methods that we shall investigate. In the first method a sequence of pictures of the planet is taken. Orientation information for the television is derived using signals from the sun sensor, Canopus tracker and potentiometers for scan platform gimbal angles.

The second method uses the fact that the inertial directions to the stars are known very accurately -- better than 1 arc-second. Moreover, since they are extremely distant from the solar system the direction to a star is unaffected by change of position within the solar system. They can therefore provide accurate reference directions in inertial space. Thus in this method a sequence of

24

SUN SENSOR

CANOPUS
TRACKER

SCAN PLATFORM

S/C STRUCTURE

(a) METHOD (i)

OVERLAP

CAMERA 1

CAMERA 2

STARS

SATELLITE

PLANET
LIMB

STARS

(b) METHOD (ii)

(c) METHOD (iii)
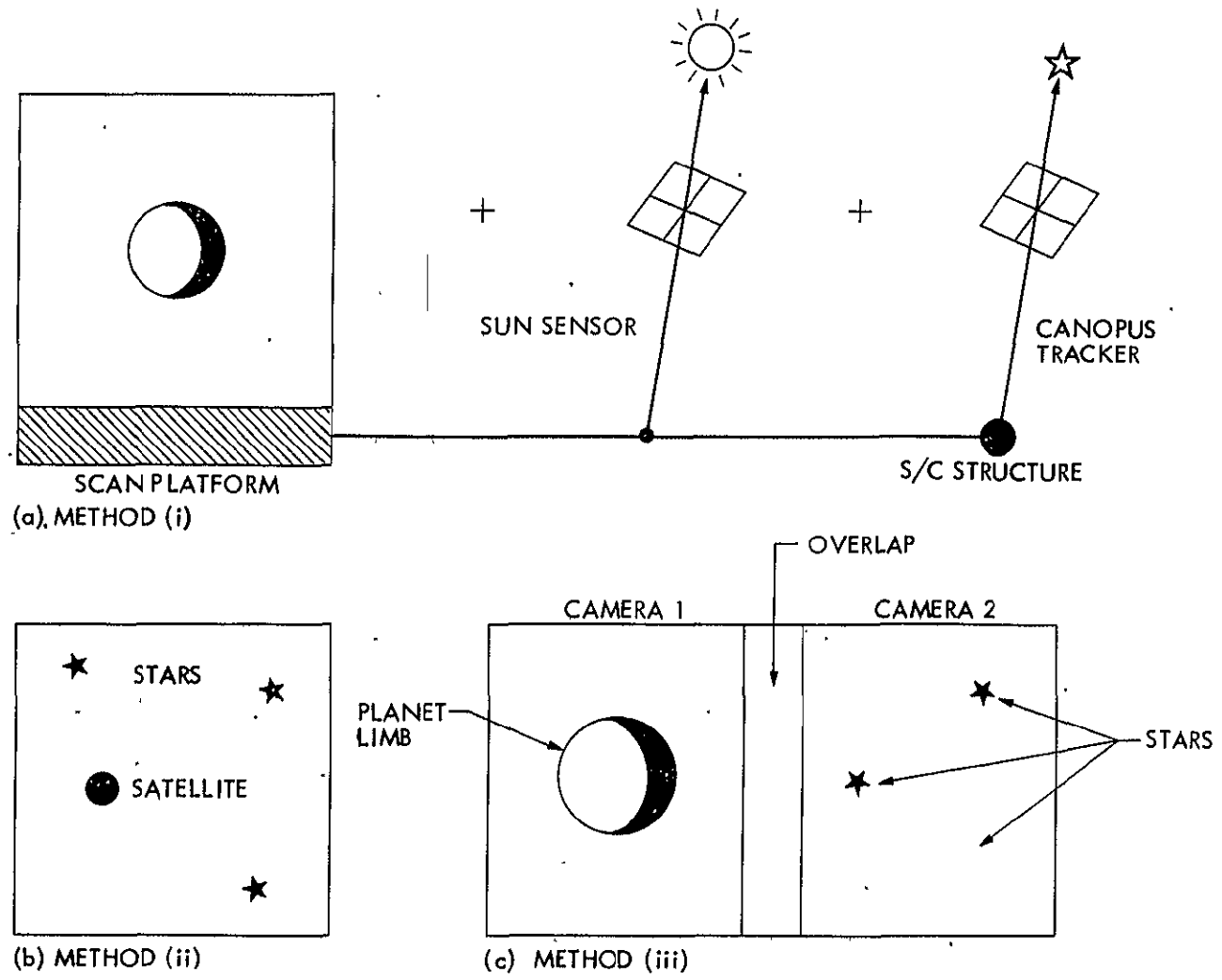
Figure 1-5. Optical Observation Types

pictures is taken, viewing the natural satellites of the target
planet against a star background. The star background serves as
an accurate reference for determining the camera pointing direction
while the natural satellite images yield the navigation information.

The second method would not normally be used to image the
planet against a star background because the planet brightness is
much larger than that of the stars. Thus camera exposure times
that would be adequate for imaging a planet would typically be too
short to simultaneously image stars in the same picture. If however
two narrow angle television cameras are available on the spacecraft
we may employ the third method where one of the cameras is used to
image the planet as in method (i), while the second is used with
longer exposure time to photograph stars. The star field, as in
method (ii), provides significantly more accurate pointing information
than is obtainable from the scan platform and attitude control
data as in method (i).

1.5 Coordinate Systems and Transformations

The major coordinate systems to be used for optical navigation

measurements are described in this section. The associated coordinate

transformations are also derived here for use later in Chapter Three.

Notation: We define a rotation R_{JK} such that

$$\underline{x}_K = R_{JK}\underline{x}_J \quad , \tag{1-5-1}$$

i.e., it is a transformation which carries a vector with components

given in system J by $\underline{x}_J$ into a vector in system K with components

given by $\underline{x}_K$. Similarly,

$$\underline{x}_J = R_{KJ}\underline{x}_K \quad , \tag{1-5-2}$$

where

$$R_{KJ} = [R_{JK}]^{-1} \quad . \tag{1-5-3}$$

We note that

(i) Since these are orthonormal matrices, we have

$$[R_{JK}]^{-1} = [R_{JK}]^{T}$$

$$= R_{KJ} \quad , \tag{1-5-4}$$

and

(ii) the associative rule holds,

$$R_{JK}\, R_{KL} = R_{JL} \tag{1-5-5}$$

Inertial xyz Coordinate System

One of the basic coordinate systems used in celestial mechanics,

and the primary system for a space-fixed frame of reference in this

dissertation is the 1950.0 Earth Mean Equator and Equinox coordinate

system (abbreviated to 1950.0 EME). The fundamental plane in this

system is the plane of the earth's mean equator as of Jan. 1 0h 1950 and the reference direction is toward the vernal equinox, which is the point of intersection of the plane of the sun's apparent motion about the earth where the sun crosses the equator from south to north. The x axis is the direction of the vernal equinox, the z axis is normal to the fundamental plane and positive toward the north, and the y axis completes a right handed system.

Celestial Coordinate System, ABC

As mentioned in Section 1.4, the orientation of the spacecraft during its flight is maintained through the use of the attitude control sensors which are nominally pointed towards the sun and Canopus respectively. The directions to these celestial bodies are used to establish the ABC Celestial coordinate system, as shown in Figure 1-6. The three axes are defined as follows:

$$\hat{c} = \text{unit vector to sun}$$

$$\hat{s} = \text{unit vector to reference star}$$

$$\hat{b} = \hat{c} \times \hat{s} / |\hat{c} \times \hat{s}|$$

$$\hat{a} = \hat{b} \times \hat{c}$$

$$\beta_s = \text{cone angle of star} = \cos^{-1} (\hat{c} \cdot \hat{s})$$

where the "cone angle" of a vector direction $\hat{p}$ is defined as the angle that the vector makes with the positive $\hat{c}$ direction (see Figure 1-7). The "clock angle" of the vector $\hat{p}$ is defined as the angle which the $\hat{c} \times \hat{p}$ vector makes with the positive $\hat{b}$ direction (see Figure 1-7).

The rotation matrix to transform a vector from the Inertial coordinate system xyz to the Celestial coordinate system ABC is

28
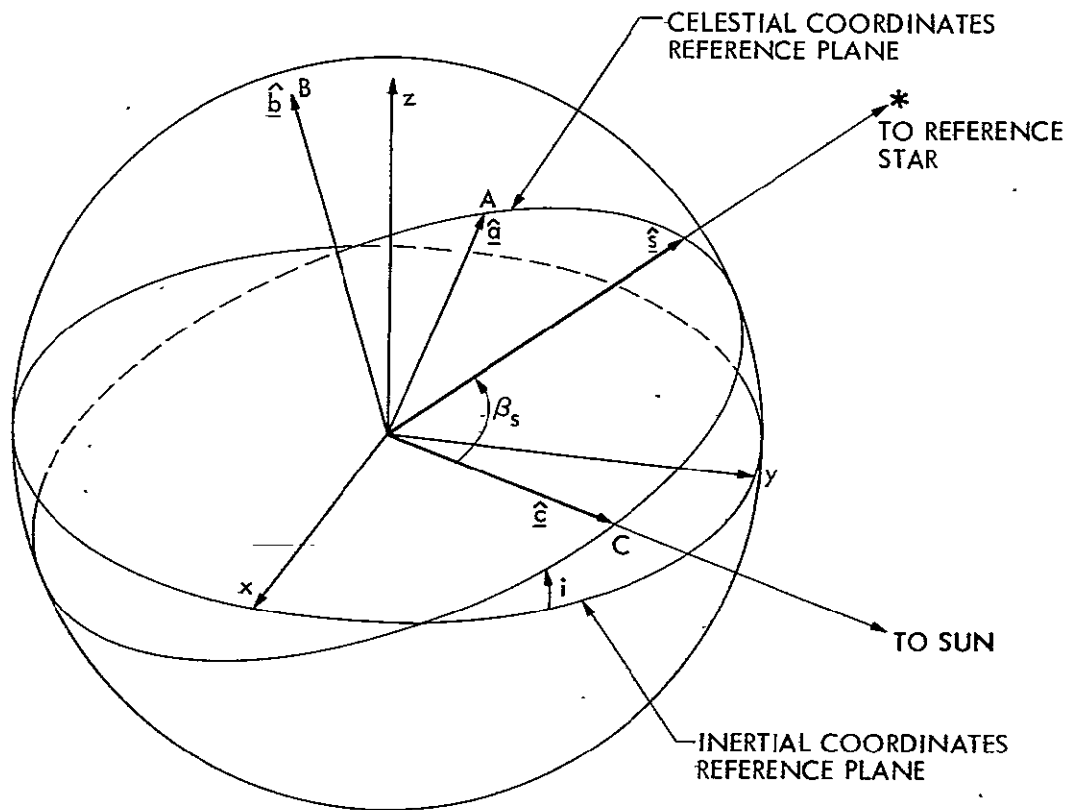
Figure 1-6. Celestial Coordinate System
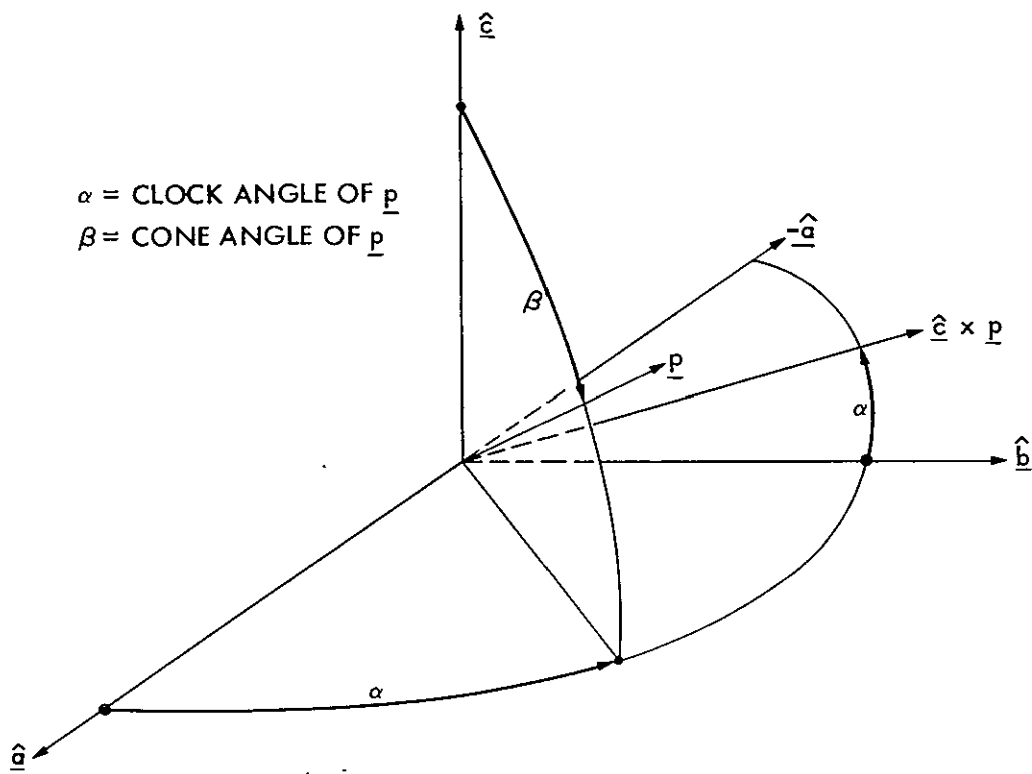
Figure 1-7.   Clock and Cone Angles

therefore given by

$$R_{IC} = \begin{bmatrix} \underline{a}^T \\ \underline{b}^T \\ \underline{c}^T \end{bmatrix} = [\underline{a} \quad \underline{b} \quad \underline{c}]^T \qquad (1\text{-}5\text{-}6)$$

or

$$R_{IC} = \begin{bmatrix} a_1 & a_2 & a_3 \\ b_1 & b_2 & b_3 \\ c_1 & c_2 & c_3 \end{bmatrix} \qquad (1\text{-}5\text{-}7)$$

where a_i, b_i, and c_i are the components of the vectors $\underline{a}$, $\underline{b}$, and $\underline{c}$ expressed in the inertial xyz system.

Spacecraft-Fixed Coordinate Systems

There are basically two spacecraft structure related coordinate systems. They are (i) the sun-star sensor coordinate system, S, and (ii) the spacecraft attitude control sensor related coordinate system, X.

(i) Corresponding to the celestially referenced ABC Celestial coordinate system, it is useful to define a Spacecraft-fixed coordinate system S_A S_B S_C which would coincide with the ABC system when the pitch, yaw, and roll attitude control system signals are zero. It is emphasized that this is a system of coordinates physically related to the instruments -- the sun sensor and the Canopus tracker -- in the spacecraft. When these sensors are pointed exactly towards the sun and Canopus, respectively, the system is coincident with the C system and the pitch, yaw, roll angles

31

are zero.

(ii) XYZ is the spacecraft pitch, yaw, and roll control axis coordinate system and is defined relative to the fixed spacecraft configuration as shown in Figure 1-4. The X and Y axes are aligned along the solar panels and the Z axis is antiparallel to the S_c axis of the spacecraft-fixed sun-star sensor coordinate system.

It is convenient at this point to introduce a new <u>celestial</u> coordinate system $X_o Y_o Z_o$ such that if the pitch, yaw, and roll control signals are all zero the $X_o Y_o Z_o$ system would be coincident with the XYZ system. This implies that the $X_o Y_o Z_o$ system has the same relationship to the ABC system as the XYZ spacecraft-fixed system has to the $S_A S_B S_C$ (also spacecraft-fixed) system.

As shown in Figure 1-8, a rotation $R_{CX_{01}}$ through the angle α_x about the C axis (axis # 3) followed by a 180° rotation about the X axis (axis # 1), $R_{CX_{02}}$, takes the ABC coordinate system to the $X_o Y_o Z_o$ system.

The rotation from ABC to $X_o Y_o Z_o$ is therefore given by

$$R_{CX_0} = R_{CX_{02}} \; R_{CX_{01}}$$

$$= \begin{bmatrix} 1 & 0 & 0 \\ 0 & -1 & 0 \\ 0 & 0 & -1 \end{bmatrix} \begin{bmatrix} \cos \alpha_x & \sin \alpha_x & 0 \\ -\sin \alpha_x & \cos \alpha_x & 0 \\ 0 & 0 & 1 \end{bmatrix}$$

$$= \begin{bmatrix} \cos \alpha_x & \sin \alpha_x & 0 \\ \sin \alpha_x & -\cos \alpha_x & 0 \\ 0 & 0 & -1 \end{bmatrix} \qquad (1\text{-}5\text{-}8)$$

-Z = TO SUN

L = PLATFORM POINTING DIRECTION

$\underline{N} = -\underline{Z} \times \underline{L} / |\underline{Z} \times \underline{L}|$

$\underline{M} = \underline{N} \times \underline{L}$

α = CLOCK ANGLE TO $\underline{L}$

β = CONE ANGLE TO $\underline{L}$

$\underline{P}$ = INSTRUMENT POINTING DIRECTION

$\underline{Q}$ = $\underline{P}$ PROJECTED ONTO THE $\underline{L}-\underline{M}$ PLANE

ψ = CONE OFFSET ANGLE OF $\underline{P}$ = $\angle$ LOQ IN THE
$\underline{L}-\underline{M}$ PLANE. POSITIVE ANGLE MEASURED FROM
L TOWARD $+\underline{M}$.

X = CROSS-CONE OFFSET ANGLE OF $\underline{P}$ = ANGLE OF
INCLINATION OF $\underline{P}$ TO THE $\underline{L}-\underline{M}$ PLANE.
POSITIVE INCLINATION MEASURED TOWARD $+\underline{N}$.
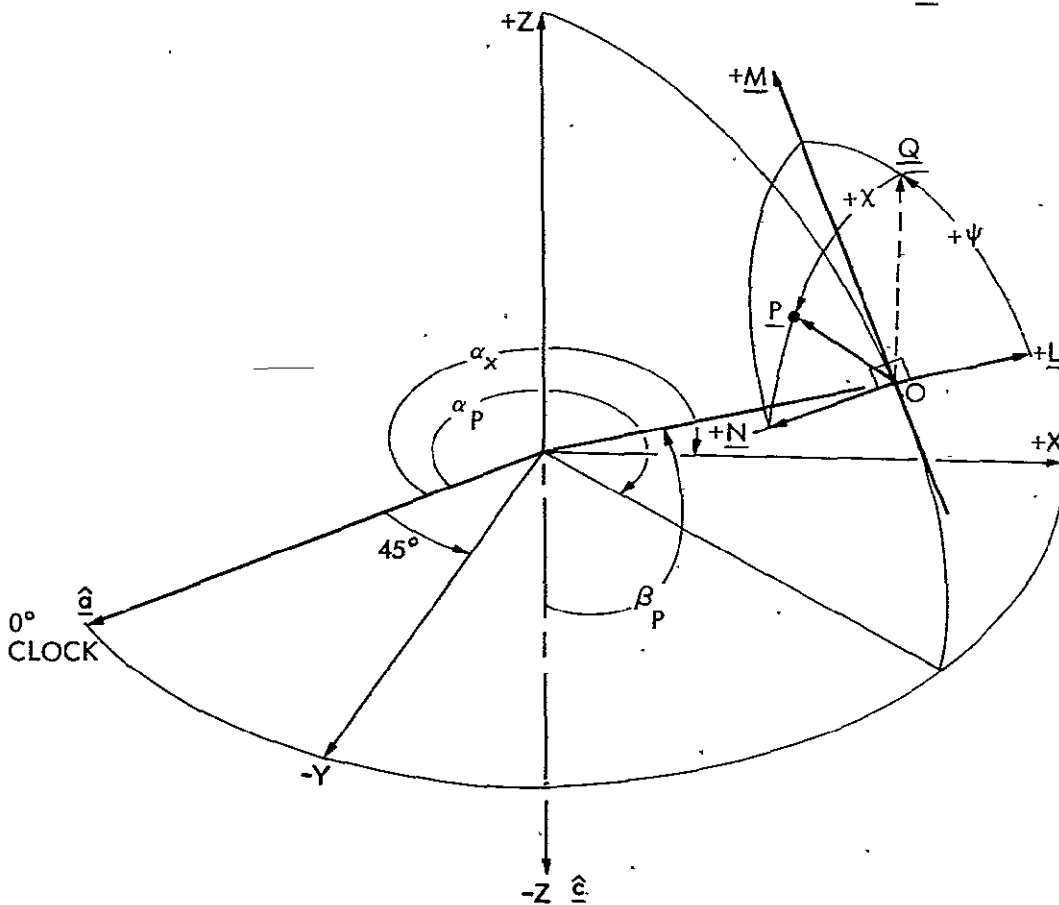
Figure 1-8. Spacecraft/Scan Platform Coordinate
System Relationship

33

To rotate from the $X_o Y_o Z_o$ system to the XYZ system requires rotating about the pitch (X) axis, yaw (Y) axis, and roll (Z) axis through the angles θ_p, θ_y, θ_r respectively. The angles θ_p, θ_y, and θ_r are determined from the control system signal voltages from the sun sensor (pitch and yaw signals) and the star tracker (roll signal). The three rotation matrices are, respectively,

$$R_{X_0 X_1} = \begin{bmatrix} 1 & 0 & 0 \\ 0 & \cos\theta_p & \sin\theta_p \\ 0 & -\sin\theta_p & \cos\theta_p \end{bmatrix} \qquad (1\text{-}5\text{-}9)$$

$$R_{X_0 X_2} = \begin{bmatrix} \cos\theta_y & 0 & -\sin\theta_y \\ 0 & 1 & 0 \\ \sin\theta_y & 0 & \cos\theta_y \end{bmatrix} \qquad (1\text{-}5\text{-}10)$$

and

$$R_{X_0 X_3} \begin{bmatrix} \cos\theta_r & \sin\theta_r & 0 \\ -\sin\theta_r & \cos\theta_r & 0 \\ 0 & 0 & 1 \end{bmatrix} \qquad (1\text{-}5\text{-}11)$$

The transformation $R_{X_0 X}$ is then given by combining Eqs. (1-5-9), (1-5-10) and (1-5-11),

34

$$R_{X_0 X} = R_{X_0 X_3} \, R_{X_0 X_2} \, R_{X_0 X_1}$$

$$= \begin{bmatrix} \cos\theta_r \cos\theta_y & \sin\theta_r \cos\theta_p + \cos\theta_r \sin\theta_y \sin\theta_p & \sin\theta_r \sin\theta_p - \cos\theta_r \sin\theta_y \cos\theta_p \\ -\sin\theta_r \cos\theta_y & (\cos\theta_r \cos\theta_p - \sin\theta_r \sin\theta_y \sin\theta_p) & \cos\theta_r \sin\theta_p \\ & & +\sin\theta_r \sin\theta_y \sin\theta_p \\ \sin\theta_y & -\cos\theta_y \sin\theta_p & \cos\theta_y \cos\theta_p \end{bmatrix}$$

$$(1\text{-}5\text{-}12)$$

The rotation transforming from the spacecraft XYZ system to the Spacecraft $S_A \, S_B \, S_C$ system, R_{XS} is just the inverse of the transformation from the Celestial ABC system to the $X_0 Y_0 Z_0$ system, R_{CX_0} obtained in Eq. (1-5-8). Using Eq. (1-5-4) we have

$$R_{CX_0} \equiv R_{SX} = R_{XS}^{-1} = R_{XS}^{T} \qquad (1\text{-}5\text{-}13)$$

We observe from Eq. (1-5-8) that R_{CX_0} is a symmetric matrix for the particular definition of the XYZ system here, therefore

$$R_{XS} = R_{CX_0} .$$

This would not be true in general. Here, then

$$R_{XS} = \begin{bmatrix} \cos\alpha_x & \sin\alpha_x & 0 \\ \sin\alpha_x & -\cos\alpha_x & 0 \\ 0 & 0 & -1 \end{bmatrix} . \qquad (1\text{-}5\text{-}14)$$

The composite rotation from the Celestial ABC system to the Spacecraft $S_A \, S_B \, S_C$ system is then given by

$$R_{CS} = R_{XS} \, R_{X_0 X} \, R_{CX_0} \qquad (1\text{-}5\text{-}15)$$

which is equivalent to writing

$$R_{CS} = R_{XS} \; R_{X_o X} \; R_{SX}$$

$$\phantom{R_{CS}} = R_{XS} \; R_{X_o X} \; R_{XS}^{\;T} \qquad\qquad (1\text{-}5\text{-}15a)$$

$$\phantom{R_{CS}} = R_{XS} \; R_{X_o X} \; R_{XS}$$

Scan Platform Coordinate System

This Platform MNL coordinate system is defined relative to the spacecraft coordinate system through the clock angle α_p and the cone angle β_p (as shown in Figure 1-8) of the Scan Platform pointing vector $\underline{\ell}$. The L axis is in the direction of $\underline{\ell}$, the M axis is in the direction of increasing cone angle β_p and the N axis is in the direction of increasing clock angle α_p.

The transformation from the Spacecraft to Platform coordinates, R_{SP}, can be written as

$$R_{SP} = R_{P_\alpha P} \; R_{SP_\alpha} \qquad\qquad (1\text{-}5\text{-}16)$$

where

R_{SP_α} = transformation from spacecraft coordinates to P_α

coordinates, through a clock angle rotation α_p

$R_{P_\alpha P}$ = transformation from P_α coordinates to Platform

coordinates through a cone angle rotation β_p.

These are given by

$$R_{SP_\alpha} = \begin{bmatrix} \cos\alpha_p & \sin\alpha_p & 0 \\ -\sin\alpha_p & \cos\alpha_p & 0 \\ 0 & 0 & 1 \end{bmatrix} \qquad\qquad (1\text{-}5\text{-}17)$$

$$R_{P_\alpha P} = \begin{bmatrix} \cos \beta_P & 0 & -\sin \beta_P \\ 0 & 1 & 0 \\ \sin \beta_P & 0 & \cos \beta_P \end{bmatrix} \qquad (1\text{-}5\text{-}18)$$

The angles α_P and β_P are determined from clock and cone gimbal potentiometer signals.

Television Camera Coordinate System

The Television Camera MNL coordinate system definition relative to the Platform MNL coordinates is also shown in Figure 1-8; arriving at the television camera coordinates involves three successive rotations through angles ψ, χ, and ω; these must be taken about the positive N axis, the negative M axis and the positive ℓ axis, respectively. The rationale for defining the coordinates in this fashion is the following:

positive ψ => increasing β ;

positive χ => increasing α (for small ψ angles);

positive ω => positive rotation about $\underline{\ell}$, the look direction;

and therefore the angles are referred to as the cone, cross-cone, and rotation offsets.

The transformation from Platform coordinates to Television coordinates is given by

$$R_{PT} = R_{PT_3} R_{PT_2} R_{PT_1} \qquad (1\text{-}5\text{-}19)$$

where

$$R_{PT_1} = \begin{bmatrix} \cos \psi & 0 & -\sin \psi \\ 0 & 1 & 0 \\ \sin \psi & 0 & \cos \psi \end{bmatrix} \qquad (1\text{-}5\text{-}20)$$

$$
R_{PT_2} = \begin{bmatrix} 1 & 0 & 0 \\ 0 & \cos\chi & -\sin\chi \\ 0 & \sin\chi & \cos\chi \end{bmatrix} \tag{1-5-21}
$$

and

$$
R_{PT_3} = \begin{bmatrix} \cos\omega & \sin\omega & 0 \\ -\sin\omega & \cos\omega & 0 \\ 0 & 0 & 1 \end{bmatrix} \tag{1-5-22}
$$

Substituting (1-5-20) to (1-5-22) into (1-5-19) we obtain

$$
R_{PT} = \begin{bmatrix} \cos\psi\cos\omega - \sin\psi\sin\chi\sin\omega & \cos\chi\sin\omega & -\sin\psi\cos\omega - \sin\chi\cos\psi\sin\omega \\ -\cos\psi\sin\omega - \sin\psi\sin\chi\cos\omega & \cos\chi\cos\omega & \sin\psi\sin\omega - \cos\psi\sin\chi\cos\omega \\ \cos\chi\sin\psi & \sin\chi & \cos\chi\cos\psi \end{bmatrix}
$$

$$\tag{1-5-23}$$

Composite Transformations

The overall transformation from inertial to television coordinates is given by

$$
R_{IT} = R_{PT}R_{SP}R_{CS}R_{IC} \tag{1-5-24}
$$

where R_{CS} is given by

$$
R_{CS} = R_{SX}^T R_{X_oX} R_{SX} \tag{1-5-25}
$$

and where R_{SP} and R_{PT} are given by Eqs. (1-5-16) and (1-5-19), respectively.

Through the use of the sensor angles θ_p, θ_y, θ_r, α_p and β_p these relationships then yield the transformations to go from an inertial frame of reference to a television frame of reference.

1.6 Historical Perspective and Scope of the Dissertation

In this section we give an outline of the historical background of optical navigation, followed by a synopsis and a brief description of the scope of this dissertation.

As outlined in Section 1.1 space navigation began with the use of radio data for the early earth orbiters and for·subsequent lunar exploration. Radio navigation methods developed through the years into use for interplanetary missions. The area of optical navigation is a relatively new one, pioneered over the last few years.

A simplified investigation was made in Reference 13 to make a preliminary assessment of the use of an onboard navigation instrument. After the proposal for exploiting the "Grand Tour" mission (Ref. 14) opportunities for multiple encounters with the outer planets, there was interest (Ref. 15) in an on-board capability for interplanetary navigation exploring the use of various instruments such as the sextant (Ref. 16) and the planet sensor (Refs. 17 and 18). The use of an onboard television camera to view the planet (method (i)) was suggested in Ref. 18 and a feasibility demonstration, made in Ref. 19. Reference 20 proposed the use of satellite-star data (method (ii)) using a television camera for navigation of the Grand Tour missions. Further studies on the effects of spacecraft acquired optical measurements upon the orbit determination of two Grand Tour trajectories were carried out in Ref. 21. The particular camera configuration in the Viking Mission made the two-camera planet-star method — method (iii) — possible, and Ref. 22 made a preliminary relative evaluation of the three methods. An in-depth application of the satellite-star and planet limb methods

was studied in Refs. 23 and 24 respectively. With interest aroused in optical navigation, the emergence of the Mariner-Jupiter Saturn mission led investigators (Ref. 25) to study the requirements for the quality of radiometric and optical data.

In the following, Chapter 2 deals with analysis and modelling issues related to the nature of the optical observation methods. Beginning with the definition of the data type, we continue with an examination of light time and stellar aberration effects, and their interaction. The errors affecting the optical data are classified according to their effects and an analysis is made of the information content of the data.

Chapter 3 describes the overall functions involved in spacecraft navigation. These functions include dynamic and measurement system modelling, data sequence design, measurement extraction, model estimation and orbit determination. The relevant details as applicable to optical navigation, for each of these functions, are developed here.

In Chapter 4 we present the application of the satellite-star and the planet-limb (one camera) methods to data obtained from the Mariner 9 mission. This includes analysis of optical navigation sensitivities to significant parameters, with an emphasis on sensitivity to the amount of radio tracking data used.

Chapter 5 uses the Viking Mission to examine in detail navigation accuracies obtained with the use, respectivity, of radio plus optical data and of optical data only. This is done for the satellite star and the planet-star two camera methods. The sensitivity to the timing of the midcourse maneuver is examined. In addition, a general method is

developed for evaluating the consistency between any two estimates. An application of this method, with interesting results, has been made using radio and optical estimates from simulated data. Finally we develop a parametric probability analysis to evaluate overall navigation system performance as a function of optical system reliabilities.

CHAPTER 2

OPTICAL DATA ANALYSIS AND MODELLING

INTRODUCTION

The optical data types concept was introduced in the first chapter. In this chapter, we shall first formalize the concept to define the data type and observation model with respect to the coordinate system in which they are measured in Section 2.1.

In Section 2.2 we shall examine the basic geometrical relationships between the S/C and the celestial bodies involved in the interplanetary navigation problem and how this relates to the optical navigation data. This is followed by a discussion of the effects of the finite velocity of light on the data recorded. These effects consist of an interaction of light-time and stellar aberration. After these are factored in, the definition of the data type is complete.

The next section, Section 2.3, deals with the sources of error contributing to the inaccuracy of the optical navigation process. The magnitude of the errors are presented along with a discussion of the reasons for these.

Section 2.4 examines the basic information content in the data as it relates to the determination of the orbit of the spacecraft. This information is studied in the context of the desired navigation data we are seeking. From the analysis presented here, restricted to two dimensions so as not to confuse the basic issues involved, some conclusions regarding the observability of the system have been drawn.

2.1 Definition of Data Types

The images viewed by the television camera for optical navigation can be a planet, one or more of its satellites and stars.

The optical data types are defined to be the centers of the images of the objects in TV coordinates as viewed in the picture. These are defined relative to the scanning process as illustrated in Fig. 2-1a.

After the camera is shuttered, the light falling on the photosensitive vidicon surface causes electron-hole pairs to be created due to the photoelectric effect, leaving a net positive charge on the surface of the vidicon. The amount of charge is a function of the number of photons striking the surface. This charge is then erased by a read-out beam which electronically scans the surface of the vidicon in a matrix of MxN digitized samples. The sampling is accomplished with the use of pulses of electrons falling over a certain "sample area" which shifts from pulse to pulse due to a horizontally imposed ramp bias to scan along a line (see Fig. 2-1(b). After the end of the line the value of the ramp bias restarts at zero and simultaneously the vertical bias shifts the sample area in the vertical direction to begin the next sampling line. Each sample area is called a picture element or "pixel." The magnitude of the current read by each pulse gives the amount of charge for that sample and this can be related in turn to the intensity of light falling upon the vidicon surface at that pixel. The resulting charge read for various samples is digitized in n binary levels which
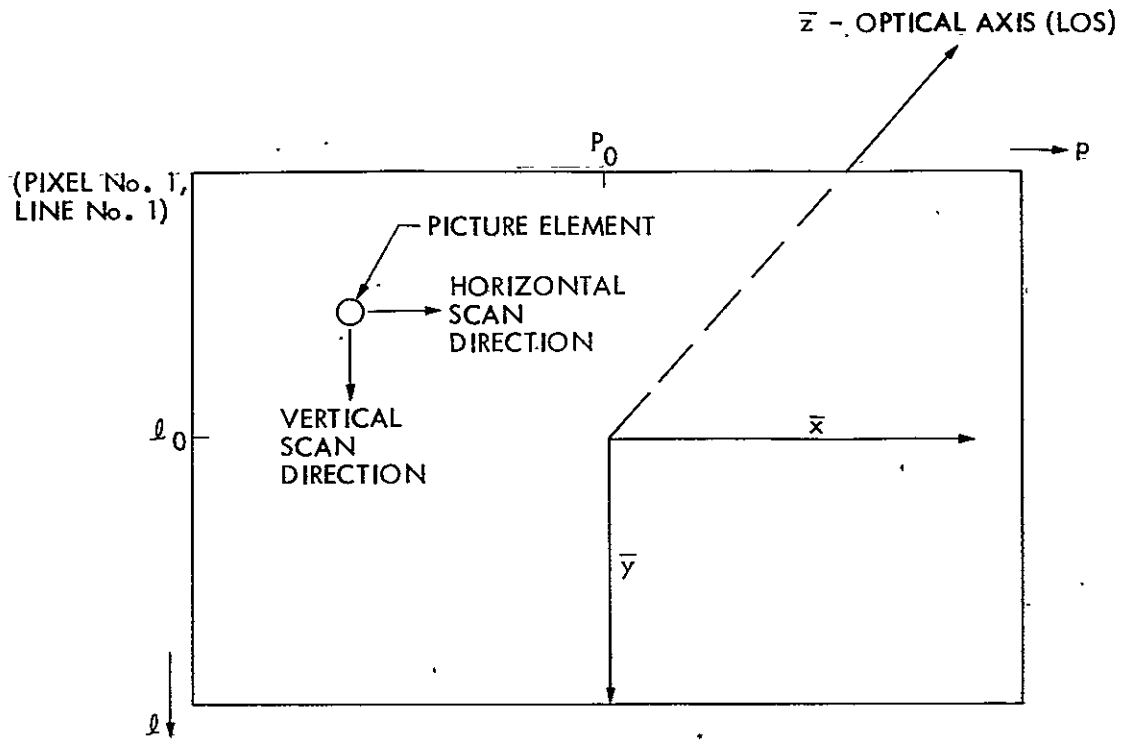
Figure 2-1 (a). TV Coordinate System and Picture Scan Process
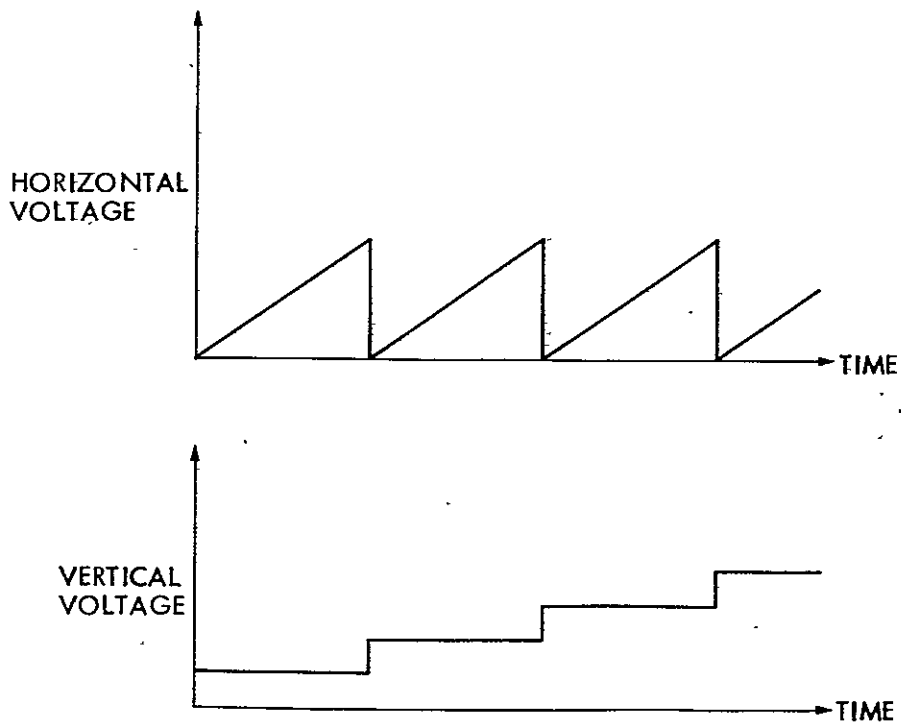
Figure 2-1 (b). Voltage Biases for Scan Readout

provide up to 2^n digitized "gray levels" of intensity called the Data Number (DN).

Coordinates

The scanning process for a given picture begins as shown in Fig. 2-1a near the upper left-hand corner. The sample there is designated Pixel number = 1, Line number = 1. The scanning directions -- increasing pixel numbers along a scan line and increasing line number -- provide the two reference directions, the p and the l coordinate directions. These along with the origin at the upper left-hand corner provide the (p, l) coordinate system.

Fig. 2-1a also shows the x, y, z coordinate system the origin of which is on the surface of the vidicon at the central line and pixel (p_o, l_o). The x and y directions are parallel to the p and l directions, respectively, while z is along the line of sight (LOS) of the camera and completes the orthogonal x, y, z right-hand system.

2.2 Basic Geometry; Stellar Aberration and Light-Time Effects

The optical data consists of the image of the object in TV coordinates. The scanner provides a window into space enclosing a solid angle which is the field-of-view (FOV) of the camera. The center of this solid angle (the camera line-of-sight or the camera look-direction) provides the pointing of the camera relative to some reference direction in space. The location of an image relative to the center of this solid angle therefore yields the information regarding direction to the object in space when transformed through the appropriate transformation of coordinates. We shall examine these in detail in Chapter Three; here we examine the overall geometry of the process of imaging an object for a single observation.

Figure 2-2 shows the relative vectors between the sun, spacecraft, planet, and the object being viewed. If

$\underline{x}$ $\triangleq$ Heliocentric spacecraft vector,

$\underline{s}$ $\triangleq$ Planetocentric spacecraft vector,

$\underline{q}$ $\triangleq$ Planetocentric object vector,

and $\underline{p}$ $\triangleq$ Heliocentric planet vector,

then

$$\underline{t} = \underline{q} - \underline{s} \qquad (2\text{-}2\text{-}1)$$

where

$\underline{t}$ $\triangleq$ spacecraft-centered object vector

and

$$\underline{y} = \underline{p} + \underline{q} \qquad (2\text{-}2\text{-}2)$$

where

$\underline{y}$ $\triangleq$ heliocentric object vector.

46
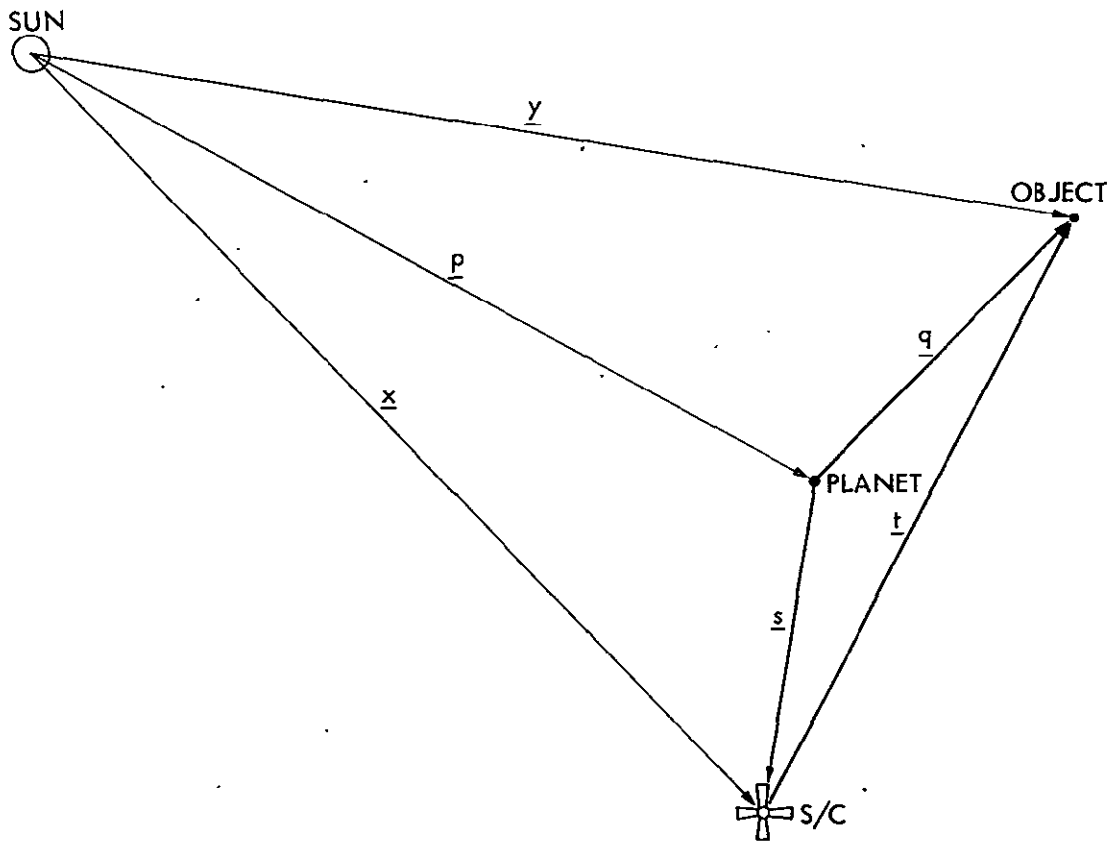
Figure 2-2. Relative Vectors Between Spacecraft and
Celestial Bodies

If the passage of light were instantaneous, the image would yield the direction $\hat{t}$, where

$$\hat{t} = \frac{t}{|t|} = \text{unit vector in the direction of } t.$$

However the situation is complicated by two distinct but intimately related effects. These are (i) light-time correction and (ii) stellar aberration. Both of them are due to the fact that the velocity of light is not infinite. The first can be considered to depend on the motion of the object and the latter on the motion of the observer; their intimate connection stems from the fact that there is no absolute frame of reference.

Light-Time Correction

Light-time correction as the name implies is the motion of the object during the time taken for the light to traverse the distance between the body and the observer. Let $\underline{u}_j(t_j)$ be the vector position, at time t_j, of the spacecraft relative to any origin in some (non-rotating) frame of reference F; let $\underline{w}_i(t_i)$ be the vector position at time t_i of the object being viewed in the same frame of reference F.

Then the light-time equation ignoring relativistic effects can be expressed as

$$\tau \equiv t_j - t_i = \frac{1}{c}|\underline{u}_j(t_j) - \underline{w}_i(t_i)| \, , \qquad (2\text{-}2\text{-}3)$$

where the light travels from $\underline{w}_i$ to $\underline{u}_j$ in frame F, and τ is the light-time. It should be noted that in general τ depends on the

48

frame of reference. The direction from the spacecraft to the object before applying the light-time correction, in the reference frame F, is

$$\hat{\underline{t}}' = \frac{\underline{w}_i - \underline{u}_j}{|\underline{w}_i - \underline{u}_j|} \ . \tag{2-2-4}$$

The light-time equation can be solved by iterating the equation. An adequate approximate expression can be derived by assuming uniform motion. The component of the object's velocity in the direction of increasing range is given by

$$v_r = \dot{\underline{w}}_j \cdot \hat{\underline{t}} \ , \tag{2-2-5}$$

where $\dot{\underline{w}}_j$ is the velocity of the object at time t_j. Therefore,

$$c(t_j - t_i) \approx |\underline{w}_j - \underline{u}_j| - \{\dot{\underline{w}}_j \cdot \hat{\underline{t}}\}(t_j - t_i) \ ,$$

or

$$t_j - t_i \approx \frac{|\underline{w}_j - \underline{u}_j|}{c \left\{1 + \dfrac{\dot{\underline{w}}_j \cdot \hat{\underline{t}}}{c}\right\}} \ . \tag{2-2-6}$$

The effect of the factor in the denominator is of the order of $\left(\dfrac{v}{c}\right)^2$ since the value of τ itself is of the order of $\dfrac{v}{c}$. We shall see shortly that effects of the order of $\dfrac{v^2}{c^2}$ can be ignored; in fact that is the basis upon which we can afford to neglect relativistic effects. Thus the value of the light-time τ can be approximated by

$$\tau = t_j - t_i \approx \frac{|\underline{w}_j - \underline{u}_j|}{c} \ . \tag{2-2-7}$$

Stellar Aberration Correction

Stellar aberration is the difference between the direction of the incoming light and the apparent direction from which the

observer sees it coming. This effect is due to the velocity of the observer not being negligible with respect to the velocity of a photon, and was originally discovered in 1725 by James Bradley. (He was attempting to find the distance to a star based on observing the parallax due to the position of the earth in its heliocentric orbit. The effect he observed was rotated approximately 90° in phase from the result he expected, i.e., it was in phase with the velocity of the earth.) Ignoring relativistic effects again, the effect is easily understood using the particle theory of light in terms of the velocity of the observer relative to the incoming photon of light. If the S/C-object direction is $\hat{\underline{t}}'$, then referring to the velocity triangle in Fig. 2-3a we have,

$$\underline{t}'' = \hat{\underline{t}}' + \frac{\dot{\underline{u}}_j}{c} , \qquad (2\text{-}2\text{-}8)$$

where $\dot{\underline{u}}_j$ is the velocity of the spacecraft at time t_j. Thus the observed direction to the object before applying the stellar aberration correction, i.e., the actual observed direction, is given by

$$\hat{\underline{t}}'' = \frac{\underline{t}''}{|\underline{t}''|} . \qquad (2\text{-}2\text{-}9)$$

Coordinate Frame

As noted earlier, the results obtained are independent of the coordinate frame used to carry out the computations. To illustrate this and to get a physical feeling for the combined magnitude of the effects, consider the situation shown in Figure 2-3b. In the figure ① represents the trajectory of the observer-spacecraft

50
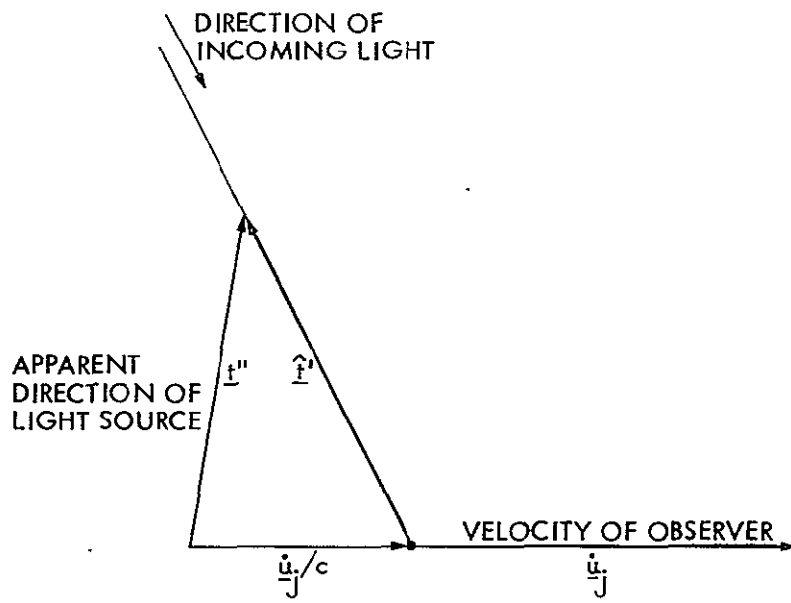
Figure 2-3 (a). Stellar Aberration
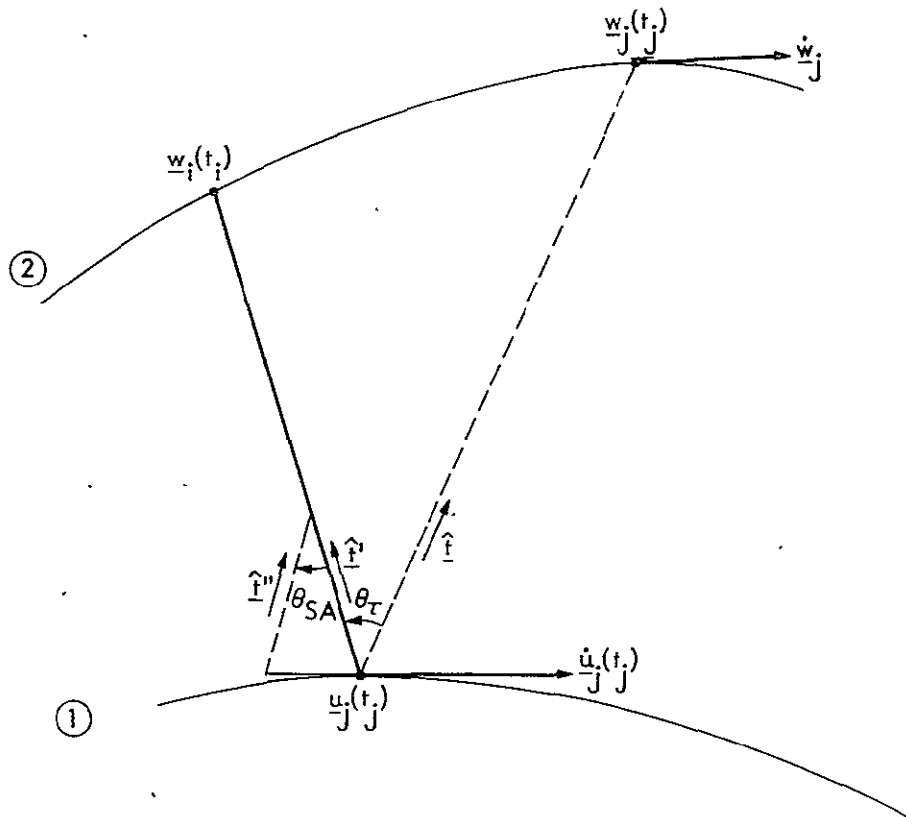
Figure 2-3 (b). Combined Light-Time and Stellar Aberration Effects

based TV camera -- and ② represents the trajectory of the object

being viewed. In general these trajectories will lie in different

planes.

The light-time τ is computed as

$$\tau = \frac{|\underline{u}_j - \underline{w}_i|}{c} .$$

Now if $\underline{\theta}_\tau$ is the vector angle correction in magnitude and direction

(following the right-hand rule) due to light-time, then we can write

$$\theta_\tau \approx \frac{\hat{t}' \times (\underline{w}_j - \underline{w}_i)}{|\underline{u}_j - \underline{w}_i|} + 0(\tau^2) . \qquad (2\text{-}2\text{-}10)$$

Now

$$\underline{w}_j - \underline{w}_i = \dot{\underline{w}}_j \tau + 0(\tau^2)$$

$$= \dot{\underline{w}}_j \frac{|\underline{u}_j - \underline{w}_i|}{c} + 0(\tau^2) . \qquad (2\text{-}2\text{-}11)$$

Therefore,

$$\theta_\tau = \frac{\hat{t}' \times \dot{\underline{w}}_j}{|\underline{u}_j - \underline{w}_i|} \cdot \frac{|\underline{u}_j - \underline{w}_i|}{c} + 0(\tau^2)$$

or,

$$\theta_\tau = \frac{\hat{t}' \times \dot{\underline{w}}_j}{c} + 0(\tau^2) . \qquad (2\text{-}2\text{-}12)$$

If $\underline{\theta}_{SA}$ is the vector angle correction due to stellar aberration,

then from Fig. 2-3b

$$\underline{\theta}_{SA} = \frac{\dot{\underline{u}}_j \times \hat{t}'}{c} + 0(\tau^2) . \qquad (2\text{-}2\text{-}13)$$

The combination of the two effects is defined as "planetary

aberration." Letting θ_P denote planetary aberration, adding the

two effects we obtain

$$\underline{\theta}_P = \underline{\theta}_\tau + \underline{\theta}_{SA} = \frac{\hat{t}' \times (\ddot{\vec{w}}_j - \underline{u}_j)}{c} + 0(\tau^2) \ . \qquad (2-2-14)$$

We note that (i) this result is independent of the frame of reference that we choose to work in, even though each of $\underline{\theta}_\tau$ and $\underline{\theta}_{SA}$ are not. This points up the close connection between the two effects, (ii) each of the corrections is of order $\frac{V}{c}$ and we are neglecting quantities of order $\frac{V^2}{c^2}$. This is justified since values for $\frac{V}{c}$ are typically $\sim 10^{-4}$, so $\frac{V^2}{c^2} \sim 10^{-8}$, and the pixel resolution of typical cameras on board interplanetary spacecraft ranges from 10 μ radians to 50 μ radians.

The situation as outlined above is complicated by the fact that since the stars are at enormous distances from the solar system, catalogs for their ephemeris are not made for proper time, i.e., it is not their actual location at time t that we record but rather their apparent location in a heliocentric frame of reference. The procedure followed when doing this is to correct for the stellar aberration caused by the heliocentric motion of the observer on the earth, but no account is taken of the light-time. This is to avoid complications in the star catalogs pertaining to the distance of the stars from and their motion relative to the solar system.

Thus for images of stars the light-time correction does not apply leaving only the stellar aberration (hence the name). This means then that the stellar aberration for the star images must be applied in the heliocentric frame of reference.

Differential Aberration

A further simplification results in the stellar aberration effect, when stars are used as the reference for the determination of camera

orientation, as in the satellite-star and planet-star (two camera) methods. What is important here is just the relative magnitude of the stellar aberration effects between the star and non-star images. This is caused solely by the difference in the unit vector directions to the two objects and is termed differential aberration.

To evaluate the approximate value of the differential aberration effect, consider two objects (one of which is a star) in directions $\underline{\hat{t}}_1$ and $\underline{\hat{t}}_2$ respectively; the stellar aberration effects will then be given by $\frac{1}{c}(\underline{u}_j \times \underline{\hat{t}}_1)$ and $\frac{1}{c}(\underline{u}_j \times \underline{\hat{t}}_2)$ respectively. Letting α be the angle between $\underline{\hat{t}}_1$, $\underline{\hat{t}}_2$, and writing

$$\Delta\underline{\hat{t}} \overset{\Delta}{=} \underline{\hat{t}}_2 - \underline{\hat{t}}_1 \qquad (2\text{-}2\text{-}15)$$

then for small values of α we will have

$$\alpha \approx |\Delta\underline{\hat{t}}| \qquad (2\text{-}2\text{-}16)$$

The differential aberration effect is then given by

$$\Delta\underline{\theta}_{SA} = \frac{1}{c}(\underline{u}_j \times \Delta\underline{\hat{t}}) \qquad (2\text{-}2\text{-}17)$$

The maximum value of this, for a given $\underline{u}_j$ and α will occur when $\Delta\underline{\hat{t}}$ is normal to $\underline{u}_j$. This maximum will be

$$\left(\Delta\underline{\theta}_{SA}\Big|\alpha\right)_{MAX} \approx \frac{|\underline{u}_j|}{c}\alpha \qquad (2\text{-}2\text{-}18)$$

Since the two objects must be viewed with a fixed orientation camera structure the maximum possible value of α is governed by the field of view of the camera for the satellite-star method, or the combined fields-of-view of the two cameras for the planet-star method. Thus using

$$\alpha_{max} \sim 0.04 \text{ radians} \qquad (2\text{-}2\text{-}19)$$

54

in Eq. (2-2-18), we obtain,

$$\left(\Delta\theta_{SA} \right)_{max} \sim 10^{-4} \times 0.04 \qquad\qquad (2-2-20)$$

$$= 4\mu \text{ radians}$$

This effect is therefore small in comparison with the other error sources and can be neglected for the current state of the art.

Differential Planetary Aberration

To compute the net effect we define another term, differential planetary aberration, as the combination of the differential aberration effect above and the light-time effect for an object other than a star. This quantity could also be alternatively obtained as the difference between the stellar aberration effect on the star and the planetary aberration effect on the other object.

2.3 Optical Data Error Modelling

Figure 2-4 illustrates the geometry involved in the use of optical data for spacecraft navigation. Conceptually the following frames of reference are successively involved in the process of obtaining the planet relative spacecraft state vector:

S: The spacecraft and its coordinate system

TV: Television camera frame of reference

N: Natural satellite frame of reference

P: Target centered frame of reference.

The N coordinate frame is only implicitly involved and that only for satellite observations. For planet observations the referencing is directly between the television frame of reference and the planet.

We notice that there are fewer transformations between frames of reference in the use of optical data compared with those for radio navigation. This fact means little without consideration of (i) the accuracies obtainable at each step in the process and (ii) the basic information content inherent in the data i.e., the observability of the navigation quantities from the data — and the effect of the errors on orbit determination. These two issues are qualitatively discussed in this and the following sections, respectively. The problem being highly non-linear, detailed quantitative studies are only possible numerically in specific applications; we do that in Chapters 4 and 5.

In this section we list the major error sources resulting from the use of optical data for navigation. The television camera is taken to be the primary sensor for all of the optical data types, the

PLANET

P

N

NATURAL
SATELLITE

S/C

T

S

→ VECTORS REFERENCED
TO THE S/C FRAME

--→ VECTORS REFERENCED
TO THE TV FRAME

S - SPACECRAFT COORDINATE SYSTEM

T - TV CAMERA COORDINATE SYSTEM

N - NATURAL SATELLITE COORDINATE FRAME

P - PLANET COORDINATE FRAME
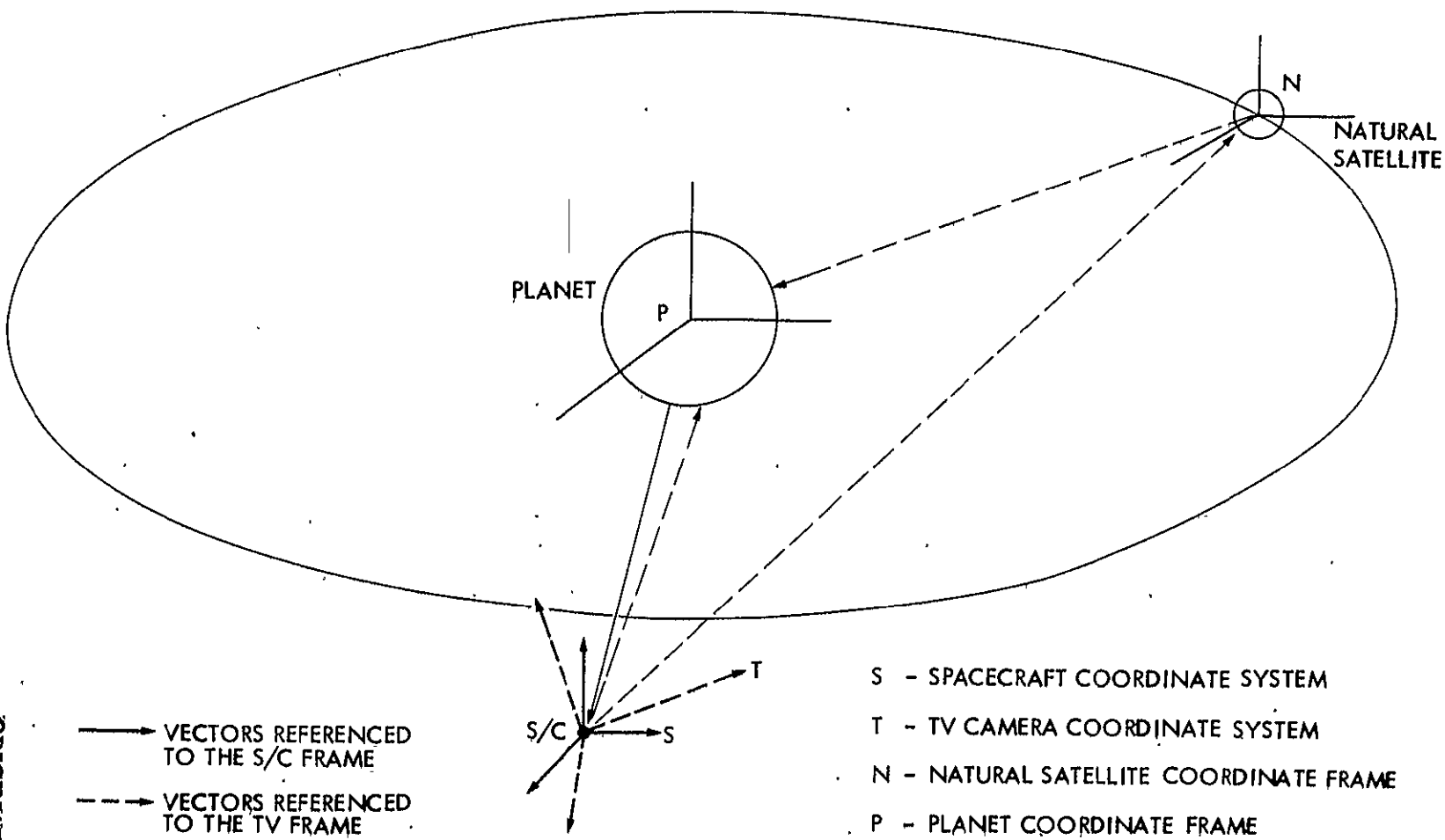
Figure 2-4. Coordinate Frames of Reference for Optical Navigation

other sensors (mentioned in Section 1.1) providing the means to relate frames of reference.

Paralleling the categorization of radio navigation errors, we can categorize the errors into the following three types:

(i)   Imaging instrument measurement imprecision errors

(ii)   Spacecraft acceleration model errors

(iii)   Errors in relating frames of reference.

Imaging Instrument Measurement Imprecision Errors

These errors arise within the television from effects related to the optical or the electronic part of the imaging system or to the photosensitive surface of the vidicon. Some of these are invariant characteristics of the television camera that affect the entire picture frame. These are independent of the image. Others are a function of the specific image being viewed. Unlike instrument related errors for radio data, these errors for optical data are not small; they can be quite significant in their effect on navigation accuracies.

1)   Image-independent errors: These consist of three types of errors listed below:

(a)   Uncertainty in the television system parameter values such as. (i) the focal length of the optical system (ii) the scale factor and non-orthogonality terms of the transformation from the optics system image plane to the line-pixel coordinates on the picture frame.

(b)   Corruption of the image due to geometric distortions in the telescope of the instrument and the electronics of the

58

vidicon tube. These are referred to as optical distortion and electromagnetic distortion respectively. Sources of optical distortion include (Reference 26) (i) imperfections in the telescope lens (ii) misalignment of the lens optical axis in direction (with respect to the normal to the target raster) and position (with respect to the center of the target raster).

Sources of electromagnetic distortion include (i) non-uniformities in the magnetic deflection and electric deceleration fields (ii) fringe field outside the deflection region of the vidicon tube (iii) interaction between the focusing and deflection fields (iv) rotation, non-orthogonality and center displacement of the scan line and pixel direction deflection fields.

(c) The television picture resolution. The image received through the optics causes a continuous charge distribution on the photosensitive surface of the vidicon. However in the electronic read-out process the electron scanning beam has a finite size which determines the size of the pixel. This forms the lower limit for the accuracy of the imaging system.

2) Image-dependent errors: Much less is known or can be determined from calibration about these errors relative to the image independent errors described above. They are related to t image formation and detection processes and may be caused by:

(a) an interaction of the characteristics of the imaging system with the method used for locating the center of the image. In addition to all of those listed above, the relevant characteristics include the point spread function of the vidicon

which causes an effect known as "image blooming," where the charge at a pixel is spread over neighboring pixels. This effect increases with the brightness of the image and leads to an error in locating the image center.

(b) an interaction between the readout scanning beam with the point spread function and with the remaining unerased charge on the vidicon. This effect, known as "beam-bending," is small for small images such as those of stars but may be quite significant for large images such as those of planets.

(c) smearing effect of the image caused by motion of the camera during the exposure time of the optical shutter. The motion is due to the limit cycle of the S/C attitude control system. This effect would increase with increasing exposure time. It would therefore usually be largest when imaging dim objects such as stars since a large exposure time would be designed in that case to insure a detectable signal on the vidicon.

Spacecraft Acceleration Model Errors

Errors in this category consist of only the gravitational acceleration errors applicable for radio navigation. These affect the motion of the spacecraft and hence the propagation of the trajectory. The non-gravitational acceleration errors do not affect optical data; their effect is peculiar to the nature of the radio observations as explained in Section 1.3.

Errors in Relating Frames of Reference

Referring to Figure 2-4 the frames of reference involved in relating the target P and the spacecraft S are, in order,

$$S - TV - N - P$$

$$\underbrace{\quad}_{(1)} \quad \underbrace{\quad}_{(2)} \quad \underbrace{\quad}_{(3)}$$

where N would be omitted in the case of planet limb observations. The errors in this process then fall into the three subdivisions indicated. The first is the error in establishing the orientation of the instrument relative to inertial space be it through use of star images or of the attitude control system and scan platform sensors. The second results from errors in the model of the planet or satellite; the last stems from inaccuracies in the satellite ephemeris.

1) Instrument Orientation Errors: Depending on whether or not stars are used to establish the inertial pointing direction of the camera, these errors can be very different in magnitude.

(a) Pointing information from engineering data: In this mode the camera pointing direction is reconstructed using (i) the pitch, yaw and roll sensor outputs to determine the attitude of the spacecraft with respect to sun-Canopus referenced celestial coordinate system (ii) signals from the clock and cone angle gimbal actuator potentiometers to determine the orientation of the scan platform with respect to the spacecraft structure (iii) fixed offset angles to reference the television to the scan platform and (iv) the location of the central line and pixel and rotation of the TV line-pixel coordinate system relative to the telescope image plane axis.

Thus errors in each of these transformations contribute to the error involved in reconstructing the camera pointing relative to

61

space-fixed coordinates. In addition there is data noise introduced into the sensor measurements for (i) and (ii) due to quantization of the engineering telemetry.

(b) Using stars to determine camera pointing: This is the mode used for the second and third optical observation methods described in Section 1.4, i.e., the satellite-star measurements with one camera and the two-camera method for planet-star measurements. The accuracy of the star image determination is governed by the errors in the measurement imprecision category described earlier. The amount of error in the camera pointing as estimated from the star images is a function of this accuracy, the number of stars and their relative location -- this issue is further addressed in Chapter 4. The errors however turn out to be of the order of the TV pixel resolution. In addition to these errors, for the planet-star two camera method there is contribution from alignment errors between the two cameras and from spacecraft limit cycle motion during the time elapsed between the shuttering of the two cameras (since they are not shuttered simultaneously).

2) Object Modelling Errors: Errors in the accurate representation of the planet or satellite figure and illuminated profile cause errors in the location of the object. Thus the true location of the object is different from the observed location due to (i) errors in the mathematical model of the shape and size of the planet or satellite, (ii) the center of mass being offset from the center of the geometrical figure, (iii) errors in the illuminated profile

caused by irregularities on the surface, (iv) limb darkening effect

due to the falling off in the brightness close to the limb, and

(v.) atmospheric effects on the surface of the planet. Tha last two

effects may significantly degrade the accuracy of limb measurements

or even its definition.

3) Satellite Ephemeris Errors: In the case of satellite

observations, errors are caused owing to uncertainties in the ephemeris

of the satellite relative to the target planet. There is an error

due to the uncertainty in the planet relative satellite vector at

an epoch and errors in the propagation of the ephemeris in time.

The planet mass and gravity field uncertainties contribute to the

latter. The spin axis of the planet is also a source of error when

the satellite theory used and the planet gravity field are referenced

to the planet equator coordinate system.

Classification of Error Sources

The random components of all error sources along with the pixel

resolution can be grouped together as data noise. We regroup the

other error sources into the following classes for ease in analyzing

their effects on navigation accuracy.

(i) TV pointing errors: All errors which produce a global

shift of all the picture elements fall into this class.

Thus all the images would be shifted a uniform amount,

but their relative locations would be unaffected by this

error. This is shown schematically in Fig. 2-5a. These

are modelled as a combination of constant angular error

and a varying time correlated component.

63
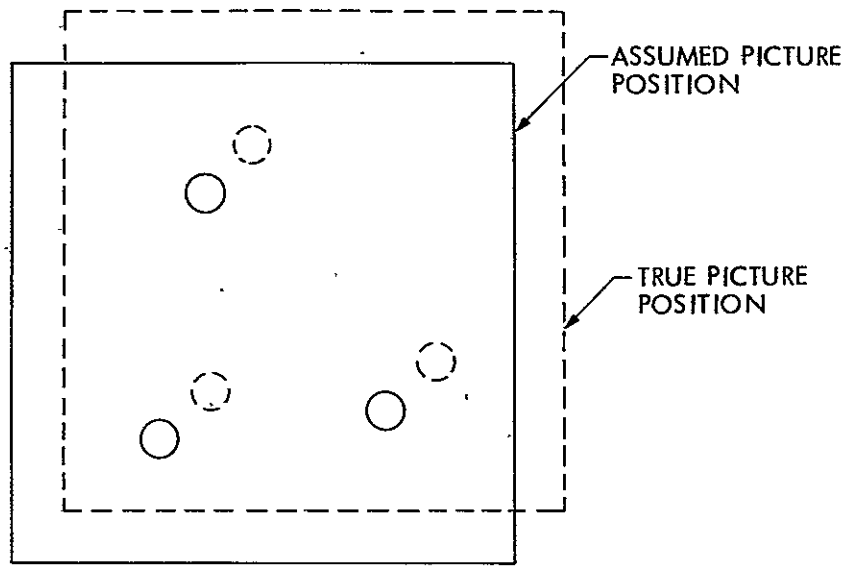
(a) TV POINTING ERRORS
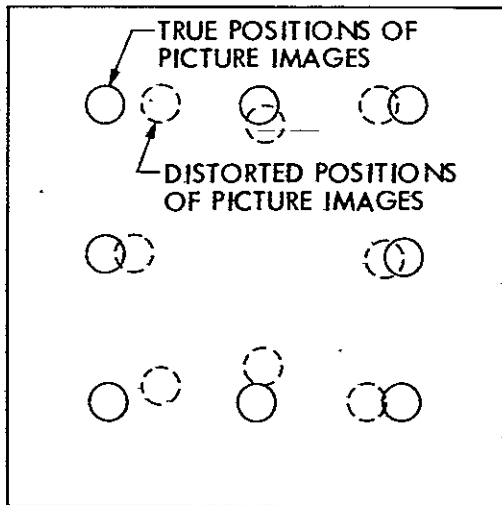
(b) GEOMETRIC DISTORTION
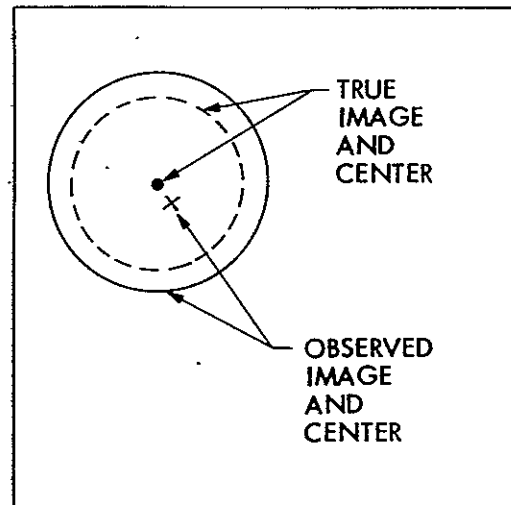
(c) CENTER FINDING ERROR

Figure 2-5. Classification of Optical Data Errors

(ii)   TV geometric distortion: These errors corrupt the
relative location of all the picture elements and
therefore of the images in a picture (shown schematically
in Fig. 2-5b). This is modelled as a polynomial of
the radial distance from the center of the vidicon.

(iii) Image center-finding errors: Errors that contribute to
the center location of a specific image fall into this
class. These errors are modelled as constant errors
proportional to the image size (see Fig. 2-5c).

(iv)   Satellite ephemeris errors: Since the position of the
spacecraft relative to Mars has to be derived using the
position of the satellites relative to Mars, uncertainties
in the satellite ephemeris have an important effect.
These are modelled as errors in the orbital parameters of
the satellite theory chosen to represent the motion of
the satellite around the planet.

2.4 Optical Data Information Content Analysis

In this section we discuss the basic information content of the optical data as it relates to navigating the spacecraft in the interplanetary approach phase of a mission. We examine the problem in two dimensions. Further simplifications are made to seek a minimal set of parameters which is sufficient to describe the problem.

Figure 2-6(a) shows the two-body motion of a spacecraft approaching a spherical planet located at coordinates (x_p, y_p). The dotted line, making an angle ψ relative to the x axis, is the approach asymptote of the hyperbolic trajectory. The eccentricity of the hyperbola is determined by the mass of the planet and the asymptotic velocity V_∞; for a massless planet the trajectory would be the dotted straight line at a perpendicular distance B from the center of the planet. The point of closest approach to the planet is labelled E (for "encounter") and the spacecraft arrives there at time T, the time of flight.

With the description above the position of the spacecraft at any time t is at a distance ℓ from E on the approach asymptote, given by

$$\ell(t) = V_\infty \tau , \tag{2-4-1}$$

where

$$\tau \triangleq T - t . \tag{2-4-2}$$

At the initial time, t = 0, the position is therefore given by

$$\ell(0) = V_\infty T .$$

66
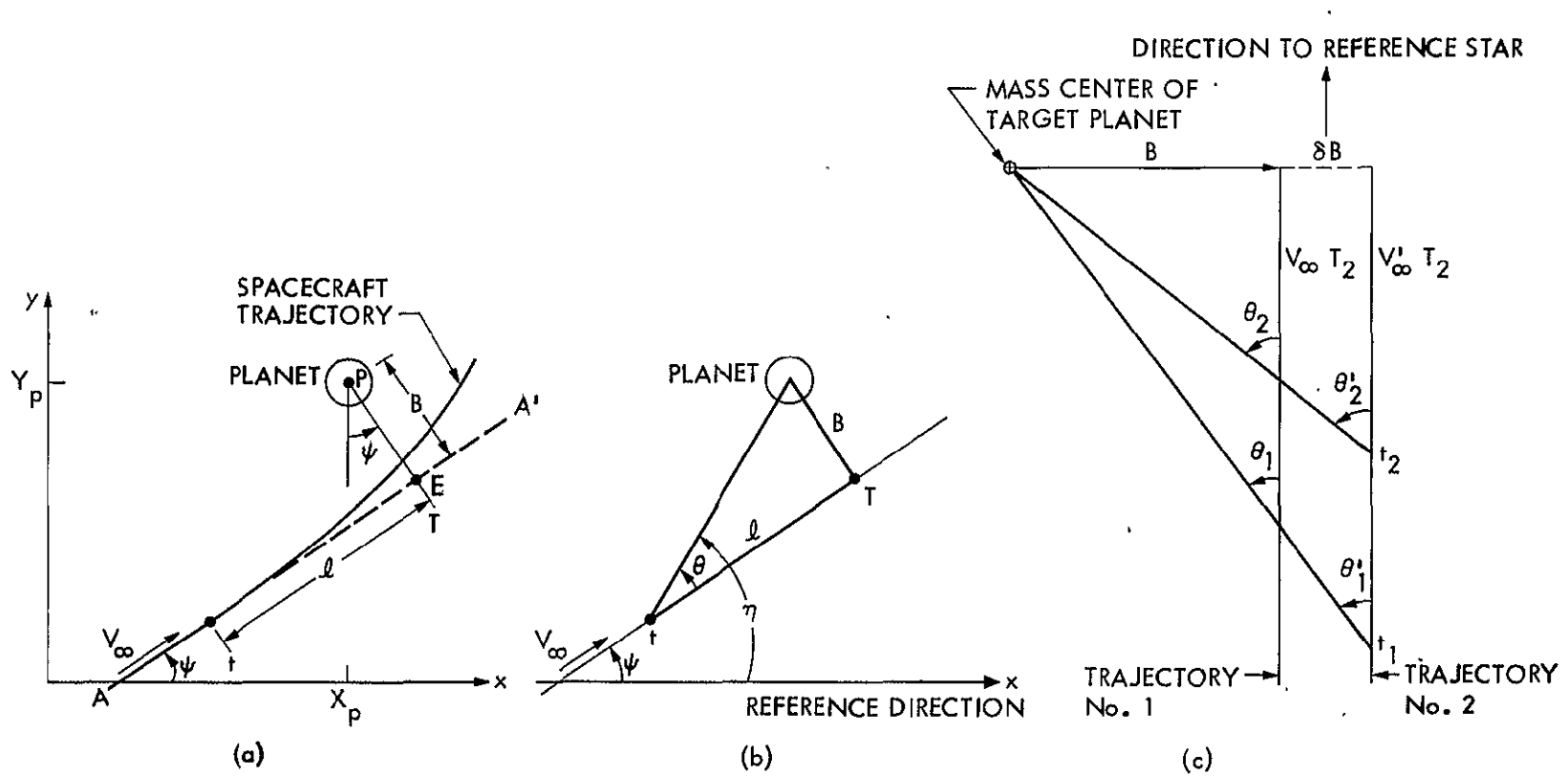
Figure 2-6. Optical Measurements during Planet Approach

Optical Data Content

Optical observations, either planet limb or natural satellites, essentially measure the angle between the target planet center of mass and a reference direction, e.g., a star direction. Let $\eta(t)$ be this angle as shown in Figure 2-6(b). For the purposes of this analysis the error in this angular measurement represents the accumulation of all error sources such as center-finding errors, satellite ephemeris errors, biases and camera pointing errors. These errors effectively result in a degradation of the observation angle.

Since we are dealing with planet-relative angular observations and a planet-relative description of the spacecraft trajectory, the coordinates (x_p, y_p) of the planet become irrelevant. The primary quantities of interest are B, τ, V_∞ and ψ, where the first two relate to the two dimensional position and the latter to the velocity.

Let $\theta(t)$ be the angle, shown in Figure 2-6(b), given by

$$\theta(t) = \eta(t) - \psi .$$

Taking variations we obtain

$$\delta\theta(t) = \delta\eta(t) - \delta\psi . \qquad (2\text{-}4\text{-}3)$$

Now $\theta(t)$ is given in terms of the trajectory parameters by

$$\tan\theta(t) = \frac{B}{\ell(t)} .$$

Since the observations are taken relatively far from the planet, $\theta(t)$ is small and

$$\theta = \frac{B}{\ell} + 0(\theta^3) . \qquad (2\text{-}4\text{-}4)$$

Neglecting higher order terms we may write

$$\frac{\delta\theta}{\theta} = \frac{\delta B}{B} - \frac{\delta\ell}{\ell} \qquad (2\text{-}4\text{-}5)$$

However from Equations (2-4-1) and (2-4-2)

$$\frac{\delta\ell}{\ell} = \frac{\delta V_\infty}{V_\infty} + \frac{\delta\tau}{\tau}$$

$$= \frac{\delta V_\infty}{V_\infty} + \frac{\delta T}{\tau} \qquad (2\text{-}4\text{-}6)$$

Substituting (2-4-6) and (2-4-3) into (2-4-5),

$$\frac{\delta B}{B} = \frac{\delta\theta}{\theta} + \frac{\delta V_\infty}{V_\infty} + \frac{\delta T}{\tau} \qquad (2\text{-}4\text{-}7)$$

$$= \frac{1}{\theta}(\delta\eta - \delta\psi) + \frac{\delta V_\infty}{V_\infty} + \frac{\delta T}{\tau} \qquad (2\text{-}4\text{-}8)$$

Substituting from (2-4-4) and rearranging,

$$\delta\eta = \delta\psi + \frac{\delta B}{V_\infty\tau} - \frac{B}{V_\infty^2\tau}\delta V_\infty - \frac{B}{V_\infty\tau^2}\delta T \,, \qquad (2\text{-}4\text{-}9)$$

which is the variation on the measurement equation.

We observe from this equation that it is not possible to

separate an error in the direction of the approach asymtpotic velocity ,

$\delta\psi$, from a bias error in the measurement angle, $\delta\eta$.

Since optical observations involve the measurement of angles

between the target planet and a reference direction, they suffer

from the inability to determine the velocity (V_∞) of the spacecraft

and the accurate time of flight. To illustrate this, consider a

spacecraft moving on trajectory No. 1 (Fig. 2-6(c)). Let θ_1 and θ_2

69

represent two angular measurements of the direction between the reference direction (which we have for simplicity assumed to be along V_∞) and the target planet. The observable equation is

$$\tan \theta_i = \frac{B}{V_\infty T_i} , \qquad (2\text{-}4\text{-}10)$$

where $T_i = T - t_i$ and t_i is the time of ith observation.

From Eq. (2-4-10) it is seen that the time of flight, T, can be determined from two perfect observations of θ. However, only the ratio B/V_∞ can be determined from observations of θ. This is because the observation history for any parallel trajectory with the same value of B/V_∞ (for example, trajectory No. 2) will be identical to the true trajectory. This could also have been observed from equation (2-4-9) above -- i.e., since the coefficients of δB and δV_∞ have the same temporal behavior it would not be possible to solve for these two parameters separately. These parallel trajectories also will have the same time of flight as and will be indistinguishable from the true trajectory. Note also that two perfect direction observations determine the plane of motion.

From Eq. (2-4-7) it is seen that even with perfect observations the limiting accuracy for B is determined by V_∞, i.e.,

$$\delta B = \frac{B}{V_\infty} \delta V_\infty . \qquad (2\text{-}4\text{-}11)$$

To obtain the time of flight, T, assume that two observations of θ are taken; then from (2-4-10),

$$T_1 \tan \theta_1 = \frac{B}{V_\infty} = T_2 \tan \theta_2 , \qquad (2\text{-}4\text{-}12)$$

or

$$(T - t_1) \tan \theta_1 = (T - t_2) \tan \theta_2 \, ,$$

which yields,

$$T = \frac{t_2 \tan \theta_2 - t_1 \tan \theta_1}{\tan \theta_2 - \tan \theta_1} \, . \qquad (2\text{-}4\text{-}13)$$

Even though in theory two perfect observations of θ uniquely determine time of flight, in practice this quantity is rather poorly determined by optical data since it is extremely sensitive to errors in θ. This can be illustrated by examining an expression for the time of flight uncertainty. Taking the variation of Eq. (2-4-12),

$$\delta T_1 \theta_1 + T_1 \delta \theta_1 = \delta T_2 \theta_2 + T_2 \delta \theta_2 \, . \qquad (2\text{-}4\text{-}14)$$

However, from $T_i = T - t_i$,

using

$$\delta T_1 = \delta T_2 = \delta T,$$

$$\delta T(\theta_2 - \theta_1) = T_1 \delta \theta_1 - T_2 \delta \theta_2 \, ,$$

or

$$\delta T = \frac{T_1 \delta \theta_1 - T_2 \delta \theta_2}{\theta_2 - \theta_1} \, .$$

Assuming independent observations, the standard deviation of T is then given by

$$\sigma_T = \frac{(T_1^2 + T_2^2)^{\frac{1}{2}}}{\theta_2 - \theta_1} \cdot \sigma_\theta \, .$$

71

Substituting for θ_i from $\theta_i = \dfrac{B}{V_\infty T_i}$, σ_T becomes,

$$\sigma_T = \frac{V_\infty T_1 T_2 (T_1^2 + T_2^2)^{1/2}}{B(T_1 - T_2)} \; \sigma_\theta \; . \qquad\qquad (2\text{-}4\text{-}15)$$

From Eq. (2-4-15) it is seen that the uncertainty in time of flight is very sensitive to the uncertainty in pointing angle when the spacecraft is far from the target planet and decreases as the spacecraft approaches the planet. The Equation emphasizes the importance of stars in the data since they minimize the contribution of pointing errors to σ_θ. It is seen that a larger B, which increases parallax, minimizes the error. A smaller V_∞ also gives more parallax by decreasing the range at which the observations are taken. Finally, for a fixed measurement time, T_1, Eq. (2-4-15) is minimized as T_2 is taken closer to encounter.

Satellite Observations

It is emphasized that the analysis presented here only applies far from encounter. As the spacecraft approaches the planet, parallax effects in the case of natural satellite observations allow one to solve for V_∞. Also the time of flight solution becomes less sensitive to pointing errors. Furthermore, sufficient data will have been taken to estimate the natural satellite's ephemeris relative to the target planet thus reducing effects of this error source.

In the case of planet limb observations, V_∞ cannot be accurately determined until planetary bending of the approach trajectory occurs. In the case of Deimos, however, parallax effects are discernible

long before planetary bending occurs. In addition, the small size of Deimos makes image center-finding errors negligible. These two factors make satellite observations significantly more accurate than Mars limb observations for approach navigation as we shall see in Chapters 4 and 5.

Combined Radio and Optical Solutions

Solutions which use a combination of doppler and optical data are of particular value during planetary approach since these data types complement one another. The primary error sources prior to encounter in solutions using only doppler data are target planet ephemeris errors, station location errors and non-gravitational accelerations. Optical data is insensitive to these errors since it directly relates the planet and spacecraft positions. On the other hand, as discussed above, optical data suffers from the inability to determine accurately time of flight and velocity of the spacecraft, quantities which, for favorable approach geometry, are well determined by doppler data. The optical data and radio data complement each other in the navigation information that they provide. Hence, the combination of radio and optical data yields extremely accurate solutions and give a good estimate of encounter conditions much earlier than either data type taken separately.

. For the radio plus optical strategies, two solutions could be generated:

1)   a combined radio plus optical solution obtained by processing radio data and optical data simultaneously

73

2)   a radio plus optical solution obtained by processing the

radio and optical data sequentially; i.e., after the radio

data processing, using the a-posteriori covariance from the

radio analysis as the apriori covariance for the optical

data arc. This process should yield solutions that are

very insensitive to radio data errors.

The radio data in each case could consist of

   (i)   only doppler

   (ii)   only range

   (iii)   both doppler and range.

CHAPTER 3

OPTICAL NAVIGATION SYSTEM

In this chapter we describe the optical navigation system required
and the details of the methods to perform the navigation task using
optical data. We will begin with a description of the overall functions
involved for navigation in general. The subfunctions are general but
are described in the context of optical navigation and the details pre-
sented for the subfunctions pertain specifically to the use of optical
data; details specific to the use of radio data can be found in
Ref. 27. All subsequent sections of the chapter deal primarily with
optical data planning and processing, with the exception of Section 3.6,
which deals with the orbit determination process, including the overall
dynamic and measurement model description, for any data type.

Figure 3-1 gives a diagram describing the functions involved in
the navigation of a spacecraft. These fall into the five major cate-
gories shown in the figure:

    (i)   system modelling,

    (ii) data constitution planning,

    (iii) measurement extraction and processing,

    (iv) estimation, and

    (v)   maneuver computation.

The navigation process begins with a characterization of the sys-
tem for both the dynamic and the measurement components. The dynamic

75
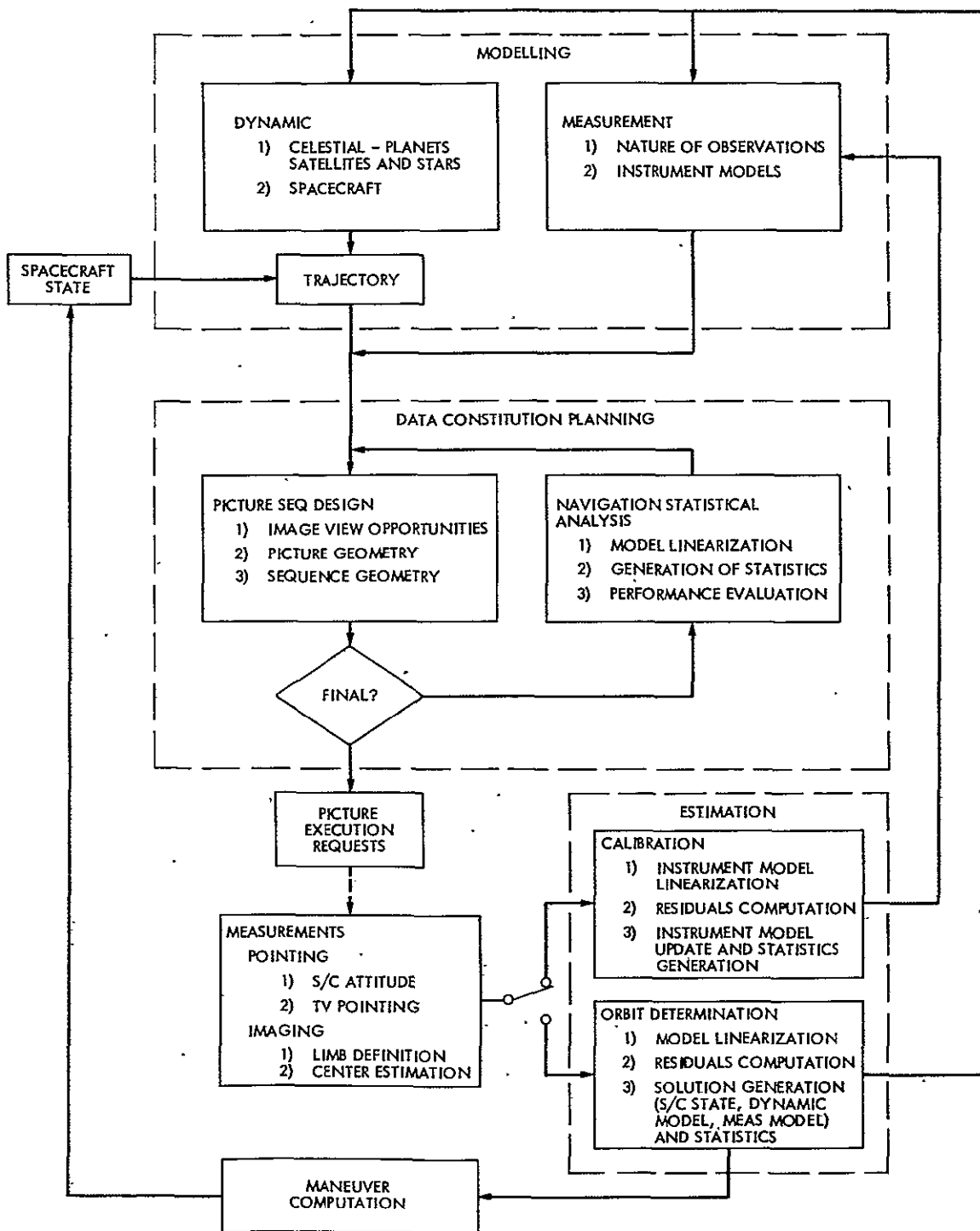
Figure 3-1. Optical Navigation Functional Flow Diagram

modelling (Section 3.1) involves a description of the time evolution of the position and velocity of the relevant celestial objects and of the spacecraft. This coupled with appropriate initial conditions yields a flight trajectory. The measurement modelling includes a definition of the data type used together with modelling the behavior of the instruments from which these data types are acquired (Sections 3.2 and 3.5).

The next step in the navigation process consists of data sequence planning and its evaluation from the standpoint of navigation requirements. For optical measurements the picture sequence design (Section 3.3) consists of (i) determining the opportunities when the desired images can be viewed within the spacecraft and environmental constraints imposed; (ii) designing individual pictures with appropriate image geometry; and (iii) from a sequence of these, determining if adequate overall data coverage is obtained or if a new spacecraft trajectory design is required. The navigational evaluation of this picture sequence is based on requirements and constraints imposed by the overall mission objectives. These include the orbit determination, trajectory control and instrument pointing accuracies needed for the scientific investigations to be conducted. The generation of these predicted accuracies is preceded by the linearization of the dynamic and measurement models about nominal conditions, which enables the use of linear estimation techniques.

After an acceptable data sequence design satisfying navigation requirements has been obtained, the spacecraft is commanded to acquire the data. After execution of these commands and return of the measurement data to earth, this data must be processed (Section 3.4). For

optical data this consists of two streams of data — the data related to instrument pointing and the video data from the television cameras. The pointing measurement reduction consists of processing the data from the spacecraft attitude control system sensors and from the scan platform gimbal angle sensors. The TV data processing consists of defining the image profile and the subsequent determination of the image center.

The use of the measurements for the estimation of parameters consists of computing residuals (departures from expected measurement values) and then using these for the generation of the solutions, along with the statistical accuracies for these. In the calibration mode (Section 3.5) only the parameters related to the instrument model are treated. In the orbit determination mode (Section 3.6) all model parameters may be treated, with the emphasis being on spacecraft trajectory estimation and possibly on dynamical model improvement. Both functions require a linearization of the respective models (Sections 3.5 and 3.7).

Based on the spacecraft orbit estimate from the orbit determination function, a trajectory correction maneuver can be computed. When executed, the maneuver alters the spacecraft state, thus yielding a new spacecraft trajectory.

In the sections to follow we discuss these functions in more detail, as indicated above. The chapter concludes in Section 3.8 with a brief description of the overall optical navigation system structure.

3.1 Spacecraft-Object Vector

The geometry of obtaining the vector from the spacecraft to the
object being imaged in the television camera was illustrated in
Figure 2-2. This section describes the process of obtaining each
of the component vectors required to establish the spacecraft-object
vector. These are (a) the spacecraft vector, (b) the target planet
vector (c) planet centered satellite vector (when the image is a
natural satellite) and (d) vector direction to a star (for star
observations).

Spacecraft Trajectory

From Newton's law of universal gravitation the force of attraction
$\underline{F}_{ij}$ acting on a particle P_i of mass m_i due to a particle P_j of mass
m_j is given by

$$\underline{F}_{ij} = G \, m_i m_j \, \frac{(\underline{r}_j - \underline{r}_i)}{|\underline{r}_j - \underline{r}_i|^3} \, , \qquad (3\text{-}1\text{-}1)$$

where G is the Gravitational Constant and $\underline{r}_i$, $\underline{r}_j$ are the position
vectors of P_i, P_j respectively. From Equation (3-1-1), it follows
that the equation for the motion of a spacecraft relative to a central
body can be written as

$$\frac{d^2 \underline{r}}{dt^2} + \frac{\mu}{|\underline{r}|^3} \, \underline{r} = \Sigma \Delta \, \underline{\ddot{r}}_k \, , \qquad (3\text{-}1\text{-}2)$$

with

$\underline{r}$ = position vector of spacecraft relative to the
  central body

$$= \underline{r}_{S/C} - \underline{r}_o \qquad (3\text{-}1\text{-}3)$$

79

and

$$\mu \stackrel{\Delta}{=} G \ (M_o + m_{S/C}) \approx GM_o \qquad (3\text{-}1\text{-}4)$$

$\underline{r}_o$, M_o = position vector and mass of the central body

$\underline{r}_{S/C}$, $m_{S/C}$ = position vector and mass of the spacecraft

$\Delta \underline{\ddot{r}}_i$ = k^{th} perturbing acceleration .

Perturbing accelerations are defined to be those that lead to departure from two-body motion, i.e., accelerations other than the second term in Eq. (3-1-2). The principal perturbing accelerations on the motion of the spacecraft arise from:

1) N-body accelerations due to the gravitational effect of bodies in the solar system other than the central body of integration;

2) the departure of the gravitational field of the central body from spherical symmetry;

3). solar radiation pressure on the spacecraft; and

4) propulsive maneuver thrusts by the spacecraft.

The abovementioned are described below:

1) N-body acceleration: The perturbing acceleration due to the ith gravitating body, $[\Delta \underline{\ddot{r}}_{NB}]_i$, is composed of two terms -- the direct acceleration on the spacecraft and the indirect acceleration due to the perturbing acceleration on the central body. Thus, using Eq. (3-1-1),

$$[\Delta \underline{\ddot{r}}_{NB}]_i = GM_i \frac{\underline{r}_i - \underline{r}_{S/C}}{|\underline{r}_i - \underline{r}_{S/C}|^3} - GM_i \frac{\underline{r}_i - \underline{r}_o}{|\underline{r}_i - \underline{r}_o|^3} \qquad (3\text{-}1\text{-}5)$$

and

$$\Delta \underline{\ddot{r}}_{NB} = \sum_{i=1}^{n} [\Delta \underline{\ddot{r}}_{NB}]_i \qquad (3\text{-}1\text{-}6)$$

80

where

$\underline{r}_i$, M_i = position vector and mass of the ith body and

N = number of perturbing bodies.

2) Nonspherical Gravitational Field: The gravitational potential, V, at the point $\underline{r}$ due to a distributed mass of density D is given by,

$$V(\underline{r}) = G \iiint \left[\frac{D(\underline{\xi})}{|\underline{r} - \underline{\xi}|} \right] dv(\underline{\xi}) , \qquad (3-1-7)$$

where $D(\underline{\xi})$ is the density and $dv(\underline{\xi})$ is the volume element at location $\underline{\xi}$. The acceleration due to V on the spacecraft at $\underline{r}$ is then given by

$$\ddot{\underline{r}} = \nabla V ,$$

where ∇ is the vector gradient operator.

The potential function can be expressed as (Reference 27)

$$V = \frac{GM}{r} - \frac{GM}{r} \sum_{n=1}^{\infty} J_n \left(\frac{a_e}{r} \right)^n P_n (\sin\emptyset)$$

$$+ \frac{GM}{r} \sum_{n=1}^{\infty} \sum_{m=1}^{n} \left(\frac{a_e}{r} \right)^n P_n^m (\sin\emptyset) \left[C_{nm} \cos m\lambda + S_{nm} \sin m\lambda \right] ,$$

$$(3-1-8)$$

where

r, $\emptyset$, λ = body-centered radius, latitude, and longitude of spacecraft

a_e = mean equatorial radius of body

P_n (sin $\emptyset$) = Legendre polynomial of degree n in sin $\emptyset$

P_n^m (sin $\emptyset$) = associated Legendre function of first kind

$C_{n,m}$, $S_{n,m}$ = numerical coefficients (tesseral and sectorial harmonic coefficients).

The associated Legendre function P_n^m is defined by

$$P_n^m (\nu) = (1 - \nu^2)^{m/2} \frac{d^m}{d\nu^m} P_n(\nu) \quad , \tag{3-1-9}$$

where P_n is the Legendre polynomial of degree n given by Rodrigues' formula

$$P_n(\nu) = \frac{1}{2^n \, n!} \frac{d^n (\nu^2 - 1)^n}{d\nu^n} \quad . \tag{3-1-10}$$

The three terms in Eq. (3-1-8) correspond to the potential of a point mass, zonal harmonics J_n and the tesseral and sectional harmonics $C_{n,m}$ and $S_{n,m}$. The perturbative acceleration can therefore be derived from terms beyond the first in Eq. (3-1-8).

3) Solar Radiation Pressure: There is a perturbing acceleration on the spacecraft, $\Delta\ddot{\underline{r}}_{SP}$, due to the impact of photons from solar radiation. This was discussed in Section 1.3 where Eq. (1-3-1) gives the acceleration in the sun-spacecraft direction. In addition to this there are two smaller forces orthogonal to this because of the asymmetry of the spacecraft configuration.

4) Propulsive Maneuver Thrusts: Accelerations due to thrusts generated by the spacecraft during propulsive maneuvers, $\Delta\ddot{\underline{r}}_{PM}$, are given by

$$\Delta\ddot{\underline{r}}_{PM} = \frac{F(t)}{m(t)} \hat{\underline{r}}_{PM}(t) \tag{3-1-11}$$

where t is the time from the start of the burn, $\hat{\underline{r}}_{PM}(t)$ is the thrust direction, $m(t)$ is the spacecraft mass, and $F(t)$ is the thrust

magnitude expressed as

$$F(t) = \sum_{i=0}^{4} F_i t^2 .$$

The mass $m(t)$ at time t is

$$m(t) = m_o + \int \dot{m}(t) dt ,$$

where $\dot{m}(t)$, the mass flow rate, is given by

$$\dot{m}(t) = - \sum_{i=0}^{3} \dot{M}_i t^2 .$$

A maneuver of very short duration can be regarded as an impulsive burn, as opposed to a finite burn. This can be represented by an instantaneous change in the velocity of the spacecraft, $\Delta \underline{V}_M$. The corresponding change in the instantaneous position is $1/2 \Delta \underline{V}_M t_b$, where t_b is the burn time.

Target Planet Vector

The vector to the target planet is obtained from the precomputed position and velocity ephemerides for the celestial bodies in the solar system. These planetary ephemerides are obtained by a simultaneous numerical integration of the N-body equations of motion for the celestial bodies (Reference 28).

Planet Centered Satellite Vector

The motion of the natural satellite in its orbit around a planet is obtained based on the analytical ephemeris theory developed by H. Struve and described in Reference 29. Wilkin's orbital elements (Reference 30) are used to define the coordinate system -- see Figure 3-2. In this theory the orbital plane of the satellite is approximated to be inclined at a constant angle to a fixed plane, called the
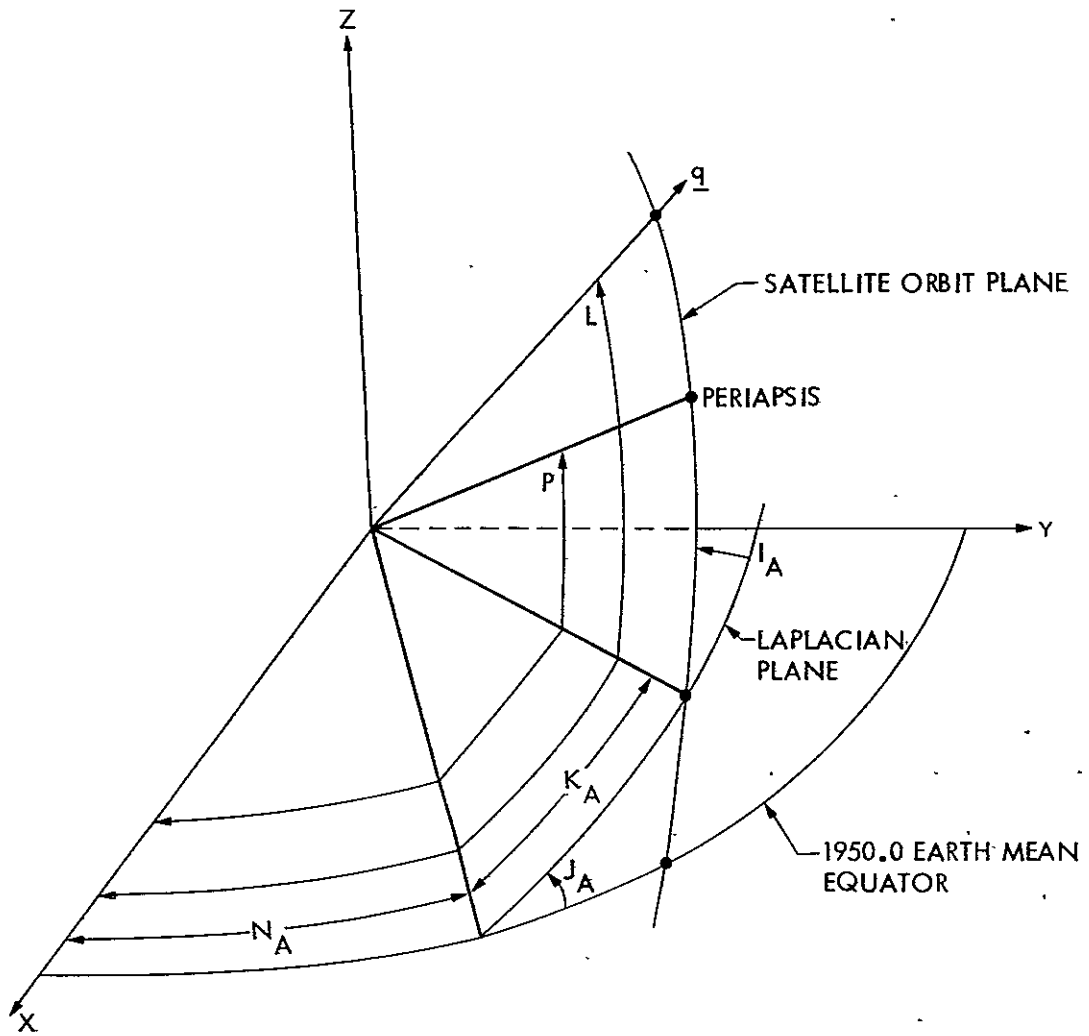
Figure 3-2. Wilkin's Angles

C-2

Laplacian plane, upon which the ascending node of the satellite orbital

plane regresses. Short period variations in the orbits are ignored.

The angles shown in Figure 3-2 are defined below:

N_A = longitude of node of fixed Laplacian plane on standard

equator (1950.0 Earth Equator).

J_A = inclination of fixed Laplacian plane to standard equator

K_A = the argument of the ascending node of the orbital plane on

the fixed Laplacian plane

I_A = inclination of the satellite orbital plane to the fixed

Laplacian plane

L = the mean longitude of the satellite measured along the

standard equator, the Laplacian plane and the satellite plane

P = the longitude of pericenter of the orbit of the satellite,

measured along the standard equator, the Laplacian plane

and the satellite orbit plane.

As mentioned earlier, I_A is held a constant in the theory. The

angles N_A, J_A, K_A, and P are modelled as linear functions of time

given by

$$N_A = N_Z + N_R t$$

$$J_A = J_Z + J_R t$$

$$K_A = K_Z + K_R t$$

and

$$P = P_Z + P_R t$$

(3-1-12)

where the elements $(\cdot)_Z$ are the values of the angles $(\cdot)_A$ at a

specified epoch and the elements $(\cdot)_R$ are their rates; the time, t,

is measured in days past the epoch.

The mean longitude, L, is modelled as having a secular acceleration and a long period variation term. This latter term is due to Born (Reference 31); it is the combined effect of the direct solar perturbation and an interation perturbation induced by the variation in inclination of the satellite orbit relative to the planet equator due to solar perturbation. The mean longitude is given by

$$L = L_Z + L_N t + L_M t^2 + L_K [\sin(K_A(t) - K_0)$$
$$- \sin(K_Z - K_0)] \qquad (3\text{-}1\text{-}13)$$

where L_K is the coefficient of the periodic variation term and K_0 is the node of the planet orbit about the sun measured relative to the planet equator. (For Deimos $L_K = 0.27$ deg; for Phobos this effect is negligible.)

At a given time, t, the position vector $\underline{q}$ of the natural satellite relative to the planet in the 1950.0 Earth Equator and Equinox Coordinate System is given by

$$\underline{q} = NJK \Join W\underline{r} \qquad (3\text{-}1\text{-}14)$$

where the rotation matrices are defined as

$$N = \begin{bmatrix} \cos N_A & -\sin N_A & 0 \\ \sin N_A & \cos N_A & 0 \\ 0 & 0 & 1 \end{bmatrix}$$

$$J = \begin{bmatrix} 1 & 0 & 0 \\ 0 & \cos J_A & -\sin J_A \\ 0 & \sin J_A & \cos J_A \end{bmatrix}$$

$$K = \begin{bmatrix} \cos K_A & -\sin K_A & 0 \\ \sin K_A & \cos K_A & 0 \\ 0 & 0 & 1 \end{bmatrix}$$

$$H = \begin{bmatrix} 1 & 0 & 0 \\ 0 & \cos I_A & -\sin I_A \\ 0 & \sin I_A & \cos I_A \end{bmatrix} \quad \text{and} \quad$$

$$W = \begin{bmatrix} \cos W_A & -\sin W_A & 0 \\ \sin W_A & \cos W_A & 0 \\ 0 & 0 & 1 \end{bmatrix}$$

The rotation angle W_A is defined by

$$W_A = w + v \qquad\qquad (3\text{-}1\text{-}15)$$

where

$$w = P - K_A - N_A \quad \text{(argument of periapsis)}, \qquad (3\text{-}1\text{-}16)$$

and

$$v = M + 2e \sin M + 5e^2 \sin 2M/4 + \dots \text{ (true anomaly)} \quad (3\text{-}1\text{-}17)$$

and where

$$M = L - P \quad \text{(mean anomaly)} \qquad\qquad (3\text{-}1\text{-}18)$$

The radius vector $\underline{r}$ is given by

$$\underline{r} = \begin{Bmatrix} r \\ o \\ o \end{Bmatrix} \qquad\qquad (3\text{-}1\text{-}19)$$

where

$$r = a \left(\frac{1 - e^2}{1 + e \cos v} \right) \qquad\qquad (3\text{-}1\text{-}20)$$

and

a, e = semi-major axis and eccentricity of orbit of the

satellite around the planet.

Vector Direction to a Star

The apparent locations of stars are obtained from a dictionary

of stars derived from the Smithsonian Astrophysical Observatory

star catalog. Other catalogs of stars can also be used. These

catalogs list the stars in terms of the right-ascension and declination

in the 1950.0 Earth Equatorial and Equinox coordinate system;

these are locations corrected for stellar aberration effects at

the time of observation and are referenced to a heliocentric frame

of reference. The direction to a star $\hat{q}$, in that frame is given by

$$\hat{q} = \begin{Bmatrix} \cos \delta \cos \alpha \\ \cos \delta \sin \alpha \\ \sin \delta \end{Bmatrix} \tag{3-1-21}$$

where α and δ are the right ascension and declination of the star,

obtained from the star catalog and corrected for proper motion since

the epoch.

3.2 Observation Equation Model

In this section we develop the observation equation in terms of the vector direction to the object, $\hat{\underline{t}}$. There are two steps involved in arriving at the observation in TV pixel-line coordinates as defined in Section 2.1:

1) obtaining the direction vector to the object in the vidicon frame of reference; and

2) mapping the vidicon referenced direction vector to pixel and line coordinates.

We now discuss both of these in the following two subsections.

1. Obtaining $\hat{\underline{t}}$ in Vidicon Coordinates

In Section 1.5 we developed the coordinate transformations to go from the frame of reference I, through the frames C, X, S, P_α and P, to the frame of reference T; these frames of reference are also defined in Section 1.5.

The television camera system, T, can be directly referenced to the Celestial system, C, by its clock angle α_T, cone angle β_T and rotation angle γ_T as shown in Figure 3-3. The transformation R_{CT}, which takes the ABC system to the _television_ MNL system (as opposed to the Platform MNL system), is then given by

$$R_{CT} = R_{CT_3} R_{CT_2} R_{CT_1} \tag{3-2-1}$$

where

$$R_{CT_1} = \begin{bmatrix} \cos \alpha_T & \sin \alpha_T & 0 \\ -\sin \alpha_T & \cos \alpha_T & 0 \\ 0 & 0 & 1 \end{bmatrix} ,$$

89
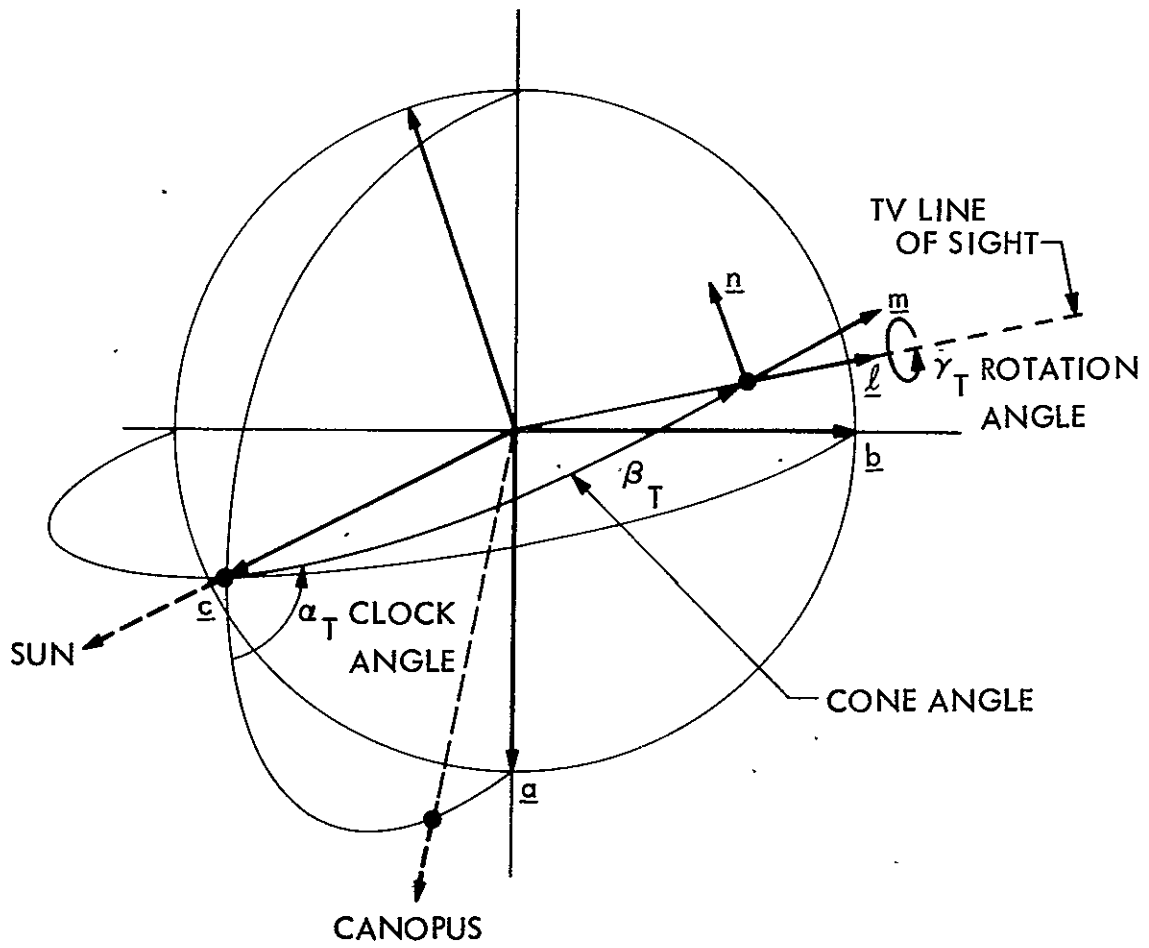
Figure 3-3. Celestial/Television Coordinate System Relationship

$$R_{CT_2} = \begin{bmatrix} \cos\beta_T & 0 & -\sin\beta_T \\ 0 & 1 & c\ 0 \\ \sin\beta_T & 0 & \cos\beta_T \end{bmatrix} \quad,$$

and

$$R_{CT_3} = \begin{bmatrix} \cos\gamma_T & \sin\gamma_T & 0 \\ -\sin\gamma_T & \cos\gamma_T & 0 \\ 0 & 0 & 1 \end{bmatrix} \quad.$$

This yields

$$R_{CT} = \begin{bmatrix} cG.cB.cA - sG.sA & cG.cB.sA + sG.cA & -cG.sB \\ -sG.cB.cA - cG.sA & -sG.cB.sA + cG.cA & sG.sB \\ sB.cA & sB.sA & cB \end{bmatrix} \quad (3\text{-}2\text{-}2)$$

where the prefixes "s" and "c" refer to $\sin(\cdot)$ and $\cos(\cdot)$ respectively

and where A, B and G refer to α_T, β_T and γ_T respectively.

Since R_{CT} can be written

$$R_{CT} = R_{PT}R_{CP} \quad, \quad\quad\quad (3\text{-}2\text{-}3)$$

using Eqs. (3-2-2), (1-5-14) and (1-5-15a) through (1-5-18) we

can determine the television camera pointing angles given: (a)

the platform pointing angles obtained from the clock and cone angle

gimbal potentiometers, and (b) the pitch, yaw and roll angles obtained

from the sun sensor and star tracker signals. It is useful to have

these angles directly when we wish to solve for the camera pointing.

Vidicon Coordinates

As discussed in Section 2.1, the definition of V, the vidicon

coordinate system xyz, is determined by the vidicon electronics --

specifically, the direction of scan during the image charge readout

process. This is rotated relative to the T coordinates through an angle ρ about the positive camera $\underline{\ell}$ axis, as shown in Figure 3-4. The corresponding rotation matrix R_{TV} is given by

$$R_{TV} = \begin{bmatrix} \cos\rho & \sin\rho & 0 \\ -\sin\rho & \cos\rho & 0 \\ 0 & 0 & 1 \end{bmatrix} \qquad (3\text{-}2\text{-}4)$$

The vector $\hat{\underline{t}}$ expressed in inertial coordinates $\hat{\underline{t}}_I$ can therefore be transformed to vidicon coordinates, $\hat{\underline{t}}_V$ through

$$\hat{\underline{t}}_V = R_{IV}\, \hat{\underline{t}}_I \qquad (3\text{-}2\text{-}5)$$

where R_{IV} is given by

$$R_{IV} = R_{TV}\, R_{CT}\, R_{IC} \qquad (3\text{-}2\text{-}6)$$

It may be observed that the rotation R could have been absorbed along with γ_T in the rotation R_{CT_3}. However, it is convenient to define the γ_T such that it has a small value (~ 0). Then, if the T offset angles ψ, χ, ω are small, the angles α_T, β_T and γ_T can be easily determined from similar angles for the platform, α, β, γ through the approximate equations

$$\alpha_T \approx \alpha + \chi/\sin\beta$$

$$\beta_T \approx \beta + \psi \qquad (3\text{-}2\text{-}7)$$

and

$$\gamma_T \approx \gamma - \chi \cot\beta + \omega$$

instead of through equation (3-2-2). We can make these approximations because the rule of vector addition holds for infinitesimal angular
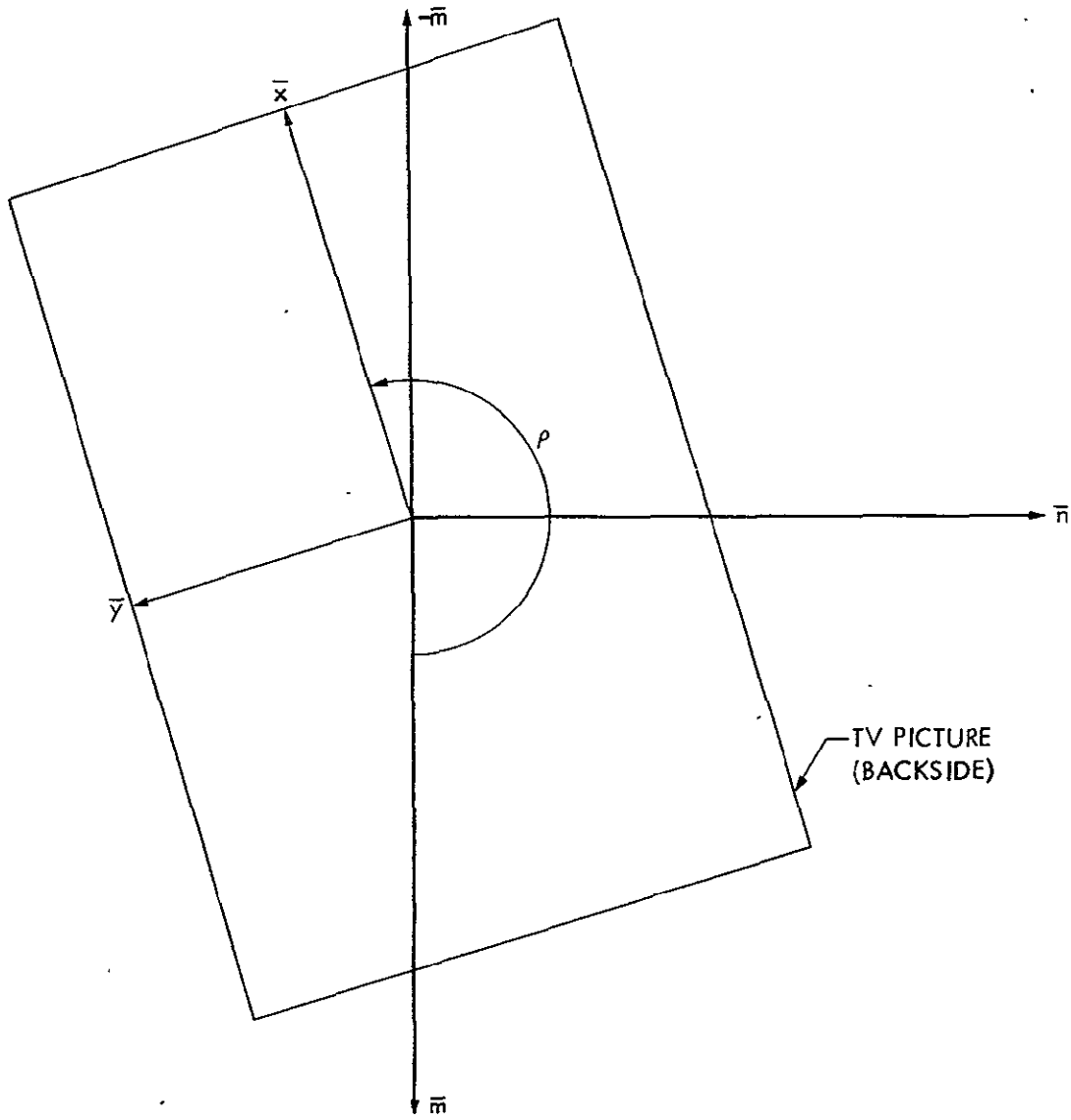
Figure 3-4.   TV Picture Orientation

rotations.

2) Image Location in Pixel and Line Coordinates

Mapping of the vector coordinates $\hat{\underline{t}}_V$ through the camera optics onto the camera image plane is quite straightforward using the collinearity equations of photogrammetry (Ref. 32), and is given by

$$\begin{Bmatrix} x \\ y \end{Bmatrix} = \frac{f}{t_{V_3}} \begin{bmatrix} 1 & 0 & 0 \\ 0 & 1 & 0 \end{bmatrix} \hat{\underline{t}}_V = \frac{f}{t_{V_3}} \begin{Bmatrix} t_{V_1} \\ t_{V_2} \end{Bmatrix} \qquad (3\text{-}2\text{-}8)$$

where f is the focal length of the optical system and

$$\hat{\underline{t}}_V = \begin{bmatrix} t_{V_1} & t_{V_2} & t_{V_3} \end{bmatrix}^T \qquad (3\text{-}2\text{-}9)$$

The transformation from the image plane to pixel and line coordinates is obtained by a mapping through a scale factor matrix K and a translation of the origin, i.e.,

$$\begin{Bmatrix} p \\ \ell \end{Bmatrix} = K \begin{Bmatrix} x \\ y \end{Bmatrix} + \begin{Bmatrix} p_o \\ \ell_o \end{Bmatrix} \qquad (3\text{-}2\text{-}10)$$

Here (p_o, ℓ_o) are the coordinates of the central pixel and line of the TV target raster; K is given by

$$K = \begin{bmatrix} k_x & k_{xy} \\ k_{yx} & k_y \end{bmatrix} \qquad (3\text{-}2\text{-}11)$$

where the diagonal elements of k are the scale factors from the image plane to the pixel-line plane while the off-diagonal terms provide a rotation with respect to x-y coordinates and a non-orthogonality of the P, L axes.

94

3.3 Picture Design

In this section various quantities necessary when designing a picture are computed.

In Section 3.2 we went through the development of the equations for the locations of the observed images in the picture. In addition to this, during the picture design, the geometry in both inertial coordinates xyz and in celestial coordinates ABC is important, due respectively to the requirement of having a good star background and the requirement that scan platform movement constraints not be violated.

If a particular right ascension, a, and declination, δ, direction (in inertial coordinates) is desired, $\hat{\underline{t}}_I$ will be given by

$$\hat{\underline{t}}_I = \begin{Bmatrix} \cos a \cos \delta \\ \sin a \cos \delta \\ \sin \delta \end{Bmatrix} \tag{3-3-1}$$

The clock and cone angles, α and β, of the direction can then be obtained using

$$\hat{\underline{t}}_C = R_{IC} \, \hat{\underline{t}}_I \tag{3-3-2}$$

and

$$\alpha = \tan^{-1} (t_{C_2}/t_{C_1})$$

$$\beta = \cos^{-1} (t_{C_3}) \tag{3-3-3}$$

where $0 \le \alpha < 2\pi$ and $0 \le \beta \le \pi$.

Similarly, for specific clock and cone angles, using

$$\hat{t}_C = \begin{Bmatrix} \cos \alpha \, \sin \beta \\ \sin \alpha \, \sin \beta \\ \cos \beta \end{Bmatrix} \tag{3-3-4}$$

and using Eq. (3-3-2) we can obtain the right ascension and declination

$$a = \tan^{-1} (t_{I_2}/t_{I_1})$$

$$\delta = \sin^{-1} (t_{I_3}) \tag{3-3-5}$$

where $0 \le a < 2\pi$ and $-\pi/2 < \delta \le \pi/2$.

For ease and accuracy of image detection there should be a minimum of smear caused by the motion of the image during the time the camera shutter is open. To compute the velocity of an image in pixel-line coordinates, let $\dot{t}$ be the velocity of the object. Then

$$\dot{t}_V \equiv \begin{Bmatrix} \dot{t}_1 \\ \dot{t}_2 \\ \dot{t}_3 \end{Bmatrix} = R_{IV} \, \dot{t}_I \tag{3-3-6}$$

From Eqs. (3-2-8) and (3-2-10) we can write

$$\begin{Bmatrix} p \\ \ell \end{Bmatrix} = f[K] \begin{Bmatrix} t_1/t_3 \\ t_2/t_3 \end{Bmatrix} \tag{3-3-7}$$

where $t_i = |\underline{t}| \, t_{V_i}$

Differentiating we obtain

$$\begin{Bmatrix} v_p \\ v_\ell \end{Bmatrix} = f[K] \cdot \frac{1}{t_3^{\,2}} \begin{Bmatrix} t_3 \dot{t}_1 - \dot{t}_3 t_1 \\ t_3 \dot{t}_2 - \dot{t}_3 t_2 \end{Bmatrix} \tag{3-3-8}$$

where v_p, v_ℓ are the image velocities in the pixel and line directions respectively. In this computation we have not considered the image

velocity due to the change in R_{IV} in Eq. (3-3-6) caused by the attitude control limit cycle motion.

To determine the illuminated shape of the image, the phase angle of the object is required, where the phase angle is defined as the angle between the directions from the object to sun and to the observer (spacecraft) respectively. Thus the phase angle gives a measure of the departure from full illumination of the object as viewed by the observer, zero degrees implying full illumination and 180° implying zero illumination. The phase angle, ψ, is computed by

$$\psi = \cos^{-1}(\hat{y} \cdot \hat{t}) \qquad (3\text{-}3\text{-}9)$$

where

$\hat{y}$ = sun-object unit vector.

The brightness of an image is characterized by the visual magnitude V of the object as viewed from the spacecraft. For stars this is available directly from the star catalogue; for other celestial bodies it is computed by

$$V = V_o + 5 \log_{10} ty - 2 \cdot 5 \log_{10} \Phi \qquad (3\text{-}3\text{-}10)$$

where

      y, t = distance of the object, expressed in astronomical units (AU), from the sun and spacecraft respectively,

      V_o = visual magnitude of the object as viewed from the sun at a distance of 1 AU,

and Φ is computed from

$$\Phi = \frac{1}{\pi} \left[\sin \psi + (\pi - \psi) \cos \psi \right] . \qquad (3\text{-}3\text{-}11)$$

An important consideration during the design of pictures
containing the natural satellite is the avoidance of the planet
in the field of view. Exposure times that are suitable for the
satellite images could cause damage to the camera if the much brighter
planet were imaged. Even if the planet is not in the field of view
but close to the edge, problems could arise in detection of the
images within the field of view due to stray light from the planet.
For typical interplanetary spacecraft, instrument pointing control
accuracies are of the order of 0.5 degrees (3 σ) in any direction;
this then causes a (3 σ) constraint to be placed on the picture
design that the separation angle between the edge of the satellite
image and the edge of the planet be larger than 1.0 deg -- i.e.,
0.5 deg to avoid imaging Mars and 0.5 deg to ensure imaging the
satellite.

To compute the separation angle, first the semi-angular diameter
$\emptyset$ of both the satellite and the planet are computed by

$$\emptyset_n = \sin^{-1} R_n / |\underline{t}|,$$
$$\emptyset_p = \sin^{-1} R_p / |\underline{s}| \qquad\qquad (3\text{-}3\text{-}12)$$

where $\emptyset$ = semi-angular diameter,

            R = radius of the object,

and subscripts n, p refer to the satellite, planet respectively.
The separation angle is then given by

$$\theta_{sep} = \Omega - (\emptyset_n + \emptyset_p), \qquad\qquad (3\text{-}3\text{-}13)$$

where Ω is the angular separation between the directions to the
centers of the satellite and planet and is given by

$$\Omega = \cos^{-1}(-\hat{\underline{s}} \cdot \hat{\underline{t}}) = \pi - \cos^{-1}(\hat{\underline{s}} \cdot \hat{\underline{t}}) \qquad (3\text{-}3\text{-}14)$$

If the value of θ_{sep} from Eq. (3-3-13) is negative, this implies

that the satellite is either (i) occulted by the planet or (ii) is

in transit across the planet as viewed from the spacecraft. These

two cases occur respectively when (i) $|\underline{s}| < |\underline{t}|$ or (ii) $|\underline{s}| \geq |\underline{t}|$.

99

3.4 Measurement Processing

As discussed in the beginning of the chapter, there are two categories of measurements required for optical data processing, viz. (i) measurements that lead to a determination of the television camera pointing direction using the spacecraft telemetry engineering data; and (ii) measurements using the television picture data leading to a determination of the image location in picture coordinates. These are referred to in the following as pointing data and imaging data respectively, and are discussed below.

Pointing Data

The process of obtaining the pointing of the television camera from spacecraft sensors was described in Section 1.5. This consists of (i) obtaining the inertially referenced spacecraft attitude from the sun-sensor and star-tracker data (i.e. the transformation R_{IS}) followed by (ii) the use of the scan platform clock and cone angle data to obtain the spacecraft relative platform orientation, R_{SP}, and therefrom the television camera orientation, R_{ST}, using

$$R_{ST} = R_{PT}\, R_{SP} \qquad\qquad (3\text{-}4\text{-}1)$$

These two pieces can then be combined to give

$$R_{IT} = R_{ST}\, R_{IS} \qquad , \qquad\qquad (3\text{-}4\text{-}2)$$

which determines the pointing direction, $\underline{\ell}$, of the television camera in inertial coordinates $(\underline{\ell}_I)$, or equivalently in celestial coordinates $(\underline{\ell}_C)$ using

$$\underline{\ell}_C = R_{IC}\, \underline{\ell}_I \qquad\qquad (3\text{-}4\text{-}3)$$

The television orientation can be expressed in terms of the television clock, cone and rotation angles, α_T, β_T and γ_T, defined in Section 3.2.

Imaging Data

The raw imaging data consists of video intensity for each pixel in a picture, discretized to 2^n gray levels; n typically ranges from seven to nine. As mentioned at the beginning of the chapter, the reduction of this raw data to image location information can be divided into two functional steps, viz. (i) some method of defining and determining the profile of the lit limb, and (ii) a method for estimating the center of the viewed object as mapped into picture frame coordinates.

For small images (~1-5 pixels), such as those of stars and of small diameter natural satellites, both of these functions may be performed by display and visual inspection of areas around the expected image locations in the form of plots showing video intensity as a function of line and pixel number. The detection of dim images can be facilitated by contrast enhancement within the picture.

For large images such as that of a planet the processing has to be more elaborate to minimize the error in locating the center. The lit limb is defined by a curve joining all points with the same predetermined level of video intensity. These points are located by reading the digital video data along a direction parallel to the P or L axis of the vidicon (P, L) coordinate system. A process is then required to determine the center of the image from these limb points.

101

If the planet is modelled as a three-dimensional ellipsoid the cross-section observed from any direction is given by an ellipse; the parameters of the ellipse are a function of the orientation of the ellipsoid relative to the line-of-sight ("look") direction, $\underline{\ell}$, from the spacecraft at the time of observation. In the following we give a development to determine these parameters.

The equation of an ellipsoid oriented with its principal axes along the coordinate axis is given by

$$\Phi \equiv \frac{x_o^2}{a_o^2} + \frac{y_o^2}{b_o^2} + \frac{z_o^2}{c_o^2} = 1 \tag{3-4-4}$$

where a_o, b_o, c_o are the semi-major, semi-mean and semi-minor axes respectively; or

$$\Phi \equiv \underline{x}^T A \underline{x} = 1 \tag{3-4-5}$$

where

$$\underline{x} \triangleq \begin{Bmatrix} x_o \\ y_o \\ z_o \end{Bmatrix} \tag{3-4-6}$$

and

$$A = \begin{bmatrix} 1/a_o^2 & 0 & 0 \\ 0 & 1/b_o^2 & 0 \\ 0 & 0 & 1/c_o^2 \end{bmatrix} \tag{3-4-7}$$

Let the vector $\underline{x}$ be represented by $\underline{x}_E$ in Ellipsoidal body-fixed coordinates, E, where the z axis is aligned with the planet pole and the

102

x axis is at longitude λ relative to the Prime Meridian reference, M, for the planet. Thus

$$\underline{x}_E = R_{ME} \, \underline{x}_M \tag{3-4-8}$$

where

$$R_{ME} = \begin{bmatrix} \cos\lambda & \sin\lambda & 0 \\ -\sin\lambda & \cos\lambda & 0 \\ 0 & 0 & 1 \end{bmatrix} \tag{3-4-9}$$

Let the planet be rotating at angular velocity ω about its pole and the planet pole direction be given by right ascension α and declination δ in inertial coordinates, I; then

$$\underline{x}_M = R_{IM} \, \underline{x}_I \tag{3-4-10}$$

where, letting $c(\cdot)$ and $s(\cdot)$ represent $\cos(\cdot)$ and $\sin(\cdot)$,

$$R_{IM} = \begin{bmatrix} c(\omega t) & s(\omega t) & 0 \\ -s(\omega t) & c(\omega t) & 0 \\ 0 & 0 & 1 \end{bmatrix} \begin{bmatrix} s\delta & 0 & -c\delta \\ 0 & 1 & 0 \\ c\delta & 0 & s\delta \end{bmatrix} \begin{bmatrix} c\alpha & s\alpha & 0 \\ -s\alpha & c\alpha & 0 \\ 0 & 0 & 1 \end{bmatrix}$$

$$\tag{3-4-11}$$

The rotation to vidicon coordinates, V, is given by R_{IV} obtained from Section 3.2; then we can write

$$\underline{x}_E = R_{VE} \, \underline{x}_V \tag{3-4-12}$$

where $\underline{x}_T$ is the vector from the center to the surface of the ellipsoid, expressed in vidicon coordinates, and where R_{VE} is given by

$$R_{VE} = R_{ME} \, R_{IM} \, R_{VI} \tag{3-4-13}$$

Substituting this into Eq. (3-4-5),

$$\Phi \equiv \underline{x}_V^T \, B \, \underline{x}_V = 1 \tag{3-4-14}$$

103

where

$$B \triangleq R_{EV} A R_{VE} \qquad (3-4-15)$$

Now, the cross-section of the ellipsoid seen will be an ellipse defined by those limb points where the tangent is parallel to the look direction $\underline{\ell}$, i.e. the gradient $\partial\Phi/\partial\underline{x}$ will be normal to the vector $\underline{\ell}$. Therefore

$$\frac{\partial\Phi}{\partial\underline{x}_V} \underline{\ell}_V = 0 \qquad (3-4-16)$$

where $\underline{\ell}_V$ is $\underline{\ell}$ expressed in V coordinates, given by

$$\underline{\ell}_V = \begin{Bmatrix} 0 \\ 0 \\ 1 \end{Bmatrix} \qquad (3-4-17)$$

Differentiating (3-4-14) and using $B = B^T$, Eq. (3-4-16) yields

$$2\underline{x}_V^T B \begin{Bmatrix} 0 \\ 0 \\ 1 \end{Bmatrix} = 0 \qquad (3-4-18)$$

Using this in Eq. (3-4-14) will yield the ellipse, the projection of which in the $V_1 - V_2$ plane is the desired limb profile. We would like to define a coordinate system U for which the reference plane is parallel to this ellipse; defining $\underline{u}$ such that

$$\underline{u}^T \equiv [u_1 \quad u_2 \quad u_3] \triangleq \underline{x}_V^T B \quad , \qquad (3-4-19)$$

or

$$\underline{x}_V = B^{-1} \underline{u}$$
$$= C \underline{u} \quad , \qquad (3-4-20)$$

where

$$C \triangleq B^{-1} \qquad (3\text{-}4\text{-}21)$$

$$= R_{EV} A^{-1} R_{VE} \quad , \qquad (3\text{-}4\text{-}22)$$

and where A^{-1} is given by

$$A^{-1} = \begin{bmatrix} a_o^2 & 0 & 0 \\ 0 & b_o^2 & 0 \\ 0 & 0 & c_o^2 \end{bmatrix} \qquad , \quad (3\text{-}4\text{-}23)$$

In obtaining Eq. (3-4-22) we used the fact that the R's are orthonormal matrices. Using Eq. (3-4-19) in (3-4-18),

$$\underline{u}^T \begin{Bmatrix} 0 \\ 0 \\ 1 \end{Bmatrix} = 0 \quad .$$

or

$$u_3 = 0 \qquad (3\text{-}4\text{-}24)$$

Substituting Eq. (3-4-20) into (3-4-14) and using (3-4-21),

$$\Phi \equiv \underline{u}^T C^T BC \underline{u} = 1$$

or, since $C = C^T = B^{-1}$,

$$1 = \Phi \equiv \underline{u}^T C \underline{u} \qquad (3\text{-}4\text{-}25)$$

$$= [u_1 \quad u_2 \ \vdots \ u_3] \begin{bmatrix} C_1 & \vdots & C_2 \\ \cdots & \vdots & \cdots \\ C_2^T & \vdots & C_3 \end{bmatrix} \begin{bmatrix} u_1 \\ u_2 \\ \cdots \\ u_3 \end{bmatrix} \qquad (3\text{-}4\text{-}26)$$

$$= [u_1 \quad u_2] \ C_1 \begin{bmatrix} u_1 \\ u_2 \end{bmatrix} \qquad (3\text{-}4\text{-}27)$$

From Eq. (3-4-26) and (3-4-20),

$$\left\{ \begin{array}{c} x_{V_1} \\ x_{V_2} \end{array} \right\} = C_1 \left\{ \begin{array}{c} u_1 \\ u_2 \end{array} \right\} \qquad\qquad (3\text{-}4\text{-}28)$$

or

$$\left\{ \begin{array}{c} u_1 \\ u_2 \end{array} \right\} = C_1^{-1} \left\{ \begin{array}{c} x_{V_1} \\ x_{V_2} \end{array} \right\} \qquad\qquad (3\text{-}4\text{-}29)$$

Substituting (3-4-29) into (3-4-27),

$$\left[\begin{array}{cc} x_{V_1} & x_{V_2} \end{array} \right] C_1^{-1} \left[\begin{array}{c} x_{V_1} \\ x_{V_2} \end{array} \right] = 1 \qquad\qquad (3\text{-}4\text{-}30)$$

Thus, if C_1 is obtained as the upper left hand 2 x 2 partition of C which is obtained using Eq. (3-4-22), then Eq. (3-4-30) gives the projected limb profile in vidicon coordinates, translated such that the center of the ellipse is at the origin.

Let this ellipse be represented as in Figure 3-5 with the x-y axes parallel to the principal axes, where a, b are the semi-major, semi-minor axes of the limb profile; p_1, ℓ_1 are the coordinates of the center of the ellipse; and ψ is the orientation angle of the ellipse as shown. The equation of this ellipse is

$$\frac{x^2}{a^2} + \frac{y^2}{b^2} - 1 = 0 \qquad\qquad (3\text{-}4\text{-}31)$$

or

$$\left(1 - \frac{c^2}{a^2} \right) x^2 + y^2 - a^2 + c^2 = 0 \qquad\qquad (3\text{-}4\text{-}32)$$
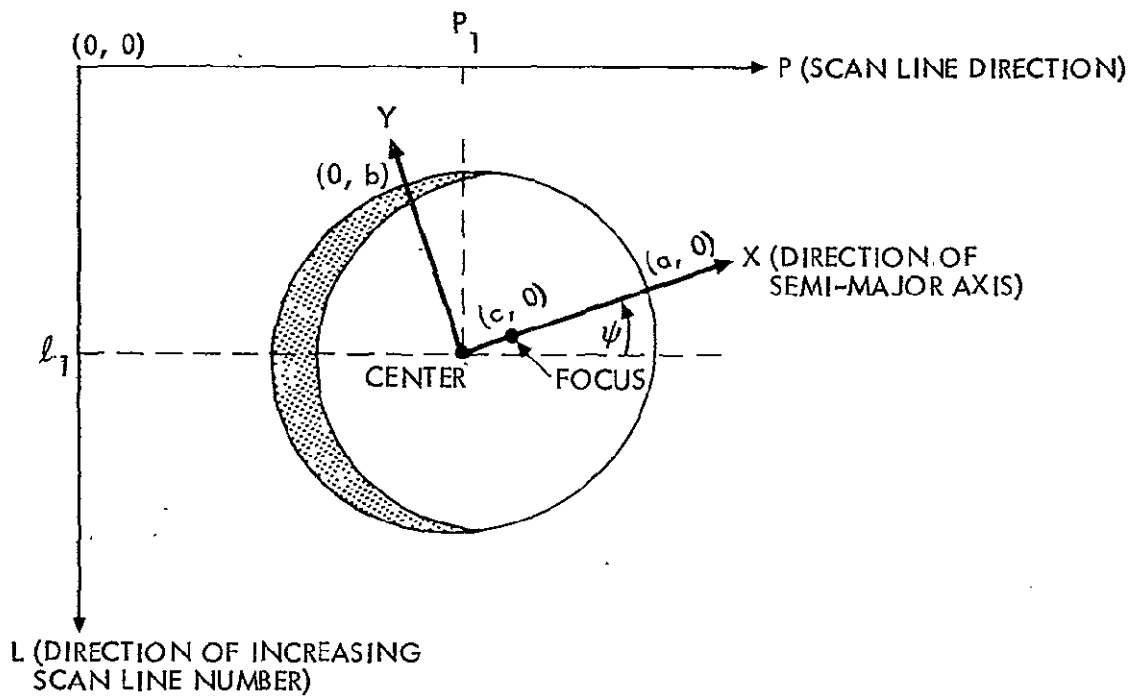
106

Figure 3-5.   Planet Limb-fitting Process

where c is the distance of the focus from the center given by

$$c = \left(a^2 - b^2\right)^{1/2}$$
(3-4-33)

The observable equation is defined to be (Ref. 19)

$$\phi = \left(1 - \frac{c^2}{a^2}\right) x^2 + y^2 - a^2 + c^2 + \xi$$
(3-4-34)

where ξ is the observation noise and where (x, y) are given in terms of the limb points (p, ℓ) by

$$\begin{Bmatrix} x \\ y \end{Bmatrix} = \begin{bmatrix} \cos \psi & -\sin \psi \\ -\sin \psi & -\cos \psi \end{bmatrix} \begin{Bmatrix} p - p_I \\ \ell - \ell_1 \end{Bmatrix}$$
(3-4-35)

A minimum variance estimation algorithm is used to identify the parameters a, c, ψ, p_1 and ℓ_1.

To determine the effect of errors in the limb points, we take the variation of Eqs. (3-4-34) and (3-4-35),

$$\delta\phi = 2 \begin{bmatrix} \left(1 - \frac{c^2}{a^2}\right) x & y \end{bmatrix} \begin{Bmatrix} \delta x \\ \delta y \end{Bmatrix}$$
(3-4-36)

$$= -2 \begin{bmatrix} -\left(1 - \frac{c^2}{a^2}\right) x \cos \psi + y \sin \psi & \left(1 - \frac{c^2}{a^2}\right) x \sin \psi + y \cos \psi \end{bmatrix} \begin{Bmatrix} \delta p \\ \delta \ell \end{Bmatrix}$$
(3-4-37)

We will use this expression in Chapter 4.

3.5 Instrumentation Error Models

In this section we present the mathematical models for the instrument related errors in optical navigation measurement processing. Referring to the classification of optical data errors in Section 2.3 the TV pointing errors and TV distortion errors stem primarily from spacecraft related errors and camera related errors respectively. These are discussed below.

1. TV Pointing Errors

The apriori TV pointing is determined using the attitude control system pitch, yaw, and roll sensor signals and the clock and cone gimbal angles for the scan platform. In addition to the error in the signals themselves, there are contributions to it from mechanical misalignments in the spacecraft instrumentation. We discuss models for these here.

Effect of Mechanical Misalignment Errors

When there are instrument misalignment errors to be modelled, the observable equation has to have these errors factored in. In general the misalignment error at any step can have components in each of the three coordinate axes; consider an error rotation about the Z coordinate axis in an xyz system. This will be given by

$$
R_{\epsilon_3} = \begin{bmatrix} \cos \epsilon_3 & \sin \epsilon_3 & 0 \\ -\sin \epsilon_3 & \cos \epsilon_3 & 0 \\ 0 & 0 & 1 \end{bmatrix}
$$

which for small values of ϵ_3 reduces to

$$R_{\epsilon_3} \approx \begin{bmatrix} 1 & \epsilon_3 & 0 \\ -\epsilon_3 & 1 & 0 \\ 0 & 0 & 1 \end{bmatrix} \qquad \qquad (3\text{-}5\text{-}1)$$

$$= (I + E_3) \quad ,$$

where I is the identity matrix and

$$E_3 = \begin{bmatrix} 0 & \epsilon_3 & 0 \\ -\epsilon_3 & 0 & 0 \\ 0 & 0 & 0 \end{bmatrix}$$

Using similar error rotations, E_1 and E_2, about the other two axes, and writing

$$R_{\epsilon_i} = I + E_i \qquad \qquad (3\text{-}5\text{-}2)$$

the general error rotation transformation can be written

$$R_\epsilon = (I + E_3)(I + E_2)(I + E_1) \qquad \qquad (3\text{-}5\text{-}3)$$

or, neglecting higher order terms,

$$R_\epsilon = I + (E_1 + E_2 + E_3) \qquad \qquad (3\text{-}5\text{-}4)$$

$$= I + E$$

where

$$E = \begin{bmatrix} 0 & \epsilon_3 & -\epsilon_2 \\ -\epsilon_3 & 0 & \epsilon_1 \\ \epsilon_2 & -\epsilon_1 & 0 \end{bmatrix} \qquad \qquad (3\text{-}5\text{-}5)$$

We note here that if R_i is a rotation through an angle θ_i (not necessarily a small angle) about the ith axis, then E_i commutes with R_i, i.e.,

$$R_i E_i = E_i R_i, \qquad i = 1, 2, 3 \qquad \qquad (3\text{-}5\text{-}6)$$

110

Using the notation in Section 1.5, the observation vector in vidicon coordinates without the effect of errors is written as

$$\hat{\underline{t}}_V = R_{TV}\, R_{PT_3} R_{PT_2}\, R_{PT_1}\, R_{P_\alpha P}\, R_{SP_\alpha}\, R_{XS}\, R_{X_0 X}\, R_{IX_0}\, \hat{\underline{t}}_I \qquad (3\text{-}5\text{-}7)$$

Each of the R's after R_{IX_0} is a one axis rotation except for $R_{X_0 X}$ which is a three axes rotation where the angles are small. R_{IX_0} is an idealized rotation of coordinates. Thus with the effect of alignment errors the coordinates $\hat{\underline{t}}_V$ will be, in general,

$$\hat{\underline{t}}_V = R_{TV}\,(I + E_T)\, R_{PT_3}\,(I + E_{P_3})\, R_{PT_2}\,(I + E_{P_2})\, R_{PT_1}\,(I + E_{P_1})$$

$$R_{P_\alpha}\,(I + E_\alpha)\, R_{SP_\alpha}\,(I + E_S)\, R_{XS}\,(I + E_X)\, R_{X_0 X}\, R_{IX_0}\, \hat{\underline{t}}_I$$

$$(3\text{-}5\text{-}8)$$

where each of the E's is a three axis error rotation matrix as represented in general by Eq. (3-5-5).

If now we make the assumption that each of ψ, χ, and ω are small (when this assumption is not true all the terms must be carried through) then each of the R_{PT_2} is a small angle rotation which can be represented by Eq. (3-5-2); thus the terms from $(I + E_T)$ through $(I + E_{P_1})$ in Eq. (3-5-8) can be represented as $R_{PT}\,(I + E_P)$ and we can write as in Ref. ,

$$\hat{\underline{t}}_V \doteq R_{TV}\, R_{PT}\,(I + E_P)\, R_{P_\alpha P}\,(I + E_\alpha)\, R_{SP_\alpha}\,(I + E_S)$$

$$R_{XS}\,(I + E_X)\, R_{X_0 X}\, R_{IX_0}\, \hat{\underline{t}}_I \qquad (3\text{-}5\text{-}9)$$

Neglecting higher order terms this gives

$$\hat{\underline{t}}_V = \hat{\underline{t}}_{V_0} + \sum_{J=1}^{4} P_J E_J Q_J \hat{\underline{t}}_I \qquad (3\text{-}5\text{-}10)$$

where

$$\hat{\underline{t}}_{V_0} = R_{IV} \, \hat{\underline{t}}_I$$

and where J represents P, α, S, X and P_J, Q_J are respectively the products of the R's preceding, following the corresponding $(I + E_J)$ term in Eq. (3-5-9).

At this point we note that any antisymmetric matrix U operating on a vector $\underline{V}$ can be represented as the cross product of two vectors. In particular, if

$$U = \begin{bmatrix} 0 & u_3 & -u_2 \\ -u_3 & 0 & u_1 \\ u_2 & -u_1 & 0 \end{bmatrix} \quad ,$$

$$\underline{u} = [u_1 \ u_2 \ u_3]^T \quad ,$$

$$\underline{v} = [v_1 \ v_2 \ v_3]^T \quad ,$$

then we have

$$U\underline{v} = -\underline{u} \times \underline{v} = \underline{v} \times \underline{u} \qquad\qquad (3\text{-}5\text{-}11)$$

and the error terms in Eq. (3-5-10) can be written

$$P_J E_J Q_J \hat{\underline{t}}_I = -P_J [(\underline{\epsilon}_J) \times (Q_J \, \hat{\underline{t}}_I)]$$

$$= -(P_J \underline{\epsilon}_J) \times (P_J Q_J \hat{\underline{t}}_I)$$

$$= -(P_J \underline{\epsilon}_J) \times (\hat{\underline{t}}_{V_0})$$

$$= (\hat{\underline{t}}_{V_0}) \times (P_J \underline{\epsilon}_J)$$

or,

$$P_J E_J Q_J \hat{\underline{t}}_I = -T_{V_0} P_J \underline{\epsilon}_J \qquad\qquad (3\text{-}5\text{-}12)$$

where $\underline{\epsilon}_J$ is the rotation vector angle corresponding to E_J,

$$\underline{\hat{t}}_{V_0} = [t_{V_{01}} \quad t_{V_{02}} \quad t_{V_{03}}]^T \qquad (3\text{-}5\text{-}13)$$

and

$$T_V = \begin{bmatrix} 0 & t_{V_{03}} & -t_{V_{02}} \\ -t_{V_{03}} & 0 & t_{V_{01}} \\ t_{V_{02}} & -t_{V_{01}} & 0 \end{bmatrix} \qquad (3\text{-}5\text{-}14)$$

Using this result in Eq. (3-5-9) we obtain

$$\underline{\hat{t}}_V = \underline{\hat{t}}_{V_0} + T_V R_{PV}[\underline{\epsilon}_P + R_{P_\alpha P}\underline{\epsilon}_\alpha + R_{P_\alpha P}R_{SP_\alpha}\underline{\epsilon}_S + R_{P_\alpha P}R_{SP_\alpha}R_{XS}\underline{\epsilon}_X] \qquad (3\text{-}5\text{-}15)$$

where $R_{P_\alpha P}$ is given in Eq. (1-5-18). Using Eq. (1-5-14) and replacing cos and sin by c and s,

$$R_{SP} = R_{P_\alpha P}R_{SP_\alpha} = \begin{bmatrix} c\alpha_P c\beta_P & s\alpha_P c\beta_P & -s\beta_P \\ -s\alpha_P & c\alpha_P & 0 \\ c\alpha_P s\beta_P & s\alpha_P s\beta_P & c\beta_P \end{bmatrix} \qquad (3\text{-}5\text{-}16)$$

and using Eq. (1-5-17) and combining terms,

$$R_{XP} = R_{SP}R_{XS} = \begin{bmatrix} c\beta_P c(\alpha_X - \alpha_P) & c\beta_P s(\alpha_X - \alpha_P) & s\beta_P \\ s(\alpha_X - \alpha_P) & -c(\alpha_X - \alpha_P) & 0 \\ s\beta_P c(\alpha_X - \alpha_P) & s(\alpha_X - \alpha_P) & -c\beta_P \end{bmatrix}$$

$$(3\text{-}5\text{-}17)$$

The errors $\underline{\epsilon}_X$ arise from the attitude control system pitch, yaw, and roll angle determinations. These angles, are determined using the voltage signals from the sun sensor and star tracker. Modelling this determination simply as

$$\theta_i = k_i \nu_i \qquad\qquad (3\text{-}5\text{-}18)$$

where ν_i are angles which are a function of the voltages, and k_i scale factors, the error is given by

$$\delta\theta_i = k_i \delta\nu_i + \delta k_i \nu_i$$

$$= k_i \partial\nu_i + \frac{\delta k_i}{k_i} \theta_i$$

or

$$\delta\theta_i = \epsilon_i + \lambda_i \theta_i \qquad\qquad (3\text{-}5\text{-}19)$$

where ϵ_i are sensor angle null offsets (biases) and λ_i are percentage errors in the scale factors. The $\underline{\epsilon}_X$ can therefore be written as

$$\underline{\epsilon}_X = \begin{Bmatrix} \epsilon_p \\ \epsilon_y \\ \epsilon_r \end{Bmatrix} + \begin{Bmatrix} \lambda_p \theta_p \\ \lambda_y \theta_y \\ \lambda_r \theta_r \end{Bmatrix} \qquad\qquad (3\text{-}5\text{-}20)$$

where the subscripts denote the pitch, yaw, and roll components respectively.

There is a redundancy of error parameters in Eq. (3-5-15) due to Eq. (3-5-6). The four $\underline{\epsilon}_J$ are transmitted successively through three single angle rotations $R_{P_\alpha P}$, R_{SP_α} and R_{XS} about axes numbers 2, 3 and 3 respectively. There are therefore three redundant parameters; the second and third components of $\underline{\epsilon}_\alpha$ will have the same effect as the second of $\underline{\epsilon}_T$ and the third of $\underline{\epsilon}_S$, while this latter will have the same effect as the bias portion of the third component of $\underline{\epsilon}_X$ also. This is also evident upon examination of Eqs. (1-5-18), (3-5-15) and (3-5-17).

If

$$\underline{\epsilon}_P = \begin{Bmatrix} \epsilon_m \\ \epsilon_n \\ \epsilon_\ell \end{Bmatrix} \qquad (3\text{-}5\text{-}21)$$

$$\underline{\epsilon}_\alpha = \begin{Bmatrix} \epsilon_\alpha \\ 0 \\ 0 \end{Bmatrix} \qquad (3\text{-}5\text{-}22)$$

and

$$\underline{\epsilon}_S = \begin{Bmatrix} \epsilon_a \\ \epsilon_b \\ 0 \end{Bmatrix} \qquad (3\text{-}5\text{-}23)$$

then Eq. (3-5-15) can be written

$$\underline{\hat{t}}_V = \underline{\hat{t}}_{V_0} + T_V R_{PV} B_e \underline{\epsilon} \qquad (3\text{-}5\text{-}24)$$

where

$$\underline{\epsilon} = [\epsilon_m \ \epsilon_n \ \epsilon_\ell \ \epsilon_\alpha \ \epsilon_a \ \epsilon_b \ \epsilon_p \ \epsilon_y \ \epsilon_r \ \lambda_p \ \lambda_y \ \lambda_r]^T \qquad (3\text{-}5\text{-}25)$$

and

$$B_e = \begin{bmatrix} [I] & \vdots & c\beta_P & \vdots & c\alpha_P c\beta_P & \vdots & s\alpha_P c\beta_P & \vdots & c\beta_P c(\alpha_X - \alpha_P) & \vdots & c\beta_P s(\alpha_X - \alpha_P) \\ & \vdots & 0 & \vdots & -s\alpha_P & \vdots & c\alpha_P & \vdots & s(\alpha_X - \alpha_P) & \vdots & -c(\alpha_X - \alpha_P) \\ & \vdots & s\beta_P & \vdots & c\alpha_P s\beta_P & \vdots & s\alpha_P c\beta_P & \vdots & s\beta_P c(\alpha_X - \alpha_P) & \vdots & s(\alpha_X - \alpha_P) \end{bmatrix}$$

$$\begin{bmatrix} s\beta_P & \vdots & \theta_p c\beta_P c(\alpha_X - \alpha_P) & \vdots & \theta_y c\beta_P s(\alpha_X - \alpha_P) & \vdots & \theta_r s\beta_P \\ 0 & \vdots & \theta_p s(\alpha_X - \alpha_P) & \vdots & -\theta_y c(\alpha_X - \alpha_P) & \vdots & 0 \\ -c\beta_P & \vdots & \theta_p s\beta_P c(\alpha_X - \alpha_P) & \vdots & \theta_y s(\alpha_X - \alpha_P) & \vdots & -\theta_r c\beta_P \end{bmatrix} \qquad (3\text{-}5\text{-}26)$$

115

The $B_\epsilon \underline{e}$ in Eq. (3-5-24) maps the effect of all the error rotations to platform coordinates. If we let

$$\begin{Bmatrix} b_m \\ b_n \\ b_\ell \end{Bmatrix} = B_\epsilon \, \underline{\epsilon} \qquad (3-5-27)$$

then similar to Eqs. (3-2-7) we can write

$$\alpha_P = \alpha - b_m/\sin\beta \qquad (3-5-28)$$

$$\beta_P = \beta + b_n \qquad (3-5-29)$$

$$\gamma_P = \gamma + b_m \cot\beta + b_\ell \qquad (3-5-30)$$

2. TV Geometric Distortion Model

As discussed in Section 2.3 distortion effects in the television arise from (a) the camera optics during the imaging process and (b) the vidicon electronics during the photoelectric charge readout scan process. Corrections to correct for these effects need to be added to the vidicon (x, y) coordinates expected for an image (see Ref. 26).

Optical Distortion: The optical distortion can be represented as the sum of four components $\underline{\xi}_i$ as follows:

(i)   a null offset $\underline{\xi}_1$ of the optical principal point from the target raster center given by

$$\underline{\xi}_1 = [\Delta x_o \quad \Delta y_o]^T \quad ; \qquad (3-5-31)$$

(ii)   a symmetric radial distortion component $\underline{\xi}_2$ given by

$$\underline{\xi}_2 = \left[\sum_{i=1}^{n_1} u_{2i-2} \, r_o^{2i-2} \right] \underline{x}_1 \qquad (3-5-32)$$

116

where $\underline{x}_o$ is the image location relative to the optical principal point, obtained by using Eq. (3-2-8) and (3-5-24);

$$r_o = |\underline{x}_o|$$

and

u_{2i-2} = symmetric radial optical distortion coefficients;

(iii)   asymmetric radial and tangential distortion effects $\underline{\xi}_3$ given by

$$\underline{\xi}_3 = \left[\sum_{i=1}^{n_2} u_{2i-1} \, r_o^{2i} \right] \left\{ \begin{array}{c} -\sin \theta_o \\ \\ \cos \theta_o \end{array} \right\} \qquad (3\text{-}5\text{-}33)$$

where

u_{2i-1} = asymmetric optical distortion coefficients

and

θ_o = orientation angle of axis of maximum tangential distortion;

(iv)   a distortion $\underline{\xi}_4$ caused by lens misalignment, given by

$$\underline{\xi}_4 = \left[\begin{array}{ccc} x_o y_o & x_o^2 & -y_o \\ \\ y_o^2 & x_o y_o & x_o \end{array} \right] \left\{ \begin{array}{c} \ell_1 \\ \ell_2 \\ \ell_3 \end{array} \right\} \qquad (3\text{-}5\text{-}34)$$

where ℓ_i are the corresponding coefficients.

Relative to target raster coordinates the location of the image after optical distortion effects but before electromagnetic distortion effects is given by

$$\underline{x}_e = \underline{x}_o + \sum_{i=1}^{4} \underline{\xi}_i \qquad (3\text{-}5\text{-}35)$$

Electromagnetic Distortion: The electromagnetic distortion can be represented as the sum of two components as follows:

(i)   a symmetric radial distortion component, $\underline{\eta}_1$, given by

$$\underline{\eta}_1 = \left[\sum_{i=1}^{n_3} \nu_{2i-2}\, r_E^{2i-2} \right] \underline{x}_E \qquad (3\text{-}5\text{-}36)$$

where

$$\underline{x}_E = \left\{ \begin{array}{c} x_E \\ y_E \end{array} \right\} = \underline{x}_e - \underline{\xi} \qquad ,$$

$\underline{\xi}$ = electromagnetic distortion null point

$r_E = \left| \underline{x}_E \right|$

and

ν_{2i-2} = symmetric electromagnetic distortion

coefficients;

(ii)   a symmetric tangential distortion component, $\underline{\eta}_2$, given by

$$\underline{\eta}_2 = \left[\sum_{i=1}^{n_4} \nu_{2i-1}\, r_E^{2i-1} \right] \left\{ \begin{array}{c} -y_E \\ x_E \end{array} \right\} \qquad (3\text{-}5\text{-}37)$$

The location of the image after the distortion corrections is given by

$$\underline{x} = \underline{x}_e + \sum_{i=1}^{2} \underline{\eta}_i$$

$$= \underline{x}_o + \sum_{i=1}^{4} \underline{\xi}_i + \sum_{i=1}^{2} \underline{\eta}_i \qquad (3\text{-}5\text{-}38)$$

The error models described above can be used for calibrating the
TV camera optical and electronic systems through the use of inflight data
(Ref. 33).

3.6 Orbit Determination Models and Processing

In this section we describe the process of spacecraft orbit determination using optical data. The basic data processing is conducted using the well-developed theory of the discrete Kalman filter (Ref. 34) for a linear dynamical system. However, to use the Kalman filter equations, it is necessary for the non-linear equations to be linearized about a nominal spacecraft trajectory. The spacecraft state vector can be augmented by other model parameters to be simultaneously estimated.

We develop the models for the processing here; the actual optical data equation linearization is described in the following section. In addition to obtaining an estimate and statistics for the state vector, a sensitivity analysis can be conducted to determine the effect of unestimated error parameters and of incorrect modelling of the apriori statistics. To facilitate interpretation and evaluation of different estimates it may be desirable to map them along with their statistics to a more convenient time and coordinate system.

The orbit determination process then consists of the following functions:

(i)   Generating a nominal trajectory based on assumed initial conditions and nominal model parameter values, by integration of the spacecraft dynamical equations;

(ii) Integration of the spacecraft variational equations to obtain the variation in spacecraft state for variations in nominal initial conditions and parameter values. This is required for the linearization about the spacecraft

120

trajectory and is conveniently done simultaneously with step (i);

(iii) Computation of the data partial derivatives, required for the linearization about the nominal measurement equation, using the result from step (ii);

(iv) Computation of the data residual — deviation of the measurement from the nominal predicted value of the observable;

(v) Filtering the data residuals to obtain the optimal·estimate and statistics, under the assumptions, for the spacecraft initial conditions and model′parameters;

(vi) Mapping the resulting spacecraft state estimate and statistics to the desired time and coordinate system .for proper evaluation (see Appendix A).

In the following we

(i) describe the dynamic and measurement models along with the treatment of stochastic variables;

(ii) present the Kalman filter equations with a consider option.

Dynamic Model

Let the six dimensional spacecraft state vector be represented by

$$\underline{u}(t) \triangleq \begin{Bmatrix} \underline{r}(t) \\ \underline{\dot{r}}(t) \end{Bmatrix} \qquad (3\text{-}6\text{-}1)$$

and the equations of motion for the spacecraft dynamics (discussed in Section 3.1) be put into the form

$$\underline{\dot{u}}(t) = \underline{f}[\underline{u}(t), \underline{v}(t), t] \qquad (3\text{-}6\text{-}2)$$

121

where the components of the vector $\underline{v}$ are physical quantities which influence the spacecraft dynamics. In general $\underline{v}$ will consist of variables $\underline{p}(t)$ — e.g. position vector of a perturbing planet, or propulsive maneuver thrust — and constant parameters $\underline{a}$ (e.g. gravity field of a perturbing planet). Thus

$$\underline{v}(t) = \left\{ \begin{array}{c} \underline{p}(t) \\ \underline{a} \end{array} \right\} \tag{3-6-3}$$

which would obey the dynamical equations

$$\left\{ \begin{array}{c} \underline{\dot{p}}(t) \\ \underline{\dot{a}}(t) \end{array} \right\} = \left\{ \begin{array}{c} \underline{\dot{p}}(\underline{p}(t), \underline{a}, t) \\ \underline{0} \end{array} \right\} \tag{3-6-4}$$

Let the solution of these equations be expressed by

$$\underline{p} = \underline{p}(\underline{p}_o, \underline{a}, t)$$

and

$$\left.\begin{array}{c} \\ \\ \underline{a} = \underline{a}_o = \text{constant} \end{array}\right\} \tag{3-6-5}$$

where $\underline{p}_o$ consists of the set of constant parameters affecting the dynamics of $\underline{p}$. Some of the parameters could be modelled as stochastic dynamic parameters — we discuss that later.

Given some initial conditions on $\underline{u}$ and the vector $\underline{v}_o$, where

$$\underline{v}_o \triangleq \left\{ \begin{array}{c} \underline{p}_o \\ \underline{a} \end{array} \right\} \quad ,$$

the nonlinear equations of motion (3-6-2) can be integrated to yield a nominal trajectory for the spacecraft. This can be symbolically written

$$\underline{u}(t)_N = \underline{u}_N\left[\underline{u}\left(t_o\right)_N, \underline{v}_{o_N}, t\right] \quad ,$$

where the subscript N denotes "nominal." This trajectory is required to compute the nominal values of the observables which we discuss in

the following subsection. Also required is a linearization about this nominal and a computation of the effect of small departures from the nominal.

Taking variations, the state deviation from the nominal trajectory, Eq. (3-6-2), is given to first order by

$$\delta \underline{\dot{u}}(t) = \frac{\partial \underline{f}[\underline{u}(t), \underline{v}(t), t]}{\partial \underline{u}(t)} \delta \underline{u}(t) + \frac{\partial \underline{f}[\underline{u}(t), \underline{v}(t), t]}{\partial \underline{v}(t)} \delta \underline{v}(t)$$

$$(3-6-6)$$

Where the variation $\delta(\cdot)$ indicates departure of the function from nominal, i.e.

$$\delta \theta(t) \equiv \theta(t) - \theta(t)_{NOM} \qquad ,$$

and where

$$\frac{\partial \underline{f}}{\partial \underline{v}} = \left[\frac{\partial \underline{f}}{\partial \underline{p}} \quad \frac{\partial \underline{f}}{\partial \underline{a}} \right] \qquad (3-6-7)$$

The variation in $v(t)$ can be written

$$\delta \underline{v}(t) = \frac{\partial \underline{v}(\underline{v}_o, t)}{\partial \underline{v}_o} \delta \underline{v}_o \qquad (3-6-8)$$

which, using Eqs. (3-6-5), can be expressed as

$$\delta \underline{v}(t) = \left[\begin{array}{c|c} \dfrac{\partial \underline{p}}{\partial \underline{p}_o} & \dfrac{\partial \underline{p}}{\partial \underline{a}_o} \\ \hline 0 & I \end{array} \right] \left\{ \begin{array}{c} \delta \underline{p}_o \\ \hline \delta \underline{a} \end{array} \right\} \qquad (3-6-9)$$

Here $\partial \underline{p}/\partial \underline{p}_o$ and $\partial \underline{p}/\partial \underline{a}$ are assumed to be available as precomputed quantities. Note that $\underline{p}_o$, and hence $\underline{v}_o$, are not restricted to the same coordinates as $\underline{p}$, $\underline{v}$, and could in general have different descriptions from $\underline{p}$, $\underline{v}$ respectively.

123

Since by the chain rule

$$\frac{\partial \underline{f}(\underline{u}(t), \underline{v}_o, t)}{\partial \underline{v}_o} = \frac{\partial \underline{f}(\underline{u}(t), \underline{v}(t), t)}{\partial \underline{v}(t)} \frac{\partial \underline{v}(\underline{v}_o, t)}{\partial \underline{v}_o} \quad . \quad (3\text{-}6\text{-}10)$$

then using Eq. (3-6-8) in (3-6-6) we can write

$$\left\{ \begin{array}{c} \delta \underline{\dot{u}}(t) \\ \\ \delta \underline{\dot{v}}_o \end{array} \right\} = \left[\begin{array}{cc} \dfrac{\partial \underline{f}(\underline{u}(t), \underline{v}_o, t)}{\partial \underline{u}(t)} & \dfrac{\partial \underline{f}(\underline{u}(t), \underline{v}_o, t)}{\partial \underline{v}_o} \\ \\ 0 & 0 \end{array} \right] \left\{ \begin{array}{c} \delta \underline{u}(t) \\ \\ \delta \underline{v}_o \end{array} \right\}$$

$$(3\text{-}6\text{-}11)$$

where the lower partitions in the matrix are zero because the $\underline{v}_o$'s are constants.

The solution of this can be written in the form

$$\left\{ \begin{array}{c} \delta \underline{u}(t) \\ \\ \delta \underline{v}_o \end{array} \right\} = \left[\begin{array}{cc} U(t, t_o) & V(t, t_o) \\ \\ 0 & I \end{array} \right] \left\{ \begin{array}{c} \delta \underline{u}(t_o) \\ \\ \delta \underline{v}_o \end{array} \right\} \quad (3\text{-}6\text{-}12)$$

where, again, the zero and identity matrices in the lower partitions arise because the $\underline{v}_o$'s are constants. The state transition matrix must obey the equation (Ref. 35)

$$\frac{d}{dt} \left[\begin{array}{cc} U & V \\ \\ 0 & I \end{array} \right] = \left[\begin{array}{cc} \dfrac{\partial \underline{f}}{\partial \underline{u}} & \dfrac{\partial \underline{f}}{\partial \underline{v}_o} \\ \\ 0 & 0 \end{array} \right] \left[\begin{array}{cc} U & V \\ \\ 0 & I \end{array} \right] \quad (3\text{-}6\text{-}13)$$

That is, U and V must obey

$$\frac{dU(t, t_o)}{dt} = \frac{\partial \underline{f}(\underline{u}, \underline{v}, t)}{\partial \underline{u}} \, U(t, t_o) \quad (3\text{-}6\text{-}14)$$

and

$$\frac{dV(t, t_o)}{dt} = \frac{\partial \underline{f}(\underline{u}, \underline{v}, t)}{\partial \underline{u}} \, V(t, t_o) + \frac{\partial \underline{f}(\underline{u}, \underline{v}, t)}{\partial \underline{v}} \frac{\partial \underline{v}(\underline{v}_o, t)}{\partial \underline{v}_o}$$

$$(3\text{-}6\text{-}15)$$

with the initial conditions

$$U(t_o, t_o) = I$$

$$V(t_o, t_o) = 0 \qquad\qquad (3\text{-}6\text{-}16)$$

Thus integration of the spacecraft variational equations (3-6-14) through (3-6-15) yields the solution Eq. (3-6-12).

We note from Eq. (3-6-12) that the transition matrices $U(t, t_o)$, $V(t, t_o)$ are the partial derivatives of the spacecraft state at time t with respect to spacecraft initial conditions and other constant parameters, i.e.

$$U(t, t_o) \equiv \frac{\partial \underline{u}(t)}{\partial \underline{u}(t_o)} \qquad\qquad (3\text{-}6\text{-}17)$$

and

$$V(t, t_o) \equiv \frac{\partial \underline{u}(t)}{\partial \underline{v}_o} \qquad\qquad (3\text{-}6\text{-}18)$$

We shall use them in the following development for the linearization of the measurement equations.

Measurement Model

The general measurement equation could be written as a non-linear function of the vectors $\underline{u}(t)$, $\underline{v}(t)$, $\underline{w}(t)$ given by

$$\underline{z}(t) = \underline{h}\left[\underline{u}\left(\underline{u}(t_o), \underline{v}_o, t\right), \underline{v}(\underline{v}_o, t), \underline{w}(t), t\right] + \underline{n}(t)$$

$$(3\text{-}6\text{-}19)$$

where $\underline{n}(t)$ is the data noise. Here $\underline{u}(t_o)$ are the spacecraft initial conditions and $\underline{v}_o$ are dynamic parameters affecting the spacecraft trajectory. We note that the $\underline{v}_o$ parameters affect the data through the spacecraft state $\underline{u}(t)$ and also directly through $\underline{v}$. For instance these

could be planetary ephemeris parameters which affect the gravitational influence on the spacecraft dynamics through the planet position vector; the latter however may also directly affect the data since the planet image can be the observable.

The $\underline{w}(t)$ are physical quantities that affect the data but are dynamically uncoupled from the spacecraft dynamics. In general $\underline{w}$ will consist of variables $\underline{q}(t)$ and constant parameters $\underline{b}$

$$\underline{w}(t) = \left\{ \begin{array}{c} \underline{q}(t) \\ \underline{b} \end{array} \right\} \tag{3-6-20}$$

in general obeying the dynamical equations

$$\left\{ \begin{array}{c} \underline{\dot{q}}(t) \\ \underline{\dot{b}}(t) \end{array} \right\} = \left\{ \begin{array}{c} \underline{\dot{q}}(\underline{q}(t), \underline{b}, \underline{v}(t), t) \\ \underline{0} \end{array} \right\} \tag{3-6-21}$$

Let the solution of these equations be

$$\left\{ \begin{array}{c} \underline{q}(t) \\ \underline{b} \end{array} \right\} = \left\{ \begin{array}{c} \underline{q}(\underline{q}_o, \underline{b}_o, \underline{v}_o, t) \\ \underline{b}_o \end{array} \right\} \tag{3-6-22}$$

where $\underline{q}_o$ is a set of constant parameters.

The $\underline{q}(t)$ could be, for example, the natural satellite position vector — which for small satellite masses would not perturb the spacecraft yet would be themselves perturbed by the planetary $\underline{v}$ parameters — or image size proportional center finding errors, which are a function of time through their dependence on range to the target. The $\underline{b}$ could be instrument error parameters. In addition, some of the parameters could be stochastic — we discuss those later.

Based on the nominal spacecraft trajectory $\underline{u}(t)_N$ and nominal time functionals $\underline{v}(t)_N$, $\underline{w}(t)_N$ we can construct the nominal measurement vector

$$\underline{z}(t)_N = h\left[\underline{u}\left(\underline{u}\left(t_o\right)_N, \underline{v}_{o_N}, t\right), \underline{v}\left(\underline{v}_{o_N}, t\right), \underline{w}(t)_N, t\right] \quad (3\text{-}6\text{-}23)$$

Given the actual measurement vector $\underline{z}(t)$, we can construct the data residual vector

$$\delta\underline{z}(t) \triangleq \underline{z}(t) - \underline{z}(t)_N \quad (3\text{-}6\text{-}24)$$

given by the model

$$\delta\underline{z}(t) = \delta\underline{h}(t) + \underline{n}(t) \quad (3\text{-}6\text{-}25)$$

Using Eq. (3-6-22) in (3-6-19) we could write

$$\underline{z}(t) = \underline{h}[\underline{u}(t_o), \underline{v}_o, \underline{w}_o, t] + \underline{n}(t) \quad (3\text{-}6\text{-}26)$$

Defining

$$\underline{m}_t \triangleq \left\{ \begin{array}{c} \underline{u}(t) \\ \underline{v}(t) \\ \underline{w}(t) \end{array} \right\} \quad (3\text{-}6\text{-}27)$$

and

$$\underline{m}_o \triangleq \underline{m}(t_o) \quad (3\text{-}6\text{-}28)$$

we can write

$$\delta\underline{m}_t = M_{t,t_o} \, \delta\underline{m}_o \quad (3\text{-}6\text{-}29)$$

where

$$M_{t,t_o} = \begin{bmatrix} U(t, t_o) & V(t, t_o) & 0 \\ 0 & \dfrac{\partial\underline{v}(t)}{\partial\underline{v}_o} & 0 \\ 0 & \dfrac{\partial\underline{w}(t)}{\partial\underline{v}_o} & \dfrac{\partial\underline{w}(t)}{\partial\underline{w}_o} \end{bmatrix} \quad (3\text{-}6\text{-}30)$$

127

. Thus for two discrete measurement times t_i and t_{i+1} the transition equation for $\underline{m}_t$ is

$$\delta\underline{m}_{i+1} = M_{i+1,i}\ \delta\underline{m}_i \qquad (3\text{-}6\text{-}31)$$

where $M_{i+1,i}$ is obtained using

$$M_{i+1,i} = M_{i+1,0}\ M_{i,0}^{-1} \qquad (3\text{-}6\text{-}32)$$

From Eq. (3-6-26) the observation at the ith measurement time t_i is

$$\underline{z}(t_i) = \underline{h}_i(\underline{m}_o,\ t_i) + \underline{n}(t_i) \qquad (3\text{-}6\text{-}31)$$

Linearizing this about a nominal vector $\underline{m}_{o_N}$ we have

$$\delta\underline{z}_i = H_i\ \delta\underline{m}_o + \underline{n}_i \qquad (3\text{-}6\text{-}32)$$

where

$$H_i \triangleq \left.\frac{\partial \underline{h}_i(\underline{m}_o,\ t_i)}{\partial \underline{m}_o}\right|_{\underline{m}_o = \underline{m}_{o_N}} \qquad (3\text{-}6\text{-}33)$$

Treatment of Stochastic Variables

The vector $\underline{m}$ in the previous subsections was developed as consisting of uncertain but constant initial conditions and bias parameters. In addition to these it is often necessary to model some of the process noise effects on the spacecraft dynamics or the errors on the measurements, from a variety of causes, as random time varying phenomena. This is done through a set of stochastic variables $\underline{s}(t)$. These could be time-varying representations of the bias parameters included in any of the vectors $\underline{u}_o$, $\underline{v}_o$, $\underline{w}_o$ or could be due to unmodelled parameters or effects. Commonly used quantities, for instance, are random nongravitational

128

accelerations on the spacecraft, primarily useful for radio data, and
camera pointing errors for optical data.

These stochastic parameters can be treated by augmenting the
state vector to include these quantities. Thus defining

$$\underline{x}(t) \triangleq \begin{Bmatrix} \delta\underline{m}_o \\ \underline{s}(t) \end{Bmatrix} \qquad (3\text{-}6\text{-}34)$$

the vector $\underline{x}(t)$ becomes the quantity to be estimated. For the estimation of $\underline{x}(t)$ we need to describe its evolution by determining the state transition matrix $\Phi(t, t_o)$, such that

$$\underline{x}(t) = \Phi(t, t_o)\,\underline{x}(t_o) + \begin{Bmatrix} 0 \\ \underline{\xi} \end{Bmatrix} \qquad (3\text{-}6\text{-}35)$$

A large variety of random processes can be modelled by the linear stochastic differential equation representing exponentially correlated process noise — i.e. the Langevin equation

$$\dot{s}(t) = -\frac{1}{\tau}\,s(t) + \xi(t) \qquad (3\text{-}6\text{-}36)$$

where τ is the correlation time constant and $\xi(t)$ is a Gaussian purely random (white) zero mean process, i.e.

$$E(\xi(t)) = 0 \qquad (3\text{-}6\text{-}37)$$

with the correlation function

$$E(\xi(t)\,\xi(\tau)) = Q(t)\,\delta(t - \tau) \qquad (3\text{-}6\text{-}38)$$

This can be integrated and converted to discrete form (Ref. 36)

$$s_{i+1} = \psi_i s_i + \xi_i \qquad (3\text{-}6\text{-}39)$$

where

$$\psi_i = \exp\,(-\Delta t_i/\tau) \qquad (3\text{-}6\text{-}40)$$

$$\Delta t_i = t_{i+1} - t_i \qquad (3\text{-}6\text{-}41)$$

and

$$E\left(\xi_i^2\right) = \left(1 - \psi_i^2\right)\sigma_{s_i}^2 \qquad (3\text{-}6\text{-}42)$$

From Eq. (3-6-39) and using Eq. (3-6-42),

$$E\left(s_{i+1}^2\right) = \psi_i^2 \, E\left(s_i^2\right) + \left(1 - \psi_i^2\right)\sigma_{s_i}^2 \qquad (3\text{-}6\text{-}43)$$

which shows that in the steady state

$$E\left(s_{i+1}^2\right) = E\left(s_i^2\right) = \sigma_s^2 \qquad (3\text{-}6\text{-}44)$$

This description can be used to represent purely random noise with $\tau \to 0$, randomly varying drifts using an appropriately non-zero finite value of τ, and constant parameter for $\tau \to \infty$; this indicates the flexibility of this stochastic sequence.

The transition matrix for a vector $\underline{s}$ of these random processes is given by

$$\underline{s}_{i+1} = [S_{i+1,i}] \, \underline{s}_i + \underline{\xi}_i \qquad (3\text{-}6\text{-}45)$$

$$S_{i+1,i} = \begin{bmatrix} \psi_i(1) & & & & \\ & \cdot & & & \\ & & \cdot & & \\ & & & \psi_i(j) & & \\ & & & & \cdot & \\ & & & & & \cdot & \\ & & & & & & \psi_i(n) \end{bmatrix} \qquad (3\text{-}6\text{-}46)$$

where j represents the jth component of the vector $\underline{s}$.

The transition matrix Φ of Eq. (3-6-35) for the vector $\underline{x}(t)$ is obtained by deterministically mapping the effect of $\underline{s}_i$ into the "initial condition" deviation vector $\delta\underline{m}_o(t_{i+1})$ using the stochastically mapped deviation of $\delta\underline{m}(t_{i+1})$. We can express

$$\underline{m}_o(t_{i+1}) = \underline{m}_o(t_i) + \frac{\partial \underline{m}_o(t_{i+1})}{\partial \underline{s}(t_i)} \, \delta \underline{s}_i \qquad (3\text{-}6\text{-}47)$$

where the second term is obtained as follows: We can obtain the matrix $M_s(t_{i+1}, t_i)$

$$M_s(t_{i+1}, t_i) \triangleq \frac{\partial \underline{m}(t_{i+1})}{\partial \underline{s}(t_i)} \qquad (3\text{-}6\text{-}48)$$

as a subset of the matrix $M_{i+1,i}$ as in Eq. (3-6-32). Then combining these with $S_{i+1,i}$ from Eq. (3-6-46) we can construct the transition relationship

$$\begin{Bmatrix} \delta \underline{m}(t_{i+1}) \\ \underline{s}(t_{i+1}) \end{Bmatrix} = \begin{bmatrix} M & M_s \\ 0 & S \end{bmatrix}_{i+1,i} \begin{Bmatrix} \delta \underline{m}(t_i) \\ \underline{s}(t_i) \end{Bmatrix} + \begin{Bmatrix} 0 \\ \underline{\xi}_i \end{Bmatrix} \qquad (3\text{-}6\text{-}49)$$

The left hand side of Eq. (3-6-49) and the inverse of the transition matrix M in (3-6-30) can be used to obtain the mapped effect of the $\underline{s}_i$ at time t_{i+1} mapped deterministically to time t_o. Indicating the functional dependence on $\underline{s}_i$ we write

$$\delta \underline{m}_o \Big|_{i+1} (\underline{s}_i) = M^{-1}_{i+1,0} \, \delta \underline{m} \Big|_{i+1} (\underline{s}_i)$$

$$= M^{-1}_{i+1,0} \, [M \quad M_s]_{i+1,i} \begin{Bmatrix} \delta \underline{m}(t_i) \\ \underline{s}_i \end{Bmatrix}$$

$$= M^{-1}_{i+1,0} \, M_{s_{i+1,i}} \, \underline{s}_i \qquad (3\text{-}6\text{-}50)$$

which yields the required transition S_m,

$$S_m \triangleq M^{-1}(t_{i+1}, t_o) \, M_s(t_{i+1}, t_i) \qquad (3\text{-}6\text{-}51)$$

131

The state transition matrix Φ of Eq. (3-6-35) for $\underline{x}$ is then given by

$$\phi(t_{i+1}, t_i) = \begin{bmatrix} I & S_m \\ 0 & S \end{bmatrix}_{i+1,i} \qquad (3-6-52)$$

S_m can in general be

$$S_m = \begin{bmatrix} S_u \\ S_v \\ S_w \end{bmatrix} \qquad (3-6-53)$$

where

$$S_\theta = \frac{\partial \underline{\theta}_o(t_{i+1})}{\partial \underline{s}(t_i)} \quad , \quad \theta = u, v, w \qquad (3-6-54)$$

Considering two cases in particular:

(i) Non-gravitational accelerations: In this case both S_v and S_w are zero;

(ii) Camera pointing errors: The entire matrix S_m is zero.

We now present the equations for processing the measurement residuals, where we will need the partial derivative matrix H_i of Eq. (3-6-33) and the state transition matrix Φ of Eq. (3-6-52).

Sequential Filtering of the Data

The Kalman filter equations can be derived in various ways and are readily available from several sources (e.g. Refs. 34 thru 37). Here we just present these equations; we then present the equations to consider the sensitivity of the estimate to unestimated parameters. In this subsection we drop the underscoring of vectors — all lower case quantities are vectors unless otherwise clear from the context.

Given the measurement model

$$z_i = H_i\, x_i + n_i \qquad (3\text{-}6\text{-}55)$$

with the initial state a zero mean gaussian random vector,

$$E[x(0)] = 0 \qquad (3\text{-}6\text{-}56)$$

and positive semidefinite assumed covariance matrix

$$E[x(0)\, x(0)^T] = X(0) \qquad (3\text{-}6\text{-}57)$$

and n_i a zero mean guassian white sequence

$$E[n_i] = 0 \qquad (3\text{-}6\text{-}58)$$

with covariance

$$E\left[n_i\, n_j^T\right] = R_j'\, \delta_{ij} \qquad (3\text{-}6\text{-}59)$$

where R_j' is a positive semidefinite matrix, the optimal estimate of x is given by

$$\hat{x}_i = \bar{x}_i + K_i(z_i - H_i\, \bar{x}_i)\, . \qquad (3\text{-}6\text{-}60)$$

The gain K_i is computed using

$$K_i = \bar{X}_i\, H_i^T \left[H_i\, \bar{X}_i\, H_i^T + R_i'\right]^{-1} \qquad (3\text{-}6\text{-}61)$$

where $\bar{x}_i$, $\bar{X}_i$ are the parameter estimate and covariance mapped from the previous measurement epoch through the equations

$$\bar{x}_{i+1} = \Phi(i+1,\, i)\, \hat{x}_i + \begin{Bmatrix} 0 \\ \underline{\xi}_i \end{Bmatrix} \qquad (3\text{-}6\text{-}35)$$

and

$$\bar{X}_{i+1} = \Phi(i+1,\, i)\, X_i\, \Phi^T(i+1,\, i) + \begin{bmatrix} 0 & 0 \\ 0 & Q_i \end{bmatrix}\, . \qquad (3\text{-}6\text{-}62)$$

Here

$$\Phi(i + 1, i) = \begin{bmatrix} I & S_m \\ 0 & S \end{bmatrix}_{i+1,i} \qquad (3-6-52)$$

and

$$E\left[\xi_i \xi_j^T\right] = Q_j \delta_{ij} \qquad (3-6-63)$$

The covariance of $\hat{X}_i$, assuming K_i is optimal, is then given by

$$X_i = \overline{X}_i - K_i H_i \overline{X}_i \qquad (3-6-64)$$

Consider Covariance Option

When the system model or apriori statistics assumed are inaccurate the filter becomes sub-optimal yet the formal covariance, without knowledge of the inaccuracies, would tend to be overly optimistic. The generalized consider option (Ref. 4) involves considering the effects of ignoring certain parameters from the estimated state vector and of assuming incorrect apriori statistics.

Let the observable equation be of the form

$$z_i = H_i x_i + G_i y_i + n_i \qquad (3-6-65)$$

where the parameters $\underline{y}$ are the consider parameters which are deemed to affect the data but are not formally estimated. Let the actual apriori covariance be given by

$$P(0) = E\left[\begin{Bmatrix} x_o \\ y_o \end{Bmatrix} \begin{bmatrix} x_o^T & y_o^T \end{bmatrix}\right] = \begin{bmatrix} P_{x_o} & P_{xy_o} \\ P_{yx_o} & P_y \end{bmatrix} \qquad (3-6-66)$$

and the actual covariance of the noise n be

$$E\left[q_i q_j^T\right] = R_j \delta_{ij} \qquad (3-6-67)$$

With the assumptions (3-6-55), (3-6-57) and (3-6-59) the filter gain in (3-6-61) is suboptimal and the computed covariance will be overoptimistic. Rewriting (3-6-65) and (3-6-60) as

$$z_i = [H \quad G] \begin{Bmatrix} x \\ y \end{Bmatrix} + n_i \qquad (3-6-68)$$

and

$$\begin{Bmatrix} \hat{x}_i \\ \hat{y}_i \end{Bmatrix} = \begin{Bmatrix} \bar{x}_i \\ \bar{y}_i \end{Bmatrix} + \begin{bmatrix} K_i \\ 0 \end{bmatrix} (z_i - H_i \bar{x}_i) \qquad (3-6-69)$$

we see that for the complete model the data partial derivative matrix and the (suboptimal) filter gain are, respectively

$$\mathcal{H} \triangleq [H \quad G] \qquad (3-6-70)$$

and

$$\mathcal{K}_i \triangleq \begin{bmatrix} K_i \\ ---- \\ 0 \end{bmatrix} \qquad (3-6-71)$$

For a filter of this structure, for any filter gain, the update consider covariance equation is

$$P_i = [\mathcal{I} - \mathcal{K}\mathcal{H}] \bar{P}_i [\mathcal{I} - \mathcal{K}\mathcal{H}]^T + \mathcal{K}R\mathcal{K}^T \qquad (3-6-72)$$

where $\mathcal{I}$ is the identity matrix; that is

$$P_i = \begin{bmatrix} (I - K_i H_i) & \vdots & -K_i G_i \\ ------ & \vdots & ----- \\ 0 & \vdots & I \end{bmatrix} \bar{P}_i \begin{bmatrix} (I - K_i H_i) & \vdots & -K_i G_i \\ ------ & \vdots & ----- \\ 0 & \vdots & I \end{bmatrix}^T$$

$$+ \begin{bmatrix} K_i \\ --- \\ 0 \end{bmatrix} R \begin{bmatrix} K_i^T & \vdots & 0 \end{bmatrix} \qquad (3-6-73)$$

The consider covariance mapping equation is

$$\overline{P}_{i+1} = \begin{bmatrix} \Phi & \vdots & 0 \\ - - - & \vdots & - - - \\ 0 & \vdots & I \end{bmatrix} P_i \begin{bmatrix} \Phi & \vdots & 0 \\ - - - & \vdots & - - \\ 0 & \vdots & I \end{bmatrix}^T + \begin{bmatrix} 0 & 0 & \vdots & 0 \\ 0 & Q_i & \vdots & 0 \\ - - - - - & - & \vdots & - - \\ 0 & 0 & \vdots & 0 \end{bmatrix}$$

(3-6-74)

where

$$\Phi \triangleq \Phi(i + 1, i).$$

136

3.7 Optical Data Measurement Equation Linearization

The description of the measurement model was given in Section 3.6. In this section the linearization of the optical data measurement equation is performed; that is, the partial derivative matrix H of Equation (3-6-33) is obtained for the optical data.

We begin with a general form of the optical data equation and proceed to linearize it, developing the partials in terms of the direct and indirect terms; for this formulation the terms are conveniently grouped, in that the direct terms all stem from instrument related parameters while the indirect terms stem from celestial geometry related parameters and are dependent on the celestial object imaged. The celestial geometry related components of the latter terms are dealt with first, for each of star, planet and satellite images. All spacecraft and planet related dynamic parameters are obtained as the solutions from the integration of the respective spacecraft and planetary variational equations in Section 3.6. Satellite related parameter variation effects are developed for the satellite theory described in Section 3.1.

Finally the variation of the data equation is taken to yield the partials for the vectors upon which the data is directly functionally dependent, thus completing the linearization.

Optical Data Partial Derivatives

From the discussion in Sections 3.2 and 3.5 for the optical data, the observed pixel and line image locations on the vidicon are functionally given by

$$\underline{z} = \underline{z}(\underline{t}, \underline{r}, \underline{b}) \qquad (3\text{-}7\text{-}1)$$

where $\underline{b}$ is a vector of instrument parameters; the direct functional

dependence on $\underline{r}$ arises through the transformation R_{IC} in Eq. 3-2-5.

If t, τ are the spacecraft observation time and light-time respectively,

and $\underline{y}(t - \tau)$ is the position vector to the object being viewed at time

$(t - \tau)$, then $\underline{t}$ is a function of $\underline{y}(t - \tau)$, $\underline{r}(t)$ and $\underline{\dot{r}}(t)$ as discussed

in section 2.2.

Representing all solve-for parameters by $\underline{m}$, we can write

$$z = z[\underline{t}, \underline{r}(t, \underline{m}), \underline{m}] \tag{3-7-2}$$

where

$$\underline{t} = \underline{t}[\underline{r}(t, \underline{m}), \underline{\dot{r}}(t, \underline{m}), \underline{y}(t - \tau, \underline{m})] \tag{2-7-3}$$

Differentiating Eq. (3-7-2) w.r.t. $\underline{m}$, we have

$$\frac{\partial z}{\partial \underline{m}} = \frac{\partial z}{\partial \underline{t}} \frac{\partial \underline{t}}{\partial \underline{m}} + \left[\frac{\partial \underline{z}}{\partial \underline{r}}\right]_t \frac{\partial \underline{r}}{\partial \underline{m}} + \left[\frac{\partial z}{\partial \underline{m}}\right]_{\underline{t},\underline{r}} \tag{3-7-4}$$

where the subscripts indicate the quantities held constant in the

partial differentiation, and

$$\frac{\partial \underline{t}}{\partial \underline{m}} = \frac{\partial \underline{t}}{\partial \underline{r}(t, \underline{m})} \frac{\partial \underline{r}(t, \underline{m})}{\partial \underline{m}} + \frac{\partial \underline{t}}{\partial \underline{\dot{r}}(t, \underline{m})} \frac{\partial \underline{\dot{r}}(t, \underline{m})}{\partial \underline{m}}$$

$$+ \frac{\partial \underline{t}}{\partial \underline{y}(t - \tau, \underline{m})} \left\{ \left[\frac{\partial \underline{y}(t - \tau, \underline{m})}{\partial \underline{m}}\right]_\tau - \underline{\dot{y}}(t - \tau, \underline{m}) \frac{\partial \tau}{\partial \underline{m}} \right\}$$

$$+ \left[\frac{\partial \underline{t}}{\partial \underline{m}}\right]_{\underline{r},\underline{y}} \tag{3-7-5}$$

The term $\partial \tau / \partial \underline{m}$ must be obtained from the solution of the light time

equation, Eq. (2-2-3) where $\underline{u}_j$, $\underline{w}_i$ are $\underline{r}(t)$, $\underline{y}(t - \tau)$ respectively.

Here however, we can afford to neglect the small effects due to

stellar aberration and light-time, for the purpose of computing the

partial derivatives. A considerable simplification of the expression
for $\underline{t}$ and $\partial\underline{t}/\partial\underline{m}$ results; we obtain

$$\underline{t} = \underline{y}(t, \underline{m}) - \underline{r}(t, \underline{m}) \tag{3-7-6}$$

$$\frac{\partial\underline{t}}{\partial\underline{m}} = \frac{\partial\underline{y}(t, \underline{m})}{\partial\underline{m}} - \frac{\partial\underline{r}(t, \underline{m})}{\partial\underline{m}} \tag{3-7-7}$$

Using the equations

$$\underline{r} = \underline{p} + \underline{s} \tag{3-7-8}$$

and

$$\underline{y} = \underline{p} + \underline{q} \tag{2-2-2}$$

in (3-7-6), the planet vector drops out, to give

$$\underline{t} = \underline{q}(t, \underline{m}) - \underline{s}(t, \underline{m}) \tag{3-7-9}$$

and

$$\frac{\partial\underline{t}}{\partial\underline{m}} = \frac{\partial\underline{q}(t, \underline{m})}{\partial\underline{m}} - \frac{\partial\underline{s}(t, \underline{m})}{\partial\underline{m}} \tag{3-7-10}$$

Combining this with Eq. (3-7-4) and using Eq. (3-7-8) we obtain
the complete equation

$$\frac{\partial\underline{z}}{\partial\underline{m}} = \left[\frac{\partial\underline{z}}{\partial\underline{t}}\right]\left[\frac{\partial\underline{q}}{\partial\underline{m}} - \frac{\partial\underline{s}}{\partial\underline{m}}\right] + \left[\frac{\partial\underline{z}}{\partial\underline{r}}\right]_{\underline{t}}\left[\frac{\partial\underline{p}}{\partial\underline{m}} + \frac{\partial\underline{s}}{\partial\underline{m}}\right] + \left[\frac{\partial\underline{z}}{\partial\underline{m}}\right]_{\underline{t},\underline{r}} \tag{3-7-11}$$

The terms $\partial\underline{p}/\partial\underline{m}$ and $\partial\underline{s}/\partial\underline{m}$ are obtained from Eqs. (3-6-9) and
(3-6-13) for all the dynamic parameters $\underline{m}$ that perturb $\underline{p}$ and $\underline{s}$ respec-
tively. The latter, $\partial\underline{s}/\partial\underline{m}$, is obtained from the solution to the space-
craft trajectory variational equations.

When the planet is the center of integration in the heliocentric
phase these yield the entire term $\partial\underline{r}/\partial\underline{m}$. We develop the terms $\partial\underline{z}/\partial\underline{t}$,
$\partial\underline{z}/\partial\underline{r}$ and $\partial\underline{z}/\partial\underline{m}$ later, after discussion of the $\partial\underline{t}/\partial\underline{m}$ terms for each of
the observable image types.

Observable Image Types and $\partial \underline{t}/\partial \underline{m}$

Star Observations: For star observations $\underline{t}$ is the heliocentric direction to the star and can be taken to be constant since

(i) the accuracy to which the star locations are known (~0.1 arcsec) is more than an order of magnitude better than typical spacecraft television camera resolutions and

(ii) the effect of $\delta \underline{r}$ is negligible compared with the distance to the star; therefore

$$\frac{\partial \underline{t}}{\partial \underline{m}} = 0 \qquad \qquad \text{(3-7-12)}$$

for stars, and the first term in Eq. (3-7-11) drops out.

Planet Observations: In this case $\underline{t}$ is given by

$$\underline{t} = - \underline{s} \qquad , \qquad \text{(3-7-13)}$$

the vector $\underline{q}$ and the partial derivative matrix $\partial \underline{q}/\partial \underline{m}$ are identically zero, i.e.

$$\frac{\partial \underline{t}}{\partial \underline{m}} = - \frac{\partial \underline{s}}{\partial \underline{m}} \qquad \text{(3-7-14)}$$

which is obtained using Eq. (3-6-13).

Satellite Observations: For observations of the natural satellite $\underline{t}$ and $\partial \underline{t}/\partial \underline{m}$ are given by Eqs. (3-7-9) and (3-7-10). We now develop the $\partial \underline{q}/\partial \underline{m}$ term needed in Eq. (3-7-10). The parameter vector $\underline{m}$ here consists of the satellite orbital elements for the Struve-Wilkins-Born Satellite theory described in Section 3.1.

At a given time, t, measured in days past epoch, the position vector $\underline{q}$ of the natural satellite of a planet in the 1950.0 Earth mean Equator and Equinox coordinate system can be written in the notation of Section 3.1 as

$$\underline{q} = N(I + \delta N)\ J(I + \delta J)\ K(I + \delta K)\ \Pi(I + \delta\Pi)\ W(I + \delta W)\ \underline{r}$$

$$\text{(3-7-15)}$$

where $\underline{r}$ is the planet relative satellite radius vector in the orbit plane, I is the (3 x 3) identity matrix, and the small angle error rotation matrices are defined as

$$\delta N = \begin{bmatrix} 0 & -\delta N_A & 0 \\ \delta N_A & 0 & 0 \\ 0 & 0 & 0 \end{bmatrix}$$

$$\delta J = \begin{bmatrix} 0 & 0 & 0 \\ 0 & 0 & -\delta J_A \\ 0 & \delta J_A & 0 \end{bmatrix}$$

$$\delta K = \begin{bmatrix} 0 & -\delta K_A & 0 \\ \delta K_A & 0 & 0 \\ 0 & 0 & 0 \end{bmatrix}$$

$$\delta\Pi = \begin{bmatrix} 0 & 0 & 0 \\ 0 & 0 & -\delta I_A \\ 0 & \delta I_A & 0 \end{bmatrix}$$

$$\delta W = \begin{bmatrix} 0 & -\delta W_A & 0 \\ \delta W_A & 0 & 0 \\ 0 & 0 & 0 \end{bmatrix}$$

141

This equation can be rewritten, keeping only first order terms, as

$$\underline{q} = NJK\,H\,W\underline{r} + N(\delta N)JK\,H\,W\underline{r} + NJ(\delta J)K\,H\,W\underline{r} + NJK(\delta K)\,H\,W\underline{r}$$

$$+ NJK\,H\,(\delta H)\,W\underline{r} + NJK\,H\,W(\delta W)\underline{r} \qquad (3\text{-}7\text{-}16)$$

which can be rewritten, following the method of Section 3.5, as

$$\underline{q} = \underline{q}_n + QN\delta\underline{N} + QNJ\delta\underline{J} + QNJK\delta\underline{K} + QNJK\,H\,\delta\underline{H} + QT\delta\underline{W} \qquad (3\text{-}7\text{-}17)$$

where

$$\underline{q}_n = NJK\,H\,W\underline{r} = T\underline{r} = \left\{ \begin{matrix} q_1 \\ q_2 \\ q_3 \end{matrix} \right\}, \qquad (3\text{-}7\text{-}18)$$

with

$$T \triangleq NJK\,H\,W \qquad (3\text{-}7\text{-}19)$$

and

$$Q \triangleq \begin{bmatrix} 0 & q_3 & -q_2 \\ -q_3 & 0 & q_1 \\ q_2 & -q_1 & 0 \end{bmatrix} \qquad (3\text{-}7\text{-}20)$$

The error vectors are defined as:

$$\delta\underline{N} = \left\{ \begin{matrix} 0 \\ 0 \\ \delta N_A \end{matrix} \right\}, \qquad \delta\underline{J} = \left\{ \begin{matrix} \delta J_A \\ 0 \\ 0 \end{matrix} \right\}, \qquad \delta\underline{K} = \left\{ \begin{matrix} 0 \\ 0 \\ \delta K_A \end{matrix} \right\},$$

$$\delta\underline{H} = \left\{ \begin{matrix} \delta I_A \\ 0 \\ 0 \end{matrix} \right\}, \qquad \delta\underline{W} = \left\{ \begin{matrix} 0 \\ 0 \\ \delta W_A \end{matrix} \right\}.$$

142

Writing the last five terms of Eq. (3-7-17) as a summation and taking variations

$$\delta \underline{q} = \delta \underline{q}_n + \sum_{i=1}^{s} T_i \, \delta E_i \qquad (3-7-21)$$

The δE_i are obtained by taking variations on Eqs. (3-1-12) through (3-1-18). From Eqs. (3-1-12),

$$\delta N_A = \delta N_Z + \delta N_R t$$

$$\delta J_A = \delta J_Z + \delta J_R t$$

$$\delta K_A = \delta K_Z + \delta K_R t \qquad (3-7-22)$$

$$\delta P = \delta P_Z + \delta P_R t$$

The term δW_A is obtained as follows: combining Eqs. (3-1-15) through (3-1-18) and taking variations

$$W_A = L - K_A - N_A + (v - M) \qquad (3-7-23)$$

$$\delta W_A = \delta L - \delta K_A - \delta N_A + \delta(v - M) \qquad (3-7-24)$$

From Eq. (3-1-17),

$$\delta(v - M) = (2e \cos M + 2.5 \, e^2 \cos 2M) \, \delta M$$
$$+ (2 \sin M + 2.5 \, e \sin 2M) \, \delta e \qquad (3-7-25)$$

and from Eq. (3-1-18)

$$\delta M = \delta L - \delta P \qquad (3-7-26)$$

The variation on Eq. (3-1-13) yields δL,

$$\delta L = \delta L_Z + \delta L_N t + \delta L_M t^2 + \delta L_K \sin(K_A - K_0)$$
$$+ L_K \cos(K_A - K_0) \, \delta K_A \qquad (3-7-27)$$

The term δq_n of Eq. (3-7-21) is obtained using Eq. (3-7-18),

$$\delta q_n = T \left\{ \begin{array}{c} \delta r \\ 0 \\ 0 \end{array} \right\} \qquad (3\text{-}7\text{-}28)$$

where from Eq. (3-1-20) we can obtain

$$\delta r = \left(\frac{1 - e^2}{1 + e \cos v} \right) \delta a - \frac{a[2e + (e^2 + 1) \cos v]}{(1 + e \cos v)^2} \delta e$$

$$+ \frac{r^2 e \sin v}{a(1 - e^2)} \delta v \qquad (3\text{-}7\text{-}29)$$

Collecting and combining the appropriate variations in Eqs. (3-7-21) through (3-7-29) we can write,

$$\delta q = \left[\frac{\delta q}{\delta q_o} \right] \delta q_o \qquad (3\text{-}7\text{-}30)$$

where

$$q_o = [a \ e \ L_Z \ I_A \ P_Z \ K_Z \ N_Z \ J_Z \ L_N \ P_R \ K_R \ N_R \ J_R \ L_M \ L_K \ L_J]$$

$$(3\text{-}7\text{-}31)$$

and $[\partial q/\partial q_o]$ is the required partial derivative matrix.

Variation on the Optical Data Observable Equation

To obtain the $\partial z/\partial(\cdot)$ terms of Eq. (3-7-11) the variation is taken of the optical state observable equation, developed in Section 3.2. Of the three remaining terms of Eq. (3-7-11) the term $[\partial z/\partial r]_t$ arises from the variation of the transformation R_{IC} due to variations in the spacecraft trajectory, since the ABC coordinate system is defined with respect to the spacecraft-sun direction. Thus clearly the effect is an angle change which is inversely proportional to the spacecraft-sun range. For example, a spacecraft position error of 100 km at

144

1 astronomical unit from the sun would have an effect of the order of (100 km/1 AU) radians $\approx 0.7 \times 10^{-6}$ radians; this effect is therefore negligible for typical spacecraft position errors, relative to the other error sources.

The terms $(\partial \underline{z}/\partial \underline{t})$ and the direct instrument related terms, $(\partial \underline{z}/\partial \underline{m})$, are evaluated in Ref. 38 and will not be developed here.

3.8 Optical Navigation System Structure

In this section we give a brief description of the structure of the optical navigation system. A schematic flow diagram for the optical navigation system is shown in Figure 3-6.

A parameter initialization program is used to create a file of basic optical parameters to be used throughout the system. The SAO star catalog is used to generate an appropriate subset of stars and the integration of the planetary and spacecraft dynamical equations yields the planetary ephemeris and a spacecraft trajectory; these are input to the Optical Geometry Program to perform the picture sequence design function, with the Plotting Program used for the necessary illustration of picture sequence geometry in the celestial, inertial and television camera coordinate systems. Once a picture sequence design is finalized spacecraft commands are transmitted for its execution.

After picture requests are implemented, the data is processed to extract pointing and imaging optical measurements. The Optical Geometry Program generates a picture sequence file for use in the Optical Observables and Partials Program which computes the residuals and performs the linearization around the nominal trajectory. For this purpose in addition to the planetary ephemeris and spacecraft trajectory, the planetary ephemeris partials and spacecraft trajectory variations are required; these are generated by integrating the respective variational equations. The data partials and residuals generated are used in the Estimation and Mapping Program to perform the Calibration or Orbit Determination functions. The data residuals both before and after the fit can be displayed by the Plotting Program, which can also display
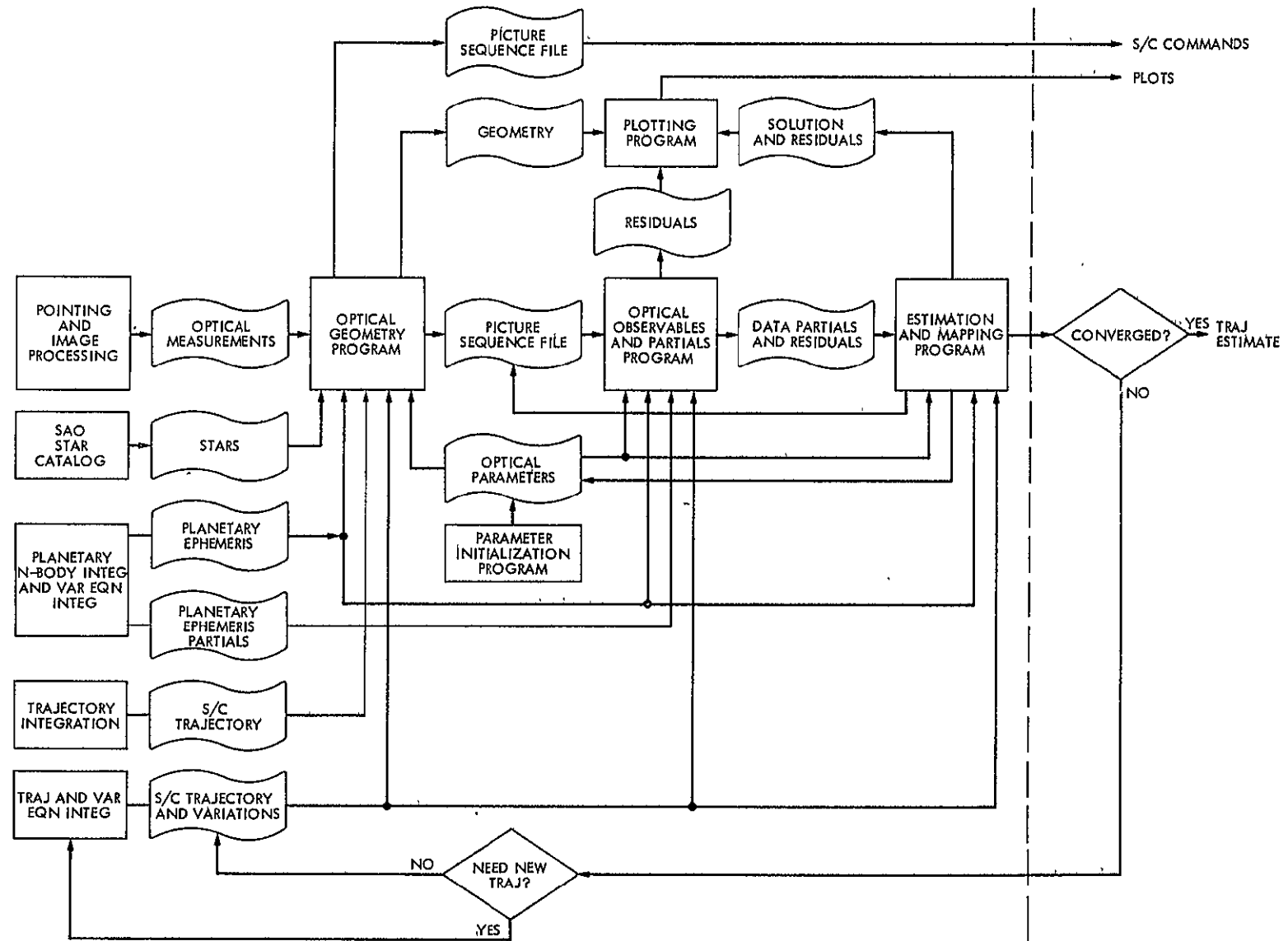
Figure 3-6. Optical Navigation System Schematic

the spacecraft trajectory estimate history mapped to the B-plane. In addition to the spacecraft trajectory estimate the filtering process produces updates for parameter values and picture pointing estimates. If necessary the entire process can be repeated with these new nominal conditions for iteration to convergence. When the trajectory has satisfactorily converged it is used to compute the maneuver commands required to correct the spacecraft course.

CHAPTER 4

OPTICAL NAVIGATION APPLICATION TO MARINER IX DATA

In this chapter the first two of the three optical navigation methods outlined in Section 1.4 are evaluated using actual flight data obtained from the Mariner IX Mission to Mars. The objective of this mission was to place the space probe into orbit around Mars so as to carry out scientific investigations related to the planet.

. The data used for the evaluation here consisted of selections from the Science TV pictures taken during the approach phase to Mars. These included pictures of Mars taken with short exposure times (10-20 msec) and of Phobos and Deimos, the two natural satellites of Mars, with the maximum exposure times possible (6.144 sec). Several stars were imaged, along with Phobos and Deimos, in the latter pictures, enabling the satellite-star method for optical navigation to be evaluated. However the exposure times for the Mars pictures was too short for the stars to be imaged. The TV pointing for these pictures was therefore obtained by using the telemetered engineering data. There was no data available for the two-camera method since the Mariner spacecraft had only one narrow-angle TV camera.

In the following discussion we first describe the data in detail in Section 4.1 followed by a summary of instrument calibration results in Section 4.2. Sections 4.3 and 4.4 respectively deal with the

analyses of the satellite-star method and the planet limb method (without stars). The results show that the satellite-star method yields greatly improved performance over "radio-only" navigation. Also, as expected, the planet-limb method is not found to be as good as the satellite-star method. However the results indicate that it does contribute to an improvement in accuracy relative to "radio-only" data; it would thus be a viable choice in situations where natural satellites may not be available.

4.1 Data Sources and Content

In this section we describe the data obtained from Mariner IX and used for the optical navigation analyses performed. The sources of data were the digitally transmitted TV pictures along with supporting engineering data.

Onboard Measurement Systems

Instruments onboard the Mariner spacecraft which were utilized to obtain the data included the narrow and wide angle science TV cameras and the attitude control sensors. TV cameras were mounted on a scan platform provided with two degrees of freedom. The 1.1-deg x 1.4-deg and 11-deg x 14-deg field-of-view vidicons with 9.6 mm x 12.5 mm selenium targets were electronically scanned in 700 lines with 832 picture elements (pixels) per line. Continuous video intensity level was sampled and digitized to 9 bits (512 levels) prior to transmission to Earth. Each picture element, therefore, would be defined by its pixel number (1 to 832), its line number (1 to 700) and its intensity (0 to 511).

The attitude control subsystem provided spacecraft stabilization and orientation. Its celestial sensors, i.e., Sun sensors and star (Canopus) sensor, produced pitch, yaw and roll position signals. The attitude control signals, together with the scan platform gimbal position data, were transmitted to the ground station through the engineering telemetry channels.

Data Types and Content

The first few pictures during the approach phase to Mars came from two sequences of planet pictures known as Mars Calibration

Sequences I and II. These had been taken to calibrate the TV cameras using Mars images and to safeguard against possibilities of damage later from excessive exposure; they are different from the scan platform calibration pictures which were taken about two months before encounter.

During the 3 day approach period prior to the insertion of Mariner 9 into orbit about Mars, three Preorbital Science picture sequences (POS I, II, and III) were taken (Fig. 4-1). Each POS sequence covered a 24-hour period with 31 pictures being recorded aboard Mariner 9 and then transmitted to Earth during a 3-hour period.

Planet Limb Data: From the two Mars calibration sequences which took place 5 and 4 days before Mars encounter (abbreviated as E-5d and E-4d, respectively), 22 narrow angle TV pictures which contained Mars lit limb images were taken. Wide angle TV pictures of Mars during the Mars calibration sequences were not processed because of poor angular resolution. During POS (preorbit Science) I, II, and III sequences which started from E-3.1d, E-1.9d and E-0.7d, respectively, 36 narrow angle TV pictures and 4 wide angle TV pictures were selected for lit limb data processing, where POS-I and II pictures would have been available before Mars Orbit Insertion (MOI). Towards the end of POS-II and throughout POS-III sequences, the Mars images taken by the narrow angle TV were so large that only a small portion of the lit limb was visible; hence such frames were not processed.

Satellite-Star Data: The positions of Deimos as viewed from Mariner 9 against the star background are shown in Figure 4-2.

152
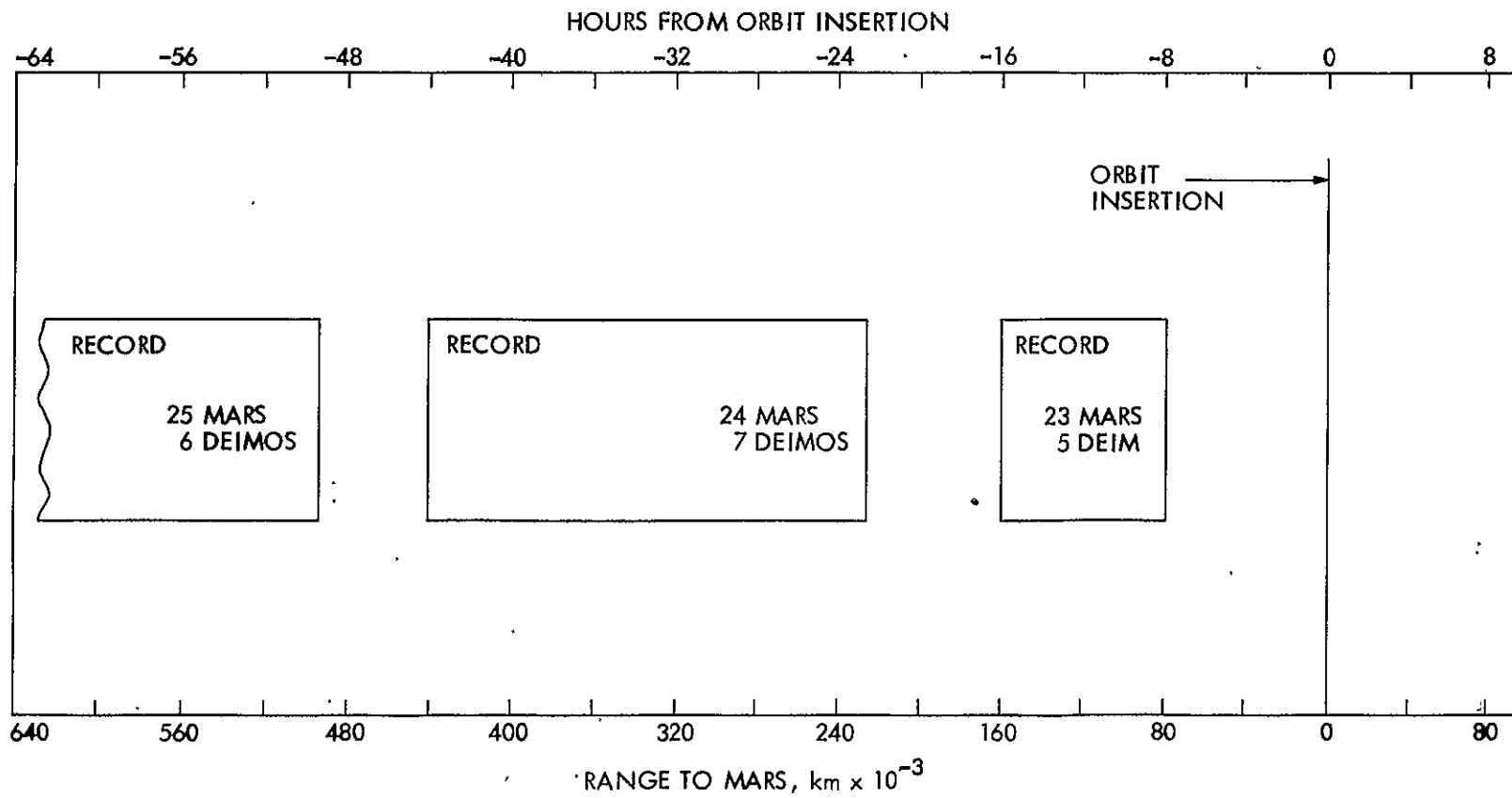
Figure 4-1. Approach Sequence
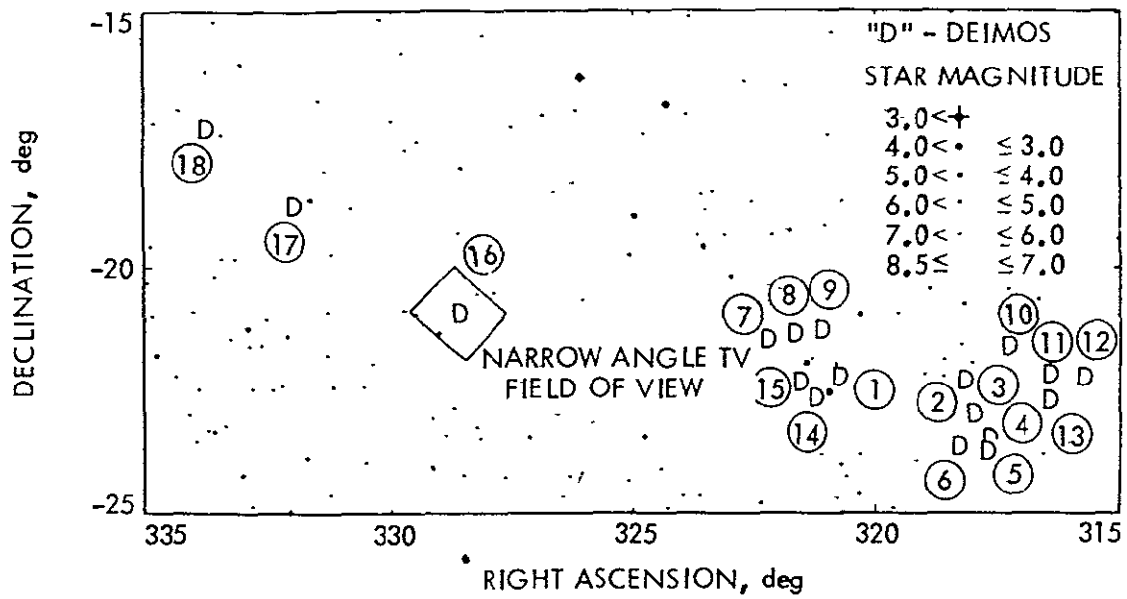
Figure 4-2. Approach Deimos/Star Geometry

The first Deimos picture frame was bad, leaving only 12 Deimos
pictures available before MOI. The POS III phase yielded five
additional Deimos pictures.

155

4.2 Instrument Calibration Summary

Two sequences of pictures, viewing dense star fields, had been
taken within two months before Mars encounter. These two sequences
of 31 pictures each, which were aimed at star clusters, single stars,
Mars and Saturn, provided a good set of data for calibration of the
scan platform subsystem, the attitude control sensors and of the
geometric distortion in the TV cameras. A summary of the results
is given here.

Scan Platform Calibration

Calibration of the scan platform subsystem was necessary to
establish the true scan platform orientation (hence TV pointing
direction) relative to the spacecraft. The calibration of the scan
platform subsystem and attitude control sensors was performed by
referencing to the orientation of the narrow angle TV imaged stars
whose locations were known apriori. The scan platform errors were
characterized by systematic errors such as gimbal mounting errors,
gimbal axis misalignments and TV instrument mounting offsets placed
on the scan platform. Attitude control sensor signal values were
needed to define the spacecraft attitude relative to the celestial
references. Systematic errors of the telemetered attitude control
sensor signals were characterized by sensor null offsets and scale
factor errors. Mechanical misalignments of the wide angle TV were
calibrated with respect to the narrow angle TV.

The star-referenced inflight calibration (Reference 39) determined
the scan platform subsystem and attitude control errors to a total
accuracy of $0.005°$ (1 σ) about the TV line of sight (LOS) and $0.020°$

in cone and cross-cone axes for the narrow angle TV camera and 0.015°

(1 σ) and 0.17° (1 σ), respectively, for the wide angle TV camera.

This then determined the camera pointing error levels for the planet

limb data type where stars are not available for accurate pointing.

Television Calibration

Calibration of the TV camera geometric distortion was necessary

to establish undistorted image direction relative to the TV coordinate

system. This was performed by utilizing both reseau marks etched

on the vidicon target and the star fields from the two calibration

picture sequences. Since ground calibration of the TV cameras

(Reference 39) revealed practically no optical distortion, optical

distortion parameters were not solved for. The star and reseau

images were fit to the analytic geometric distortion model described

in Chapter 3.

The geometric distortion, was calibrated (Reference 40) to

the accuracy of 0.5 (1 σ) pixels and 0.7 (1 σ) pixels in the line

and pixel directions, respectively for the narrow and wide angle TV

cameras. Figure 4-3 illustrates the changes of observed reseau

locations in narrow angle TV pictures determined by the calibrations.

These are reasoned to have been caused by the absence of Earth's

magnetic field, and possibly a slight displacement of TV beam deflection

coils.
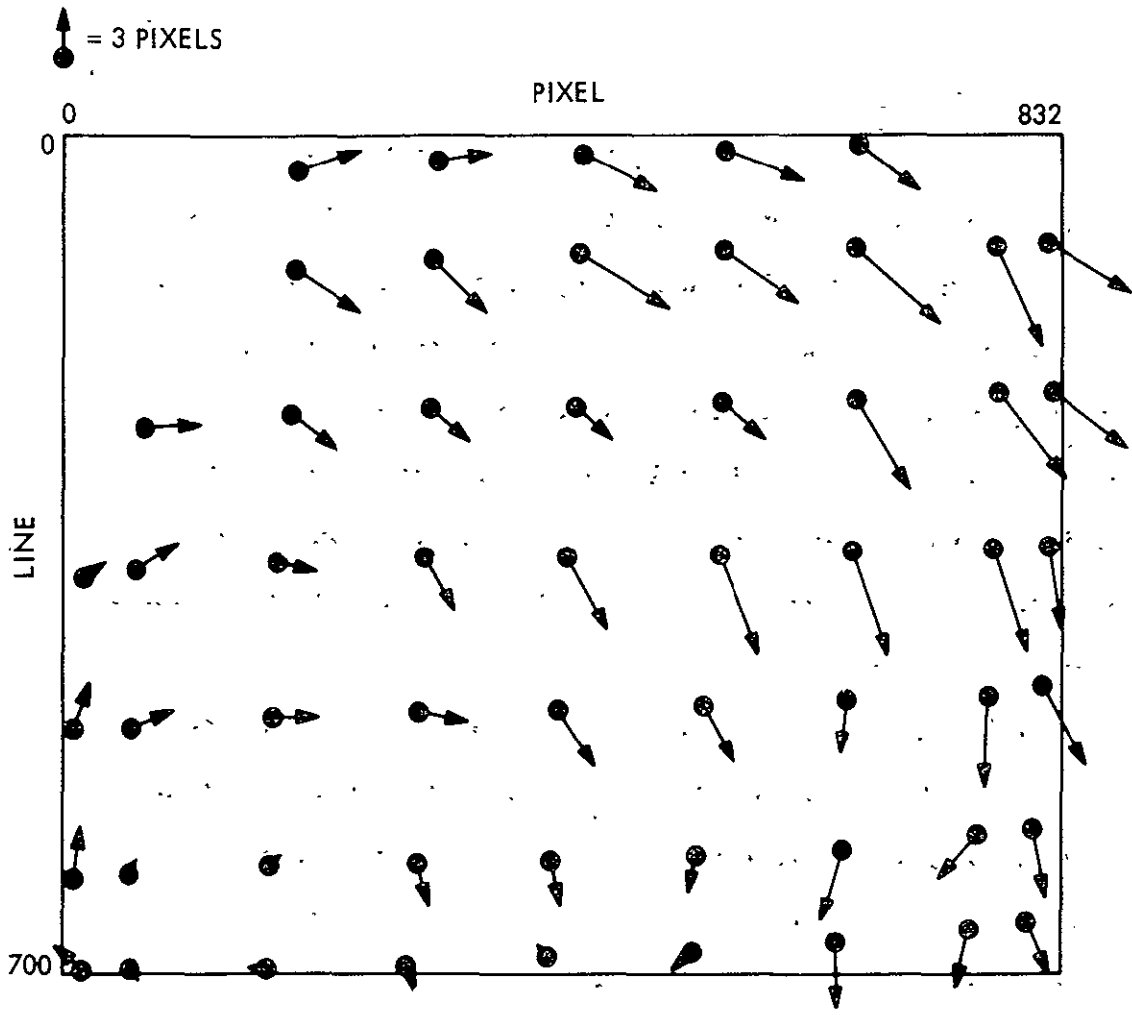
Figure 4-3. Change in Observed Reseau Locations of Narrow-Angle TV

4.3 Analysis of Satellite-Star Data

In this section we present results of the analysis of the satellite-
star data from Mariner IX. The analysis consists of an evaluation of
the data for orbit determination, followed by its sensitivity to
number of stars in the field of view, TV distortion, planet ephemeris
error, and the amount of radio tracking data.

An approach picture is shown in Figure 4-4 which has the images
of Deimos, ten stars of magnitude 3.9 to 9.2, and the 7 x 9 reseau
grid. Stray light from Mars is seen in the lower left portion of
the picture. The picture was enhanced to bring out the dim images.
Figure 4-5 is a computer drawn version of the picture which is used
to distinguish the star pattern from noise or vidicon blemishes.

Orbit Determination Using Satellite-Star Data

The optical data was processed in three iterations (Reference 23).
In the first iteration, star images were processed to remove TV
pointing errors. Pointing errors were generally large enough to
introduce nonlinearities into the data processing because of the
nonlinearity of the TV distortion model. In the second iteration,
star and satellite images were processed. Residual TV pointing
errors from linear corrections in the first iteration were removed.
Also, Deimos ephemerides and the spacecraft trajectory were estimated
to reduce Deimos data residuals within a linear region. A trajectory
based on radio data only was used in the second iteration; however,
a loose apriori uncertainty (thousands of km) was used. The third
iteration produced combined spacecraft trajectory and Deimos
ephemeris estimates using Deimos data and radio Doppler data. After

159
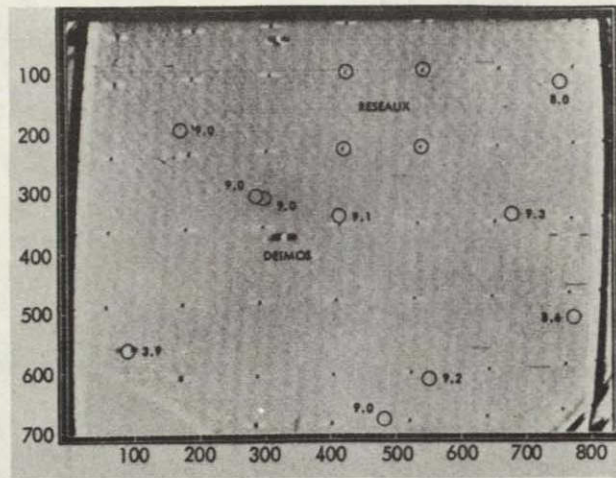
Figure 4-4.   Approach Deimos Picture
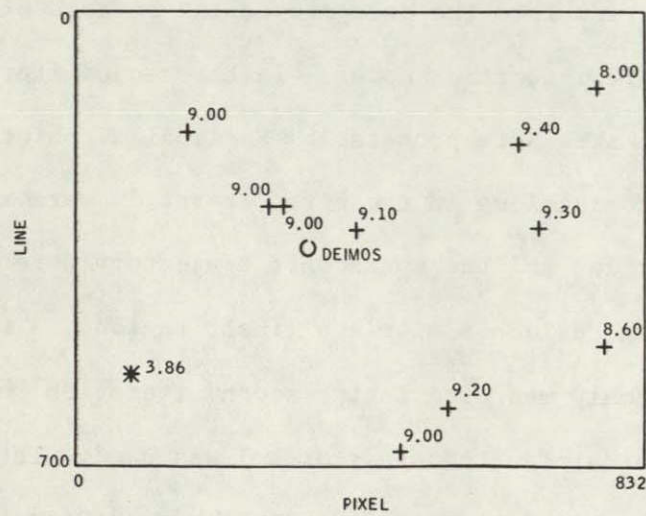
Figure 4-5.   Predicted Approach Deimos Picture

160

a Deimos ephemeris update from POS I data, the second and third iterations could be combined.

The optical residuals (difference between observed and computed image locations) for Deimos (D) and stars (o) are shown in Figure 4-6. The residuals in Figure 4-6a were obtained using apriori Deimos ephemerides, a trajectory based on radio data to encounter minus 19 hours (E-19 hours), and TV pointing based on reduced spacecraft telemetry data. The clusters of star residuals reflect the global offset of the images due to TV pointing errors. It is noted that the TV pointing errors become large at the end of POS II and throughout POS III in the pixel direction but were smaller and more random in the line direction.

The residuals in Figure 4-6b were generated using the same conditions as those in Figure 4-6a with the exception the TV pointing errors have been removed by using the star images. Note that the star residuals which are only sensitive to TV pointing errors are zero mean. With TV pointing errors removed, the Deimos residuals reflect Deimos ephemeris errors (20-hour period) and spacecraft trajectory errors. The Deimos ephemeris errors are evident in the · 30-hour periodic cycle seen in POS II and POS III residuals. The spacecraft trajectory error is seen as a slope in the line residuals.

The residuals in Figure 4-6c were generated after solving for the spacecraft trajectory and Deimos ephemerides. A 100 km Deimos ephemeris error and 80 km spacecraft trajectory error were determined. The residuals are seen to be random with zero mean and a standard deviation of less than 0.5 pixels (3 arc sec).
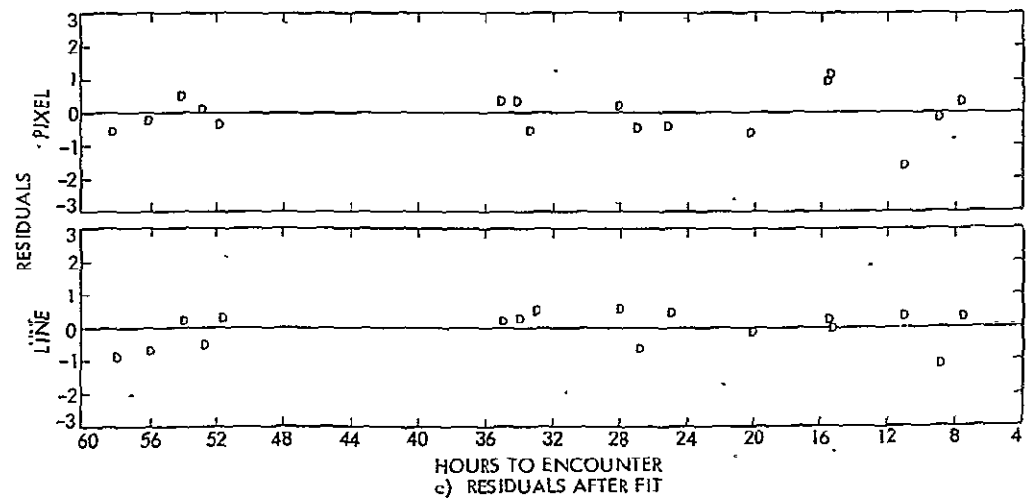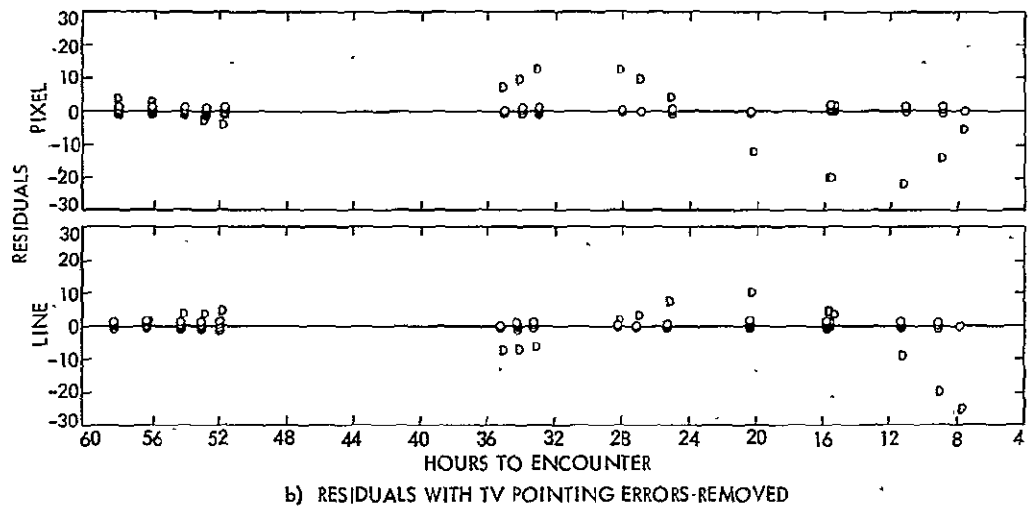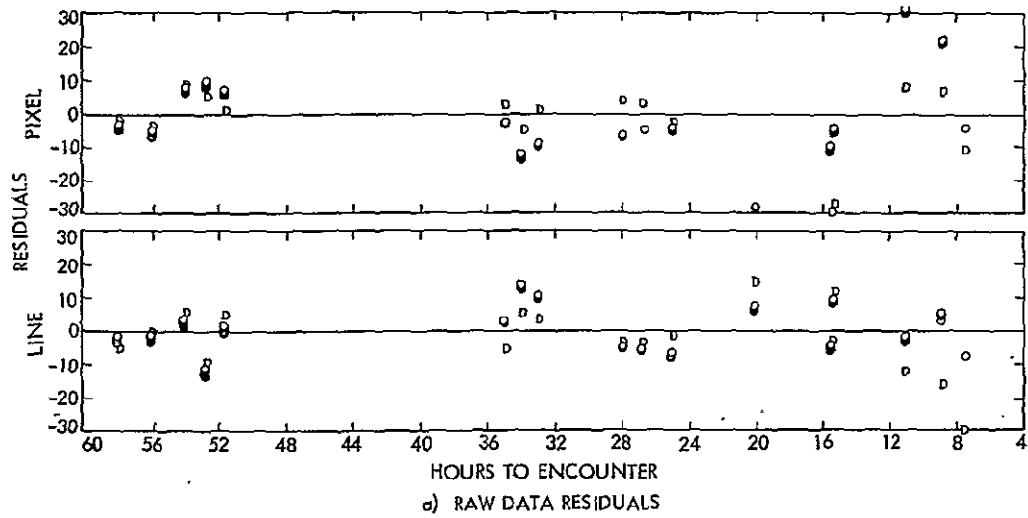
Figure 4-6. Deimos Observation Residuals

162

Figure 4-7 shows the B-plane trajectory estimates which were generated. The radio only solution and its 1 σ error ellipse were based on data to E-13 hours. The radio plus optical iterated solution and 1 σ error ellipse were based on radio data to E-19 hours and optical data from POS I and POS II. The current best estimate is denoted as CBE.

Sensitivity to Stars

The orbit determination (OD) accuracy sensitivity to the number of stars per picture was investigated. The following three cases were studied: A) no stars/picture; B) one star/picture; and C) an average of five stars/picture. All three cases had apriori TV pointing information from reduced spacecraft telemetry data. Also, the nominal trajectory was based on radio data only from E-30 days to E-16 hours. OD accuracies for the three cases are shown in Figure 4-8 and the associated trajectory estimates are shown in Figures 4-9 through 4-11.

Figures 4-10 and 4-11 show that the first picture in POS I for cases B and C drives the trajectory estimate to within 15 km of the CBE. The time behavior of cases B and C are very similar, with the trajectory estimates to within a 2 km agreement at the end of POS III data. The expected accuracies of cases B and C (Fig. 4-8) are the same.

TV pointing derived from spacecraft telemetry is an order of magnitude less accurate than pointing derived from star images. This degradation is reflected in both the expected accuracy and the actual trajectory estimate of case A (Fig. 4-9) as compared to cases B and C.

163
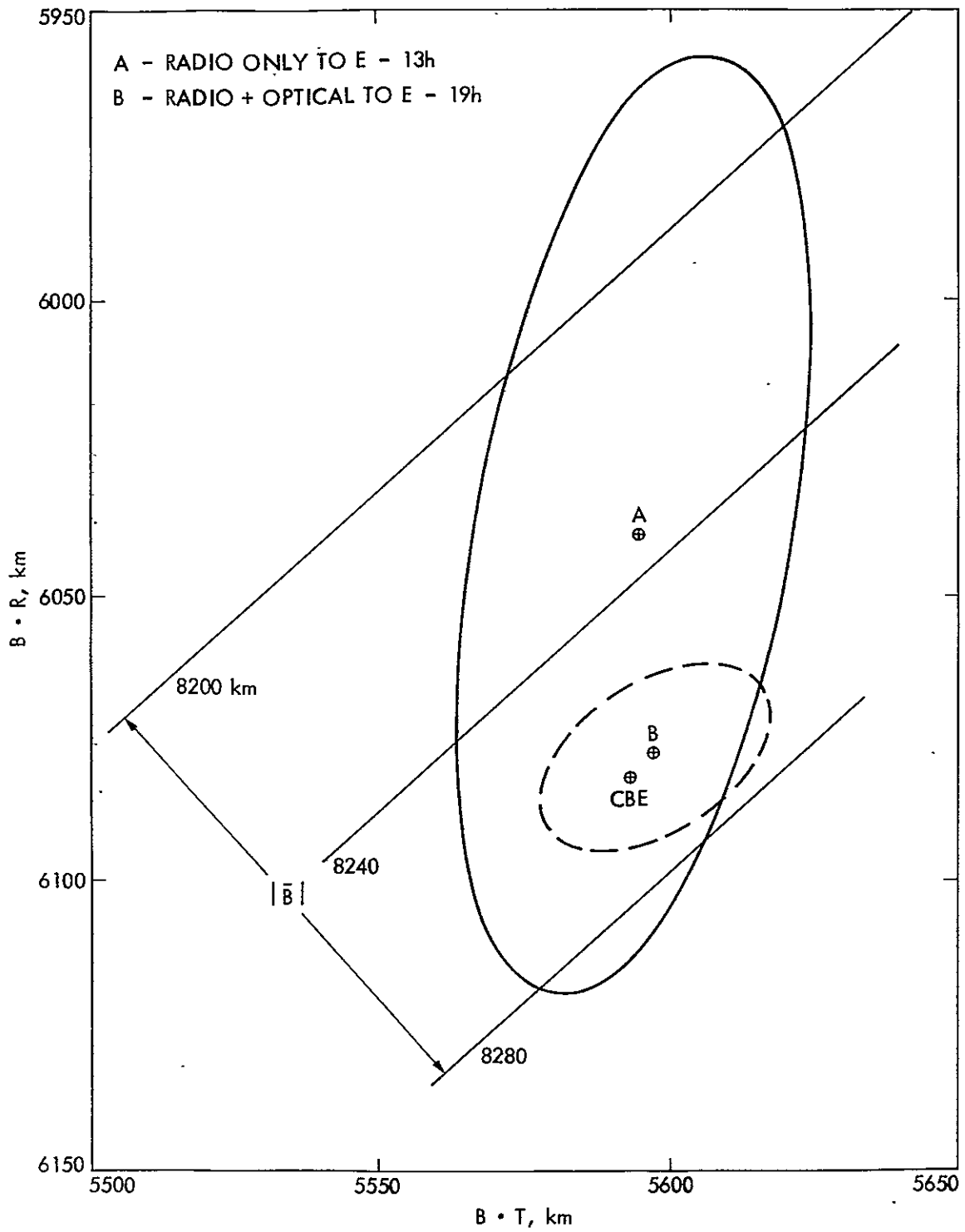
Figure 4-7. B-Plane Trajectory Estimates

164
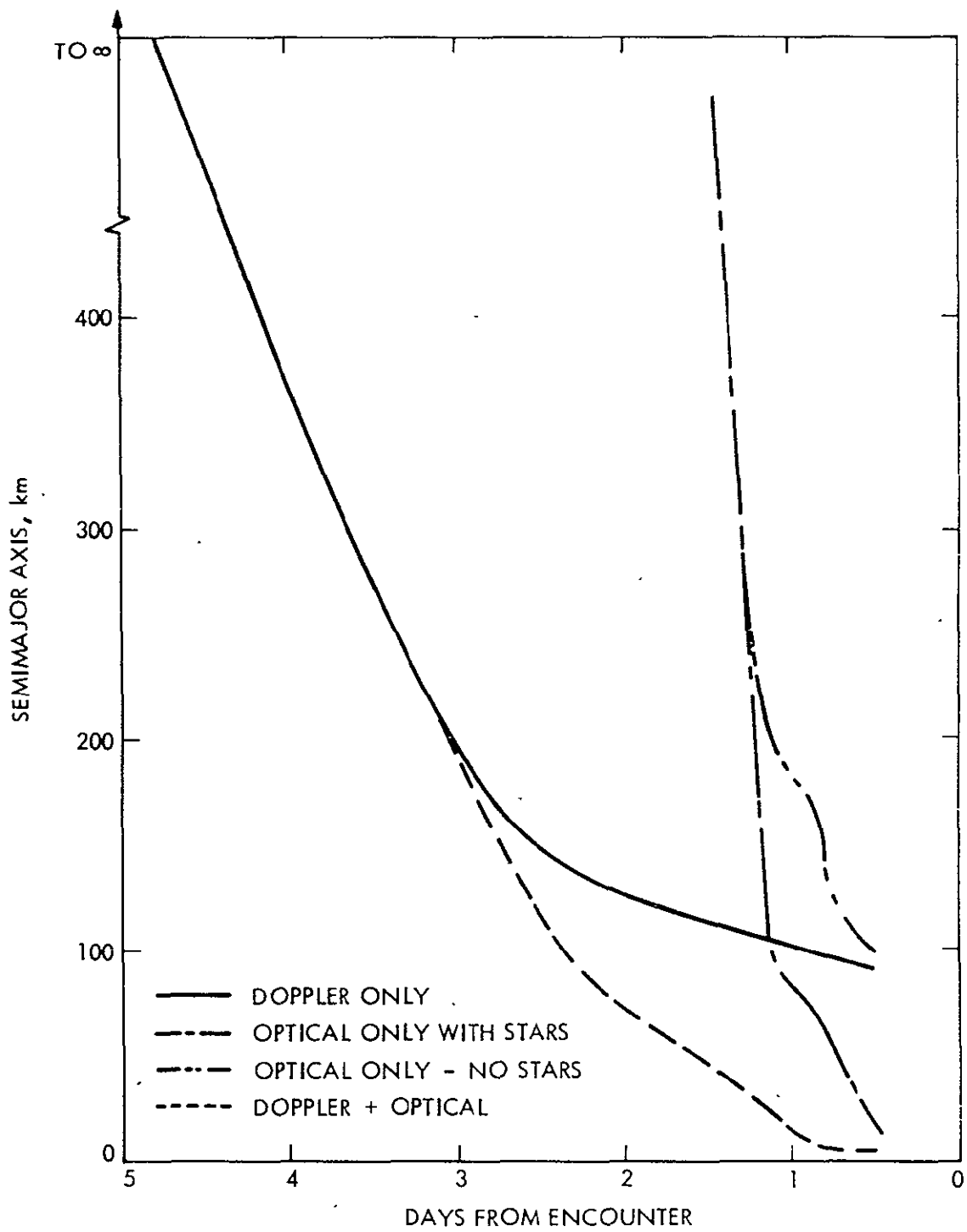
Figure 4-8. Expected Trajectory Accuracy
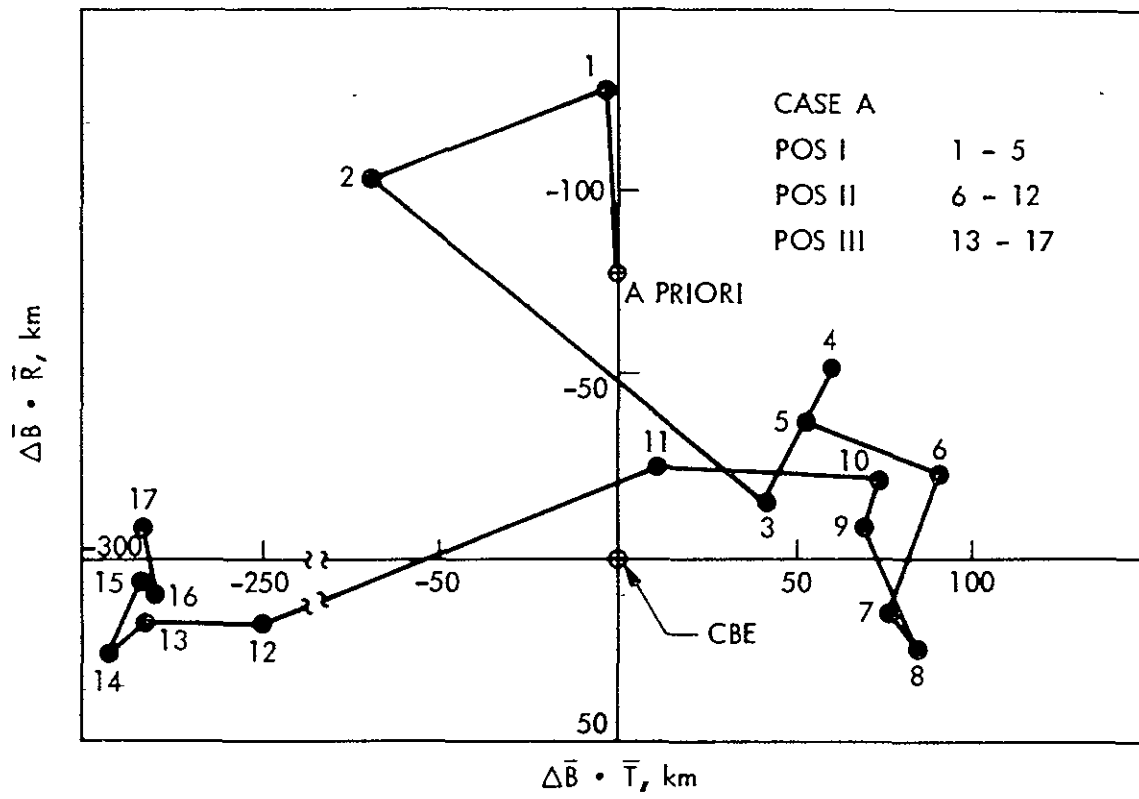
Figure 4-9. Trajectory Estimate Using No Stars
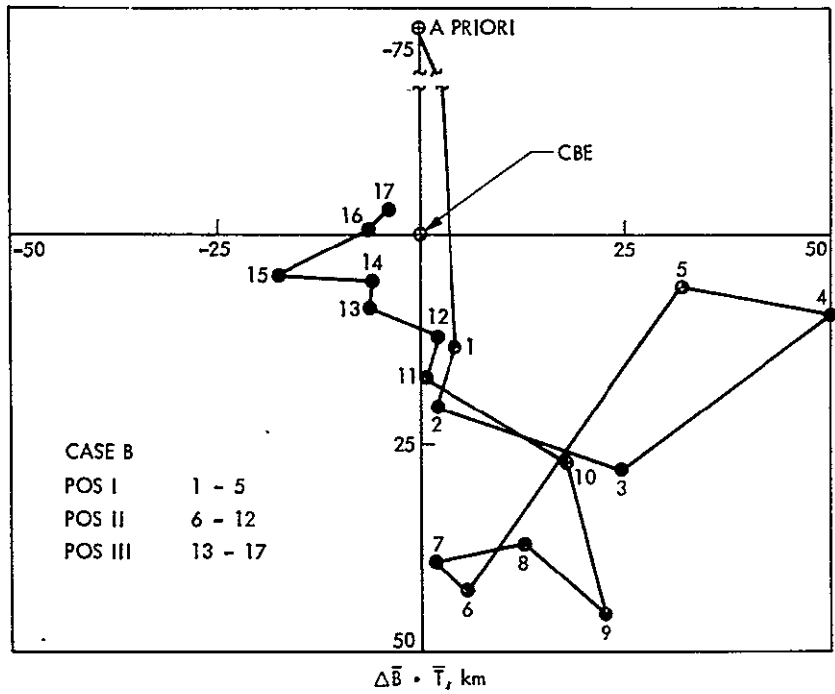
Figure 4-10. Trajectory Estimate Using One Star/Picture
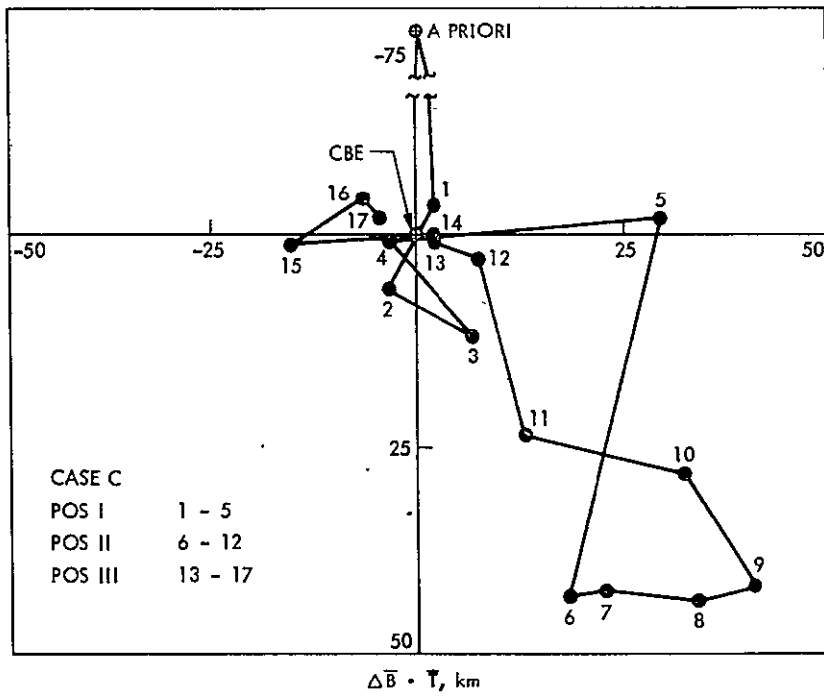
Figure 4-11. Trajectory Estimate Using Many Stars/Picture

167

The case A trajectory estimate is well behaved when compared to its expected accuracy until the last picture in POS II. Then the large non-random TV pointing errors (modeled as random errors) in the remaining pictures drives the trajectory estimate to a 3 σ error.

The full accuracy potential of the optical data can be obtained with only one star/picture. These star sensitivity results can be explained by examining the TV pointing errors. For a given picture, all sources of pointing errors can be modeled as three independent rotations about the axes of an orthogonal coordinate system (e.g., TV pointing has three degrees of rotational freedom). One star image (a pixel and line observation) yields two of the three degrees of rotational freedom. The third degree of freedom is obtained from a second star or from apriori TV pointing which has an accuracy of a few tenths of a degree. Apriori TV pointing to this accuracy can be obtained from either reduced spacecraft telemetry data (0.015 deg-1σ) or from the desired pointing (0.15 deg-1σ). Additional stars, however, do not improve the Deimos-inertial reference information in a picture. Deimos image location measurement errors control this accuracy and are not affected by star observations.

Even though only one star/picture is needed, it is desirable to have many stars/picture from a reliability standpoint. Many stars/picture give independent checks on the TV pointing and also indicate the accuracy of the TV distortion model. Any discrepancy between image location residuals within a given picture would flag it for further evaluation.

Sensitivity to TV Distortion

A comparison was made of navigation performance as a function

168

of the data type used to estimate TV distortion and also the order of polynomial used to model distortion. Data used for distortion calibration included: 1) only reseau images from ground pictures; 2) only reseau images from flight pictures; and 3) only star images from flight pictures. Distortion polynomials of 1st (linear) and 3rd order were compared to results from the nominal 6th order polynomial.

In comparing calibration data, it was found that all three types gave equivalent trajectory estimation results. The TV distortion did not change from prelaunch to the end of the mission. Only a linear shift and rotation of the reseau grid of a few pixels was measured, which was easily absorbed in the TV pointing error model. Approximately 200 star images from Plieades pictures and optical navigation pictures were used to produce equivalent results as from reseau data. Stars are a more desirable data type for distortion calibration because they also enable the calibration of optical distortion, in addition to electromagnetic distortion and are more easily detected than reseaux.

A tradeoff for increased optical data linearity at the expense of reduced model accuracy was evaluated. It was found that the linear and 3rd order distortion polynomial gave equivalent trajectory estimates to the nominal 6th order model. The increased linearity was accompanied with a slightly noisier trajectory estimate behavior which, however, was well within ghe predicted accuracy. Therefore, it is concluded that a 1st order (linear) model would suffice if time constraints would not allow iteration of the optical data.

If time is available, which will generally be the case, the 3rd order model gives the full accuracy potential of the optical data with iteration of the data.

Sensitivity to Mars Ephemeris

One major source of error in the use of Doppler data for navigation estimates is planetary ephemeris errors. This results from the fact that the data is taken by stations on Earth and must be related to the target planet by using assumed station locations and a planetary ephemeris. However, from onboard optical data the spacecraft state is directly related to the target planet.

To demonstrate the independence of optical navigation estimates from the planetary ephemeris errors, a solution was made with a Mars ephemeris error of about 500 km. The results of processing the optical data with this ephemeris error are shown in Figure 4-12, giving the B-plane solution history. The origin of the plot is at the current best estimate (CBE). The figure shows that the first pass through the data moves the estimate from an apriori more than 500 km away to within 10 km of the CBE. The final iteration moves the estimate to within 2 km of the CBE.

Sensitivity to Radio Tracking Data

To evaluate the strength of optical data, a trajectory solution was made without the aid of any other tracking data. From Section 2.4 it is expected that POS I and II data alone would an accurate $\overline{B} \cdot \overline{R}$ and $\overline{B} \cdot \overline{T}$ solution but limited pictures and observed parallax would degrade the time of flight accuracy. However, POS III data containing both Deimos parallax and trajectory bending would yield a complete

170
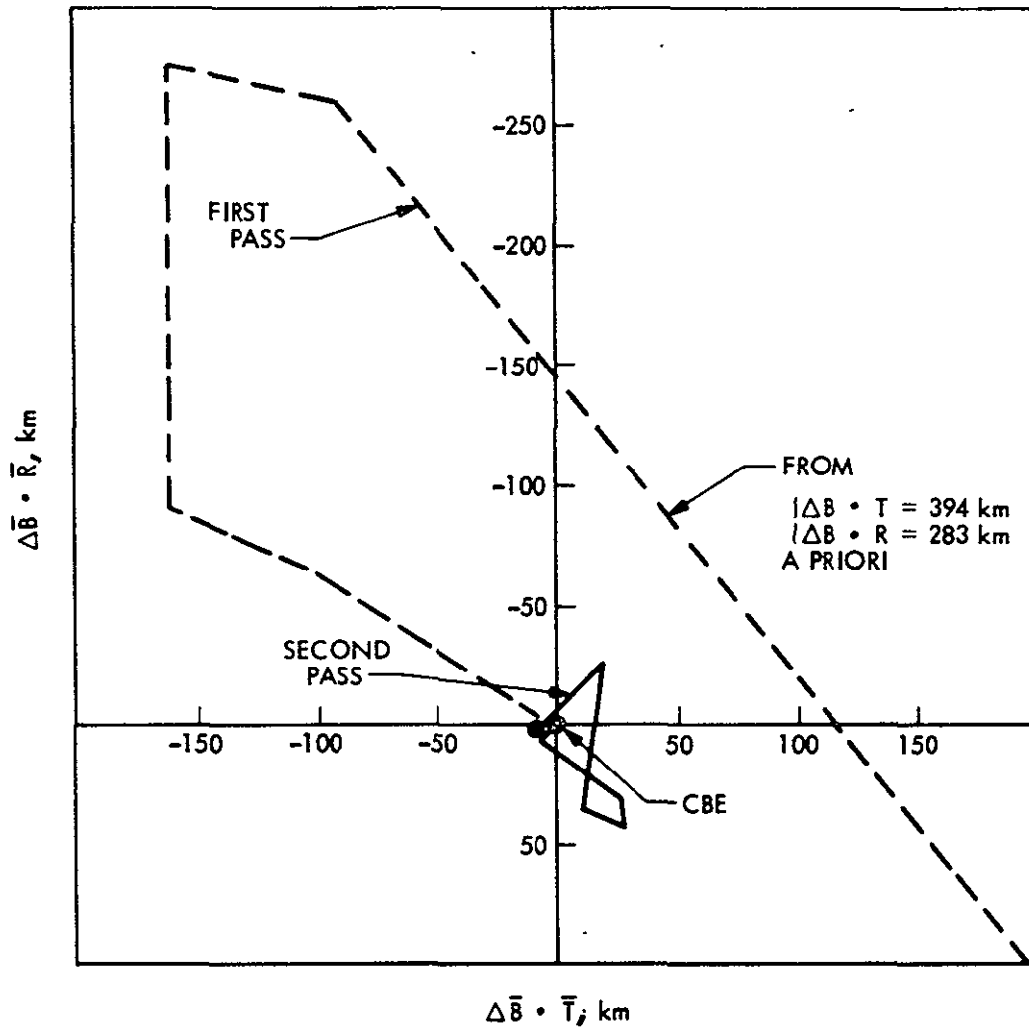
Figure 4-12. Sensitivity to Mars Ephemeris Error

171

trajectory determination from only the optical data.

A nominal trajectory was generated from Atlas/Centaur injection conditions. These injection conditions gave a 25,000 km aim point bias at Mars for planetary quarantine. The use of this trajectory did not allow the optical data to "know," apriori, that a midcourse maneuver had been performed five days after launch. The midcourse maneuver changed the actual trajectory aim point by 15,000 km and arrival time by about a day (250,000 km). In other words, this apriori trajectory gave the optical data only a vague indication that the spacecraft was going in the vicinity of Mars.

Initially, only POS I and II data was iterated. These results could have been available in real time since the POS III data was played back after insertion. Five complete iterations of the POS I and II data were needed to obtain a converged solution because of the nonlinearity due to the 250,000 km apriori trajectory error. After a converged solution was obtained for the POS I and II data, an additional solution was made which included the POS III data. This final solution allowed the full potential of the approach optical data to be evaluated.

The B-plane trajectory estimates are shown in Figures 4-13 and 4-14 at the end of a complete iteration of POS I and II data. It can be seen that an accurate estimate of $\bar{B} \cdot \bar{T}$ and $\bar{B} \cdot \bar{R}$ can be obtained using only POS I and II data as expected. The B-plane estimate after 5 iterations was within ten km and ten seconds of the current best estimate. Adding the POS III data brought the B-plane estimates from optical data only to within five km and three
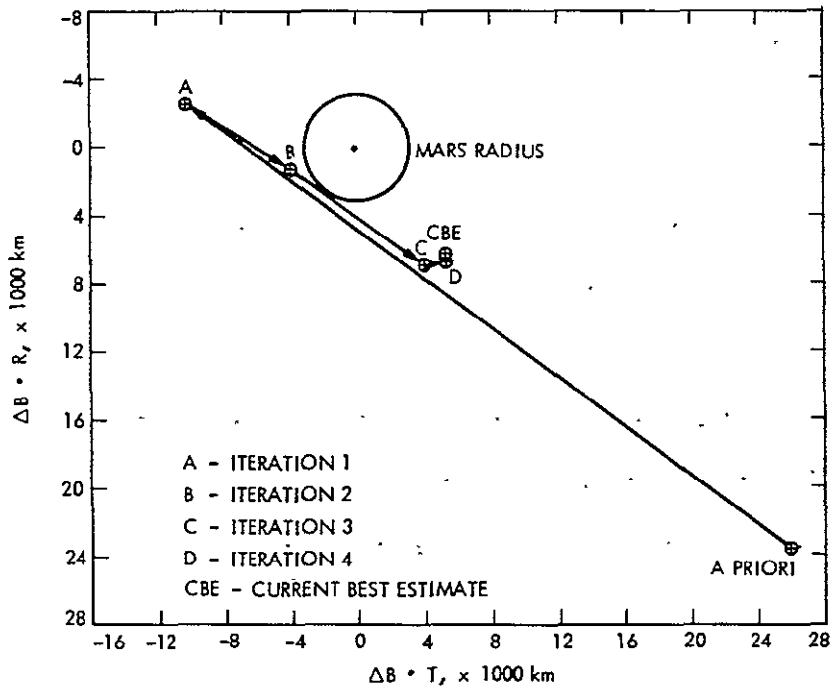
Figure 4-13. Trajectory Solution from Injection
Using Only Optical Data
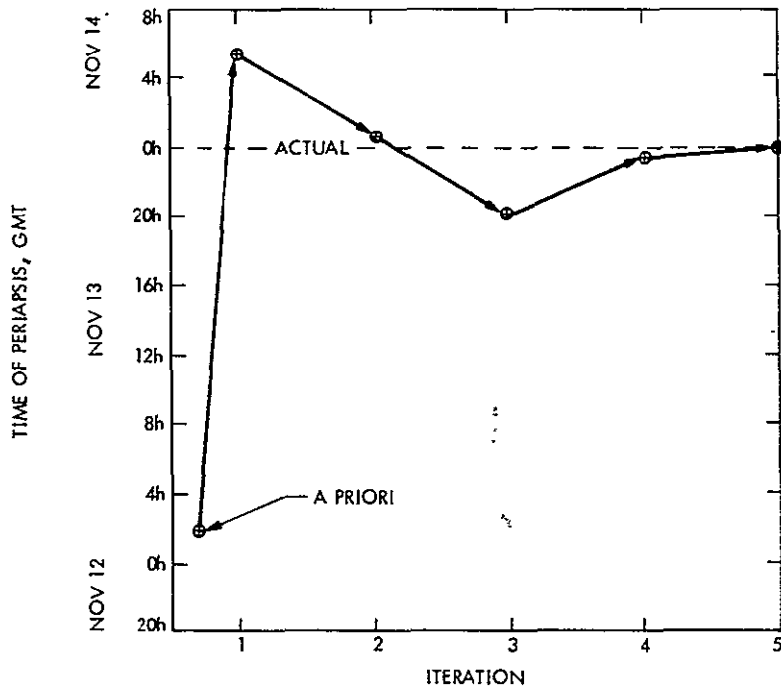
Figure 4-14. Flight Time Solution Using Only Optical Data

173

seconds of the current best estimate.

The time of flight estimate and expected uncertainty from the final solution are shown in Figure 4-15. It is seen that the uncertainty does not go below a few seconds until 10 hours from encounter. This level of accuracy would be available about a day before encounter from radiometric data. It is concluded, therefore, that the optical data by itself only can yield an accurate trajectory estimate, using data within 10 hours from Mars encounter. By combining optical and radio data, an estimate of comparable accuracy can be obtained much earlier.
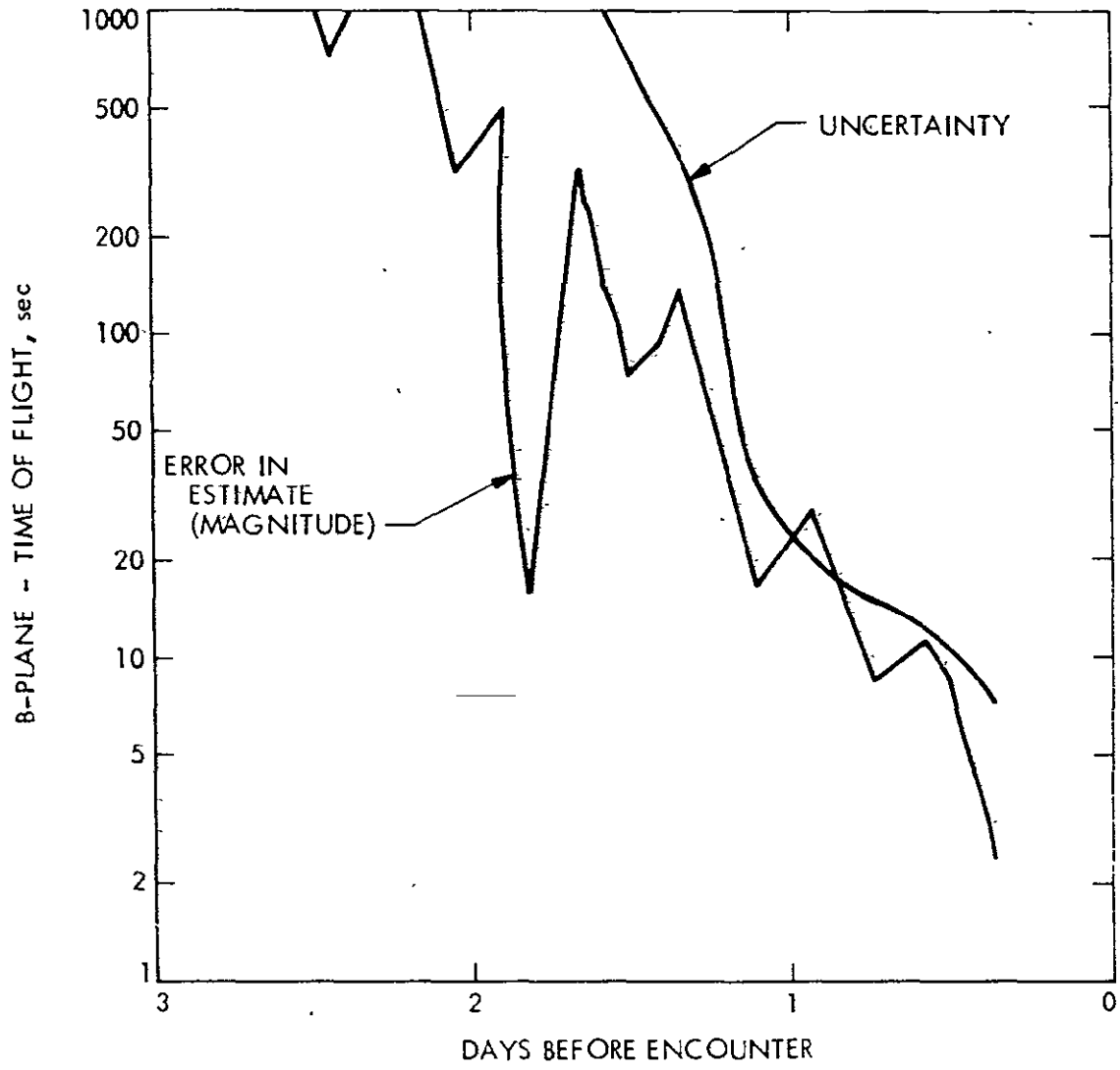
Figure 4-15. Flight Time Estimate Using Only Optical Data

4.4 Analysis of Planet-Limb Data

In this section we present results of the analysis of the planet limb data from Mariner IX. This consists of the processing of the raw limb data to locate the center of the planet image, followed by an evaluation of the spacecraft orbit determination performance using this data, and its sensitivity to the amount of radio tracking data.

Limb Data Processing

A typical picture is shown in Figure 4-16. As described in Section 3.4, the limb-finding algorithm searched the digital video data TV scan line by scan line. That is, the limb search started from a point off the planet image and continued onto the limb. The first of three adjacent pixels, all having video intensity levels exceeding a predetermined threshold level, was selected as the location of the lit limb on that line. The requirement for three adjacent pixels eliminated the detection of false limb point caused by one- or two-pixel bit-error noise (Fig. 4-17).

Typical lit limb structure imaged by the narrow angle camera (Fig. 4-17) indicates a relatively sharp increase in brightness near the equator and a gradual increase at the pole regions. The transition region between the dark background and the apparent limb ranged from 15 km to 25 km wide near the equator, and 25 km to 30 km wide at the pole regions.

To model the imaged lit limb, Mars was assumed to be an ellipsoid; as discussed in Section 3.4, with this assumption the image of Mars can

176
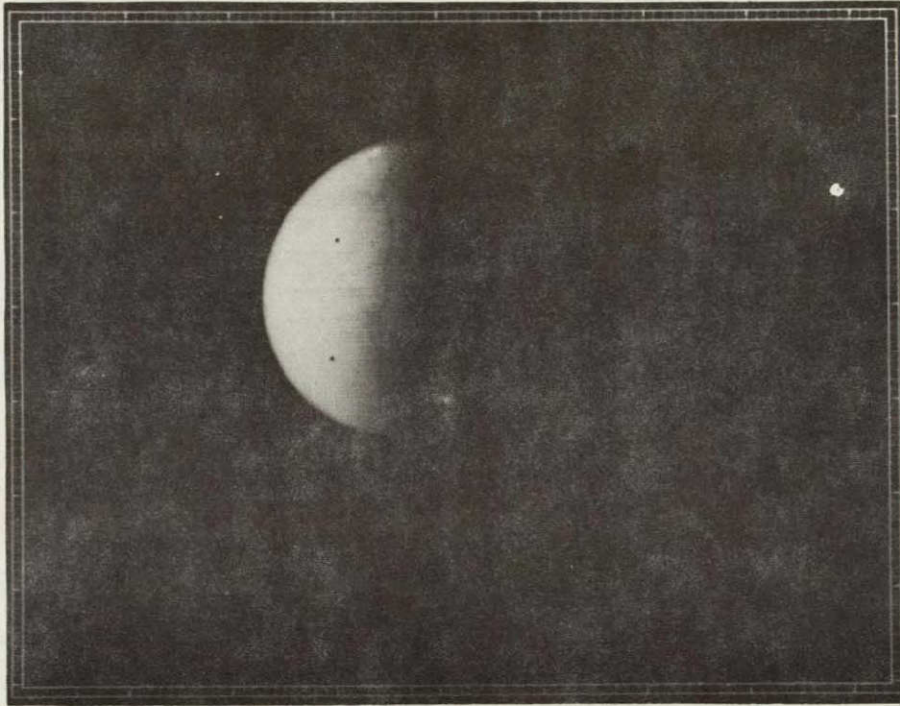
Figure 4-16.   Typical Mars Lit Limb TV Picture
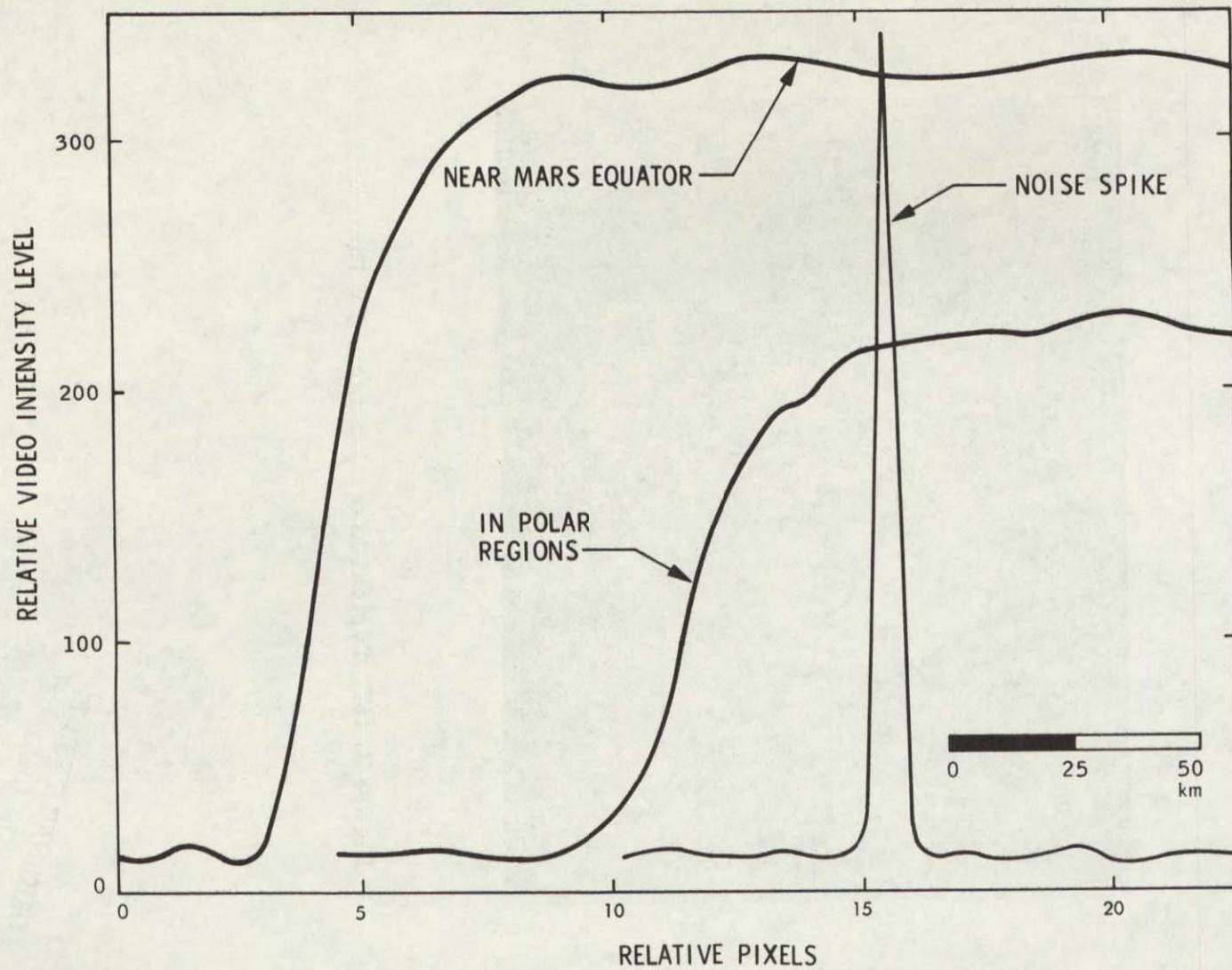
Figure 4-17.   Mars Limb Image Structures

be reasonably well modeled by an ellipse, with the center of the
ellipse being coincident with the center of the ellipsoidal planet
body.

The radius estimates obtained from the lit limb data (Fig. 4-18)
are approximately 100 km greater than the mean equatorial radius
(3393.4 km) determined by the S-band occultation experiment (Reference 41).
Similarly, the identified shape parameter of the planet (Fig. 4-19)
is smaller than the expected value (e = 0.145) by about 3 percent.
That is, the Mars images were somewhat larger and more circular than
expected. These results also indicate that the lit limb of the
imaged planet does not represent the Martian surface but light
scattered from the Martian atmosphere: They may also have been
caused by the limb darkening effect at the polar regions and lightening
near the south polar cap, marked albedo change near the lit limb,
atmospheric activities, i.e., the dust storm which prevailed in the
Martian atmosphere throughout the approach phase, and the spectral
response characteristics of the TV camera subsystem.

The limb fit residuals, which are a measure of the observation
data noise after a successful limb parameter estimation process, were
evaluated for each scan line containing a limb measurement (Fig. 4-20)
with the units of $(pixel)^2$. The observation data noise had been
caused by quantization in picking discrete limb points, uncalibrated
geometric distortion of the TV, residual limb image from the previous
picture (triggering a false limb data), and limb model approximation
error. To interpret the limb residual statistics with nearly zero-
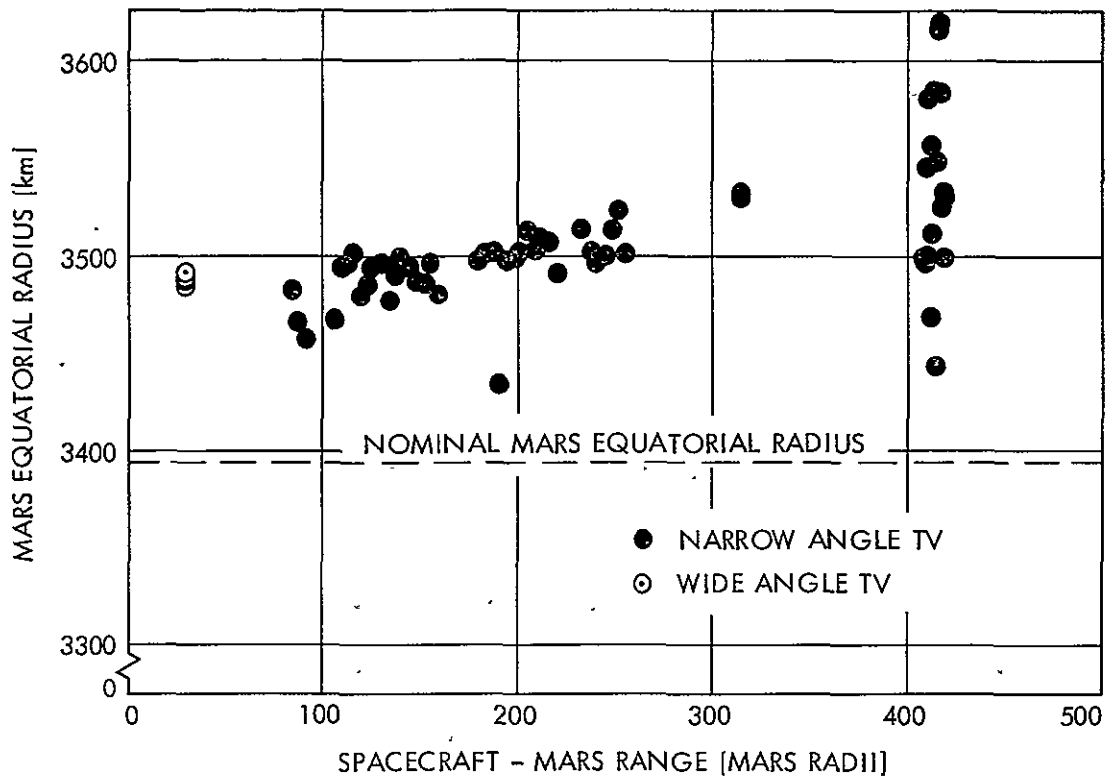mean and a variance of several tens of $(pixel)^2$, the residual random
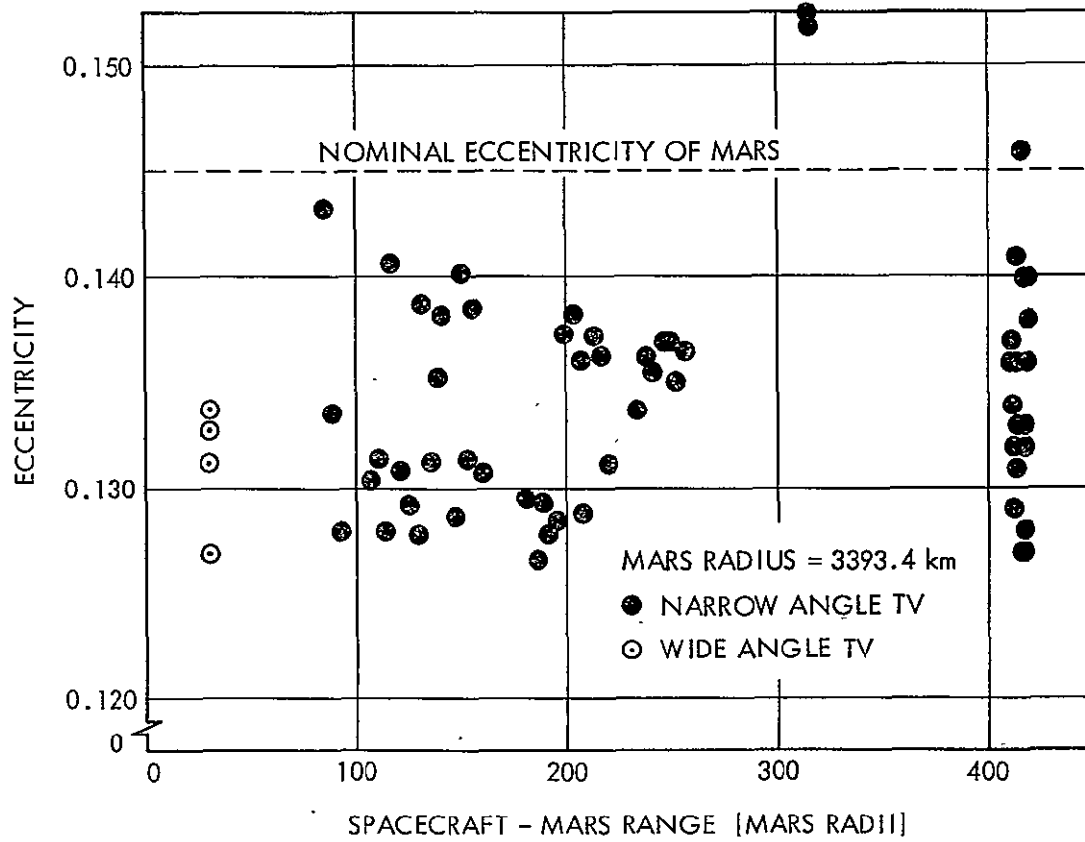
Figure 4-18. Observed Mars Mean Equatorial Radius
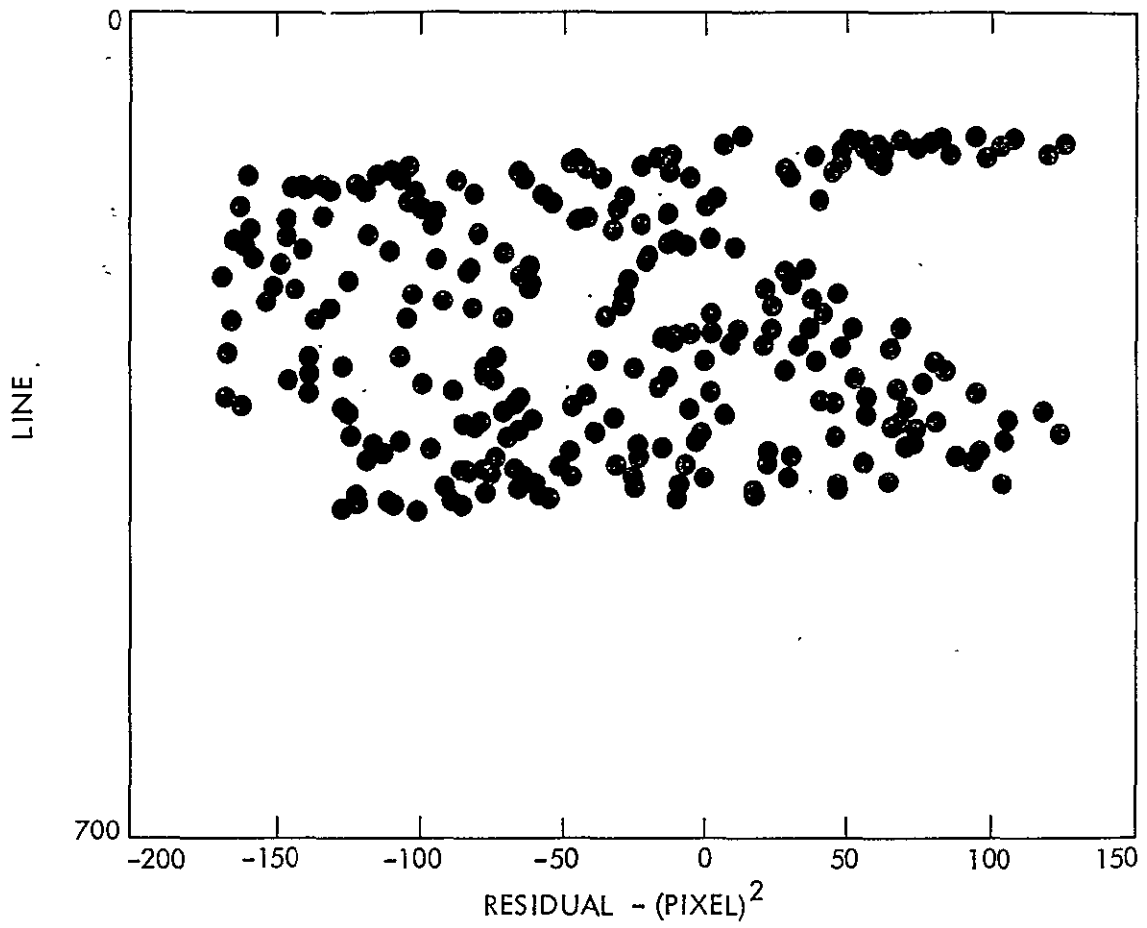
Figure 4-19. Observed Mars Shape Parameter

Figure 4-20. Mars Lit Limb Fit Residuals

process is mapped onto an equivalent random process along the limb

image in the TV coordinate system. From Eq. (3-4-37) we obtain

$$\text{Var}(\delta\emptyset) = c_p^2 \,\text{Var}(\delta p) + c_\ell^2 \,\text{Var}(\delta\ell) \,, \qquad\qquad (4\text{-}4\text{-}1)$$

where

$$c_p^2 = 4\left[-\left(1 - \frac{c^2}{a^2}\right) x \cos\psi + y \sin\psi\right]^2 \qquad\qquad (4\text{-}4\text{-}2)$$

$$c_\ell^2 = 4\left[\left(1 - \frac{c^2}{a^2}\right) x \sin\psi + y \cos\psi\right]^2 . \qquad\qquad (4\text{-}4\text{-}3)$$

If it is assumed that the observation noise affects equally in line

and pixel directions, Eq. 4-4-1 can be rewritten as

$$\text{Var}(\delta p) = \text{Var}(\delta\ell) = \frac{\text{Var}(\delta\emptyset)}{c_\ell^2 + c_p^2} \,, \qquad\qquad (4\text{-}4\text{-}4)$$

or for typical values for the known parameter relations, e.g.,

$$\frac{c}{a} = 0.145 \,,$$

and

$$x^2 + y^2 \approx a^2 .$$

Eq. (4-4-4) is approximated by

$$\text{Var}^{\frac{1}{2}}(\delta p) = \text{Var}^{\frac{1}{2}}(\delta\ell) \approx \frac{\text{Var}^{\frac{1}{2}}(\delta\emptyset)}{2a} . \qquad\qquad (4\text{-}4\text{-}5)$$

Eq. (4-4-5) typically took a value of 0.3 pixels, reasonably well

coinciding with the limb quantization error statistics (a uniform

distribution over a pixel).

Orbit Determination Using Planet Limb Data

The TV data through POS II was processed using as apriori a

183

trajectory based on radio tracking data processed through E-13 hours. The picture data from Mars calibration sequences I and II and POS sequences I and II were used for the analysis. Of these pictures the Mars calibration II pictures (at E-4 days) were dropped due to vary large data residuals caused by large pointing errors.

Figure 4-21 shows the B-plane solution history of the trajectory estimate obtained by processing the optical data. The parameters estimated were the spacecraft Cartesian state at epoch, TV pointing biases and errors, and image center finding errors. The origin in the figure is at the current best estimate (CBE). The apriori value shown for the optical data arc was the aposteriori estimate from a short radio data arc (5 days) through E-13 hours. The estimate stabilized only towards the last few pictures. Two iterations were performed, indicated by the dashed and full lines, respectively, with the last two points on the full line representing the estimates obtained from adding POS III data. The error ellipse for the final estimate at the end of POS II data had a semimajor axis of 70 km. However, the estimate was within 25 km of the current best estimate (CBE).

Figure 4-22(a) shows the raw data residuals, in the pixel and line directions, for the POS data. Figure 4-22(b) shows the residuals after the solved for pointing biases and trajectory error have been removed. The magnitude of the pointing biases estimated agreed with scan calibration results. The center-finding errors, modeled here as being proportional to the image size, appeared to be very small and independent of phase angle. The pointing errors in the raw data included systematic as well as random components.
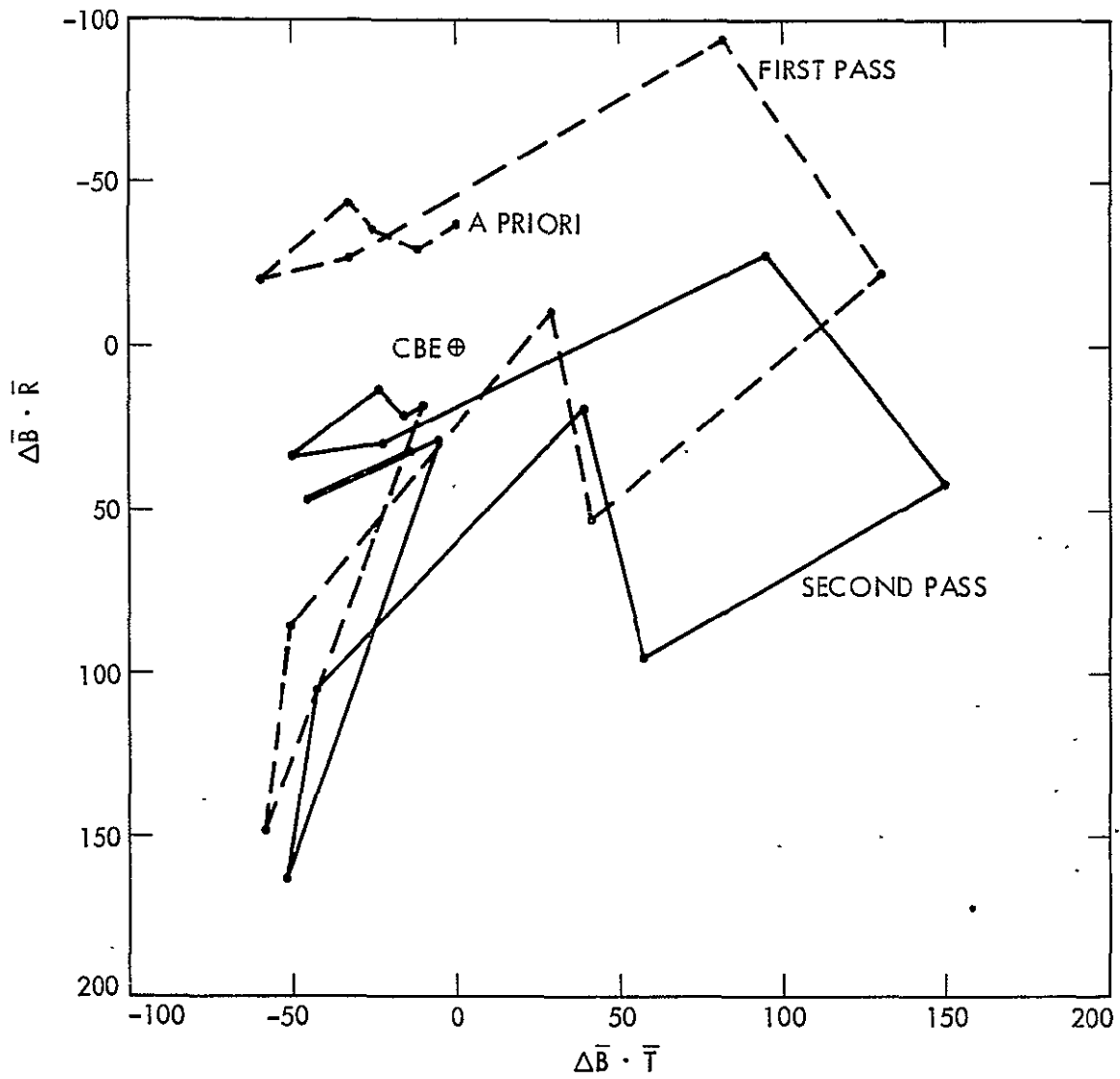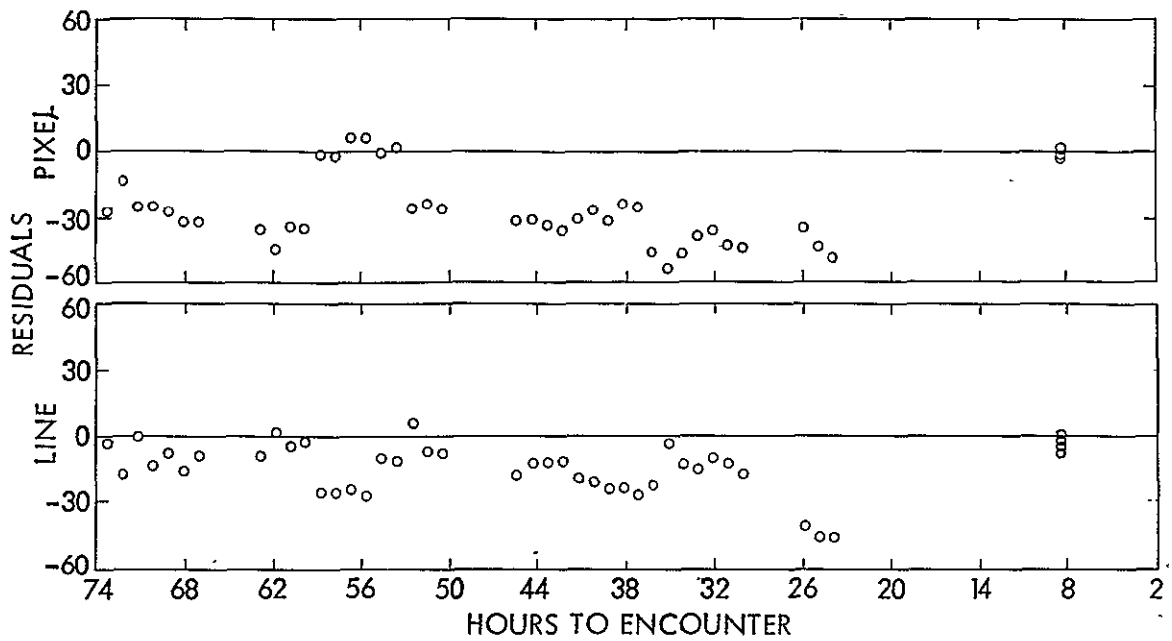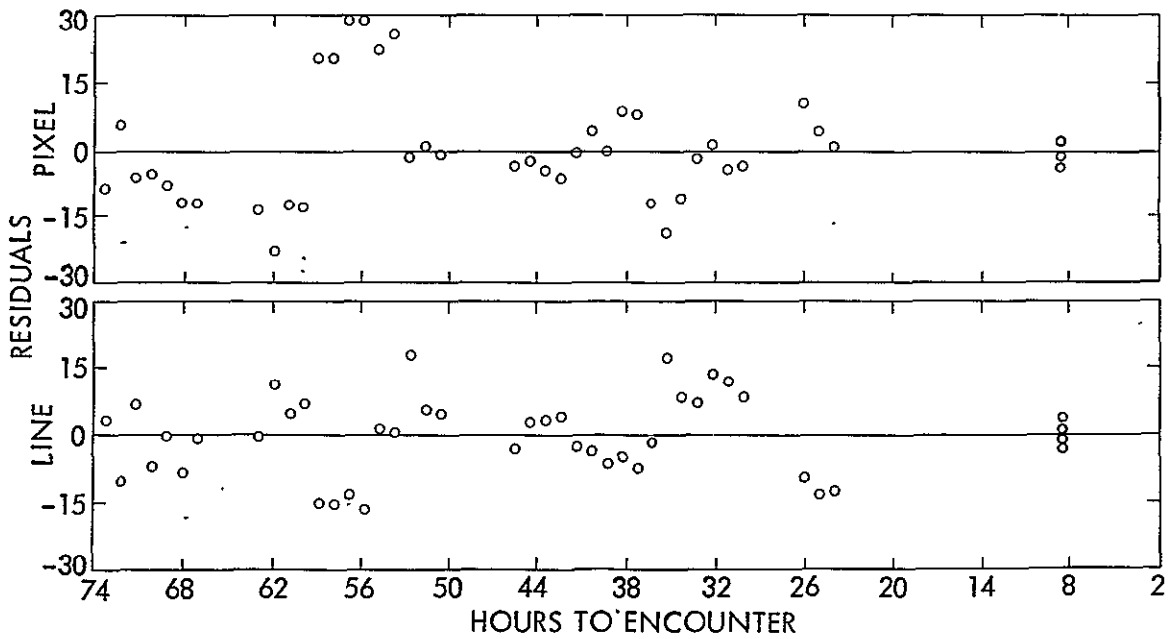
184

Figure 4-21. Trajectory Estimate Using Lit Limb Data

Figure 4-22. POS Lit Limb Data Residuals

The raw data residuals for the Mars calibration sequence I

pictures are shown in Figure 4-23. The expanded time scale facilitates

the identification of attitude control limit cycle motion of the

spacecraft with a period of about 1.2 hours. This residual limit

cycle motion may be due to scale factor errors in the attitude

control model. These were, however, not separately included in the

estimation but were absorbed in the pointing errors.

The orbit determination (OD) accuracies (Fig. 4-24) indicate

a slow reduction of the SMAA and SMIA with time up to about E-50

hours. Rapid reduction in uncertainty occurs thereafter. At the end

of POS II the SMAA is about 70 km while at the end of POS III it

is about 30 km. The time of flight uncertainty shows little

improvement, as would be anticipated from our discussion of the

approach trajectory.

Sensitivity to Radio Tracking

As indicated before, optical data suffer a serious limitation

in that an accurate determination of the time of flight and V_∞ is

not obtained. However, for the Mariner IX trajectory geometry these

are precisely the parameters that can be accurately determined from

radio data. A combination, then, of optical and radio data, to give

better estimates of encounter conditions much earlier than either

data separately could, would be ideal. To study the reliance of

optical limb data solutions on apriori values obtained from radio

data arcs, two different analyses were carried out. In the first,

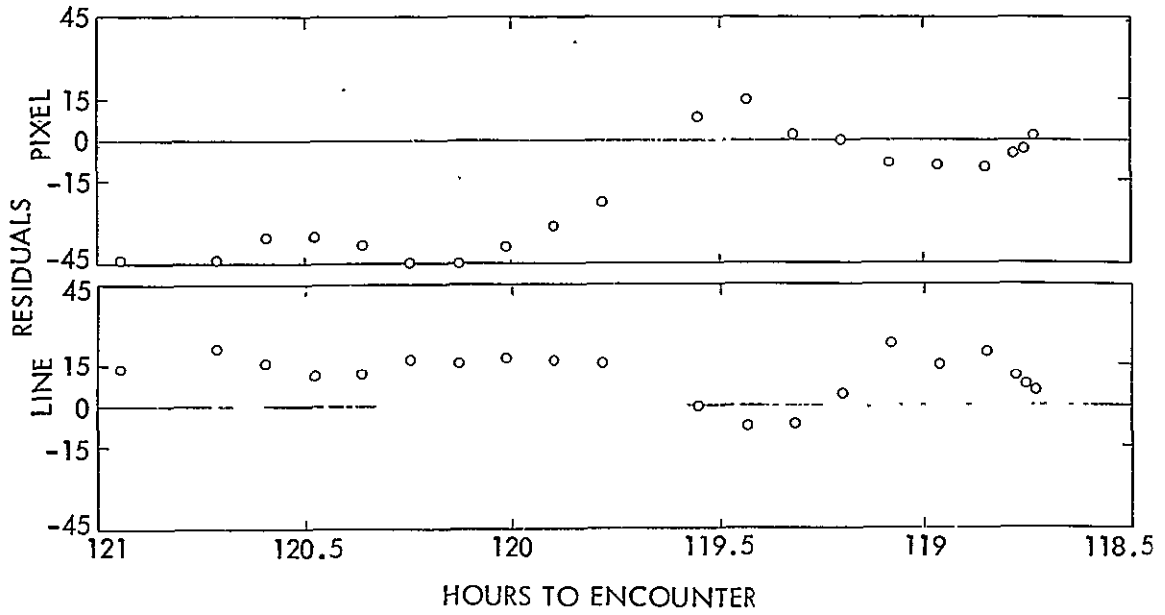a few hours of radio tracking was assumed beyond the first midcourse

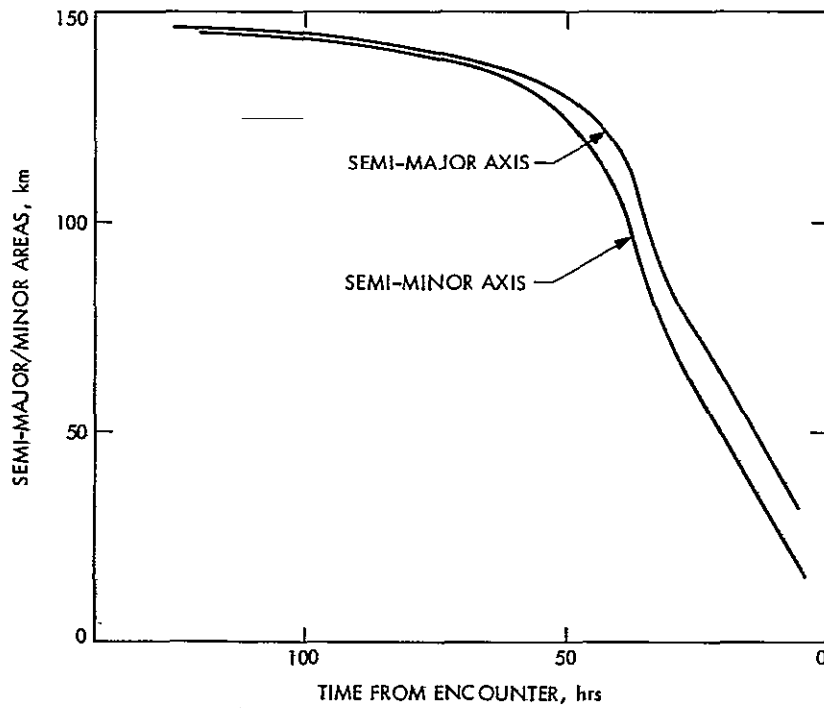Figure 4-23. Mars-Calibration Sequence Raw Data Residuals

Figure 4-24. Trajectory Estimation Accuracy Using Lit Limb Data

maneuver at launch (L) + 5 days, and no more radio data thereafter. The spacecraft state estimate and covariance at that time were input . as apriori estimates to the optical data arc. The mapped B-plane uncertainties were very large at this point owing to large maneuver execution uncertainties being mapped several months forward. The analysis was conducted using only the TV pictures through POS II for the first pass.

The B-plane solution is shown in Figure 4-25. The apriori estimate was more than 2500 km from the CBE in the B-plane. The first pass moved the estimate at the end of POS II to within 450 km of the CBE. The next pass did not appreciably move the POS II solution, but the POS II solution, but the POS III data moved the estimate to within 30 km.

The second analysis was performed with no radio data at all. The injection conditions, for purposes of planetary quarantine (PQ), had a 25,000 km aim-point bias and 22 hours lag in time of flight at Mars. The analysis made here for this optical-only solution was not cognizant of the mid-course maneuver performed at L + 5 days which removed the PQ bias. The B-plane trajectory solution (Fig. 4-26) stabilized at about 7000 km from the CBE, with negligible improvement in time of flight.

The large final error involved here indicates that for optimum results using optical limb data, some radio data is necessary. Even small radio data arcs when used to give apriori estimates and covariances, improve the effectiveness of optical limb data enormously (Fig. 4-25).
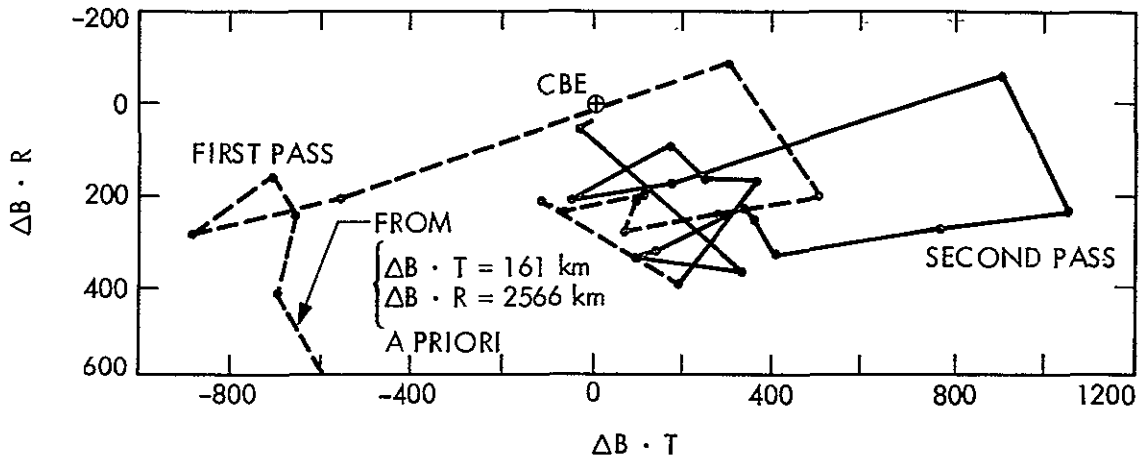
Figure 4-25.   Optical Data Solution from Mid-Course Maneuver Using
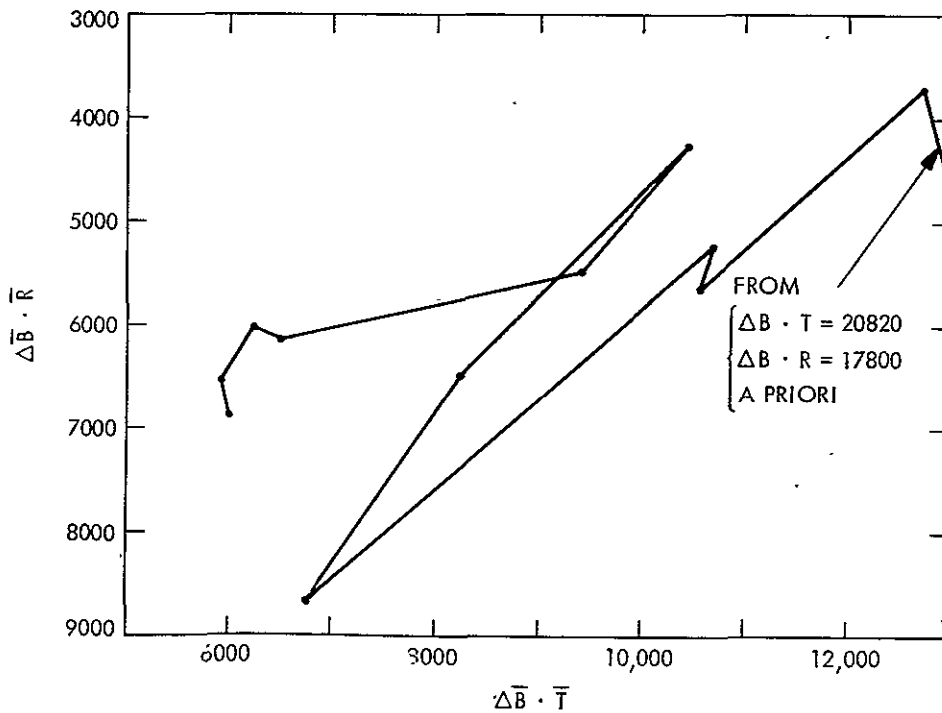Lit Limb Data Only

Figure 4-26.   Optical Data Solution from Injection
Using Lit Limb Data Only

CHAPTER 5

OPTICAL NAVIGATION APPLICATION TO VIKING

The Viking Mission consists of two unmanned spacecraft, Viking 1 and Viking 2, launched in August 1975, which will be inserted into Mars orbit in June and August 1976 respectively and will softland instrumented packages on the surface of Mars. The primary purpose of the Mission is to further our understanding of the origin and evolution of the solar system and of life in the solar system. In this chapter we evaluate the application of optical navigation to the Viking mission during the approach phase to the planet.

In section 5.1 we discuss optical navigation related mission design aspects, and considerations for selection of data types to be used. Section 5.2 evaluates the navigation accuracies obtainable using a combination of radio and optical data; this is followed by "optical only" accuracies in section 5.3 where we also examine the effect of various different data arcs in combination. In section 5.4 a method is developed to evaluate consistency between any two solutions and is shown through a simulation application to be very effective in the detection of data anomalies. We conclude the chapter in section 5.5 by the description of a parametric probability analysis technique developed to evaluate navigation performance as a function of system reliabilities.

5.1 Optical Navigation Considerations in Mission Design

In this section we briefly describe the mission to place in perspective the navigation critical times. This is followed by a discussion of the optical navigation data types selected for each phase of the mission and the rationale for doing so. We close the section with the possible impact of some of the optical navigation considerations on trajectory selection and mission planning.

Typical Interplanetary Mission Profile

Most space missions go through a similar pattern of events. Shortly after launch the spacecraft is placed into a parking orbit around the earth from which it is then injected into the desired trajectory away from the earth for the remainder of the mission. At the current state of the art the major portion of the space flight occurs primarily in "free fall" — i.e. under the gravitational influence of bodies in the solar system. This free fall is interrupted at selected times to alter the trajectory through spacecraft propulsion maneuvers; these are the navigation critical times.

For interplanetary trajectories, midcourse maneuvers are required shortly after injection into the heliocentric interplanetary orbit and shortly before arrival at the target planet. Typically a minimum of one and a maximum of two midcourse maneuvers are designed at each of these two phases — the near earth phase and the planet approach phase.

The near-earth maneuvers are needed to correct for an aiming bias imposed at injection due to the planetary quarantine (PQ) constraint requirement. In addition to removing any remaining aimpoint PQ bias, the planet-approach maneuvers are needed to correct any trajectory

errors prior to reaching the planet. The last approach maneuver designed determines the accuracy of the spacecraft delivery at planet encounter and provides the first opportunity to control this delivery; it is referred to as the "control" point.

To insert the spacecraft into a planet centered elliptical orbit a maneuver is essential near the periapsis of the approach hyperbolic trajectory of the spacecraft relative to the planet. At some time prior to this, referred to as the "knowledge" point, the best orbit estimate known is used to calculate the commandable quantities of the maneuver; the precision of this determines the accuracy of the orbit insertion. The knowledge point and the control point are the times when navigation accuracies are most critical for the planet approach phase of a space mission.

For Viking an approach maneuver could be executed from 30 days before Mars Orbit Insertion (MOI) at the earliest to 10 days before MOI at the latest.

Television Cameras and Data Type Selection

The Viking spacecraft orbiter (Fig. 1-4) contains two identical narrow angle television cameras the boresight of which is offset in the cross-cone direction by 1.38 degrees. The field of view of each camera is 1.51 degrees by 1.69 degrees with a scan of 1056 lines by 1204 pixels/line yielding a resolution of 25 microradians. The focal length is 475 mm and the exposure time varies up to a maximum of 2.66 seconds. The two cameras can be shuttered at a minimum time spacing of 4.48 seconds.

The investigation in Reference 22 demonstrated that the satellite-star method — method (ii) of section 1.4 — yields the best results, followed by the planet-star two camera approach, at both the control and the knowledge phases. Howevere as we discussed in section 3.3 a constraint that must be met when designing pictures is to ensure a separation angle of twice the accuracy of pointing obtainable — i.e. a separation angle of 1.0 degrees for Viking. Figure 5-1 shows the plot of the separation angle between the Mars limb and Deimos for the Viking 1 trajectory. The 15 hour sinusoidal variation is observed because the spacecraft approach is inclined relative to the orbit of Deimos and the period of Deimos is approximately 30 hours.

As can be seen from Fig. 5-1 the earliest that we can safely take Deimos star pictures based on the pointing constraint is about MOI - 104 hours. The semi-major axis of Deimos is 23500 km while that of Phobos is 9400 km; the availability of Phobos-star pictures therefore occurs considerably later. This explains why Deimos is the better satellite to concentrate on for approach optical navigation purposes at the knowledge phase. Moreover since the control point is at MOI - 10 days we must rely on the planet-star two camera method for the control optical navigation. These planet-star picture pairs are referred to as diads. These can be extended to star-planet-star triads; obtaining the planet picture frame pointing direction by interpolating between the pointing obtained from the star picture frames we can thereby eliminate the effect of attitude control system limit cycle motion during the time elapsed between camera shutters.
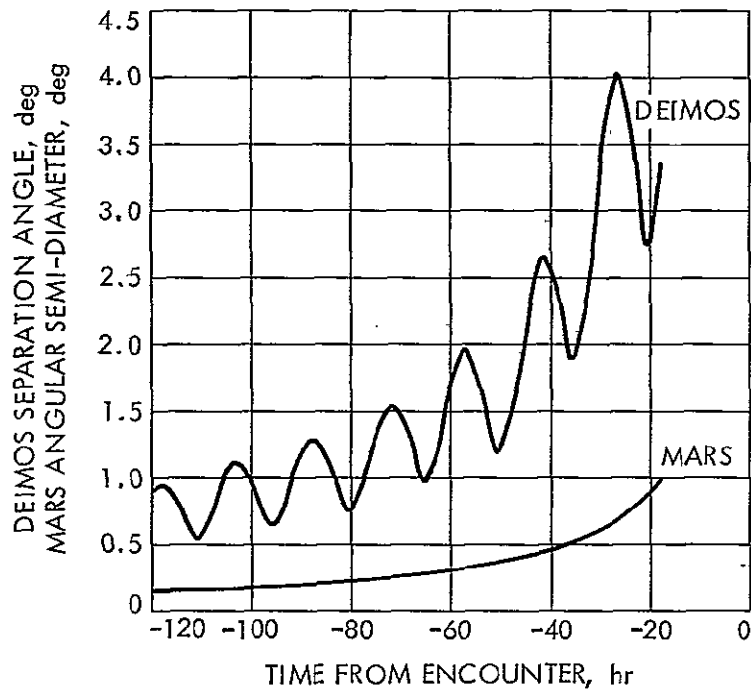
194

Figure 5-1. Mars Angular Semi-Diameter and Deimos
Separation Angle Evolution

Trajectory Selection Considerations

For radio navigation an important geometrical consideration during the Mission planning process of selecting a set preferred trajectories is the low declination problem. As we discussed in section 1.3 this could cause severe degradation in radio navigation accuracies; Viking 2 radio only navigation accuracies are worse than those for Viking 1 for primarily this reason.

For optical navigation there is a counterpart consideration during the mission planning process. This is in the availability of stars in the field of view that are bright enough to be imaged by the vidicon. Thus, for example, if the sensitivity of the camera was such that it could view no objects dimmer than, say 7.5 visual magnitude, then there must be stars of this magnitude or less available in the picture sequence planned. This can be a constraint when designing the control point picture sequence.

During the planet approach the spacecraft follows approximately a hyperbolic trajectory relative to the planet. The solar gravitational influence on the spacecraft and on the planet (neglecting its mass) is about the same since both are approximately in the same orientation and location relative to the sun. Therefore the inertially referenced spacecraft hyperbolic asymptote changes very little during planetary approach. The T.V. look direction to Mars differs from this because of (i) bending of the spacecraft hyperbolic trajectory and (ii) the parallax angle between the spacecraft velocity and look directions. Since these effects do not become appreciable until very close approach to the planet, the inertial look direction does not change .

appreciably (see Figures 5-2a and 5-2b) during the control phase.
Therefore the star background variety is quite limited; if the star
availability for particular trajectories turns out to be sparse, this
could pose a severe problem for control optical navigation for those
trajectories.

This problem does not occur for knowledge phase picture sequence
design since the satellite motion around the planet provides adequate
look direction variability and therefore star background coverage (see
Figure 5-3). However, another problem could arise here for approach
geometries where the spacecraft trajectory is in a plane parallel to
the satellite orbit plane. In that event viewing of the satellite
would be prohibited for a major portion of the satellite orbit, due
to the presence of the bright planet, possibly leading to (i) limited
regions of star background variability and (ii) limited mean anomaly
coverage which may hinder solving for the satellite orbit.
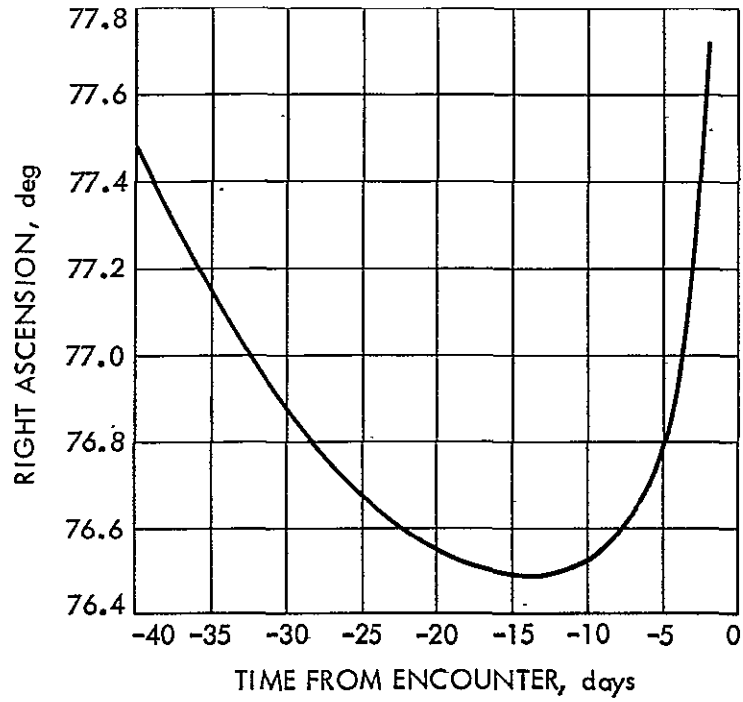
(a) Mars Right Ascension
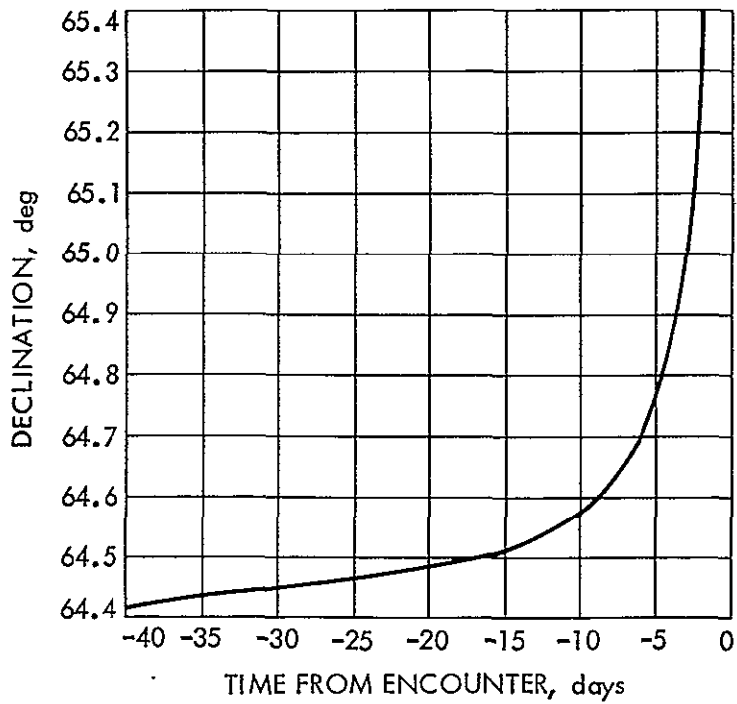
(b) Mars Declination

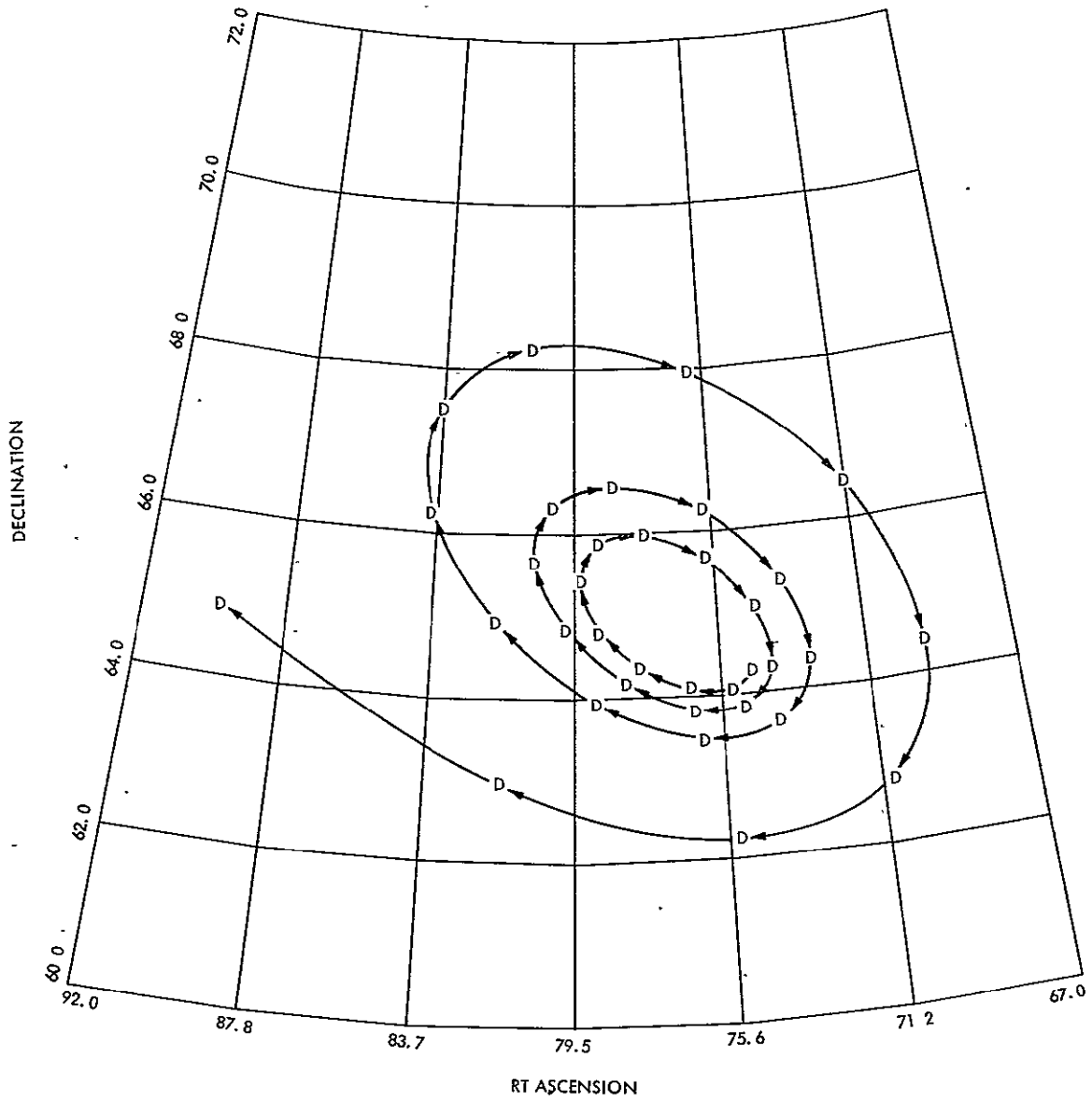Figure 5-2. Spacecraft Based Mars Inertial Geometry at Control

Figure 5-3. Spacecraft Based Inertial Geometry at Knowledge

199

5.2 Radio Plus Optical Navigation Accuracy Analysis

This section describes a study made to evaluate the orbit determination (OD) accuracies obtainable during the interplanetary approach phase of the mission using both radio and optical data. The evaluation is conducted using a strategy yielding accuracies deemed representative of the OD performance expected. Several combinations of data arcs are analyzed to enable the assessment of the sensitivity of overall navigation performance to the timing of the approach midcourse maneuver.

The following subsection gives an explanation of the various approach maneuver scenarios to be investigated. This is followed by subsections describing the assumed composition of the data and the filter configuration employed. Finally the OD accuracies are given, mapped to the B-plane at Mars encounter (E).
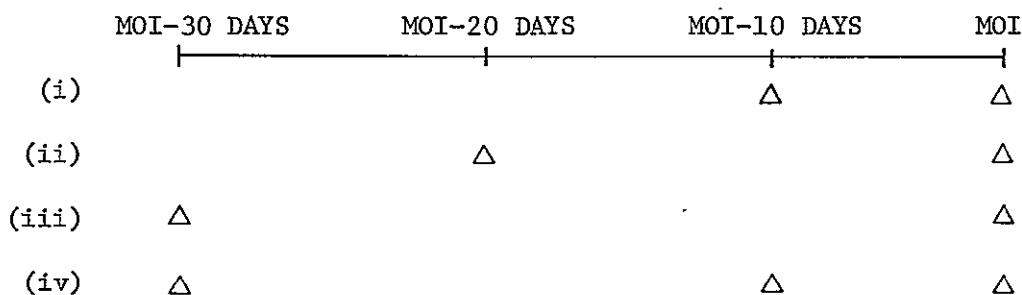
Maneuver Scenarios

The study consisted of evaluating the OD accuracy before each of a series candidate approach midcourse maneuver epochs and before the Mars orbit insertion (MOI) maneuver.

In conjunction with the scheduled MOI maneuver, four different approach midcourse maneuver strategies were conceptualized, namely:

(i)   only one approach maneuver at the control point — 10 days before encounter.

(ii) only one approach maneuver at 20 days before encounter

(iii) only one approach maneuver at 30 days before encounter

(iv) two approach maneuvers at E-30 days and at E-10 days, respectively.

200

These maneuver scenarios are shown schematically below. Of these the first is the nominal plan.

```
         MOI-30 DAYS      MOI-20 DAYS      MOI-10 DAYS        MOI
         ├──────────────────┼────────────────┼──────────────────┤
  (i)                                             △             △

  (ii)                          △                               △

  (iii)      △                                                  △

  (iv)       △                                    △             △
```

Maneuver Scenarios

Data Constitution

For the radio data two-way doppler data was assumed to be available from 40 days before encounter (E-40 days), and simulated as such in a multistation tracking strategy. The three tracking stations assumed for the simulation are those at Goldstone, CA. (DSS 14), Madrid, Spain (DSS 61), and Canberra, Australia (DSS 42). Simultaneous data was not assumed during the overlapping view periods from a pair of stations. The station switching pattern was based on elevation angle and specification of a preferential order of station coverage desired. The order specified was DSS 42, DSS 14, and DSS 61, with all data eliminated below an elevation of 15°.

For the simulation, one range-rate point was sampled every hour, with the data weight adjusted to simulate continuous data. In addition to the range-rate data, one two-way range point was sampled for each pass of each tracking station. The range point was always sampled when the spacecraft was at the zenith for that pass.

For the optical data a 3 day arc of Mars-Stars data was assumed available prior to the midcourse maneuver. This would consist of a

pair or triad of frames using the two-camera approach wherein Mars would be viewed in frames from one camera and a star field in those from the other. The pictures are near-simultaneous (a few seconds apart) with the scan platform held fixed between shutter times.

An arc of data extending from M-4 days to M-1 day (where M is the time of the approach midcourse maneuver) was assumed available at a rate of one set every six hours, regardless of when the maneuver occurs. Thus for an E-30 day maneuver the arc extends from E-34 days to E-31 days and for an E-10 day maneuver from E-14 days to E-11 days.

For the knowledge phase, the data consists of pictures of Deimos against a star background within the same frame. This is possible here since the visual magnitude of Deimos is sufficiently high (i.e. the brightness is sufficiently low) to enable both Deimos and some stars to be viewed with the same exposure setting without saturating the vidicon. A data arc extending from E-3 days to E-18 hours was assumed with one picture every three hours.

Analysis Strategy and Filter Configuration

Covariance analyses for the different maneuver scenarios were performed using combined radio and optical data. The achievable accuracies were established for each of the control and knowledge phases. The strategy employed for the combination of the radio and optical data was to use the a-posteriori covariance from a radio analysis as the apriori covariance for the optical data arc. One of the incidental facets of this procedure is that the effect of adding increasing quantities of optical data to a fixed amount of radio data can be displayed and examined.

202

The only parameters estimated in the baseline study were the spacecraft state. Other parameters were considered as error sources but not explicitly estimated by the filter. For the radio analysis these included the equivalent station location errors, attitude control accelerations and solar radiation pressure reflectivity coefficients, Brouwer and Clemence Set III planetary ephemeris parameters (see Ref. 42) for the Earth-Moon barycenter and Mars, and the mass of the moon and of Mars.

For the control point optical data arc the parameters considered as error sources were the measurement and camera pointing biases and the image proportional center-finding errors. For the knowledge point processing the optical data related errors considered were the Wilkin's parameters for the Deimos ephemeris errors and again the camera pointing biases. For these pictures the camera pointing biases assumed reflect the accumulation of error due to uncalibrated electromagnetic and optical distortion, local distortion owing to the Deimos image read-out process and asymmetric image blooming effects in the vidicon. These biases in the control data arc have, in addition, the errors due to the offsets between the two cameras and the motion of the spacecraft during the time between the shutter times of the two cameras. The satellite ephemeris parameters would normally be estimated in-flight along with the spacecraft state as one of the solutions generated. In the initial phases of the trajectory estimation, in fact, a greater degree of reliance may be placed on this solution than on a solution based on estimating the spacecraft state only. However it is reasonable to expect that the satellite ephemeris parameters thus estimated could

be in error up to a level compatible with the apriori uncertainties for those parameters assumed in the analysis here. Thus the results presented here would be only slightly conservative.

The error levels assumed for the various parameters considered are consistent with the baseline error model given in Table 5-1. The apriori uncertainty at the solution epoch was assumed to be 100,000 km (1 σ) for position and 1 km/sec (1 σ) for velocity in each direction.

Accuracy Results

The control point, for purposes of this accuracy analysis was defined as the time at which the approach midcourse occurs, and radio data was assumed up to that time. The knowledge point on the other hand was defined as MOI-12 hours; only radio data up to E-2 days was assumed to be factored into the knowledge point accuracy assessments.

With these assumptions the maneuver strategies outlined above required a covariance analysis sequence with data arcs as indicated below. In each case the last sequence listed for each maneuver was for the knowledge case where the optical data was Deimos-Stars, while the others were for control accuracy and the optical data was Mars-Stars.

		Radio Data Arc	Optical Data Arc
(i)	a)	E-40 days to E-10 days	E-14 days to E-11 days
	b)	E-10 days to E-2 days	E-3 days to E-18 hours
(ii)	a)	E-40 days to E-20 days	E-24 days to E-21 days
	b)	E-20 days to E-2 days	E-3 days to E-18 hours
(iii)	a)	E-40 days to E-30 days	E-34 days to E-31 days
	b)	E-30 days to E-2 days	E-3 days to E-18 hours

TABLE 5-1

Baseline Error Model

Parameter	One-Sigma Error
Equivalent Station Location Errors	
Spin axis distance (all stns.)	1.5 m
Height off equator (all stns.)	15.0 m
Longitude (all stns.)	3.0 m
(Correlation between all longitudes = 0.9)	
Attitude Control	
Acceleration (each component)	1.2×10^{-12} km/sec^2
Solar Radiation	
Reflectivity coefficient (each component)	0.05
Planetary Ephemeris	
Earth-Moon Barycenter	20 km
Mars	30 km
Satellite Ephemeris (Deimos)	
N_A	$0°.1$
J_A	$0°.1$
K_Z	$1°.0$
K_R	$0°.0003$
I	$0°.02$
L_Z	$0°.1$
L_N	$0°.0001$
P_Z	$5°.0$
P_R	$0°.003$

TABLE 5-1

Baseline Error Model (Contd)

Parameter	One-Sigma Error
Satellite Ephemeris (Deimos) (Contd)	
a	0.1 km
e	0.001
Planetary Masses	
GM Mars	$0.3 \text{ km}^3/\text{sec}^2$
GM Earth	$0.4 \text{ km}^3/\text{sec}^2$
GM Moon	$0.02 \text{ km}^3/\text{sec}^2$
Camera Pointing Errors	
Biases (each component)	0.003 deg
Random (each component)	0.02 deg
Center-Finding Errors	
Image proportional c.f. error	
Cone direction	2% of image diameter
Cross-cone direction	1% of image diameter
Data Noise	
Radio:	
Range rate (2-way)	0.015 Hz (= 1 mm/sec)
Range (2-way)	100 nsec (= 15 m)
Optical:	
Star image location (each direction)	1.0 pixels
Satellite image location (each direction)	1.5 pixels
Mars image location (each direction)	2.0 pixels

	Radio Data Arc	Optical Data Arc
(iv) a)	E-40 days to E-30 days	E-34 days to E-31 days
b)	E-30 days to E-10 days	E-14 days to E-11 days
c)	E-10 days to E-2 days	E-3 days to E-18 hours

Keeping the initial epoch fixed at E-40 days for the radio data automatically builds in a degree of conservativeness desired for the earlier midcourse maneuvers. Note that (iv)a and (iv)c are identical to (iii)a and (i)b respectively. Thus only seven analysis sequences were required to cover all the maneuver scenarios. An additional sequence has been added to examine the sensitivity of (i)b to adding radio data upto E-18 hours instead of only E-2 days.

Figures 5-4 and 5-5 summarize the effect on OD of varying maneuver times. Figure 5-4 shows the control accuracy obtainable as a function of days before encounter for the maneuver epoch. The radio only curves are also shown for comparison. The curves clearly indicate that the maneuver should be performed as late as feasible, from the point of view of OD accuracy, particularly so as to benefit from the power of the optical data.

Figure 5-5 shows the effect on knowledge accuracy of moving the maneuver time. Also shown are the values for "optical only" OD (to be described in the following Section — Section 5.3), which are unaffected by maneuver timing. The x shows the effect of adding more radio data beyond E-2 days. It is seen that for Viking 1 there is an appreciable effect but not for Viking 2.

Figure 5-6 shows the variation in Radio plus optical accuracy for the knowledge point as a function of days from encounter. It displays
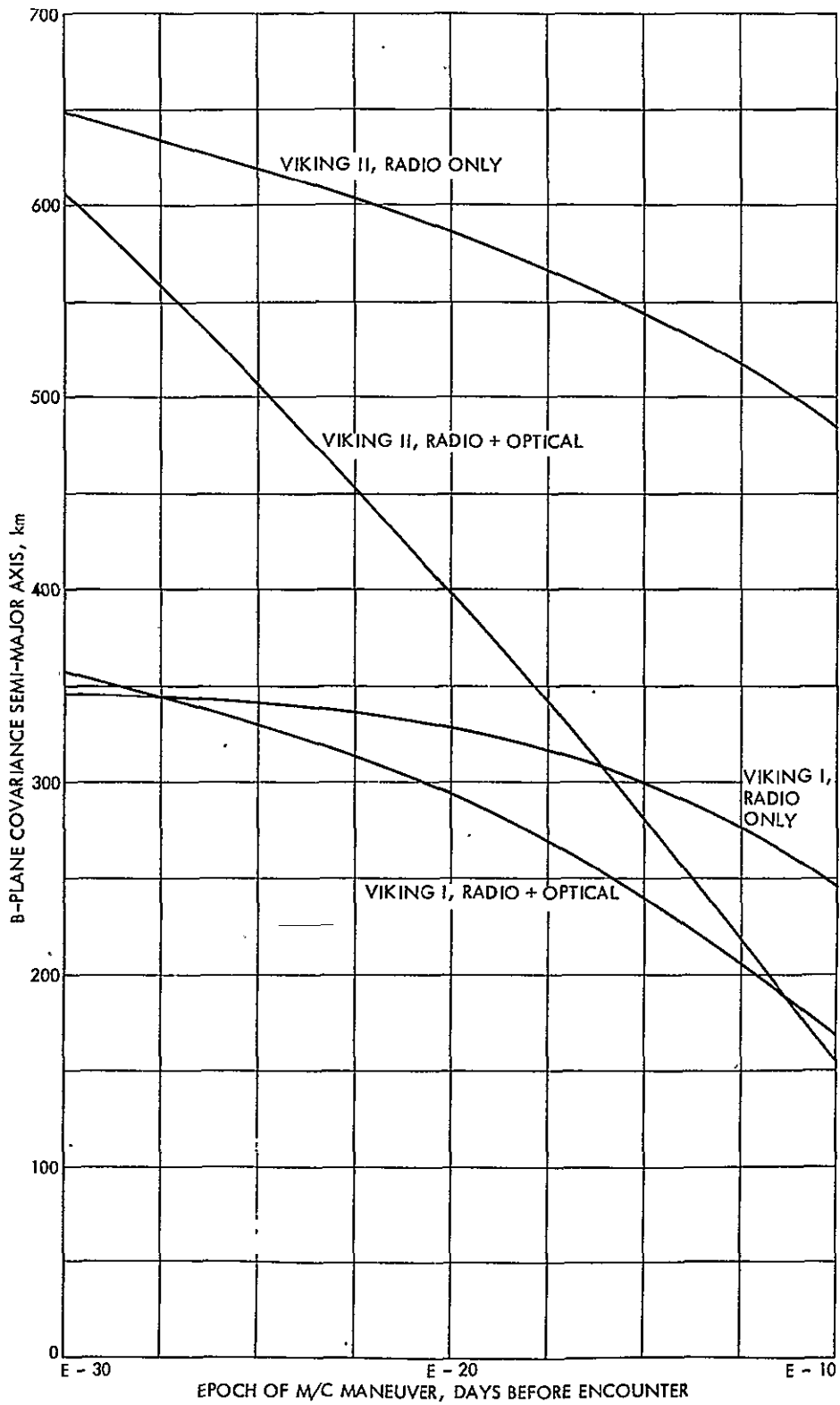
Figure 5-4. Effect of Maneuver Timing on Control
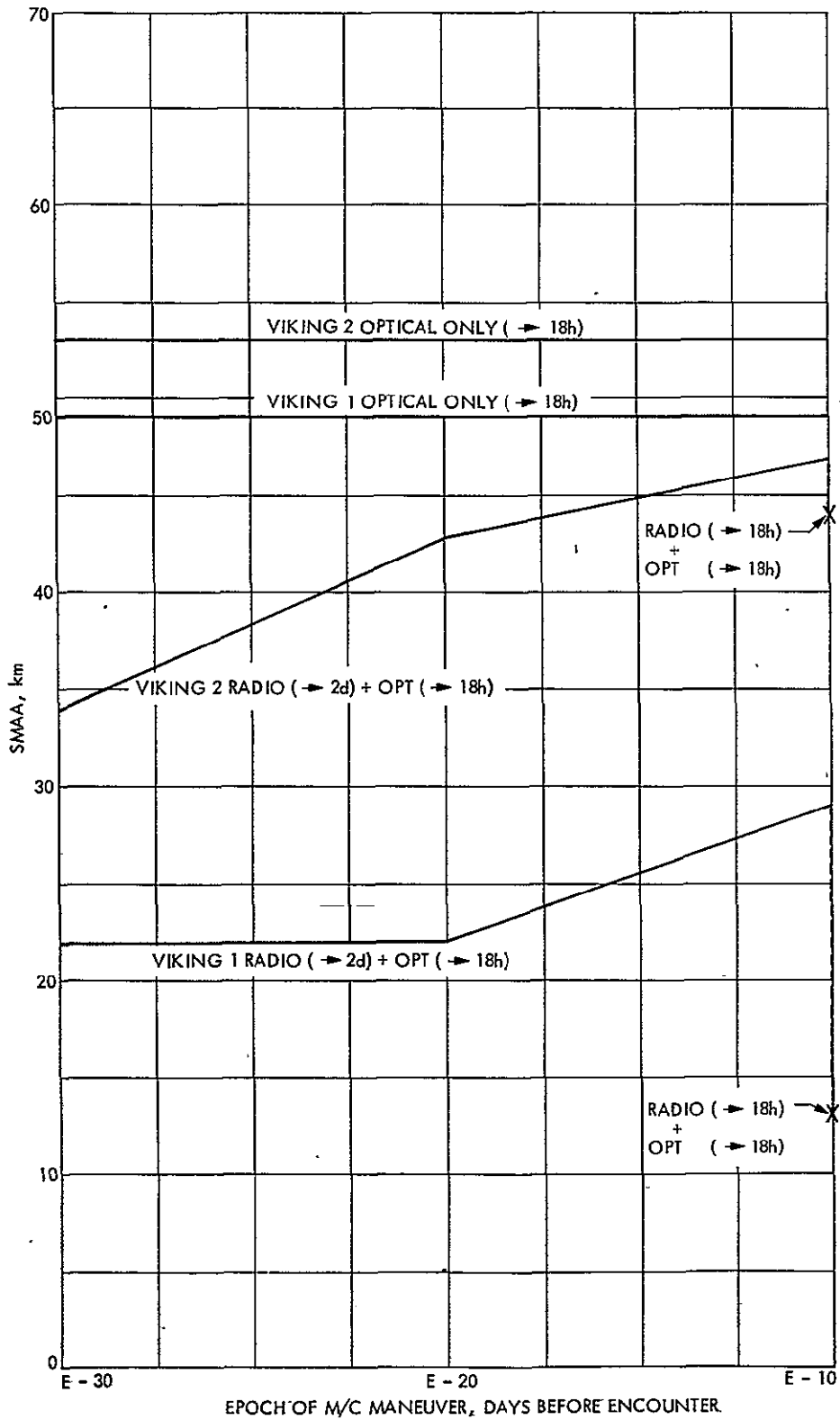Radio + Optical Accuracy

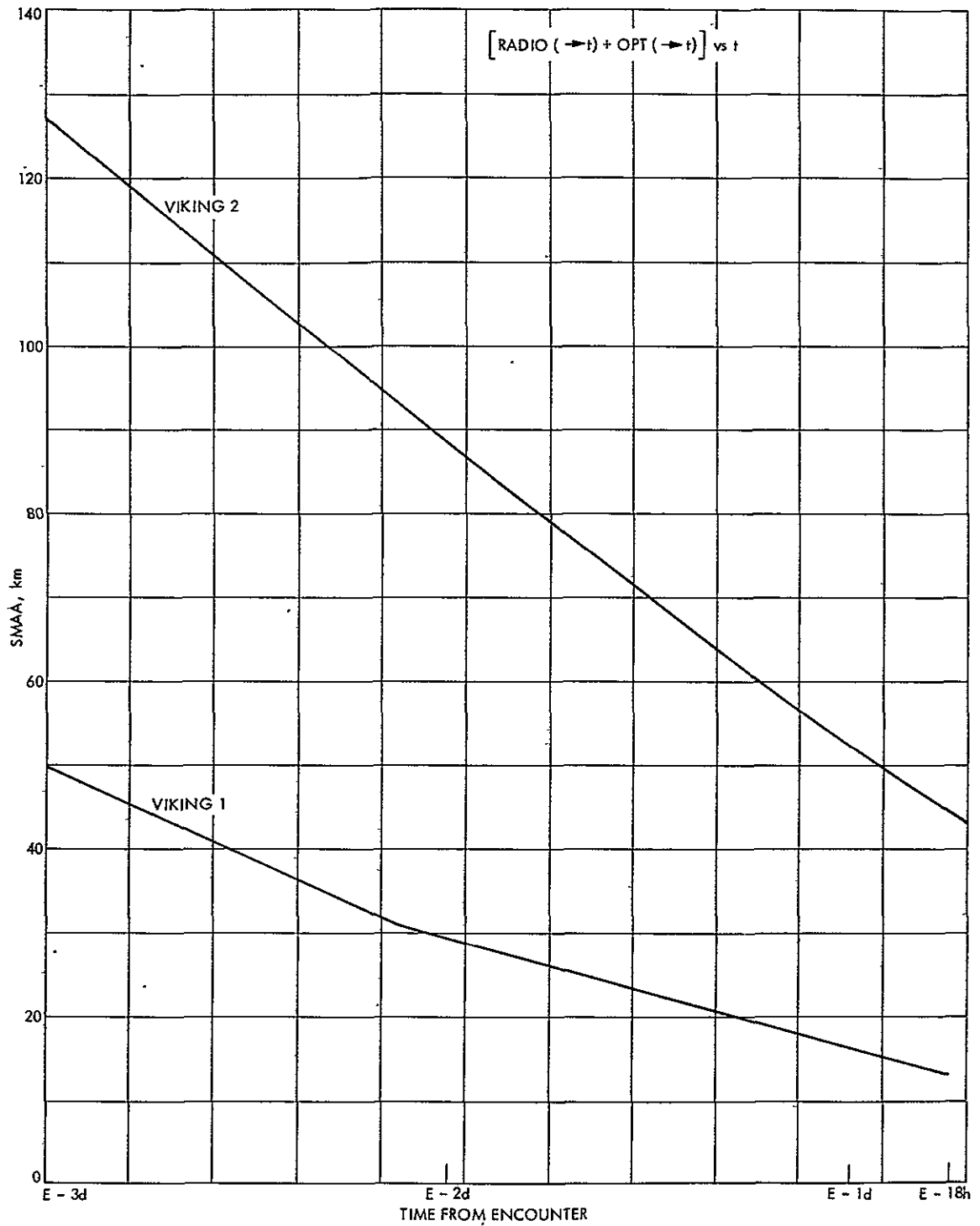Figure 5-5. Effect of Maneuver Timing on Knowledge
Radio + Optical Accuracy

Figure 5-6. Knowledge Accuracy as Function of Radio and Optical Data Taken Concurrently

the accuracy (SMAA) as a function of adding radio and optical data concurrently. In contrast, all of the following plots will show the effect of adding increasing quantities of optical data after all the radio data has been processed first.

Figures 5-7 and 5-8 give the control and knowledge results respectively, for the Viking 2 trajectory, of the strategies and solution arcs outlined above. For each case the plot shows the B-plane SMAA and SMIA. The control accuracy results are given first for the cases (iii)a, (ii)a, (i)a and (iv)b respectively; next are given the results for the knowledge case (i)b, and of the special case to study the sensitivity of (i)b to adding radio data up to E-18 hours instead of up to only E-2 days. These are followed by results for the knowledge cases (ii)b, (iii)b respectively.

In the Viking 1 E-30 day Control case the SMAA shows degradation when optical data is added. This is caused by the bias error assumed in the optical data which has an $r\delta\theta$ perturbation in the B-plane (where r is the range and $\delta\theta$ is the pointing bias), it is therefore smaller for the E-20 day and E-10 day cases where the range is smaller. This explains why the effect is not observed for those cases. In the case of Viking 2 the computed covariance, due to data noise, without adding the effect due to the sensitivity to error parameters, is much higher then for Viking 1 but the bias perturbation is at the same level as for Viking 1 (since it is governed by the range). The latter is therefore not as noticeable in Viking 2.
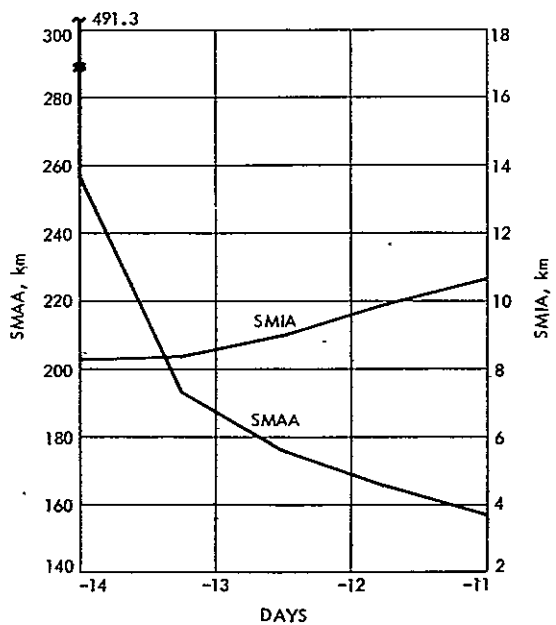
Figure 5-8 shows that for the knowledge case the accuracies undergo marked fluctuations with a period of Deimos' orbit around Mars.
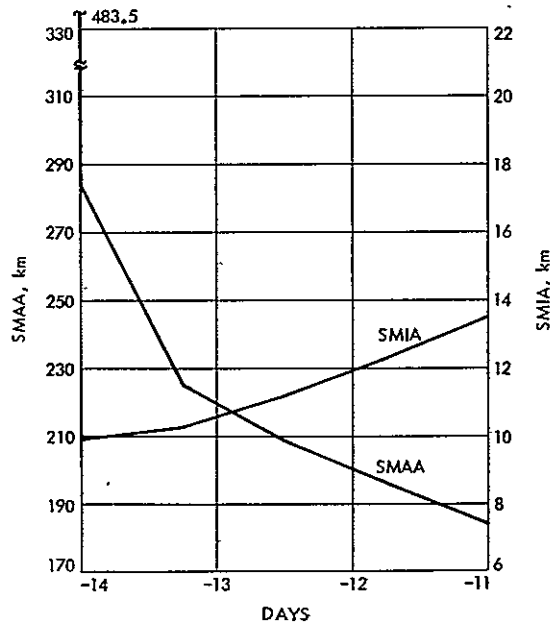
211
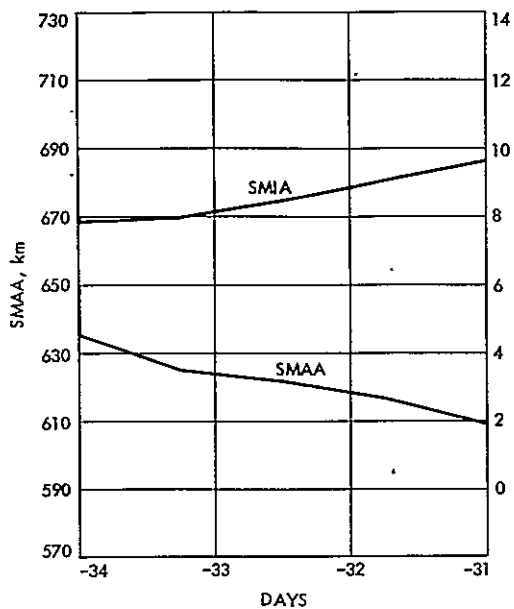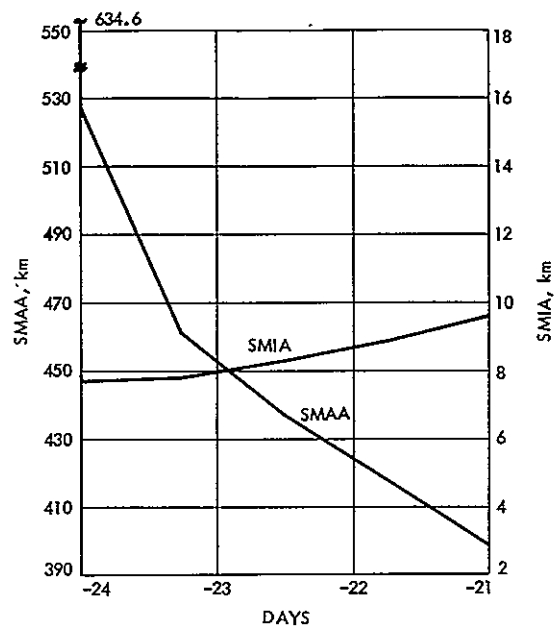
(a) E - 40 d to E - 30 d
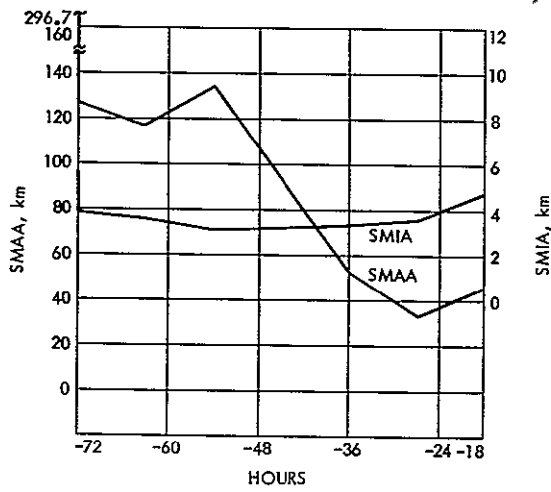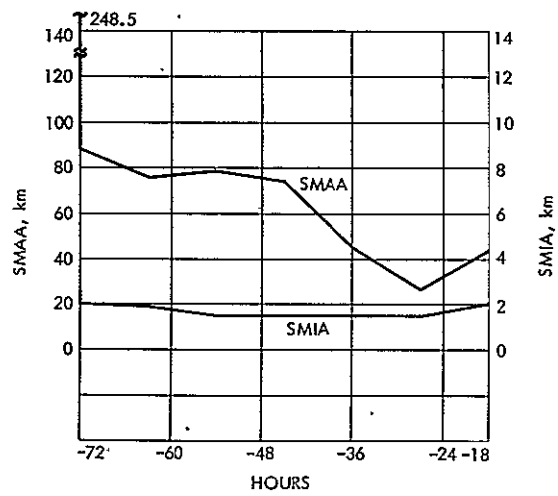
(b) E - 40 d to E - 20 d

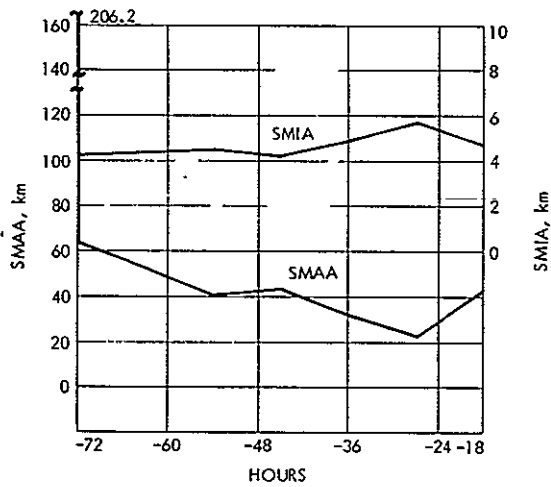(c) E - 40 d to E - 10 d

(d) E - 30 d to E - 10 d

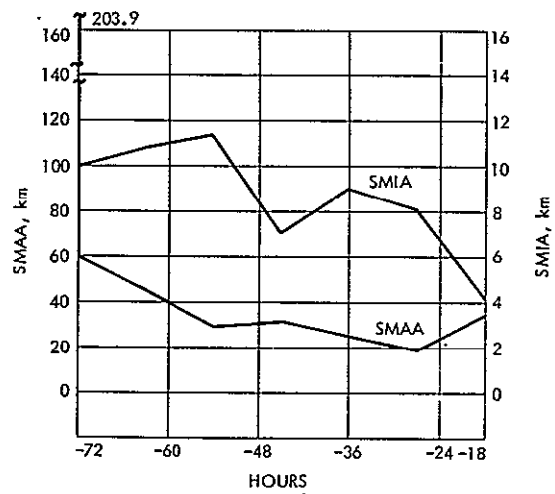Figure 5-7. Radio + Optical Control Accuracies

212

(a) E - 10 d to E - 18 h

(b) E - 10 d to E - 18 h;
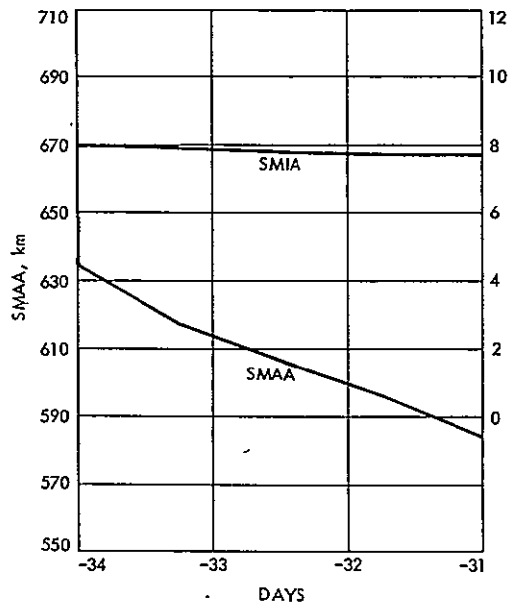Radio up to E - 18 h

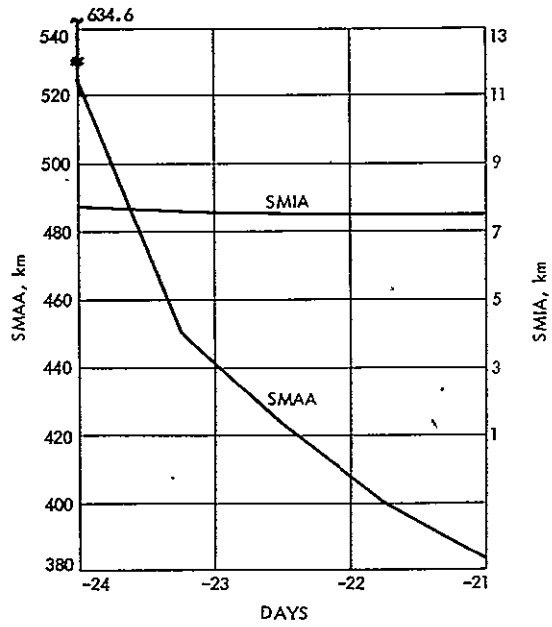(c) E - 20 d to E - 18 h

(d) E - 30 d to E - 18 h

Figure 5-8. Radio + Optical Knowledge Accuracies

The variations are due to errors in the Deimos ephemeris. The fact that the consider statistics show this behavior should not be alarming. These fluctuations would disappear if the satellite ephemeris were formally estimated. However the latter results would be too optimistic. The quotation of the consider statistics is an admission that there may be unmodelled effects in the data which would limit the ability to effectively solve for the satellite ephemeris to accuracy levels below those we are using for the analysis.

The formal results. for control and knowledge, of estimating all parameters (instead of "considering" them) along with the spacecraft state are shown in Figures 5-9 and 5-10 respectively for the Viking 2 trajectory. The results in those plots should be regarded as the most optimistic expectation of the radio plus optical OD performance.

(a) E - 40 d to E - 30 d

(b) E - 40 d to E - 20 d
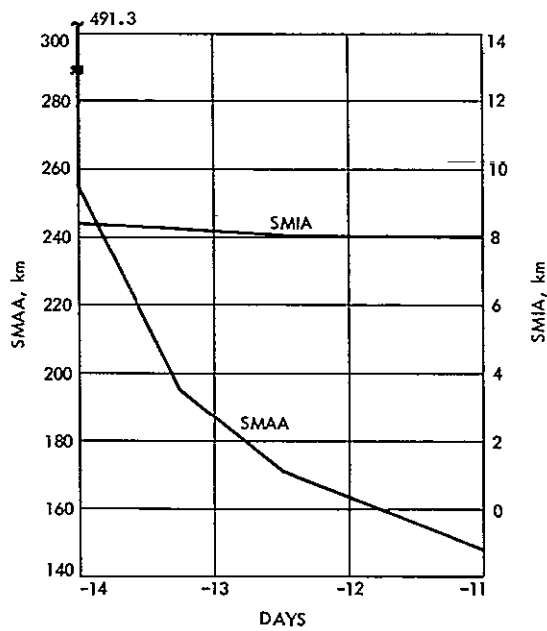
(c) E - 40 d to E - 10 d

(d) E - 30 d to E - 10 d

Figure 5-9. Radio + Optical Control Accuracies;
Solving for all Parameters

215

(a) E - 10 d to E - 18 h

(b) E - 10 d to E - 18 h;
Radio up to E - 18 h

(c) E - 20 d to E - 18 h

(d) E - 30 d to E - 18 h

Figure 5-10.   Radio + Optical Knowledge Accuracies;
Solving for all Parameters

5.3 Accuracy Analysis Using Optical Data Only

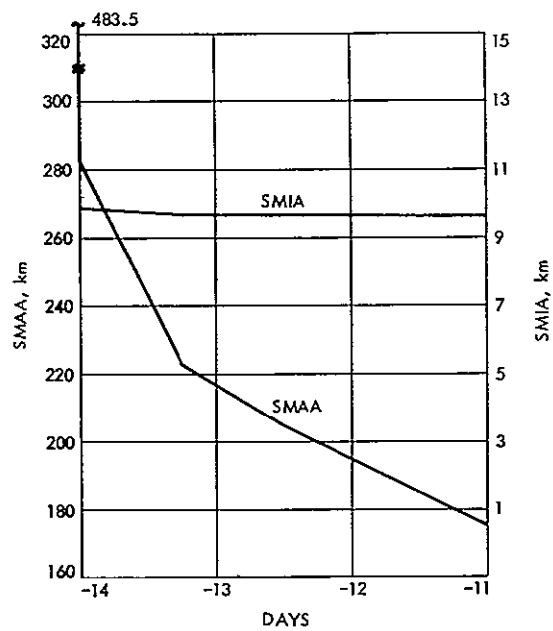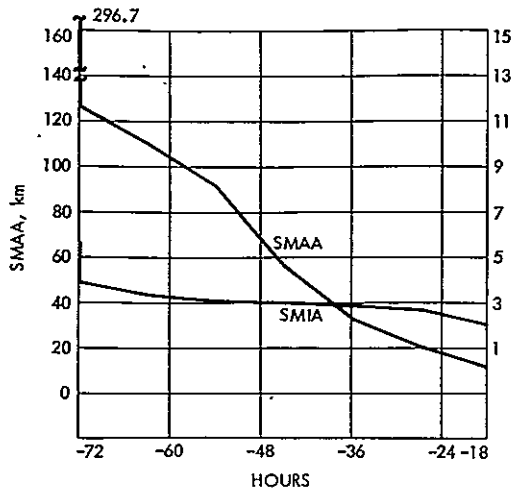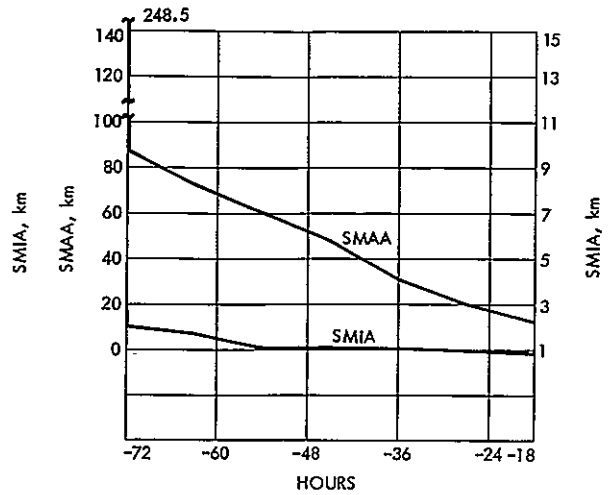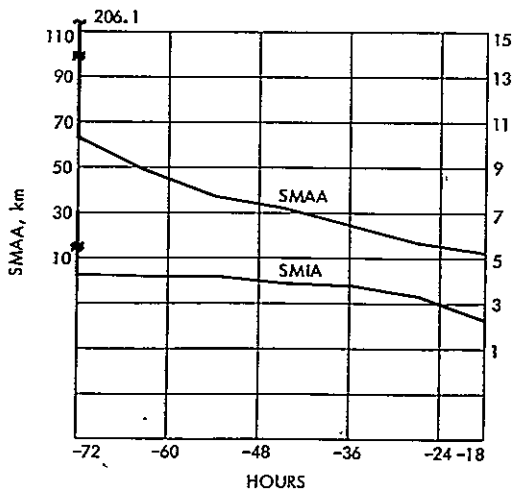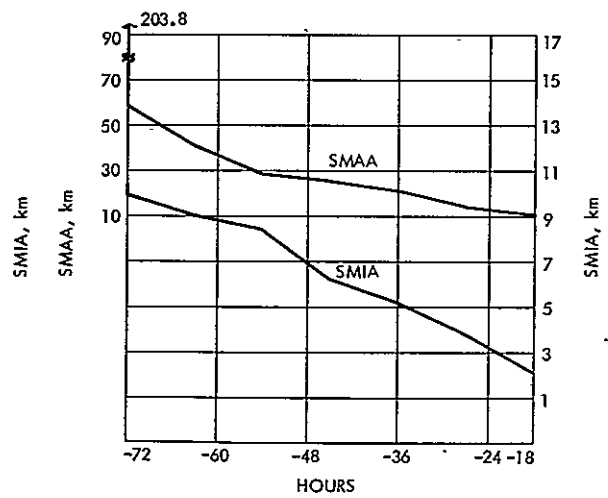In this section we describe the results of a study to evaluate the accuracy analysis obtainable using optical data only, with no radio data at all. In addition to providing significant information regarding the strengths of optical data alone, having "optical only" solutions could serve as a check for radio data; we shall discuss this consistency analysis aspect in more detail in the next section. We shall examine the accuracies obtained by various different combinations of optical data arcs.

Nominal Data Arcs

The maneuver scenarios examined and the optical data constitution assumed here are the same as outlined in section 5.2, as is also the filter configuration described there for the optical data arc. The apriori uncertainty (1 σ) for the spacecraft state was assumed at 10000 km for position and 1 m/sec for velocity in each direction; this is not as large as for the radio plus optical analysis, which was close to infinite, but is sufficiently loose to enable the navigation evaluation of optical data by itself; the figures are certainly reasonable if preceded by even a small amount of radio tracking.

The results, in terms of the B-Plane SMAA, of this analysis are shown as part of Figures 5-11 and 5-12 for the control and knowledge phases respectively. As indicated in Figure 5-11 the curves labelled 0(I), 0(II) and 0(III) give the results for each M-4 day to M-1 day optical data arc processed by itself. The corresponding curve in Figure 5-12 for the knowledge data arc is the one entitled "nominal sequence." The knowledge phase optical only accuracy is only marginally
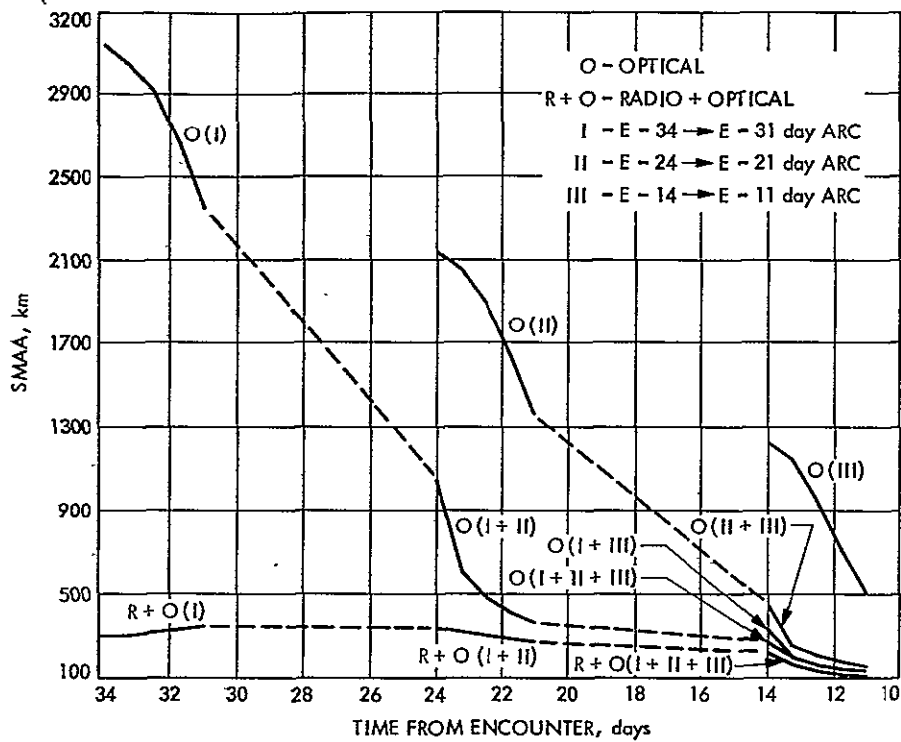
Figure 5-11. Control OD Accuracy Using Optical Data Only
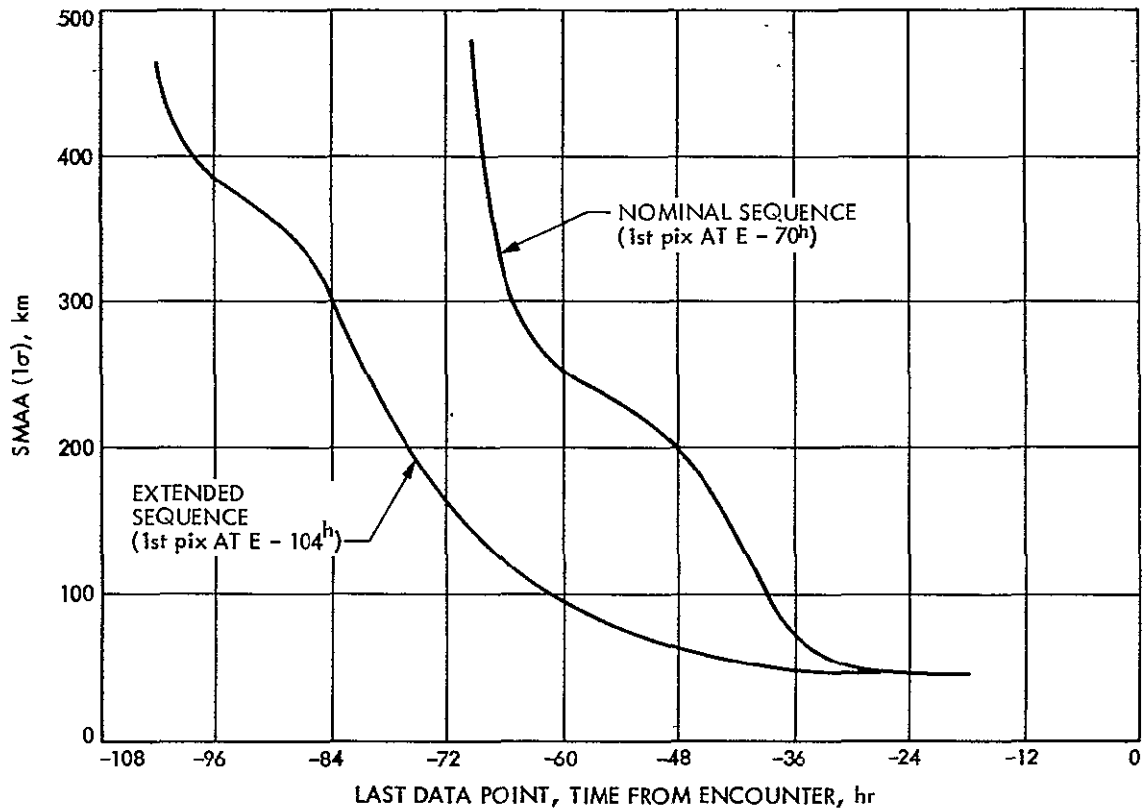
Figure 5-12. Knowledge OD Accuracy Using Optical Data Only

worse than the radio plus optical accuracy in section 5.2. The results

clearly indicate that as expected from our discussion in section 2.4,

the planet limb data is relatively weak as compared with the satellite

star data. This is despite the improved pointing accuracies from the

processing of the star images in the adjoining camera. Of course it

must be borne in mind that for the planet limb data there is also the

additional effect here due to the much larger range at which those

pictures are taken.

Extended Data Arcs for Control

Figures 5-11 and 5-12 also show the results of an additional study

made to evaluate the effect of extending the data arcs. For the con-

trol case the three data arcs, entitled (I), (II) and (III) in the fig-

ure, were processed in various combinations as follows:

(a)   I + II + III

(b)   I + III

(c)   II + III

Also shown in the figure is the effect of including all three arcs for

the radio plus optical processing, entitled R + O(I + II + III).

It is immediately apparent from the curves in Figure 5-11 that:

(i)   the accuracies of processing the single data arcs improve

dramatically for O(I), O(II), O(III) respectively — i.e. a

considerable improvement in navigation performance would be

obtained by delaying the maneuver epoch as much as possible.

(ii)   the accuracies at any maneuver epoch would improve con-

siderably with the addition of some more pictures earlier

thus extending the total span of the data arc — e.g. comparing O(III) and O (II + III) or O(II) and O(I + II).

(iii) the effect above increases monotonically with the length of the total span but the improvement obtained is marginal after a point (comparing for instance O(II + III) and O(I + III)).

(iv) given a total data span determined by the first and last pictures, the presence of additional data within the span does not contribute at all (in terms of accuracy at the final point), as evidenced by a comparison of curves O(I + III) and O(I + II + III).

(v) the radio plus optical accuracy improves considerably from the 167 km SMAA of the nominal R + O(III) processing (Figure 5-7c) to 100 km using the entire optical span here.

(vi) the radio plus optical accuracy is only slightly better than the optical only accuracy at E-10 days, given a long enough span of optical data; this is clear from curves O(I + III) and R + O(I + II + III).

The indication from these observations is that although as expected from the discussion in Section 2.4 we do need velocity information, this is available by taking a long span of data — i.e. it is not always essential to obtain velocity information from radio data. Moreover the strategy for the data acquisition should be to take a long span of data for the velocity information and to take the last few pictures as late as possible before the control maneuver epoch for accurate position information.

221

Extended Data Arc for Knowledge

Examining the effect of extending the data arc for the knowledge case we observe from Fig. 5-12 that

(i)   the final accuracy obtained is the same for the extended E-104 hours to E-18 hour arc as it is for the shorter E-70 hour to E-18 hour arc.

(ii)   this limiting accuracy is obtained much earlier in the case of the extended arc; this consideration could often be quite important for estimate reliability considerations in the decision for the final orbit insertion maneuver.

Satellite star pictures would not normally be available much before the extended arc in Fig. 5-12 begins. However the planet-star two camera data could be taken before that during the knowledge phase. A study made to examine the effect of this on the knowledge point accuracy yielded results similar in character to the change from the shorter to the extended arc of only satellite-star pictures of Figure 5-12 — i.e. limiting accuracies were the same but were achieved earlier in time.

5.4 Radio and Optical Consistency Analysis

A primary concern for any application of estimation theory is that of validating the data — that is, ensuring that the data coming from the real world is consistent with the models assumed. We show in this section how optical data, in addition to its use with radio data in improving navigation accuracy, can contribute in the alleviation of this concern by corroborating the validity of the radio data. This would thus yield enhanced performance for the total navigation system. The method described also serves to establish consistency between the radio and the optical data.

As discussed in Chapter Two the optical and radio data are complementary in their information content and their major error sources are different. The "best-estimate" of the spacecraft trajectory would therefore normally be a radio plus optical solution. However before the selection of the best estimate is made the optical only and radio only solutions should be checked for consistency. This is necessary so as to obtain confidence that there are no significant unexplained anomalies remaining and to establish overall consistency between the radio and optical data sets. If by this time consistency has not been established within the radio only and optical only solution sets respectively, the optical data solutions can also aid in the detection of inconsistencies within the radio data solutions, as discussed below.

In the following we first give a general procedure for conducting a consistency analysis between any two different estimates of the same physical quantity, evaluated in terms of a defined figure of merit. Then we develop an analysis for obtaining the covariance of the estimate

difference, required to compute the figure of merit, when the two estimates are obtained using any two different data types, or their combination. This is followed by a discussion of the use of the set of figures of merit to give indications of possible problem areas when the two observation sets consist of radio and optical data, and the discrepancy resolution philosophy, if an inconsistency were suspected. Finally we give a particular application of this, using simulated radio and optical data, which demonstrates the effectiveness of the process.

Consistency Analysis Process

The following procedure should be conducted for each pair of solutions to be examined for consistency:

1) Form the vector difference between the two estimates of the system state vector $\underline{x}$,

$$\Delta\underline{\hat{x}} = \underline{\hat{x}}_1 - \underline{\hat{x}}_2 \tag{5-4-1}$$

2) Calculate the covariance of this difference, Λ. In general this will be a function of the physical model assumed for the system and the particular filter or filters used to obtain the estimates $\underline{\hat{x}}_1$ and $\underline{\hat{x}}_2$.

3) Calculate a figure of de-merit, f, defined by

$$f \triangleq \left[\Delta\underline{\hat{x}}^T \ \Lambda^{-1} \ \Delta\underline{\hat{x}} \right]^{1/2} \tag{5-4-2}$$

The value of this figure of de-merit indicates the extent of the discrepancy between the pair of estimates $\underline{\hat{x}}_1$ and $\underline{\hat{x}}_2$; it is, qualitatively, an indication of the difference between the estimates, normalized with respect to the uncertainty, and with all the dimensions collapsed into one scalar measure.

Discrepancy Statistics for Different Observation Types

We now develop the covariance Λ to be used in Eq. (5-4-2) for the case when the solutions $\hat{x}_1$, $\hat{x}_2$ arise from the use of two different data types. As in section 3.6, let the observation vector z depend on the estimated spacecraft state vector x and the unestimated "consider" parameter vector y through the equation

$$z = Ax + By + n \tag{5-4-3}$$

where

$$E(n) = 0 \quad ,$$

$$E[n(t_i)\, n(t_j)] = R\delta_{ij}$$

and where we have made the notational replacement of A and B for G and H respectively, to conform with conventional batch least squares filter notation.

Given any two data types, denoted here by (r) and (o), the vector y can in general be

$$y \triangleq \begin{Bmatrix} y_r \\ y_o \\ y_b \end{Bmatrix} \tag{5-4-4}$$

where y_r, y_o and y_b are respectively comprised of parameters to which (i) only data type (r), (ii) only data type (o) and (iii) both data types, are sensitive. The corresponding matrix B can then be written

$$B \triangleq [B_r \vdots B_o \vdots B_b] \tag{5-4-5}$$

Let the observations be similarly grouped with subscripts 1, 2, 3 respectively; the corresponding equations will then be

$$z_1 = A_1 x + B_1 y + n_1 \tag{5-4-6}$$

225

$$z_2 = A_2 x + B_2 y + n_2 \qquad\qquad (5\text{-}4\text{-}7)$$

$$z_3 = A_3 x + B_3 y + n_3 \qquad\qquad (5\text{-}4\text{-}8)$$

with

$$E[n_i(t_j)n_i(t_k)] = R_i \delta_{jk} \quad , \quad i = 1, 2, 3 \qquad\qquad (5\text{-}4\text{-}9)$$

$$B_1 \triangleq [B_{r1}|B_{o1}|B_{b1}] = [B_{r1}|0|B_{b1}] \qquad\qquad (5\text{-}4\text{-}10)$$

$$B_2 \triangleq [B_{r2}|B_{o2}|B_{b2}] = [0|B_{o2}|B_{b2}] \qquad\qquad (5\text{-}4\text{-}11)$$

the zero matrices arising because of the definition of z_1, B_o and of z_2, B_r. Since subscript 3 denotes both data equations together, we will have

$$z_3 = \begin{Bmatrix} z_1 \\ z_2 \end{Bmatrix} \quad , \quad n_3 = \begin{Bmatrix} n_1 \\ n_2 \end{Bmatrix} \quad , \qquad\qquad (5\text{-}4\text{-}12)$$

$$A_3 = \begin{bmatrix} A_1 \\ A_2 \end{bmatrix} \quad \text{and} \quad B_3 = \begin{bmatrix} B_1 \\ B_2 \end{bmatrix} \qquad\qquad (5\text{-}4\text{-}13)$$

and, since n_1, n_2 are independent white noise,

$$R_3 = \begin{bmatrix} R_1 & 0 \\ 0 & R_2 \end{bmatrix} \qquad\qquad (5\text{-}4\text{-}14)$$

The least squares estimate, $\hat{x}$, with x estimated and y considered from equation (5-4-3) and assuming no apriori on x is

$$\hat{x} = \left[A^T R^{-1} A \right]^{-1} A^T R^{-1} z .$$

$$= X A^T R^{-1} z \qquad\qquad (5\text{-}4\text{-}15)$$

where X is the "computed" covariance of $\hat{x}$,

$$X \triangleq E\left\{[\hat{x} - x|y = 0]\ [\hat{x} - x|y = 0]^T\right\}$$

$$= \left[A^T\ R^{-1}\ A\right]^{-1} \tag{5-4-16}$$

Substituting z from Eq. (5-4-3) into Eq. (5-4-15) we obtain

$$\hat{x} - x = S_{xy}\ y + XA^T\ R^{-1}\ n \tag{5-4-17}$$

where S_{xy} is the sensitivity of $\hat{x}$ to errors in y, given by

$$S_{xy} = XA^T\ R^{-1}\ B \tag{5-4-18}$$

Using Eqs. (5-4-16) to (5-4-18) we can obtain the expressions

$$P_x \triangleq E[(\hat{x} - x)\ (\hat{x} - x)^T]$$

$$= S_{xy}\ P_y\ S_{xy}^T + X \tag{5-4-19}$$

$$P_{xy} \triangleq E[(\hat{x} - x)\ y^T]$$

$$= S_{xy}\ P_y \tag{5-4-20}$$

or

$$S_{xy} = P_{xy} \cdot P_y^{-1} \tag{5-4-21}$$

where

$$P \triangleq \begin{bmatrix} P_x & P_{xy} \\ P_{xy}^T & P_y \end{bmatrix}$$

Since y is not estimated P_y is constant, given by

$$P_y \equiv P_y(t_o) \tag{5-4-22}$$

227

For each data set z_i and matrices A_i, B_i, R_i the equations above will hold yielding the corresponding estimate $\hat{x}_i$ with the estimated covariance X_i, consider covariance

$$P_i = \begin{bmatrix} P_{x_i} & P_{x_i y} \\ P_{yx_i} & P_y \end{bmatrix} \quad .$$

and sensitivity $S_{x_i y}$ which will consist of

$$S_{x_i y_o} = \begin{bmatrix} S_{x_i y_r} & S_{x_i y_o} & S_{x_i y_b} \end{bmatrix} \tag{5-4-23}$$

We note, using Eq. (5-4-10) and (5-4-11), that

$$S_{x_1 y_o} \equiv 0$$

$$\tag{5-4-24}$$

$$S_{x_2 y_r} \equiv 0$$

The quantity that we need to evaluate relative consistency between any two estimates $\hat{x}_i$, $\hat{x}_j$ is the covariance of their difference, Λ, given by

$$\Lambda_{ij} = E[(\hat{x}_i - \hat{x}_j)(\hat{x}_i - \hat{x}_j)^T]$$

$$= E\left[\left\{(\hat{x}_i - x) - (\hat{x}_j - x)\right\}\left\{(\hat{x}_i - x) - (\hat{x}_j - x)\right\}^T\right]$$

$$= P_{x_i} - P_{x_i x_j} - P_{x_j x_i} + P_{x_j} \tag{5-4-25}$$

where $P_{x_i x_j}$ is the cross variance between the estimates $\hat{x}_i$ and $\hat{x}_j$,

$$P_{x_i x_j} \triangleq E\left[(\hat{x}_i - x)(\hat{x}_j - x)^T\right]$$

$$= \left(P_{x_j x_i}\right)^T \tag{5-4-26}$$

228

which, using Eq. (5-4-17), gives

$$P_{x_i x_j} = E\left[\left(S_{x_i y} y + X_i A_i^T R_i^{-1} n_i\right)\left(S_{x_j y} y + X_j A_j^T R_j^{-1} n_j\right)^T\right]$$

$$= S_{x_i y} P_y S_{x_j y}^T + X_i A_i^T R_i^{-1} E\left(n_i n_j^T\right) R_j^{-1} A_j X_j$$

$$(5-4-27)$$

Since n_i are white noise,

$$E\left(n_1 n_2^T\right) = 0 \qquad\qquad (5-4-28)$$

and

$$E\left(n_i n_3^T\right) = E\left[n_i\left(n_1^T \;\vdots\; n_2^T\right)\right]$$

$$= \left[R_i \delta_{i1} \;\vdots\; R_i \delta_{i2}\right]$$

$$= R_i \left[\delta_{i1} \;\vdots\; \delta_{i2}\right] \qquad , \qquad i = 1, 2 \qquad (5-4-29)$$

Therefore the second term of Eq. (5-4-27) is zero for ($i \neq 3$, $j \neq 3$);

for $j = 3$ it is given by

$$[2\text{nd Term}\,|\,j = 3] = X_i A_i^T R_i^{-1} R_i \left[\delta_{i1} \;\vdots\; \delta_{i2}\right]\begin{bmatrix} R_1^{-1} & 0 \\ 0 & R_2^{-1} \end{bmatrix}\begin{bmatrix} A_1 \\ A_2 \end{bmatrix} X_3$$

$$= X_i A_i^T \left(R_1^{-1} A_1^T \delta_{i1} + R_2^{-1} A_2^T \delta_{i2}\right) X_3$$

$$= X_3 \qquad , \qquad i = 1, 2 \qquad (5-4-30)$$

Therefore Eq. (5-4-27) with (5-4-20) yields

$$P_{x_1 x_2} = S_{x_1 y} P_y S_{x_2 y}^T$$

$$= P_{x_1 y} P_y^{-1} P_{x_2 y}^T \qquad\qquad (5-4-31)$$

229

and

$$P_{x_i x_3} = S_{x_i y} P_y S_{x_3 y}^T + X_3$$

$$= P_{x_i y} P_y^{-1} P_{x_3 y}^T + X_3 \quad , \quad i = 1, 2 \quad (5\text{-}4\text{-}32)$$

where X_3 is given by

$$X_3 = \left(X_1^{-1} + X_2^{-1} \right)^{-1} \quad (5\text{-}4\text{-}33)$$

Substituting these expressions into Eq. (5-4-25) yields Λ_{ij}; thus

$$\Lambda_{12} = P_{x_1} - P_{x_1 y} P_y^{-1} P_{x_2 y}^T - P_{x_2 y} P_y^{-1} P_{x_1 y}^T + P_{x_2} \quad (5\text{-}4\text{-}33)$$

and

$$\Lambda_{i3} = P_{x_i} - P_{x_i y} P_y^{-1} P_{x_3 y}^T - 2X_3 - P_{x_3 y} P_y^{-1} P_{x_i y}^T + P_{x_3}$$

$$(5\text{-}4\text{-}34)$$

In particular, for Λ_{12}, using Eqs. (5-4-23) and (5-4-24) in

Eq. (5-4-31) and assuming a block diagonal form for P_y,

$$P_{x_1 x_2} = \begin{bmatrix} S_{x_1 y_r} & 0 & S_{x_1 y_b} \end{bmatrix} \begin{bmatrix} P_{y_r} & 0 & 0 \\ 0 & P_{y_o} & 0 \\ 0 & 0 & P_{y_b} \end{bmatrix} \begin{bmatrix} 0 \\ S_{x_1 y_o} \\ S_{x_1 y_b} \end{bmatrix}$$

$$= S_{x_1 y_b} P_{y_b} S_{x_2 y_b}^T \quad (5\text{-}4\text{-}35)$$

which reduces to zero if y_b is a null vector, i.e. if the error sources

for the two data types are completely disjoint. In this case Λ_{12}

reduces to

$$\Lambda_{12} = P_{x_1} + P_{x_2} \quad , \quad (y_b = 0) \quad (5\text{-}4\text{-}36)$$

The consistency analysis process described above should be conducted to examine consistency of the optical only solution with each of the following radio solutions;

    (i)   doppler only

    (ii) range only

    (iii) doppler plus range.

The difference between the optical estimate $\hat{\underline{x}}_o$ and each of the radio estimates $\hat{\underline{x}}_j$, j = (i), (ii), (iii), should be formed as in Eq. 5-4-1. Since the dominant error sources affecting the radio and optical data are quite different, the covariance of this difference, Λ_j is given from Eq. 5-4-36 by

$$\Lambda_j = \Lambda_o + \Lambda_{r_j}$$

where Λ_o is the covariance of the reference optical solution $\hat{\underline{x}}_o$ and Λ_{r_j} are the covariances corresponding to the different radio solutions $\hat{\underline{x}}_j$ described above. The figures of de-merit f_j are then computed according to Eq. (5-4-2). The magnitude of these will indicate the extent of the discrepancy between the optical solution and the different radio solutions; this could be interpreted to be an indication of consistency for small values of f_i, or inconsistency for large values of f_i.

Eight ($=2^3$) different situations are possible from the results of these three cases, if the solutions are regarded as being either consistent or not consistent with the reference optical solution. These are tabulated in Table 5-2, where a check ($\sqrt{}$) or a cross (X) implies consistency or inconsistency, respectively.

TABLE 5-2

Consistency Analysis

Situation No.	Opt. vs Dopp.	Opt. vs Range	Opt. vs (Dopp + Rng)
1	X	X	X
2	X	X	√
3	X	√	X
4	X	√	√
5	√	X	X
6	√	X	√
7	√	√	X
8	√	√	√
Note: √ implies consistency X implies inconsistency			

The probable interpretations of the different situations are, respectively:

1) Either (a) anomaly in optical data or (b) anomaly (or anomalies) affecting both doppler and range,

2) Anomalies in both doppler and range, having effects of comparable magnitude but opposite direction,

3) Anomaly in doppler with possible range effect,

4) Anomaly in doppler,

5) Anomaly in range with possible doppler effect,

6) Anomaly in range,

7) Combination strategy for doppler and range suspect, or

8) No anomalies — the desired goal.

As is evident, the doppler plus range case (case iii) is useful primarily in providing supporting information for knowledge acquired from cases (i) and (ii). However, in addition to answering whether or not an inconsistency may exist between radio and optical data, the values of the figures of de-merit for all three cases can give indications of possible problem areas. These values would therefore be of significant assistance in analysis.

The process for the resolution of a discrepancy would necessarily be an adaptive one. The following factors should be examined:

1) Solutions obtained by deleting the suspect data type and combining the rest,

2) Solutions obtained by solving for the parameters pertaining to the dominant error sources of the suspect data type,

233

3) History of the suspect solutions to see if it shows

convergent or divergent behavior,

4) Comparison of residuals of each data type against trajectories

based on the other data types so as to detect any structure

within the residuals.

Application to Simulated Data

We now present an example for the application of the analysis

techniques described above, using simulated radio and optical data;

this example illustrates the efficacy of the consistency analysis

techniques in tracking down problems.

The first four items in Table 5-3 list the B-plane estimates and

covariances of representative solutions obtained using

1) optical data only

2) doppler data only

3) range data only

4) doppler plus range data.

The corresponding solutions are shown graphically in Figure 5-13. In

all the radio data solutions only the spacecraft state was solved for.

The optical data solution was obtained solving for both state and

satellite ephemeris. The effect of satellite ephemeris error is

generally apparent from the optical data residuals (see for instance

Fig. 4-6b of Chapter 4) therefore this strategy is reasonable.

The figures of de-merit for cases (2), (3), and (4) were computed

using the optical only solution, (1), as the reference for comparison.

These are listed in the last column in Table 5-3. It is immediately

apparent that there exists

234

TABLE 5-3

Application Example: Radio-Optical Consistency Analysis

| Solution Set		Estimate, $\underline{x}_i$		Covariance, Λ_i		Figure of De-Merit, f_i
No.	Description	$\overline{B} \cdot \overline{R}$	$\overline{B} \cdot \overline{T}$			
1	Optical only	6432	6779	$\begin{bmatrix} 191 & 62 \\ 62 & 264 \end{bmatrix}$		---
2	Doppler only	6583	7901	$\begin{bmatrix} 45690 & -70397 \\ -70397 & 163423 \end{bmatrix}$		5.77
3	Range only	6221	7751	$\begin{bmatrix} 27242 & 10974 \\ 10974 & 4577 \end{bmatrix}$		52.77
4	Doppler + Range	6537	7921	$\begin{bmatrix} 9548 & 3843 \\ 3843 & 1584 \end{bmatrix}$		65.48
5	Range only (after range fix)	6600	6829	$\begin{bmatrix} 26235 & 10544 \\ 10544 & 4388 \end{bmatrix}$		1.36
6	Doppler + Range (after range fix)	6877	6975	$\begin{bmatrix} 9652 & 3873 \\ 3873 & 1691 \end{bmatrix}$		4.61
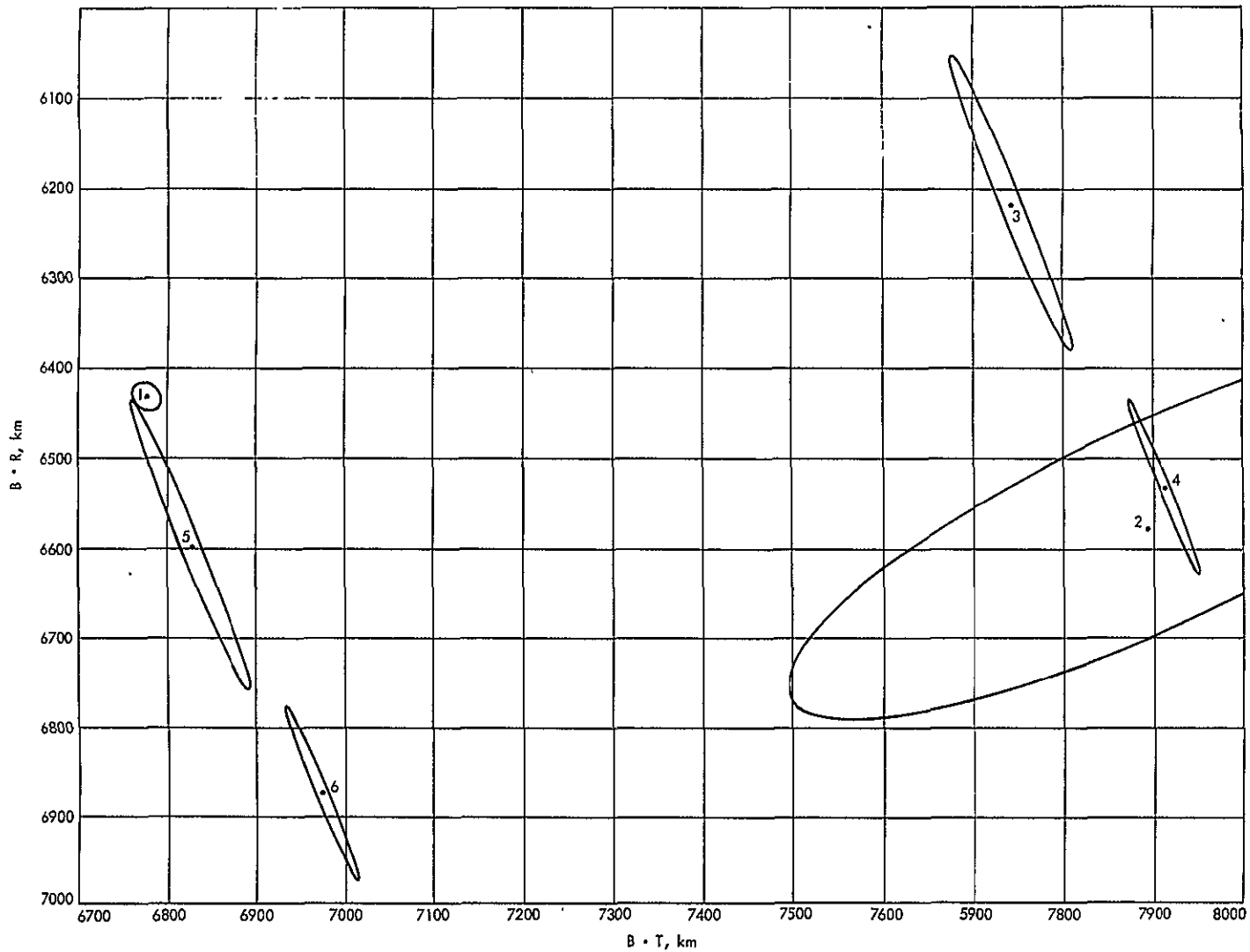
Figure 5-13. Radio and Optical B-Plane Solutions

(i) an unacceptable inconsistency of the optical data solution

with the doppler data solution, and

(ii) a gross inconsistency of the optical only solution with both

the range only and the doppler plus range solutions.

The indication from this is that there is an inconsistency between

doppler data and range data, probably due to some gross problem with

the latter; in addition there may be another anomaly affecting the

radio data (both doppler and range) or the optical data.

The mathematical representation of the range observable ρ is

(Ref. 27)

$$\rho = (\Delta t)_{LT} \ F, \ \text{modulo} \ M$$

where

$(\Delta t)_{LT}$ = round-trip time of the signal in seconds of station time

F = conversion factor from seconds of station time to the

units of the range observable

M = modulo number. The largest integer multiple of M which

is less than $(\Delta t)_{LT}$ F is removed from this quantity,

leaving the observable ρ, which is less than M. This

operation on a number n is referred to as "modding"

n by M.

The problem with the data in the example was that the range was

"out of mod" due to a large error in the apriori trajectory used; this

caused solutions containing range to have the statistically large dis-

crepancy with solutions using doppler and optical data. Reintegrating

a trajectory from an optical plus doppler solution and refitting the

range data brought the range back within the correct "mod".

The range only and doppler plus range solutions, using the reintegrated trajectory, are cases (5) and (6) respectively, in Table 5-3 and in Figure 5-13. The figures of de-merit, f, for these and for the doppler only solution (case 2) show that there still exists an inconsistency at an unacceptable level between the optical and the radio data solutions. Since the values of f are quite different for doppler and range the indication is that there may be an error in the radio data which affects doppler data more than the range data — e.g., station location errors. This indication was then confirmed when the station location errors were subsequently solved for.

5.5 Navigation System Fuel Costs Analysis

In this section we develop a reliability analysis of the combined radio plus optical navigation system from the standpoint of fuel costs. This consists of a parametric probability analysis to study navigation performance sensitivity of the overall radio + optical system to optical subsystem reliabilities. The result of this is a method which can be an aid in identifying possible promising areas for enhancing overall radio and optical orbit determination reliability.

The criterion for the measurement of navigation performance here is chosen to be the amount of propulsion fuel savings achieved. The fuel is measured in units of the absolute value of incremental velocity, ΔV, that can be imparted to the spacecraft. This is normally a major concern for a mission since the spacecraft has limited fuel capacity and therefore limited capability to make velocity changes. For an ideal mission which goes perfectly according to plan with no errors, there would be a certain nominal amount of ΔV needed for required propulsive maneuvers. The difference between the nominal and the actual ΔV required in the mission in the presence of statistical dispersions is termed ΔV_{STAT}. There is a total budget provided for these statistical variations. The total expenditure of fuel in excess of the nominal must stay within the budget, and is a measure of navigation performance for a given phase of the mission; ΔV_{STAT} is therefore a measure of the predicted navigation performance.

The relative likelihood of failure of any one television camera, or of both cameras, can be assessed as a function of spacecraft component reliabilities. Failure of one camera would eliminate the use of

239

the planet-star two-camera data type required at the control point; failure of both cameras would eliminate optical navigation entirely. The lack of a suitable star background could also eliminate optical navigation at the control point, as was discussed in section 5.1.

There are therefore four possible optical navigation (ON) system operating modes as follows: optical navigation

      (i)   operative at both the control and the knowledge point,

     (ii)   inoperative — i.e. radio-only at both control and knowledge,

   (iii)   operative only at knowledge — i.e. only radio available at control; this can occur (a) if only one camera is operational or (b) due to an inadequate star background; and

    (iv)   operative only at control.

Let "C" and "K" refer to, respectively, the events of having optical data at control and knowledge; then denote the probability of the four cases by, respectively, $P(C, K)$, $P(\sim C, \sim K)$, $P(\sim C, K)$ and $P(C, \sim K)$ where "$\sim$" means "no optical data at;" we then have

$$P(C, K) + P(\sim C, \sim K) + P(\sim C, K) + P(C, \sim K) = 1 \qquad (5\text{-}5\text{-}1)$$

However,

$$P(C, \sim K) \approx 0 \qquad\qquad (5\text{-}5\text{-}2)$$

because this could occur only in the extremely unlikely event that in the interval between control and knowledge, both cameras fail. This leaves only three optical navigation operating modes and we therefore have

$$P(C, K) + P(\sim C, \sim K) + P(\sim C, K) = 0 \qquad (5\text{-}5\text{-}3)$$

The total probability density of ΔV_{STAT} can be expressed as

$$f(\Delta V) = f(\Delta V/C, K) \, P(C, K) + f(\Delta V/\sim C, K) \, P(\sim C, K)$$
$$+ f(\Delta V/\sim C, \sim K) \, P(\sim C, \sim K) \qquad (5-5-4)$$

Based on control and knowledge radio only and radio plus optical
covariances, a Monte Carlo maneuver analysis gives ΔV_{STAT} histograms
for each of the three ON operating modes; these correspond to the three
conditional probability densities in Eq. (5-5-4).

Since the three probabilities in Eq. (5-5-4) are related by
Eq. (5-5-3), there are only two independent parameters on which the
distribution of ΔV_{STAT} depends. The two parameters chosen for analysis
here are P(OPT) and P(C/OPT), i.e., the probability of having any
optical data, and the probability of having optical at control given
that one has optical at all. The first parameter, which implies the
existence of any optical data at all, is rather an obvious choice,
since we are interested in determining the efficacy of the optical
navigation system in its contribution to the overall reliability of the
orbit determination, as measured by ΔV_{STAT} reduction. The second
parameter, P(C/OPT), can be used to assess the influence of obtaining
optical data at the control-point.

In terms of these two parameters, noting that "OPT" $\equiv$ "K", we
can write

$$P(C, K) = P(C/OPT) \cdot P(OPT) \qquad (5-5-5)$$

and

$$P(\sim C, \sim K) = P(\sim C/\sim K) \, P(\sim K)$$
$$= [1 - P(C/\sim K)] \, [1 - P(K)]$$

241

which, due to Eq. (5-5-2), gives

$$P(\sim C, \sim K) = 1 - P(OPT) \tag{5-5-6}$$

Similarly (or using Eq. 5-5-3)

$$P(\sim C, K) = P(OPT) \cdot (1 - P(C/OPT)) \tag{5-5-7}$$

Using Eqs. (5-5-5) through (5-5-7) in (5-5-4) and computing ΔV_{STAT} based on

$$\int^{\Delta V_{STAT}} f(\Delta V) = 0.99 \tag{5-5-8}$$

we can therefore parameterize ΔV_{STAT} in terms of P(OPT) and P(C/OPT).

The results of this parameterization are displayed in Figure 5-14(a) and (b) for a case where the radio OD was considerably degraded owing to very large (10 km) station longitude uncertainties assumed. Figure 5-14(a) demonstrates the importance of obtaining optical data in order to reduce ΔV_{STAT}. In the complete absence of optical data (P(OPT) = 0) ΔV_{STAT} is 265 m/sec; (typical allocation budgets are ~125 m/sec). On the other hand, with P(OPT) = 1, the acquisition of optical data at control reduces ΔV_{STAT} to 26 m/sec. Even with optical data available at only the knowledge point ΔV_{STAT} is 97 m/sec. Also, we note that increasing the reliability of successful control OD is effective (in the sense of significantly reducing ΔV_{STAT}) only with a fairly high reliability of the overall optical system — i.e. P(OPT) greater than 90%.

The sensitivity of ΔV_{STAT} TO P(C/OPT) for constant P(OPT) is illustrated in Figure 5-14(b); for instance, for a single camera system reliability of P(OPT) = 94% (if at least one camera system is

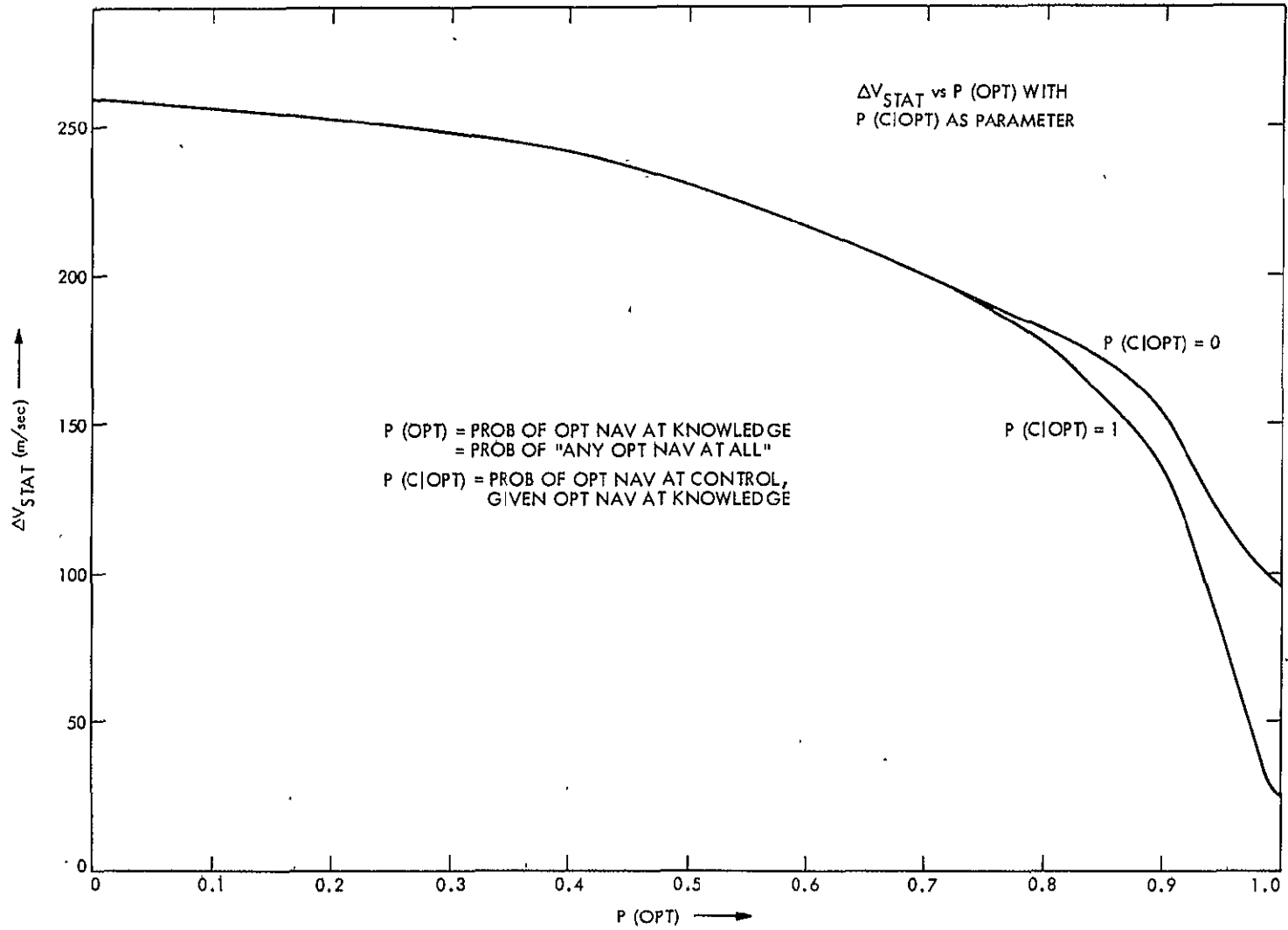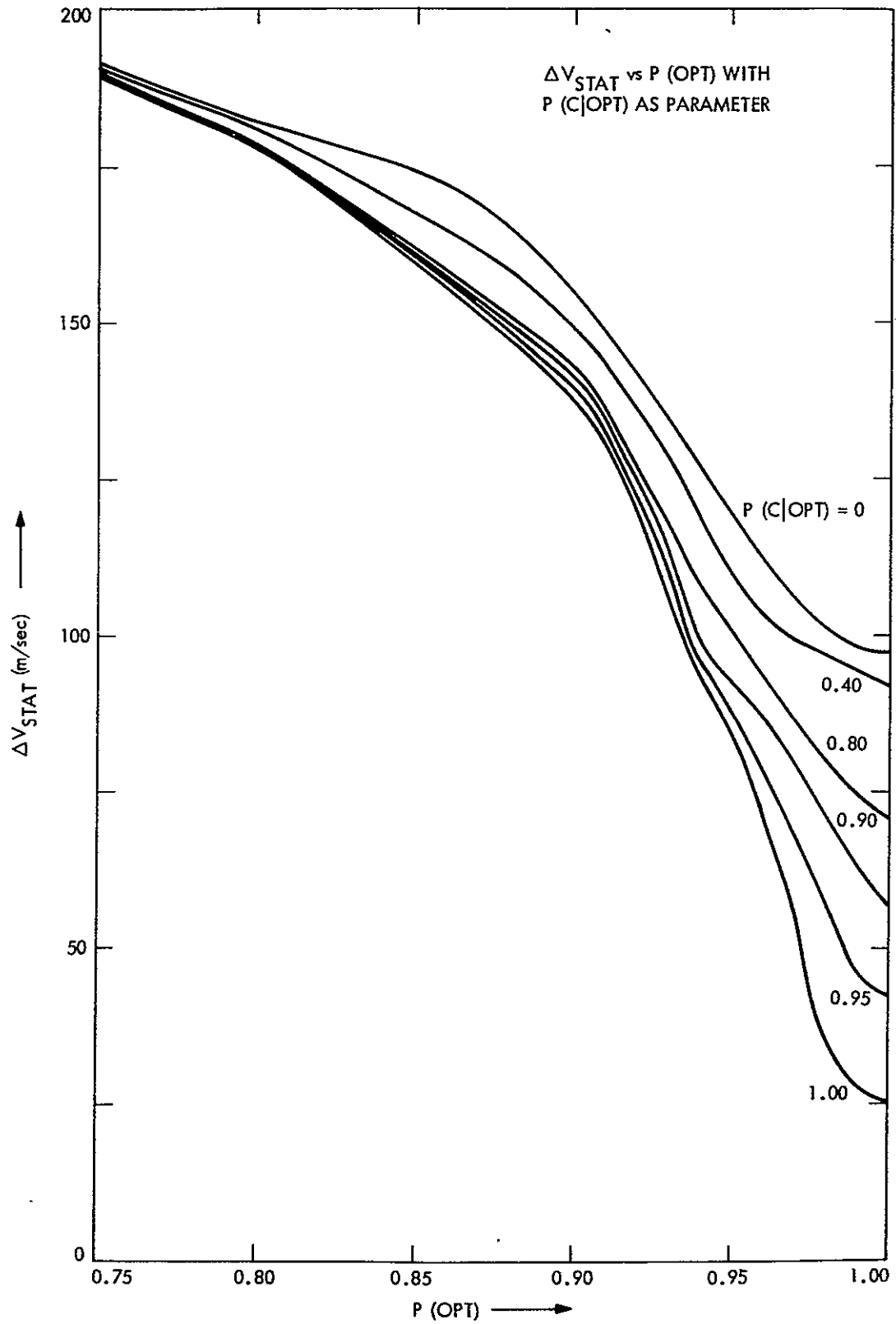Figure 5-14(a).   Parametric Probability Analysis

Figure 5-14(b). Parametric Probability Analysis Detail

operating, we are assured of optical data at knowledge), ΔV_{STAT} varies from 127 m/sec for P(C/OPT) = 0 to 93 m/sec for P(C/OPT) = 1.

The marked reduction in ΔV_{STAT} for high values of P(C/OPT) indicates that it would be beneficial to maintain this probability as high as possible. In fact, this relates to the star availability discussion in section 5.1. We have

P(C/OPT) = P(2 camera ON system/1 camera ON system)

x P(stars)

= P(2 TV/at least 1 TV) x P(stars)

$\approx$ P(2 TV) x P(stars)

where P(stars) is the probability of viewing stars on the vidicon at control. Since this probability may be zero in some extreme cases, it would be desirable to plan the flight trajectory so as to ensure a suitable star background at control.

CHAPTER 6

CONCLUSIONS

The central conclusion of the dissertation is that Optical

Navigation can be a very effective means of navigating an interplanetary

spacecraft during its approach phase to the planet, particularly with

the combined use of radio and optical data. More specifically, in the

following we discuss the principal conclusions of the investigations

reported here.

1) Of the three observation methods examined the satellite-star

method yields the best accuracies followed by the planet-star

two-camera method. The former is therefore the preferred

method for the knowledge phase; for the control phase the

latter must be used due to camera pointing limitations.

Optical navigation using the planet limb without stars is the

weakest method, but does contribute to an improvement in

accuracy relative to "radio-only" navigation; it would be a

viable choice in situations where the other two methods are

not available.

The primary error sources for the three methods are, respec-

tively, satellite ephemeris errors for the satellite-star

method, camera offset biases and planet center-finding errors

for the two-camera method, and TV pointing errors for the

planet-limb one-camera method.

2) Light-time effects are important and must be considered, but stellar aberration effects can be neglected. This is because (i) in the data types using stars, only star relative information is sought and differential stellar aberration effects are very small and (ii) in the planet limb one-camera method, camera pointing errors are an order of magnitude larger than the stellar aberration effect. Relativistic effects can be neglected for the current state of the art.

3) The optical navigation performance is not heavily dependent on the number of stars in the field of view when this is greater than one. However, calibration of the television and of the spacecraft instrumentation, prior to acquisition of optical data, is of significant aid in improving data accuracy.

4) The optical data and the radio data are complementary in their inherent information content for spacecraft navigation. The optical data types are relatively weak in their ability to determine velocity and time of flight information; radio data determines these same quantities quite precisely. On the other hand radio data is weak in the determination of the out-of-plane (ecliptic) component of position, where the optical data can contribute significantly.

5) The major error sources of the optical and radio data are quite different. For the latter the primary errors stem from uncertainties in the tracking station locations, planetary

ephemerides and non-gravitational accelerations. Optical data
is insensitive to these errors. On the other hand optical
data is affected by uncertainties in the satellite
ephemeris, TV pointing and camera characteristics, to all of
which radio data is insensitive.

6) The accuracies of the optical navigation processes, using the
three optical observation methods, differ markedly in their
sensitivity to the amount of radio data used. The final
accuracy using the satellite-star method is almost unaffected
by changes in the amount of radio data; the planet-star two-
camera method is significantly affected; and the planet limb
one-camera method is practically useless without some radio
data. However, the dependence of the two-camera method on
radio data reduces considerably if the data arc is lengthened,
and almost disappears for sufficiently long optical data
spans. In these situations the optimal strategy is to acquire
data at the beginning and at the end of the data span, with no
data in between.

In all cases a combination of optical and radio data yields
the best results and much earlier than either separately.

7) From the orbit determination point of view, the maneuver
timing should be delayed as much as feasible, so as to benefit
from the strength of the optical data, which increases with
decreasing range from the planet.

8) The consistency analysis technique should be applied to the
radio and optical estimates. This can help in establishing

248

the validity of each data type or aid in the detection and resolution of inconsistencies.

9) The sensitivity study of navigation fuel costs versus optical subsystem reliability shows that enhancement of control orbit determination reliability is effective only for a high overall optical system reliability (greater than 90%). Since this latter reliability should typically be quite high, attention to control optical OD, particularly in the area of star availability, would be fruitful.

Looking towards the future of space navigation, the next major step will be in the area of Autonomous Navigation (see Ref. 43). Since this must be a completely self-reliant system with no earth-based dependence, optical navigation will play a major role in its development. In addition some means to supplement optical angular data with a data type providing range information may be needed in the future.

REFERENCES

1. Hamilton, T. W., and W. G. Melbourne, "Information Content of a Single Pass of Doppler Data from a Distant Spacecraft," Jet Propulsion Laboratory, Pasadena, California, Space Programs Summary Number: 37-39, May 31, 1966, Vol. III.

2. Light, J. O., "An Investigation of the Orbit Redetermination Process Following the First Midcourse Maneuver," Jet Propulsion Laboratory, Pasadena, California, Space Programs Summary Number: 37-33, June 30, 1965, Vol. IV.

3. Curkendall, D. W., and S. R. McReynolds, "A Simplified Approach for Determining the Information Content of Radio Tracking Data," Journal of Spacecraft & Rockets, Vol. 6, May 1969.

4. Curkendall, D. W., Problems in Estimation Theory with Applications to Orbit Determination, Ph.D. in Engineering, Engineering Systems Department, University of California, Los Angeles, 1971.

5. Jordan, J. F., G. A. Madrid, and G. E. Pease, "The Effects of Major Error Sources on Planetary Spacecraft Navigation Accuracies," (Paper presented at the AAS/AIAA Astrodynamics Conference, August 19-21, 1970, Santa Barbara, California.)

6. Battin, R. H., Astronautical Guidance, McGraw Hill, New York, 1964.

7. Bean, B. R., and E. J. Dutton, Radio Meteorology, Dover Publications, New York, 1968.

8. Rishbeth, H., and O. K. Garriott, Introduction to Ionospheric Physics, Academic Press, New York, 1969.

9. Fliegel, H. F., and R. N. Wimberly, "Time and Polar Motion," in "Tracking System Analytic Calibration Activities," Jet Propulsion Laboratory, Pasadena, California, Technical Report 32-1587, March 1974.

10. Trask, D. W. and P. M. Muller, "Timing: DSIF Two-Way Doppler Inherent Accuracy Limitations," Jet Propulsion Laboratory, Pasadena, California, Space Programs Summary Number 37-39, May 31, 1966, Vol. III.

11. Melbourne, W. G., et al., "Constants and related information for astrodynamic calculations," Jet Propulsion Laboratory, Pasadena, California, Technical Report 32-1306, July 15, 1968.

12. Martin Marietta Aerospace, "The Viking Mission to Mars," Report 75-16764, 1975.

250

13. Gates, C. R., and H. J. Gordon, "Planetary Approach Guidance," *Journal of Spacecraft and Rockets*, Vol. 2, No. 2, March-April 1965.

14. Silver, B. W., "Grand Tours of the Jovian Planets," *Journal of Spacecraft and Rockets*, Vol. 5, No. 6, June 1968.

15. Friedlander, A. L., "Guidance Analysis of the Multiple Outer Planet (Grand Tour) Mission," *Journal of Spacecraft and Rockets*, Vol. 6, No. 4, April 1969.

16. Flanders, J. H., D. C. Fraser, and J. R. Lawson, "Technology for Guidance and Navigation of Unmanned Deep Space Missions in the 1970's," AIAA Paper 68-1104, Philadelphia, Pa., 1968.

17. Chamberlain, F. R., "Development of an Approach Guidance Optical Planet Tracker," Jet Propulsion Laboratory, Pasadena, California, Space Programs Summary Number 37-52, August 31, 1968, Vol. III.

18. Breckenridge, W. G., and T. C. Duxbury, "Investigation of Planetary Navigation using Spacecraft-Based Measurements," paper presented at the ION National Space Meeting, NASA Manned Spacecraft Center, Houston, Texas, April 22-24, 1969.

19. Duxbury, T. C., "Navigation Data from Mariner Mars 1969 TV Pictures," *Navigation*, Vol. 17, No. 3, Fall 1970.

20. Duxbury, T. C., "A Spacecraft-Based Navigation Instrument for Outer Planet Missions," *Journal of Spacecraft and Rockets*, Vol. 7, No. 8, August 1970.

21. Garcia, H. A., "The Contribution of Onboard Optical Instrumentation to Deep Space Navigation," paper presented at the AAS/AIAA Astrodynamics Specialists Conference, Ft. Lauderdale, Florida, August 17-19, 1971.

22. Jerath, N., "Evaluation of Optical Data for Mars Approach Navigation," paper presented at the Institute of Navigation Annual Meeting, West Point, New York, June 27-29, 1972.

23. Duxbury, T. C., G. H. Born, and N. Jerath, "Viewing Phobos and Deimos for Navigating Mariner 9," *Journal of Spacecraft and Rockets*, Vol. 11, No. 4, April 1974.

24. Jerath, N., and H. Ohtakay, "Mariner IX Optical Navigation Using Mars Lit Limb," *Journal of Spacecraft and Rockets*, Vol. 11, No. 7, July 1974.

25. Ondrasik, V. J., G. A. Ransford, and C. E. Hildebrand, "An Analysis of Outer Planet Navigation Systems," paper presented at the AIAA/AAS Astrodynamics Conference, Palo Alto, California, September 11-12, 1972.

26. Wong, K. W., _Photogrammetric Quality of Television Pictures_, Ph.D. Dissertation, Cornell University, Ithaca, New York, January 1968.

27. Moyer, T. D., "Mathematical Formulation of the Double-Precision Orbit Determination Program (DPODP)," Jet Propulsion Laboratory, Pasadena, California, Technical Report 32-1527, May 1971.

28. Lieske, J. H., et al., "Simultaneous Solution for the Masses of the Principal Planets from Analysis of Optical, Radar, and Radio Tracking Data," _Celestial Mechanics_, Vol. 4, 1971.

29. "Explanatory Supplement to the Astronautical Ephemeris and the American Ephemeris and Nautical Almanac," Her Majesty's Stationery Office, London, 1961.

30. Wilkins, G. A., "The Analysis of the Observations of the Satellites of Mars," _Modern Questions in Celestial Mechanics_, G. Colombo ed., Edizione Cremoshese, Rome, 1967.

31. Born, G. H., and T. C. Duxbury, "The Motions of Phobos and Deimos from Mariner 9 TV Data," _Celestial Mechanics_, Vol. 12, 1975.

32. Thompson, M. M., ed., _Manual of Photogrammetry_, 3rd ed., Vol. 1, American Society of Photogrammetry, Falls Church, Va., 1966, pp. 461-490.

33. Duxbury, T. C. and H. Ohtakay, "In-Flight Calibration of an Interplanetary Navigation Instrument," _Journal of Spacecraft and Rockets_, Vol. 8, No. 10, October 1971, pp. 1038-1042.

34. Kalman, R. E., "A New Approach to Linear Filtering and Prediction Problems," _Journal of Basic Engineering_, Vol. 82D, March 1960.

35. Meditch, J. S., _Stochastic Optimal Linear Estimation and Control_, McGraw Hill, New York, 1969.

36. Jazwinski, A. H., _Stochastic Processes and Filtering Theory_, Academic Press, New York, 1970.

37. Leondes, C. T., ed., _Theory and Applications of Kalman Filtering_, NATO-AGARDograph No. 139, February 1970.

38. Duxbury, T. C., and N. Jerath, "Optical Observable and Partial Generator Program," Jet Propulsion Laboratory, Document No. 900-474, October 31, 1971 (JPL internal document).

39. Pace, G. D., G. I. Jaivin, and R. A. Virzi, "Mariner Mars 1971 Scan Platform Pointing Calibration," _Jet Propulsion Laboratory, Quarterly Technical Review_, Vol. 2, No. 1, April 1972.

40. Ohtakay, H., and N. Jerath, "Mariner Mars '71 Optical Lit Limb Data Measuring Techniques and Navigation Results," paper presented at the AIAA 11th Aerospace Sciences Meeting, Washington, D.C., January 10-12, 1973.

41. Cain, D. L., et al., "Approximations to the Mean Surface of Mars and Mars Atmosphere using Mariner 9 Occultations," Journal of Geophysical Research, Vol. 78, No. 20, 1973.

42. Brouwer, D. and G. M. Clemence, Methods of Celestial Mechanics, Academic Press, New York, 1961.

43. Kohlhase, C. E., "Autonomous Navigation Preparations for Future Unmanned Space Missions," Navigation, Vol. 22, No. 1, Spring 1975.

44. Kizner, W. A., "A Method of Describing Miss Distance for Lunar Distance for Lunar and Interplanetary Trajectories," External Publication No. 674, Jet Propulsion Laboratory, Pasadena, California, August 1959.

APPENDIX A

B-PLANE DEFINITION

The target parameters used for accuracy analysis are the $\underline{B}$ plane parameters (Ref. 44) defined in Figure A-1. The uncertainty in these parameters is mapped into the 1 σ aim plane dispersion ellipse.

The following definitions for the B-plane refer to Figure A-1.

Parameter	Definition
$\underline{B}$	The vector from the center of the target body directed perpendicular to the incoming asymptote of the target centered approach hyperbola.
$\underline{S}$	Unit vector from the center of the target body, in the direction of the incoming asymptote of the target centered approach hyperbola.
$\underline{T}$	Unit vector from the center of target body, defined by the intersection of the plane normal to the incoming asymptote with a reference plane (usually at the true ecliptic of date) centered at the target body.
$\underline{R}$	Unit vector perpendicular to $\underline{T}$ in the $\underline{B}$, $\underline{T}$ plane (defined as the B-plane), positive toward the $-z$ direction of the reference plane.
$\underline{B} \cdot \underline{R}$	The component of $\underline{B}$ along $\underline{R}$.
$\underline{B} \cdot \underline{T}$	The component of $\underline{B}$ along $\underline{T}$.
SMAA	The semi-major axis of the one-sigma uncertainty ellipse in the $\underline{R}$, $\underline{T}$ plane.

254
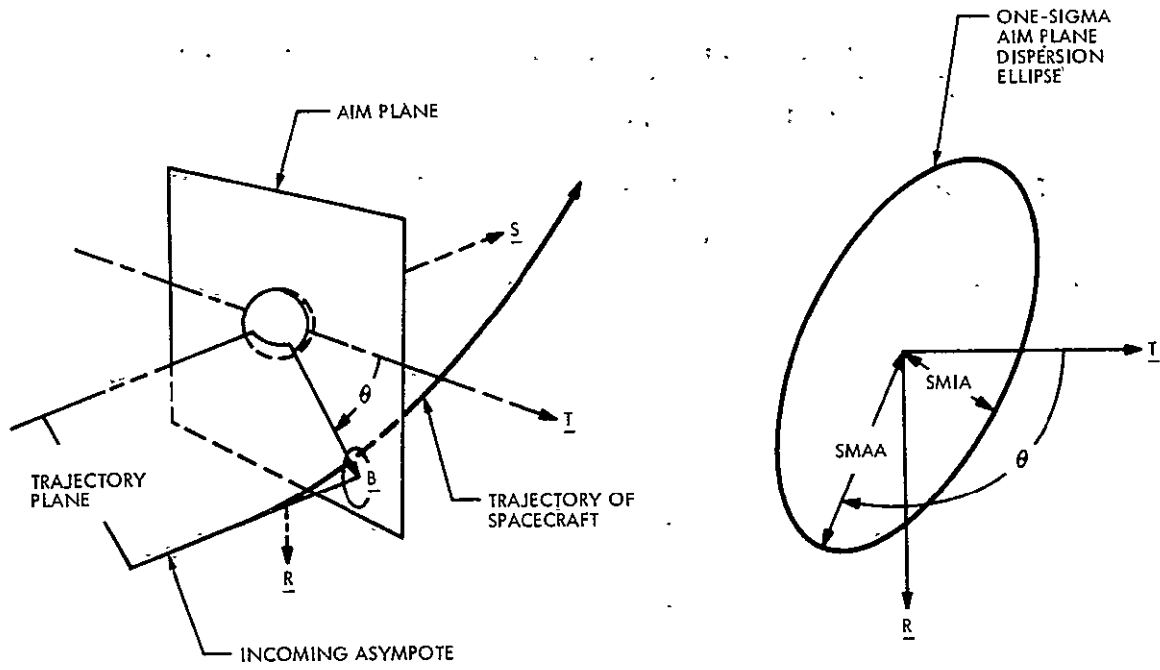
Figure A-1. B-Plane Definitions

Parameter	Definition
SMIA	The semi-minor axis of the one-sigma uncertainty ellipse.
θ	The orientation angle of SMAA measured positive clockwise from $\underline{T}$ to $\underline{R}$.
T_f	The uncertainty of time of closest approach to the target.